THE ELASTIC SCATTERING OF 3.0 MeV POLARISED NEUTRONS BY MEDIUM MASS NUCLEI

Thesis

Submitted by

HADI SAVALONI, B.Sc., M.Sc.

for the degree of

DOCTOR OF PHILOSOPHY

University of Edinburgh,

JANUARY, 1985.

To my parents

C O N T E N T S

C O N T E N T S (Contd.)

C O N T E N T S (Contd.)

ABSTRACT

In fast neutron scattering experiments, the calibration of the system is of prime importance. Since in elastic scattering neutron measurements a discrimination level has to be set, hence the relation between scintillator light output and energy is important. For this reason, the response of four NE213 organic scintillators to electrons and protons are measured, using standard gamma sources, an Am-Be neutron source, and mono-energetic neutrons from D-D and D-T reactions.

After establishing an acceptable way of neutron detector calibration, in order to fill the gap between two sets of analysing power data for light nuclei and heavy nuclei, accurate measurements of analysing power and differential cross sections were made on the medium weight nuclei, for which data are scarce, namely Cd, Sn, Sb, Te and I, using a neutron polarimeter holding 24 (12 pairs) NE213 liquid scintillation counters. A new Pulse Shape Discrimination circuit in conjunction with a newly built up detector (scintillation counter) provided an improved system for reduction of the background, while the background was reduced by a new arrangement of the shielding around the polarimeter as well.

The measured data on the analysing power and differential cross sections were corrected for finite sample size effects. The analysing power and differential cross section data are compared with the predictions of the Optical Model, while compound nucleus formation is also considered. A few sets of optical potential parameters were tried as well as the Best Fit optical potentials, which were obtained individually for each nucleus. The inclusion of an Imaginary Spin Orbit term is also considered in part of the data analysis, while

the analysing power data only is compared with the predictions of the Optical Model in another part of the data analysis. Coupled channels calculations did not affect the results obtained for Cd, Te and Sn, although the first two nuclei are well known vibrational nuclei.

CHAPTER I

INTRODUCTION

1.1 Nuclear Reactions

The interaction of an incident particle with a target is considered as a nuclear reaction or nuclear scattering process, if the projectile energy is sufficiently high to be able to ignore the extra-nuclear structure of the target atoms. Detailed theories of nuclear reaction were patterned after two apparently contradictory models of nuclear structure, the liquid drop model and the shell model. In one theory, Bohr[1] suggested the formation of the compound nucleus. A nuclear projectile incident on a nucleus would interact strongly with all the nucleons in the nucleus and quickly share its energy with them (strong coupling model). A reaction that proceeds by way of compound nucleus formation is regarded as a two-step process, the formation process and the break up. It is assumed that the time lapse between the two events is sufficiently long (several times the period of oscillation of a nucleon in the nucleus) that at the time of break up (decay of compound nucleus) no trace is left that identifies the particular process of formation. This was found to be a successful model for interpretation of nuclear reactions at low energies.

The success of the shell model cast some doubt upon the fundamental assumption of the strong coupling model. As a consequence of observations on nuclei in the ground state and at low excitation energies the shell model gave much evidence that a

nucleon can traverse freely inside the nucleus without apparently changing the quantum state of the target nucleus, although there was no clear evidence that this apparent absence of interaction is also valid at those excitation energy ($\sim$ 8 MeV) which are created in nuclear reactions with neutrons of a few MeV.

In the reaction theory based on the shell model, it was proposed by a number of authors[2,3 and 4] that an incident nucleon would interact with the nucleus via the shell model potential and that the probability of absorption into the compound nucleus would be relatively small.

Weisskopf[5] and Feshbach[6] have unified these different aspects of a nuclear reaction into a single theory. In this theory, any nuclear interaction proceeds through a series of stages (Fig. 1.1). The nuclear reaction is divided into three successive stages, the independent particle stage, the compound-system stage, and the final stage. When the incident particle reaches the edge of the nuclear potential, the first interaction will be a partial reflection of the wave function, called Shape Elastic Scattering. The part of the wave function which enters the nucleus undergoes absorption. The first step in the absorption process consists of a two-body collision. If the incident particle (a single nucleon) interacts with a single nucleon in the nucleus and if the struck nucleon, which is raised to an unfilled level, leaves the nucleus, a Direct Reaction has occurred. A more complicated situation occurs if the struck nucleon stays in the nucleus and secondary collisions take place between either the incident nucleon or the struck nucleon with a second nucleon, in turn raising the second

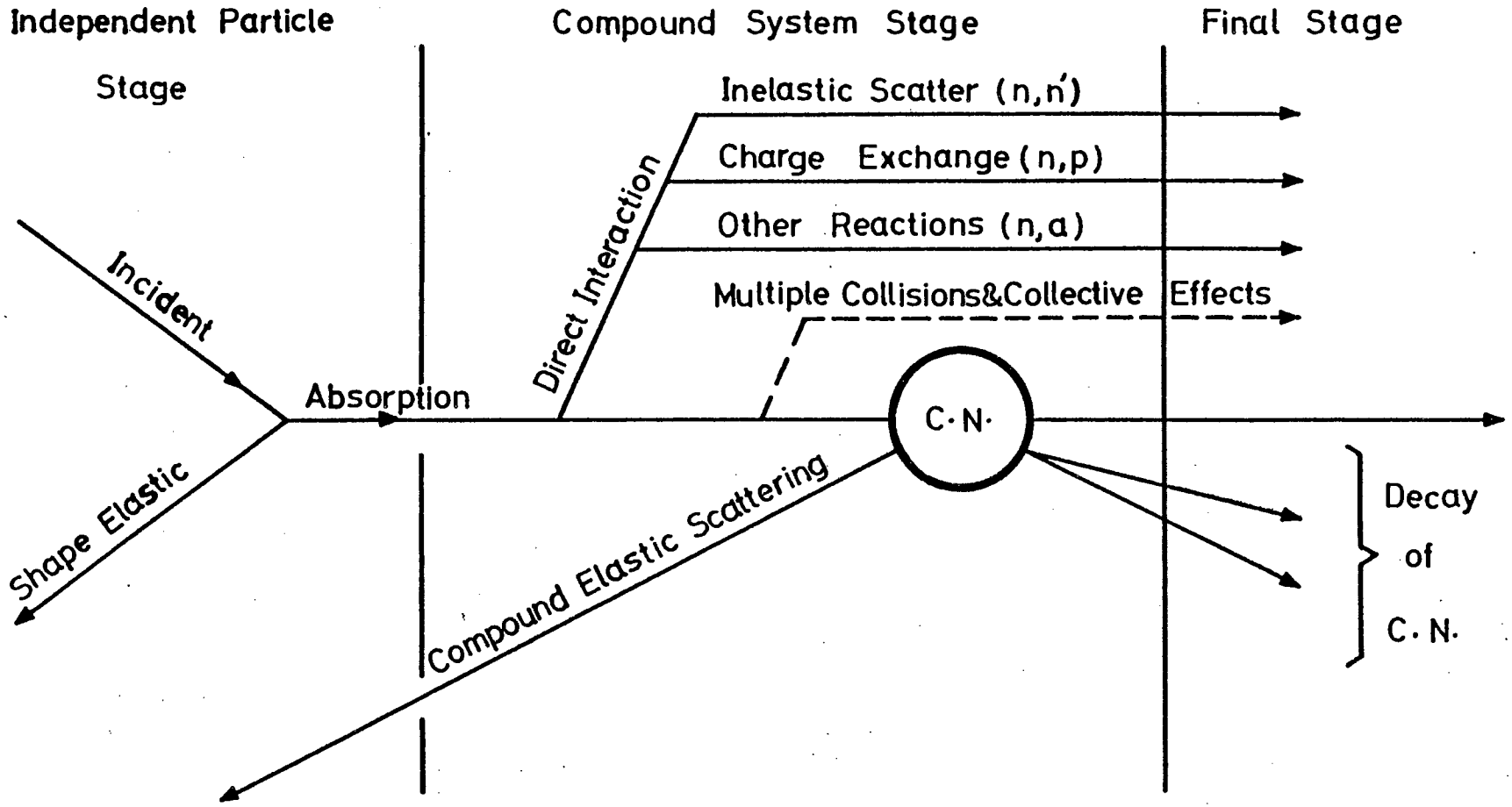
Independent Particle
Stage
Compound System Stage
Final Stage
Inelastic Scatter (n,n')
Charge Exchange (n,p)
Other Reactions (n,a)
Multiple Collisions&Collective Effects
Direct Interaction
Incident
Absorption
C·N·
Shape Elastic
Compound Elastic Scattering
Decay
of
C·N·

Fig·1·1·

nucleon to an unfilled level. If it does not leave the nucleus, then a more complicated situation due to third and higher order collisions occurs until finally the energy sharing is ended by formation of the compound-nucleus.

If the compound nucleus decays in a way that the emitted particle is the same kind as the incident particle with the same (c.m.) energy, this is called Compound Elastic Scattering. This particle can not be distinguished from a shape elastically scattered particle, except in principle by a slight time delay, which is not remotely approached by the time resolution of existing experimental apparatus. The angular dependence of the compound scattering is nearly isotropic, while direct processes produce a highly anisotropic distribution.

1.2 Neutron Elastic Scattering

Since neutrons are uncharged particles they play an important role in studying the interaction mechanism between nucleons and nuclei. Neutrons do not involve the Coulomb interaction and hence are not repelled by the target nucleus.

In the collision between neutrons and heavy nuclei, the elastic scattering is of primary interest, the cross section for which can be found directly from the counting rate at particular scattering angles, assuming the detection efficiencies and neutron incident flux are known.

$$\frac{d\sigma_{el}(\theta)}{d\Omega} = \frac{Sr^2}{IN}$$

where S is the scattered neutron flux at angle θ, N is the number of nuclei in the scatterer, I is the neutron flux incident on the scatterer and r indicates the average distance between the scatterer and the detector. The elastic scattering cross section can be expressed as

$$\sigma_{el} = \sigma_{SE} + \sigma_{CE}$$

where σ_{SE} is the shape elastic cross section and σ_{CE} is the compound elastic cross section, the processes discussed in Section 1.1. The elastic cross section has an angular dependence and is expressed as

$$\sigma_{el} = \frac{d\sigma_{el}}{d\Omega}(\theta)d\Omega$$

where $\frac{d\sigma_{el}(\theta)}{d\Omega}$ is the differential cross section.

The term polarisation as applied to nucleons refers to the orientation of the intrinsic spins of the nucleons. For spin $\frac{1}{2}$ particles, protons and neutrons, quantization limits the number of possible spin orientations to two, often referred to as "up" and "down" with respect to the plane of the reaction. The polarisation of a beam of spin $\frac{1}{2}$ particles may be written as

$$P = \frac{N^+ - N^-}{N^+ + N^-}\ \underline{n}$$

where N^+ and N^- are the number of particles with spins parallel

(up) and antiparallel (down) to the quantization axis defined by $\underline{n}$.

Fig. 1.2 illustrates a method which is commonly employed for fast neutron polarisation experiments. A beam of unpolarised charged particles (of energy E) along the direction $\underline{K}_o$ incident on the target produces neutrons of polarisation $P_n(E,\theta_1)$ and energy E_n in the direction $\underline{K}1$. These neutrons are intercepted by a scattering sample, referred to as the analyser. Thus the beam of polarised neutrons is scattered through angles θ and ϕ. The number of neutrons scattered by the analyser through angles θ and ϕ is proportional to the differential cross section which can be expressed as

$$\sigma(E_n,\theta,\phi) = \sigma(E_n,\theta)[1 + P_n(E,\theta_1)A(E_n,\theta_2)\cos\phi]$$

where $A(E_n,\theta_2)$ is the elastic scattering analysing power and equals the polarisation $P_s(E_n,\theta_2)$ that would result if unpolarised neutrons of energy E_n were elastically scattered through θ_2 by the scattering sample. Therefore the right - left asymmetry in the reaction plane defined by $K_o \times K_1$ can be expressed as

$$r = \frac{L}{R} = \frac{1 + P_n(E,\theta_1)P_s(E_n,\theta_2)}{1 - P_n(E,\theta_1)P_s(E_n,\theta_2)}$$

where L and R are the intensities scattered to the left and to the right, respectively. The above relation yields the following expression

$$P_n P_s = \frac{L - R}{L + R} = \frac{r - 1}{r + 1} \quad .$$

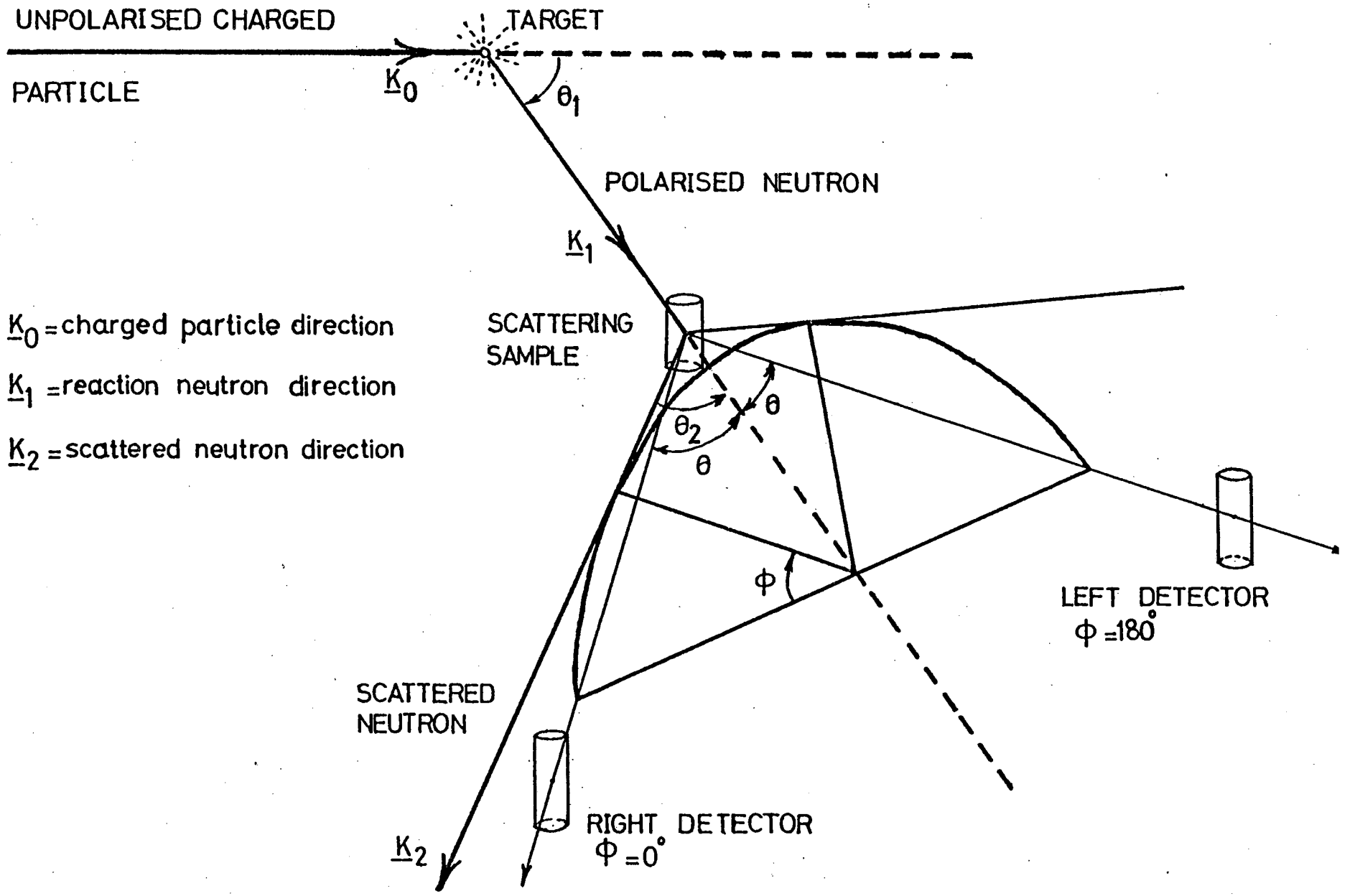

Figure-1-2, BASIC LAYOUT OF POLARISATION EXPERIMENT

The direct method of obtaining P_s requires a double scattering process in which unpolarised neutrons of energy E_n are elastically scattered twice, while the target and the scattering sample are of the same kind. This approach has been used only with ^4He and with ^{12}C.

When P_s is known the value of polarisation P_n can be obtained. With P_n known the system can be used to find the polarisation resulting from elastic scattering by other nuclei.

In a conventional double-scattering experiment, Fig. 1.2 according to the "Basel convention"[7] the polarisation is positive if in the direction $n = \frac{(K_1 \times K_o)}{|K_1 \times K_o|}$.

1.3 Optical Model

Feshbach et al.[4] amalgamated the shell model and the compound nucleus model into the nuclear Optical Model, as an attempt to explain the consequences of a reduced interaction between the nucleon and the nucleus, i.e. the actual formation of a compound state occurs only with a probability less than unity, once the particle has entered the nucleus. The particle has a finite probability of leaving the nucleus without any exchange of energy or momentum and so a real potential can describe this interaction between the particle and the nucleus. If the incident particle suffers an exchange of energy with the formation of a compound state, then the interaction would have aspects of the absorption of the particle and should be described by a

complex potential. Hence in the Optical Model, the nucleus is treated as a translucent medium in which the probability of absorption of a nucleon by a nucleus is reduced due to the limited number of final states available according to the Pauli principle. This description obviously oversimplifies the interaction between particle and nucleus, and naturally can not reproduce all features of nuclear reactions. In particular, it will not reproduce any resonance phenomena which are connected with many possible quantum states of the compound system. Therefore this model only describes the features of nuclear reactions (cross sections) which are averaged over the resonances of the compound nucleus.

Following these ideas the calculation of cross sections can be performed with a local central complex potential

$$V(r) = - Uf(r) - i\,Wg(r)$$

where U and W are potential depths and $f(r)$ and $g(r)$ are form factors describing the radial variation of the potential. The real potential is expected to be uniform in the nuclear interior in accordance with the short range and the saturation properties of the nucleon-nucleon forces and also to show exponential fall-off with increasing radius, a feature characteristic of the nucleon-nucleon interaction. The imaginary part may be expected to be a combination of volume and surface absorption terms. However, where the density is high, the absorption of nucleons is reduced by the Pauli exclusion principle, so that the absorption is surface peaked.

The nucleons scattered from nuclei are generally observed to be polarized and a spin-orbit potential is included, which is assumed to be proportional to $\vec{\ell}\cdot\vec{\sigma}$ where $\vec{\ell}$ and $\vec{\sigma}$ are the angular momentum and Pauli spin operators, respectively. For symmetry reasons the spin-orbit potential is expected to be small inside the nucleus but appreciable in the surface region[8].

$$V_{so} = U_{so}\left(\frac{\hbar}{\mu_\pi c}\right)^2 \frac{1}{r}\left(\frac{d}{dr}\right)\left|f(r)\right| \vec{\ell}\cdot\vec{\sigma}$$

where the constant μ_π denotes the pion mass.

1.4 Review and Outline of the Present Study

Evaluation of an optical model potential which can describe total cross sections, differential cross sections and analysing powers requires a great deal of experimental data which covers a wide range of nuclei.

Since the discovery of neutrons, experiments with neutrons have played an important role in advancing the understanding of nuclear reaction mechanisms. One reason is, of course, the freedom from complexities of Coulomb effects when using a neutral particle as a probe.

The elastic scattering cross sections and differential elastic scattering cross sections have been reproduced quite successfully by neutron optical model potentials[9-11]. Measurements of analysing power in fast neutron scattering provides the most direct check of the magnitude of the spin-orbit term in the optical model used to describe the nucleon-nucleus interaction. Owing to the difficulties

in performing experiments with polarised neutrons such data of good accuracy are scarce for neutron scattering at all energies.

Indeed, apart from the work by Wiedmann et al.[12] and by Ellgehausen et al.[13] for nuclei of mass less than Zr, only during the course of the present work have measurements of analysing power of good accuracy and wide angular coverage been reported. This recent improvement in accuracy and angular coverage has been achieved in three ways, each of which has provided more efficient data collection. One, for work with 10-14 MeV neutrons[14] by use of a pulsed polarized deuteron beam to produce the neutrons for scattering, another by use of an uncommonly intense d.c. deuteron beam to produce 7 MeV neutrons[15] and the third by use of 22 detectors to measure the analysing power at 11 scattering angles simultaneously[16] in work with 3 MeV neutrons.

The present project is concerned with the analysing power of elastic scattering of 3 MeV neutrons. Amongst the best of previous measurements in this energy region are the measurements by Ellgehausen et al., and by Annand. Ellegehausen et al. found that the angular dependence of the analysing powers of Ti, Cr, Fe, Cu and Zn were well fitted by optical model calculations which also fitted the available differential cross sections. For much heavier nuclei, Annand found that of analysing power measurements on W, Hg, Tl, Pb, Bi and U only the Hg data showed good agreement with calculation. It was therefore decided to investigate the situation for nuclei which would extend the work of Annand towards the mass region studied by Ellegehausen et al. In particular Cd, Sn, Sb, Te and I were selected for study.

The neutron scattering work which has been performed during

the last three decades at energies less than 5 MeV is summarised below.

1956 Beyster et al.[17]: Measured the differential elastic scattering cross section at 2.5 MeV neutron energy for Aℓ, Fe, Zr, Sn, Ta and Bi over 15° - 160° and at 7.0 MeV for Be, C, Aℓ, Fe, Zr, Sn, Ta and Bi over 12° - 150°. Inelastic cross sections were also measured for a number of elements at 1.0, 1.77, 2.5, 3.25 and 7.0 MeV neutron energies. They compared their results with cross sections calculated using an Optical Model of the elastic scattering. For the energies (> 4 MeV) above which appreciable compound elastic scattering occurs a reasonable agreement with the experimental values was obtained.

1957 McCormac et al.[18]: Measured the analysing power over 30° - 135° for Be, C, Cu, Zr, Sn and Pb at 3.1 MeV. Poor agreement with the few available Optical Model calculations was observed. No spin-orbit term was included in the optical potential.

1958 Clement et al.[19]: Measured the analysing power for 21 nuclei from V to U at 55°, 90° and 130° in the neutron energy range 0.38 to 0.98 MeV. The optical model calculations failed to reproduce satisfactorily the experimental results.

1958 Pasechnik et al.[20]: Measured the differential elastic cross section for Fe, Cu, Zn, Cd, Sn, Sb, Hg, Pb and Bi at 2.8 MeV neutron energy. Comparison of the experimental data with an optical model of the nucleus with a rectangular potential well showed that it is impossible to explain the experimental angular distribution of scattered neutrons in this way. Replacement

of the rectangular potential well by a diffused-edge nuclear potential considerably improved the agreement between experimental values and theoretical calculations.

1961 Brown et al.[21]: Measured the analysing power of 0.5 to 1.5 MeV neutrons scattered by Cu, Zn, Mo and Cd at 55° and Cu and Mo at 90°. Considerable discrepancy was observed between the results and predictions of optical model calculations, including a real spin-orbit term.

1963 Gilboy et al.[22]: Measured the differential cross sections for twenty elements, from Na^{23} to U^{238}, including ten rare earth elements over 30° to 137° at 1.0 MeV by the neutron time-of-flight technique. Most of the data were fitted quite well by the prediction of optical model calculations (apart from Na and Aℓ). The quality of the fits to the data for the distorted nuclei in the rare earth region was just as good as for the fits to the closed shell nuclei.

1964 Elwyn et al.[23]: Measured analysing power and differential cross sections for Zr, Nb, Mo and Cd at neutron energies below 1 MeV at 24°, 56°, 86°, 118° and 150°. Inclusive of a complex spin-orbit potential in an optical model equivalent to the non-local model of Perey and Buck[24] lead to a qualitative consistency.

1964 Olness et al.[25]: Measured the analysing power at 51.5° for 18 medium-heavy and heavy nuclei at 1.5 MeV. An additional term proportional to neutron excess, $(N - Z)/A$, was required in the real part of the optical potential in order to fit

the data for both medium - heavy and heavy nuclei.

1966 Ferguson et al.[26]: Measured the analysing power of 0.4, 0.7 and 1.0 MeV neutrons scattered by 14 nuclei from Ti to Bi at 55°. Comparison of the data with calculations using Perey and Buck's non-local optical potential[24] showed a reasonable agreement taking into account the experimental errors, except for the heavy deformed nuclei.

1966 Vonach et al.[27]: Measured differential elastic and inelastic cross sections of Ag, In and Cd in the neutron energy range 0.3 to 1.5 MeV over 20° to 145° by the neutron time-of-flight technique. The results were in good agreement with previously reported results of other authors, and showed a good fit to the calculated values based upon an optical model having validity over an extended mass-energy region.

1966 Buccino et al.[28]: Measured differential cross sections for twelve elements ranging in mass from 90 to 238 at an energy of 5.0 MeV by the time-of-flight technique. The results were compared with a local potential optical model as well as the non-local potential optical model of Perey-Buck[24]. Both models reproduced reasonably good agreement with experiment for most elements, with the exception of Radio Pb and Tℓ.

1966 Kazakova et al.[29]: Measured the analysing power of 3.25 MeV neutrons through 120° by the nuclei of twenty light and medium elements ranging from Li to Ba. The results are not in agreement with the optical model calculations based on Björklund-Fernbach potential[30].

1966 Becker et al.[31]: Measured differential elastic cross sections for 36 elements in mass range A = 26 - 209 over 20° - 130° degrees at 3.2 MeV energy. They tried to establish a set of global potential parameters which reproduce cross sections for all nuclei, but this was unsuccessful. Rosen's parameters[32] also gave similarly unsuccessful results.

1967 Mahajan[33]: Measured the analysing power at 40°, 60° and 90° for twenty elements from Ti to Bi at 4.4, 5.0 and 5.5 MeV neutron energies. A reasonable agreement was found between the experimental data and the predictions of an optical model potential using Real, Imaginary and Spin-Orbit components introduced by Rosen[32] allowing for the poor statistical accuracy of the data.

1968 Gorlov et al.[34]: Measured the analysing power and differential elastic cross sections over 10° - 170° for elements from Be to Bi at an energy of 4.0 MeV. They used an optical potential with the Real central potential including a neutron excess term (i.e. $V_1 = V_o\ (1 - \frac{N-Z}{KA})$ with $V_o = 50$ and $K = 3$), and also a spin-orbit potential. A unified set of parameters was obtained which sufficiently well described the scattering of polarized neutrons by nuclei with mass numbers from 60 to 209 at 4.0 MeV. The accuracy of the analysing power data was not high.

1968 Holmqvist[35]: Measured differential elastic cross sections in the energy range 1.5 to 8.1 MeV from Aℓ, S, Ca, Cr, Mn, Fe, Co, Ni, Cu, Zn, In and Bi over 20° - 160° by the neutron time-of-flight technique. Optimum values of optical model parameters were obtained individually for each element.

Very good agreement between theory and experiment was achieved. Except for the even mass number elements, the optical model parameters were independent of the neutron energy. The real and imaginary radii were found not to follow the simple expression $R = r_o A^{1/3}$.

1968 Korzh et al.[36]: Analysed their data[37] and those of other Laboratories on the differential cross sections for neutrons of 1.5 MeV energy for nuclei of 32 elements from Na to U^{238}. They showed that for deformed nuclei it was impossible to obtain agreement between the calculations and the experimental data by adjusting the parameters of the potential of the spherical model.

1969 Wiedmann et al.[12]: Measured the analysing power over 30° - 140° for Mg, Aℓ, Si and S at an energy of 3.25 MeV. Their result positively disagrees with optical model prediction.

1969 Ellgehausen et al.[13]: Measured the analysing power of 3.25 MeV neutrons over 30° - 140° degrees for elements Ti, Cr, Fe, Cu, Zn and Zr. These are some of the most accurate analysing power data. A reasonable agreement was found between the prediction of an optical model potential introduced by Rosen[38] and the experimental data for all nuclei except for Zr.

1973 Gupta et al.[39]: Measured differential cross-sections at the angles 10° and 180° for Pb and Sn at an energy of 3.65 MeV using the associated particle technique. The results at 180° were anomalously high compared with optical model predictions.

1974 Zijp and Jonker[40]: Measured the analysing power for 3.2 MeV neutrons for 20 elements from Ti to Bi over a range of 30° - 150° and 30° to 75°. None of the known potentials[10,24,34,31] gave a good description for all elements. But even with individual analyses no satisfactory agreement was achieved. Coupled channels calculations were performed. They concluded that the influence of the direct excitation of low lying levels on the elastic scattering is very large and can explain the difficulties encountered in the spherical optical model analyses.

1979 Galloway and Waheed[42]: Measured elastic differential cross sections and analysing power for Fe, Cu, I, Hg and Pb over 20° to 160° at a neutron energy of 2.9 MeV. Known global potentials and other previously suggested potentials gave general trends of Fe and Cu distributions. Parameters optimised for individual elements showed even poor agreement with I, Hg and Pb analysing power distribution.

1981 Begum and Galloway[43]: Measured analysing power and differential cross sections for W, Tℓ, Bi and U over 20° to 160° at a neutron energy of 2.9 MeV. The measurements were compared with the results of combining optical-model and Hauser-Feshbach calculations based on global parameter sets and with the results of searches for optimum optical-model fits to the data. Calculations which take account of the level width fluctuation correction showed a better fit to the data.

1982 Annand[16]: Measured analysing power and differential cross sections for 3.0 MeV neutrons for W, Hg, Tℓ, Pb, Bi and U

over 20° to 167° at 22 angles. These measurements are of a good accuracy and wide angular coverage. Only Hg data showed good agreement with the prediction of optical model potential. Coupled channels calculations were also performed for W, Pb and U. No attempt was made to search for best fit deformation parameters.

1984 Smith et al.[44]: Measured differential cross sections of elemental Y, Zr, Nb, Mo, Rh, Pd, Ag, Cd, In, Sn and Sb in the neutron energy range $\tilde{\sim}$ 1.5 to 4.0 MeV, at intervals of $\lesssim$ 100 keV, over 20° to 160° obtained by the neutron time-of-flight technique. The experimental results were inconsistent with optical model concepts based upon fixed geometrical parameters. A 'regional' optical model parameter set, quantitatively describing the neutron-nucleus interaction in this mass-energy domain, was deduced from the observed cross sections.

The increasing success of optical model calculations in describing the angular distributions of neutrons elastically scattered from medium and heavy nuclei has heightened the need for more extensive and more accurate experimental determinations. In particular, there are four characteristics of the model which need clarifying:

I) The energy dependence of the parameters

II) The dependence on spin of the nucleus

III) Distortions arising from deformations of the nucleus

IV) The magnitude of compound-elastic scattering, where the contribution is considerable (< 5 MeV).

A few sets of good quality differential cross section data are available, those of Holmqvist[35] and those of Smith et al.[44], while for analysing power those of Ellgehausen et al.[13] and Zijp and Jonker[40] and Annand[16] are probably the most accurate measurements. Concerning the medium mass nuclei selected for this work (Cd, Sn, Sb, Te, I) the differential cross section and analysing power data are either scarce or of poor accuracy or are restricted only to forward angles.

Cd: Two sets of elastic differential cross section data, refs. (31,44) at 0.2 MeV energy difference. The former did not show agreement with model predictions, while with the latter the optical model showed a good description of the data. There is only one set of analysing power data[40], which only goes up to 75 degrees with poor accuracy.

Sn: There are two sets of differential cross section data for natural Tin[31,45] and one set for Isotopic Tin (^{120}Sn)[46]. There are two sets of analysing power data, those of McCormac et al.[18] with very poor accuracy, and those of Zijp and Jonker[40].

Sb: There are differential cross sections of Becker et al.[31] at 3.2 MeV and of Smith et al.[44] at 3.0 MeV. The analysing power data available is from ref. (40) at 3.2 MeV up to 75 degrees only and from Kazakova et al.[29] at 3.25 MeV at 120 degrees only.

Te: No differential cross section is available, and for analysing power the data of ref. (40), goes up to 75 degrees only with poor accuracy.

I : The data of ref. (42) gives differential cross section and analysing power with poor accuracy.

CHAPTER 2

THE RESPONSE OF NE213 TO ELECTRONS AND PROTONS

2.1 Introduction

One of the technical problems in fast neutron elastic scattering measurement is that inelastically scattered neutrons are also detected and contribute to the recoil proton spectra. In order to reject inelastically scattered neutrons a discrimination level must be set and so the relation between scintillator light output and energy is important in fast elastic scattering polarization and differential cross section measurement.

It is a common practice to use gamma ray sources for calibration and to use published data which relate the energy dependence of the light output from the scintillator due to electron excitation to that due to proton excitation to set the discriminator level for rejection of inelastically scattered neutrons. For this reason, and because of interest to see how significant are the variations of response from detector to detector, the response of four NE213 organic scintillators in use in the laboratory to electrons and protons were measured, using standard gamma sources, an Am-Be neutron source, and monoenergetic neutrons from D - D and D - T reactions. The results are compared with available published data. There is, however, a significant spread in these data as illustrated in Ref. (47) and in Fig. 2.7.

There is considerable evidence that the response functions for organic scintillators are dependent upon geometrical factors (including the size and shape of scintillator, phototube reflection

effects)[48], their chemical composition and purity, as well as their histories of exposure to light and other radiations[49] and on the electronics of the associated circuitry.

Scintillators respond directly to ionization generated by charged particles. Neutral radiation (e.g. gamma rays and neutrons), are detected if they produce recoil electrons or recoil nuclei within the scintillator material. The detection of neutrons in organic material can be through the process of proton recoil, while gamma rays are detected primarily through the process of Compton electron recoil.

A relatively small fraction of the ionization energy lost by a charged particle in a scintillator is converted into fluorescent light energy. The rest of the energy is dissipated non-radiatively, mainly as heat. The fluorescence is characteristic of the molecular structure of the scintillator. Since organic scintillators contain light elements whose nuclear recoil can be detected easily, they are very good neutron detectors.

The fraction of ionization energy converted to fluorescent light differs for each type of scintillator and also depends on the type of charged particle producing the ionization.

Electrons generate more light than do heavy particles (e.g. protons and ^{4}He particles) of equal energy when stopped in organic scintillators.

The light output of electrons in organic scintillators is known to be a linear function of energy for electrons above approximately 100 keV[50-53].

D.T. Ingresoll et al.[53], have reported the linearity of the gamma ray pulse height for an organic (NE213) liquid scintillator

up to 11.5 MeV. Furthermore, linear extrapolations of the electron response from higher energies generally pass within a few keV of the origin[54]. But the response to heavier particles is non-linear up to much higher energies.

For electron energies above 100 keV, the relation of light pulse to electron energy is given by the equation $P = C(E - b)$, where P is the relative pulse height, E the electron energy, b the energy intercept ($= 20 \pm 5$ keV), and C the slope which is characteristic of the system used[52].

2.2 The Response Mechanism of Organic Scintillators to Protons and Electrons

Although neutrons interact with hydrogen and carbon nuclei of organic scintillators by several different mechanisms, the detection of neutrons by an organic scintillator depends primarily upon elastic scattering collisions between neutrons and protons.

From the scattering collisions a continuous distribution of recoil protons is obtained. These protons range in energy from zero up to the energy of the neutrons which produced them. The energy response function of the scintillator is non-linear, therefore the pulse height distribution obtained from the scintillation counter will not be directly proportional to the energy spectrum of the recoiling protons. When the response function is determined, the pulse-height distribution can be converted to the recoil-proton energy spectrum and a differentiation process can then yield the energy spectrum of the incident neutrons.

This method is applicable both when the incident neutron energy spectrum is monoenergetic and when it is continuous.

Other reactions of neutrons with the atoms of the detector serve to produce scintillations which may be considered as perturbations to the recoil-proton energy spectrum. Some of these reactions are:

a) Second scattering of the neutrons from hydrogen nuclei

b) Loss of recoiling protons through the end of the detector

c) Elastic scattering, inelastic scattering and other reactions with carbon atoms of detector.

Gamma-rays interact with the scintillator primarily by the Compton scattering process. As a result of these scattering collisions, recoiling electrons are produced which range in energy from zero up to maximum energy called the Compton edge. The response of the scintillator to these recoil electrons is linear. This linear response provides a method by which the energy scale of the pulse-height analyser can be calibrated before each experiment with gamma-ray sources.

2.3 Neutron-Proton Elastic Scattering

If a beam of neutrons of energy E_o with a flux N_o is incident upon a hydrogeneous scintillator of area A and length L, it follows that the total number of protons Np produced by single scattering collisions is given by

$$Np = N_o A \varepsilon(E_o, L) \tag{2.1}$$

where $\varepsilon(E_o, L)$, the efficiency of the scintillator for producing

recoil protons by single scattering collisions, is given by[55]

$$\varepsilon(E_o,L) = n_h\sigma_h L(1 - e^{-aL})/aL = n_h\sigma_h Lf(aL) \qquad (2.2)$$

with $a = n_h\sigma_h + n_c\sigma_c$ and $f(aL) = (1 - e^{-aL})/aL$.

In this formula, n_h and n_c refer, respectively, to the numbers of hydrogen and carbon atoms per unit volume of the scintillator, σ_h is the neutron-proton scattering cross-section, and σ_c is the total carbon interaction cross-section for neutrons.

This formula for the single-scattering efficiency neglects the possible production of recoil protons by neutrons once scattered by hydrogen or carbon.

It can be shown kinematically that the number of recoiling protons per unit energy in the laboratory system is proportional to the differential elastic scattering cross-section per unit solid angle in the centre of mass system. If the neutron-proton scattering is considered to be isotropic in the centre of mass (c.m.) system, the recoil proton distribution in the scintillator is given by the following formula for a monoenergetic incident beam.

$$Np(E) = A\, dNp/dE = [N_o A\varepsilon(E_o,L)]/E_o \quad . \qquad (2.3)$$

If the spectrum of the incident neutrons is not monoenergetic but has a distribution dNn/dE_o (neutrons per unit area per energy interval), then we must include the contribution to $Np(E)$ of all neutrons above the energy E_o. Thus in general

$$Np(E) = \int_E^\infty [A\varepsilon(E_o,L)/E_o](dNn/dE_o)dE_o \quad . \qquad (2.4)$$

Differentiation of both sides with respect to E and solving gives the energy spectrum of the incident neutrons in terms of the slope of the recoil-proton energy spectrum:

$$\left(\frac{dN_n}{dE_o}\right)_E = \left(\frac{dN_n}{dE}\right) = -\left(\frac{dN_p(E)}{dE}\right)\left(\frac{E}{A\varepsilon(E,L)}\right) \qquad (2.5)$$

Thus from the energy of the recoiling protons, the energy spectrum of the incident neutrons can be obtained.

However, an organic scintillator produces a pulse-height distribution which is non-linear with respect to recoil-proton energies.

Birks[49] reported the following formula for fast electrons:

$$L = SE \qquad (2.6)$$

or expressed in differential form

$$dL/dX = S\, dE/dX \qquad (2.7)$$

where L is the scintillation response

X is the range in the scintillator measured in Cm air equivalent or in mg Cm^{-2}

S is the absolute scintillation efficiency

dE/dX is the specific energy loss

dL/dX is called the specific fluorescence.

For heavier particles, such as protons or alpha-particles or for electrons of $E < 100$ keV, dE/dX is increased compared with that for fast electrons, and it is observed that the differential scintillation efficiency dL/dX is reduced below S, and that L increases non-linearly with E_o.

Birks assumes that high ionization density along the particle track is responsible for the quenching effect which is observed for protons and other heavily ionizing particles. He obtained the following expression:

$$\frac{dL}{dX} = \frac{S(\frac{dE}{dX})}{[1 + KB \frac{dE}{dX}]} \qquad (2.8)$$

In this theory the molecules along the ionization column are grouped into two categories labelled "damaged" and "undamaged" for convenience. The ratio of the number of "damaged" molecules to the number of "undamaged" molecules is assumed to be BdE/dX and K is the corresponding relative quenching probability.

The damaged molecules are those with the greater capacity for dissipating the ionization energy non-radiatively (quenching).

The damaged molecules actually occupy highly excited or ionized states and they de-excite quickly (< 1n sec) to the undamaged condition. The product KB is treated as a single adjustable parameter since there are no means available for measuring K or B separately.

It is clear that the results for heavy ions can not be described by any simple extrapolation of the response data for lighter particles.

Chou[56] has given a semi-empirical analysis which leads to a relation of the form

$$\frac{dL}{dX} = \frac{S \frac{dE}{dX}}{1 + KB(\frac{dE}{dX}) + C(\frac{dE}{dX})^2} \qquad (2.9)$$

which may be regarded as a generalization of equation (2.8). He introduced one additional adjustable parameter. If $C = 0$ eq. (2.9) degenerates into eq. (2.8).

Now, we may rewrite eq. (2.9) in the form,

$$\frac{dL}{dE} = S[1 + KB(\frac{dE}{dX}) + C(\frac{dE}{dX})^2]^{-1} \qquad (2.10)$$

where dL is the quantity of fluorescence light generated when a charged particle with energy E loses a quantity of energy dE through ionization along a path increment dX within the scintillator.

The integral of the eq. (2.10) with respect to particle energy is:

$$L(E) = S \int_o^E d\mathcal{E}[1 + KB(\frac{dE}{dX}) + C(\frac{dE}{dX})^2]^{-1} \qquad (2.11)$$

where $L(E)$ is the total light emitted by a charged particle which expends all of its energy E within the scintillator. For electrons with energies $\geq$ 100 keV, $dE/dX \approx 0$ and equation (2.11) becomes a linear expression

$$L_e(E) = SE + L_o \quad .$$

The most frequent use of the differential energy loss information occurs in the measurement of nuclear cross sections, where the number of target nuclei per unit area of the target must be determined.

In practice the relationship $P = \alpha E^{\beta}$ can be used as a good approximation to the relation between proton energy P and electron energy E for equal light output, the constants α and β being determined for each spectrometer[57].

2.4 Detectors

Two small NE213 liquid scintillators:

i) 50 mm diameter by 50 mm long glass cell with external nitrogen bubble (NE VH1 cell, white painted externally) mounted on 56AVP photomultiplier.

ii) 50 mm diameter by 50 mm long aluminium cylinder internally painted with titanium dioxide paint (NE561) mounted on 56AVP photomultiplier

and two large NE213 liquid scintillators:

i) 305 mm diameter by 50 mm long internally painted aluminium cell with nitrogen expansion bubble in PTFE capillary tube (NE BA1 cell) coupled by conical perspex light guide to XP1040 photomultiplier[58]. This scintillator had been in use for about 10 years.

ii) 305 mm diameter by 50 mm long scintillator, light guide and photomultiplier combination as in (i) above but with scintillator cell freshly filled for the present measurements.

were used, both as scatterer (e.g. detector D1 Fig. 2.1) and/or detector D2 Fig. 2.1.

NE213 liquid scintillator is an organic compound consisting of specially purified xylene, naphthalene, activators and POPOP spectrum shifter with a refractive index equal to 1.508, a density of 0.874 g/Cm^3 and a ratio of hydrogen to carbon atoms equal to 1.213. Its light output is 78% of anthrancene light output.

NE213 shows relatively good efficiency and resolution in neutron spectrometry and excellent discrimination of gamma-rays based on the pulse rise time.

Since NE213 is non-crystalline, it is isotropic in response to neutrons and is not sensitive to mechanical or thermal shock. These desirable characteristics of NE213 can easily be made to vanish by the presence of any impurity, commonly oxygen, in the liquid[49,59]. The presence of oxygen in the liquid reduces the light output and deteriorates pulse shape discrimination considerably.

2.5 Experimental Arrangement

The response of a scintillator to charged particles can be measured by two methods. The direct method is to bombard the scintillator with external beams of charged particles.

The indirect method is to bombard a scintillator with mono-energetic beams of neutral particles such as gamma-rays and neutrons of which a portion will elastically scatter from charged particles within the scintillator.

Unique energy recoil will be recorded only if one detects the elastically scattered neutral radiation in a second detector, placed at a specific angle relative to the incident beam direction, in time coincidence with the recoil pulse.

Furthermore, the relative response of a scintillator to different charged particles can be measured with greater reliability since the penetrating primary radiations generally produce recoils rather uniformly throughout the bulk of the scintillator thereby minimizing the geometrical effects.

The spectrometer consists basically of two scintillation counters, Fig. 2.1. The principle of the spectrometer requires an incident neutron to scatter elastically from a proton in the first scintillator,

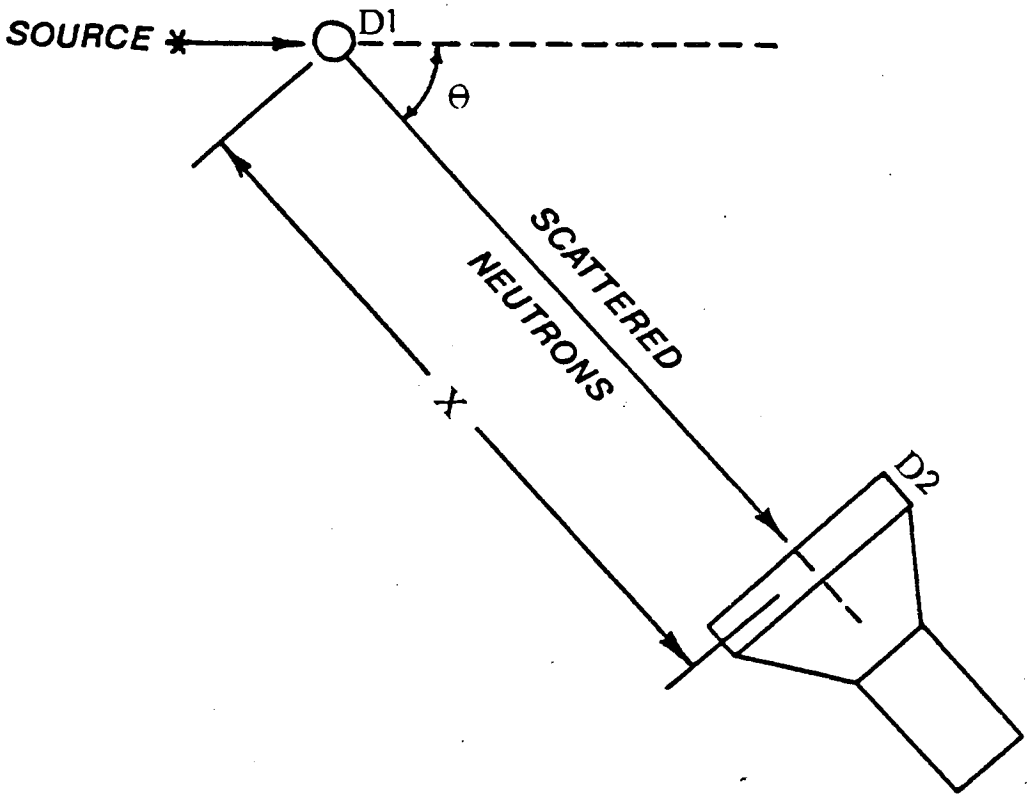

Figure 2.1. The scattering and time-of-flight arrangement, X = 90 cm.

travel over a known flight path, and interact in the second scintillator. The time interval between the scintillation pulses in the two detectors is the time-of-flight of the scattered neutron. The neutron energy resolution could be improved if a longer flight path is chosen. However, it should be noticed that increasing the flight path decreases the count rate by a factor of $\frac{1}{X^2}$ where X is the factor by which the flight path is increased.

An Americium 241/Beryllium source is used as a neutron source in this work, with an emission rate of 2.9×10^5 neutrons per second. The Am 241/Be source gives neutrons with energies up to 11 MeV, but predominantly neutrons with average energy of about 5 MeV.

The mechanism for production of neutrons from Am 241/Be source is through the following reaction:

$$^{9}Be(\alpha,n)^{12}C \quad .$$

The predominant energy of alpha particles emitted from Americium is 5.48 MeV[60], but ionization losses in the source ensure that alpha particles of all energies up to this maximum are present.

The block diagrams of the electronics used for measurement of response of detector D1 is shown in Fig. 2.2(a), while the electronic system for measurement of response of detector D2 is shown in Fig. 2.2(b).

The scattered neutrons and gammas, collected by detector D2, were delayed and used to provide the "stop" pulse for the time to amplitude convertor (T.A.C.), while the fast pulses from detector D1 due to the scattering event itself was used to provide the "start" pulse.

To measure the response of D1, a linear pulse from D1 was

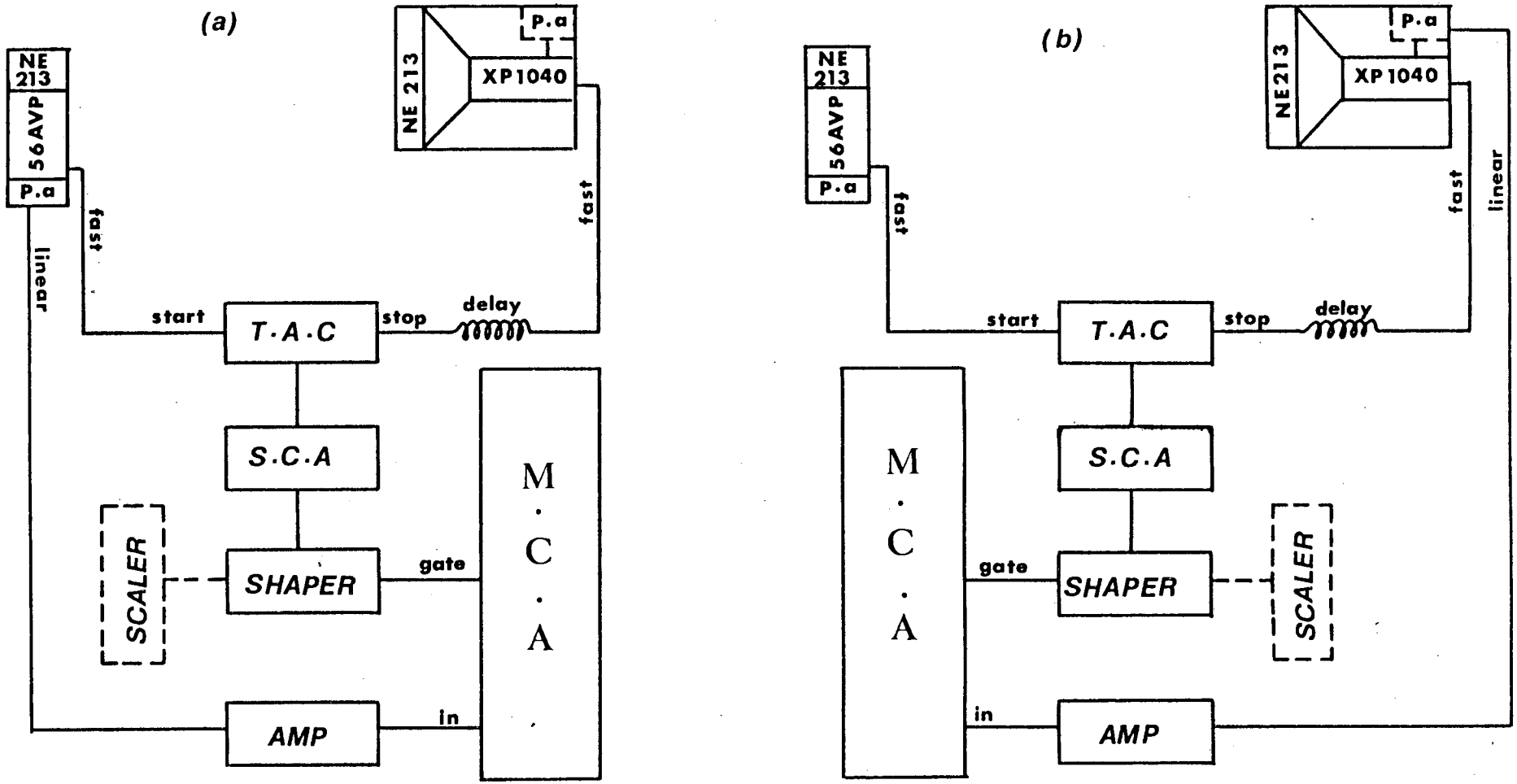

Figure 2.2(a). Block diagram of the electronic system used to observe the recoil proton pulse-height spectrum from detector D1 associated with a selected time-of-flight of scattered neutron.
(b) Block diagram of the electronic system used to observe the recoil proton pulse-height spectrum from detector D2 associated with a selected time-of-flight of incident neutron.

recorded in coincidence with the logic output from a single channel analyser (S.C.A.), which determines the energy of the selected neutrons. A delay of 1.0 μs was introduced between the linear input and the gating pulse to suit the 400 channel multi channel analyser (M.C.A.).

Gamma-rays scattered between D1 and D2 detectors could not produce the desired coincidence because the short flight-time of the gamma-rays does not fall within the predetermined time-of-flight window for neutrons.

A pulse generator was used to produce pulses of the correct amplitude corresponding to the upper and lower channels of the required time-of-flight gate and these were used to set up the (S.C.A.). For both detectors, measurements were taken of the gated linear spectrum for several time-of-flight ranges.

The existence of any sort of shielding material in the experimental room served to increase the number of multiply scattered neutrons and consequently produced a deterioration of the neutron spectrum.

The electron calibration was carried out following the procedure adopted by Flynn et al.[52]. It is necessary to have calibration points, such as the peaks of the Compton spectra, which are insensitive to the pulse height resolution of the detector.

In the detection of gamma-rays by a liquid scintillator, the Compton distribution will be smeared by the finite resolution. The position of the Compton edge was identified by 72% of the mean number of counts around the maximum in the distribution.

Prescott and Rupaal[61], from calculations folding together Gaussian and Klein-Nishina distributions, and Beghian and Wilensky[62] from Monte Carlo calculations concluded that the Compton edge should

be located at about 66% of the maximum in the distribution, while Knox and Miller[63] concluded from experimental measurements that it should be at 89 ± 7%. Recently Dietze[64] and Dietze and Klein[65] have emphasised the dependence of the location of the Compton edge on energy and on the resolution of the detector and have investigated the behaviour of four different sizes of NE213 scintillator, both by Monte Carlo calculation and by experiment. The calculations and measurements displayed for gamma-rays of ^{22}Na and ^{137}Cs both indicate the Compton edge at about 75% of the number of counts at the maximum in the distribution. Their results show that the position of the Compton edge is nearer to the half maximum position for small detectors than for large detectors. The position of the maximum (L_{max}) and half height of the maximum ($L_{\frac{1}{2}}$) relative to the Compton edge (L_C) versus the detector resolution ($\frac{\Delta L}{L_C}$), ΔL (fwhm), for four detectors of different sizes used in this work and photons from ^{137}Cs (E_γ = 0.66 MeV), ^{60}Co (E_γ = 1.17 and 1.33 MeV) and ^{22}Na (E_γ = 1.26 MeV), is shown in Fig. 2.3. The detectors used in this work did not show the effect observed by Dietze, and Dietze and Klein. In fact our results are changed very little by changing the definition of the location of the Compton edge within the above range. The largest change would come from adopting the definition of Knox and Miller[63] which would increase the light output values in Table 2.1 by about or less than the indicated uncertainty and would have no perceptible influence on the graphical presentation of the data in Fig. 2.6. Thus, incidentally, it would seem that differences between past measurements of the response of NE213 as in Fig. 2.7, are unlikely to be due to different ways of locating the Compton edge.

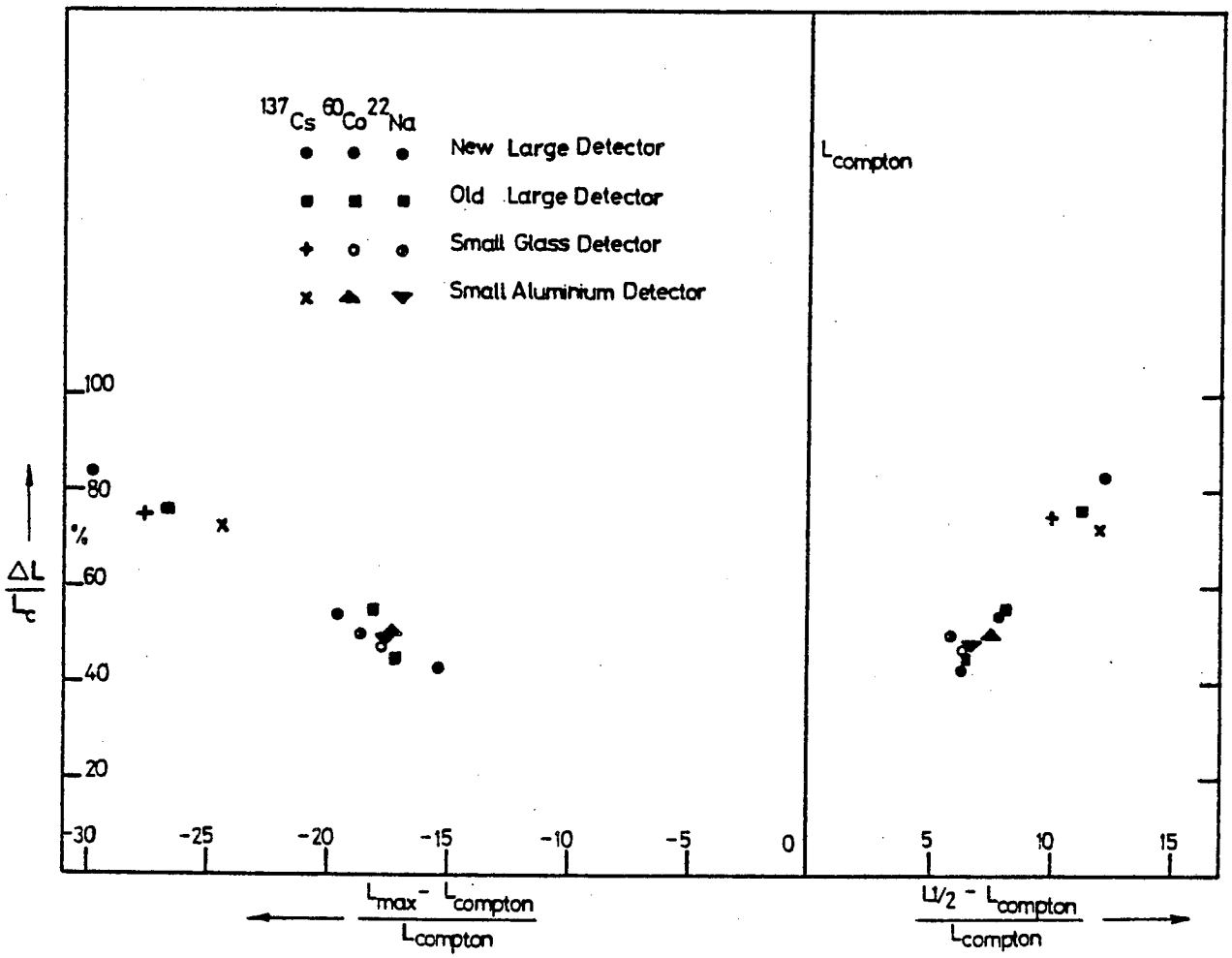

Figure 2.3. The position of the maximum L_{max} and of the half maximum $L_{\frac{1}{2}}$ in a Compton electron spectrum relative to the position of the Compton edge $L_{Compton}$ as a function of the relative resolution of the scintillation detector at $L_{Compton}$ for various energies.

For a gamma-ray with energy E_γ, the maximum Compton-electron energy E_c is given by:

$$E_c = \frac{E_\gamma}{1 + \frac{m_o c^2}{2E_\gamma}} = \frac{2E_\gamma^2}{2E_\gamma + m_o c^2}$$

where $m_o c^2 = 0.511$ MeV.

From this equation the maximum electron energies that correspond to 0.51 and 1.28 MeV gamma-rays emitted from ^{22}Na source are 0.34 and 1.07 MeV respectively.

The sources ^{22}Na, ^{137}Cs and ^{60}Co were used to calibrate all detectors for comparison of light output for electrons and protons. Frequent electron response calibrations were made during the time spent on proton response measurement. Therefore the analyser was calibrated in units of equivalent electron energy by associating the channel numbers with the electron energies of the peak of the Compton spectra, and allowing for the finite bias at the analyser input.

A typical pulse height spectrum from detector D1 associated with a selected scattered neutron flight time is shown in Fig. 2.4(a).

The peak maxima were located and used in calculating the relative response. The procedure used to indicate the location of peak maxima and the corresponding estimated uncertainties are also shown in Fig. 2.4(a) and (b). Thus by selecting different scattered neutron flight times the response of detector D1 to protons of different energies could be found. In interpreting the spectra such as Fig. 2.4, account was taken of the uncertainty in the location of the peak and of the uncertainty in the associated mean proton recoil energy as deduced from the uncertainty in the mean energy of the

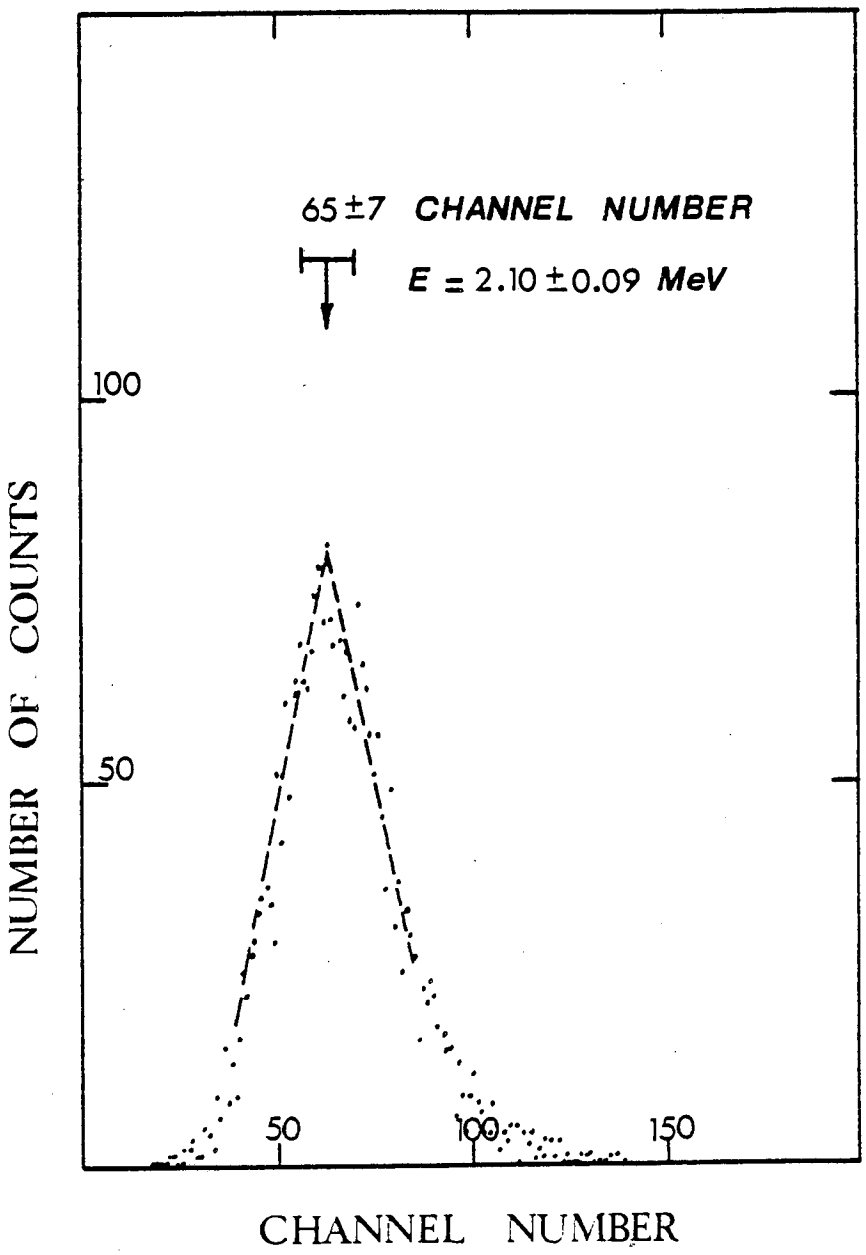

Figure 2.4(a). A typical recoil proton spectrum from detector D1 associated with a particular scattered neutron time-of-flight. The mean proton recoil energy was 2.10 ± 0.09 MeV.

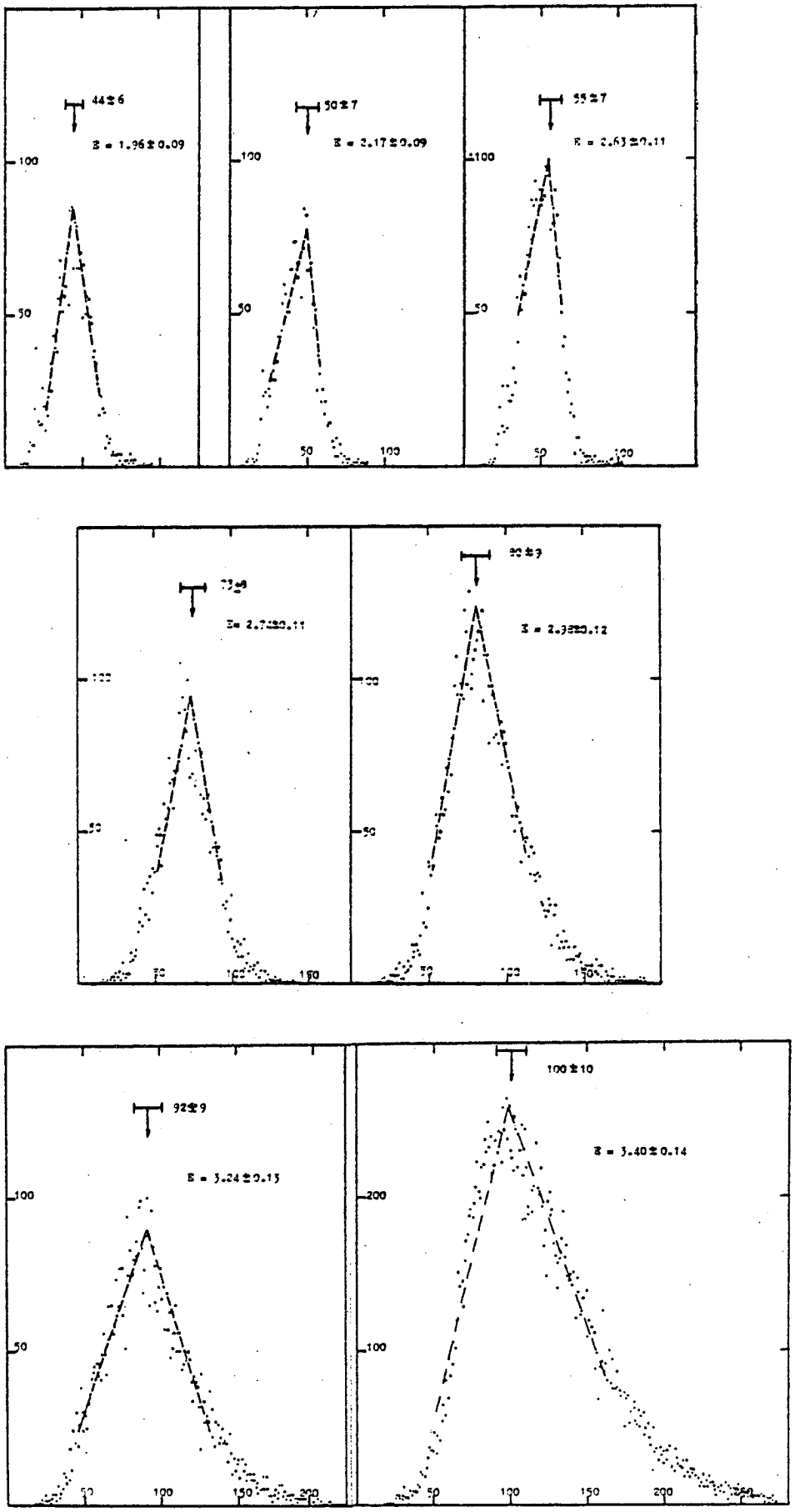

Figure 2.4(b). Recoil proton spectra from Aluminium container NE213 scintillator.

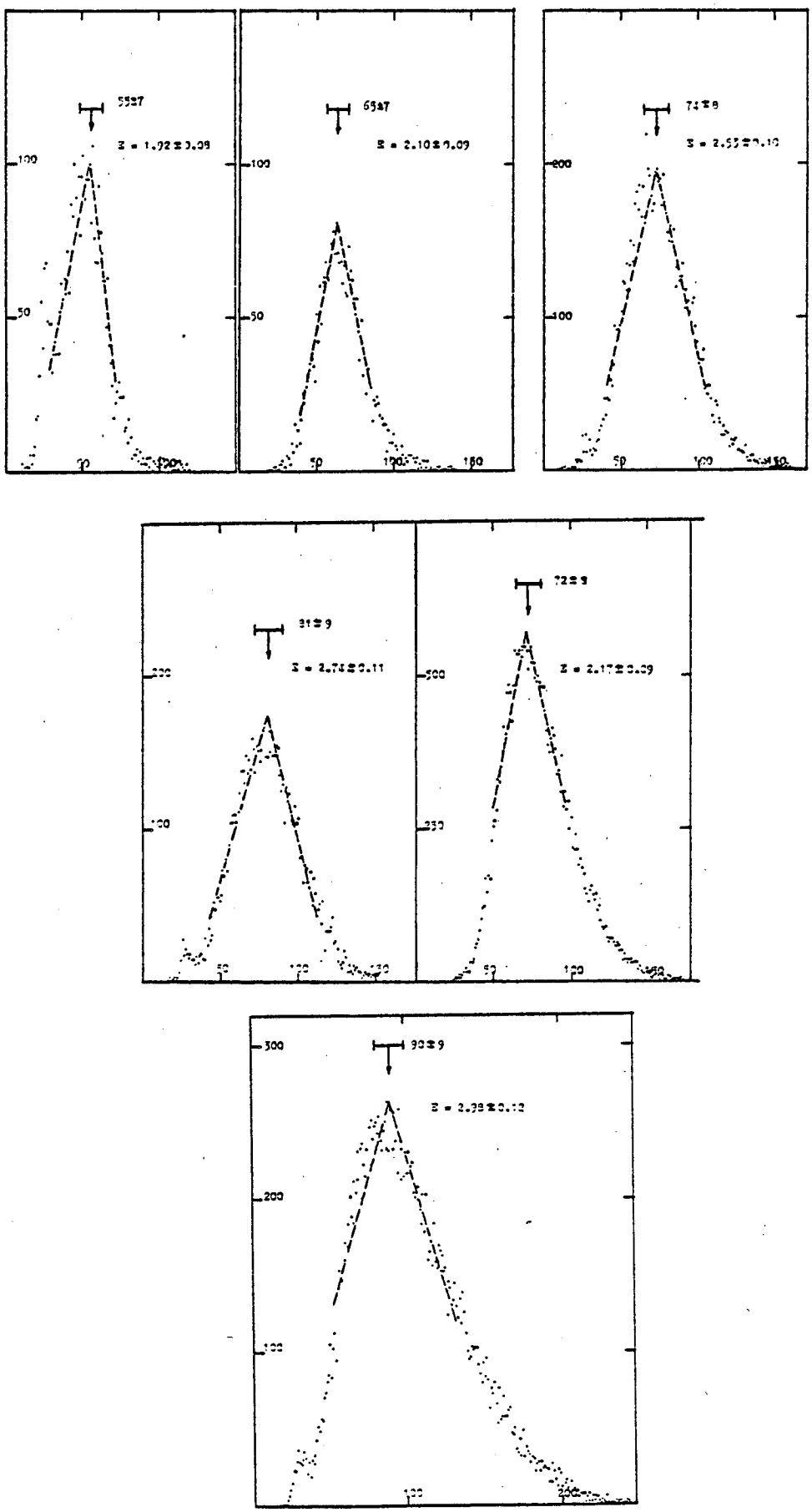

Figure 2.4(b). Recoil proton spectra from Glass container NE213 scintillator.

selected scattered neutrons. Most of the response data for the two small detectors (50 mm × 50 mm) in Table 2.1 and Fig. 2.6 was obtained in this way.

The pulse height spectrum from detector D2 associated with a particular flight time is the normal proton recoil spectrum for monoenergetic neutrons incident, as in Fig. 2.5(a) and (b).

The light output for each neutron energy is obtained by finding the midlevel of the abrupt edge near the maximum pulse height of the spectrum. The procedure is illustrated in Fig. 2.5; such spectra provided most of the response data for the two large detectors (305 mm × 50 mm) in Table 2.1 and Fig. 2.6.

By comparing the electron energy calibration obtained using a number of gamma sources with the proton energy calibration, the electron and proton energies for equal light output were determined. The ratio between pulses from protons and from electrons of the same energy, was obtained. The results of such measurements for all detectors are shown in Table 2.1. One pulse height unit is presented by Compton edge of 0.48 MeV gamma-rays of ^{137}Cs source.

The relative response of proton energy versus equivalent electron energy for the four detectors are shown in Fig. 2.7, while the results of several other authors are also plotted.

The correctness of the method, which is used to indicate the location of peak maximum for light output measurements for both detectors, was checked by using the large detector D2 as scatterer when small detector D1 was positioned at an angle of 45° with respect to the direction of the incident neutrons at the first detector (D2) at the end of the flight path.

In this case a peak for the large detector and a rectangular

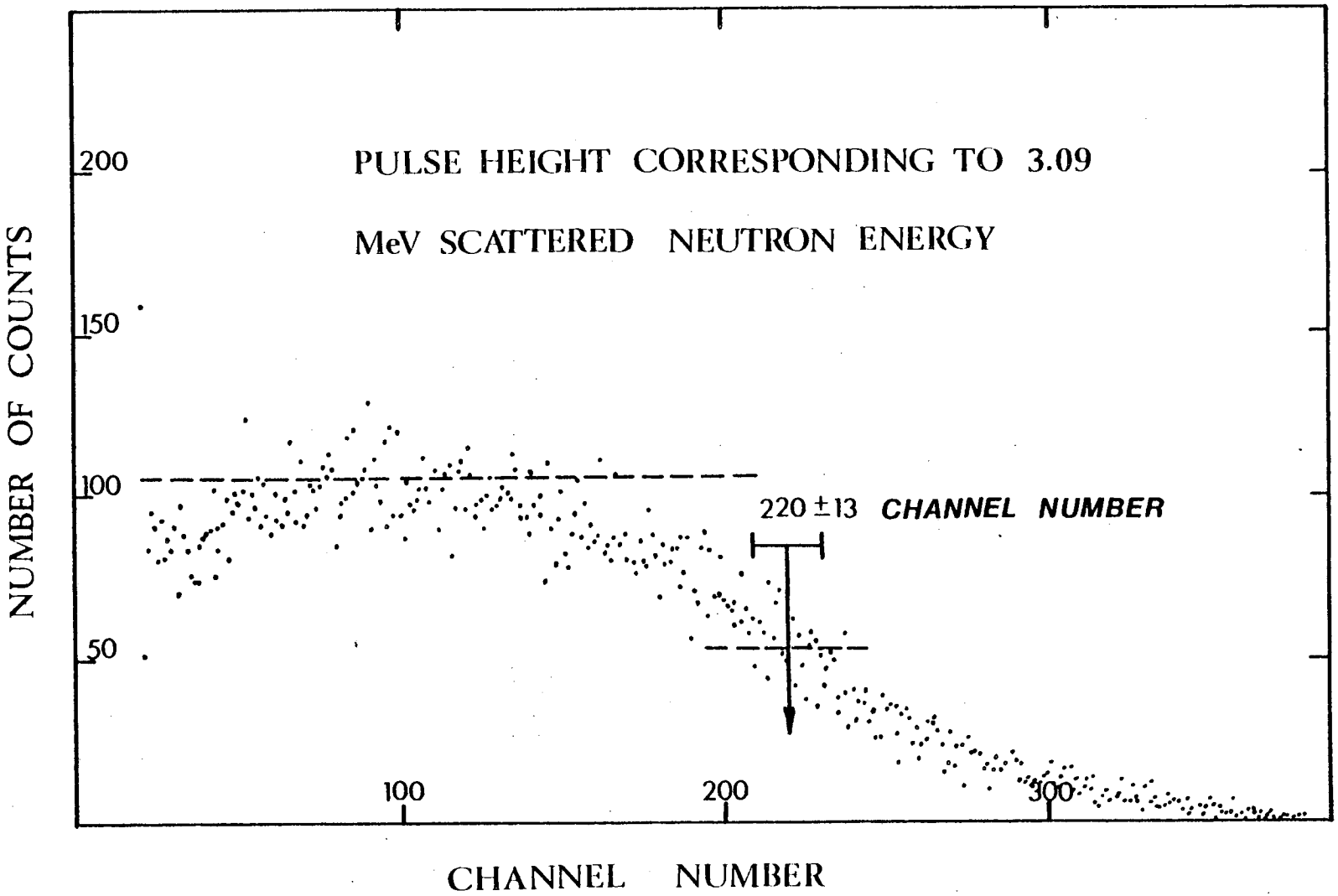

Figure 2.5(a). A typical recoil proton spectrum from detector D2 associated with a particular neutron time-of-flight.

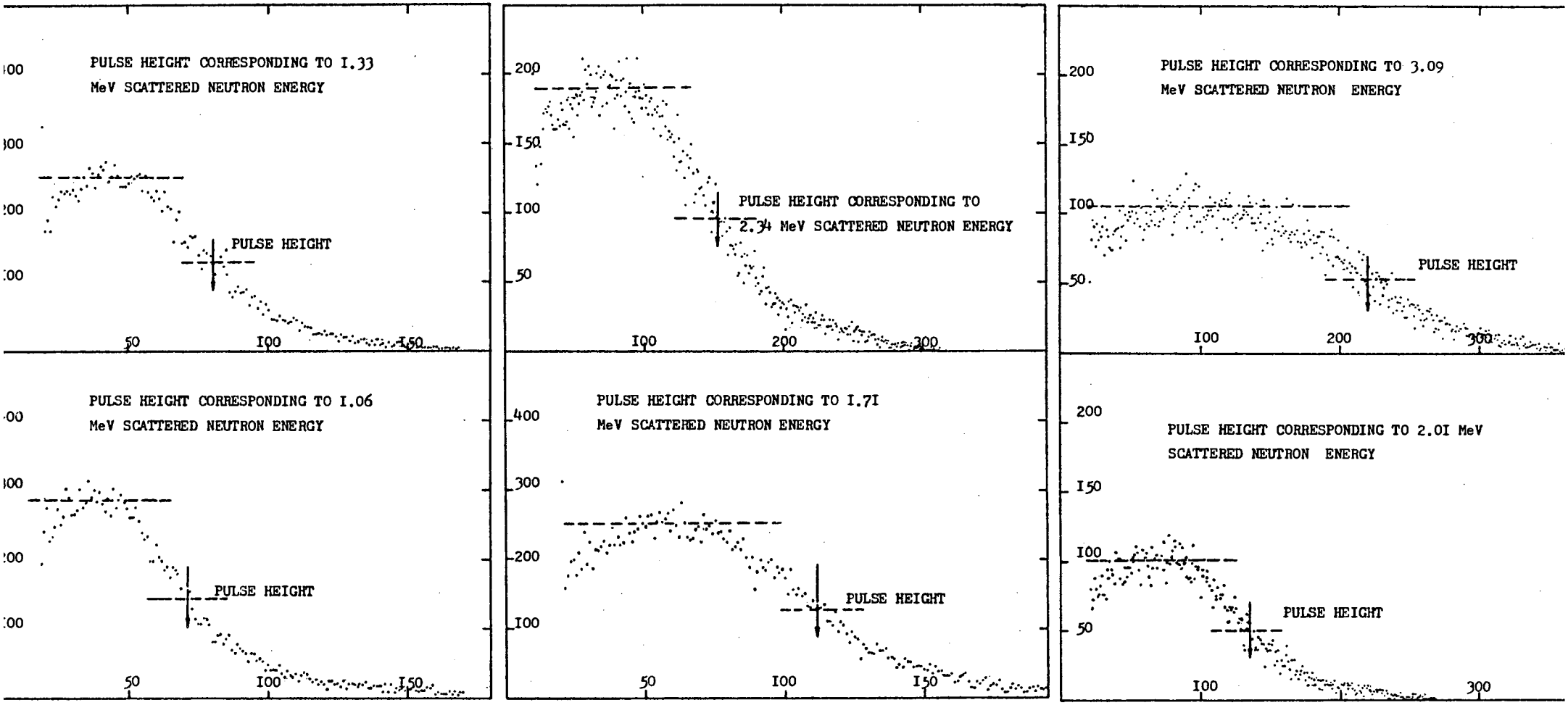

Figure 2.5(b). Recoil proton spectra from new bubbled large detector.

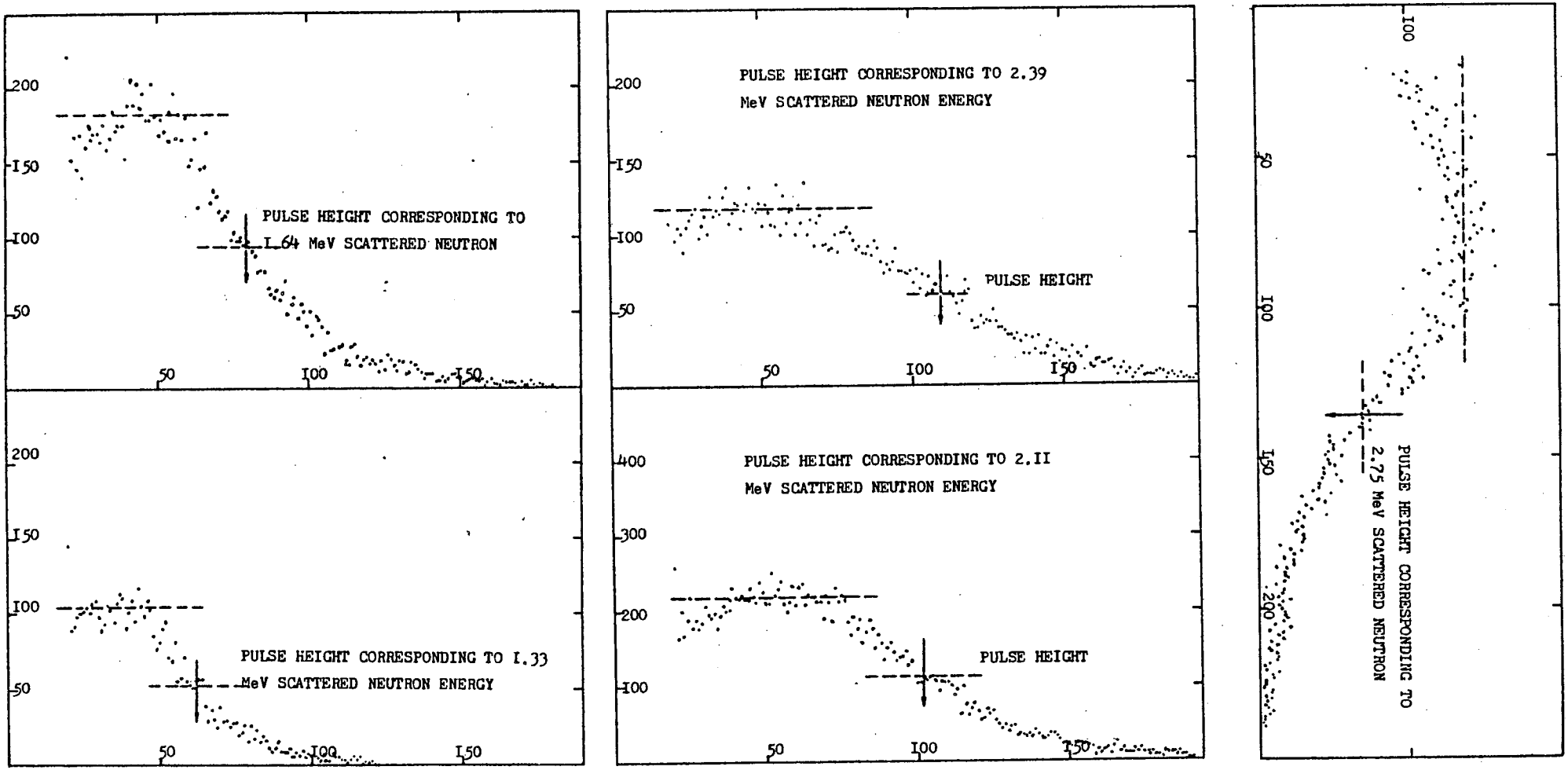

Figure 2.5(b). Recoil proton spectra from old large detector.

TABLE 2.1

Proton response of NE213 detectors. The light output Lp(E) is in arbitrarily chosen units such that one unit corresponds to the light output due to an electron of 0.48 MeV

50 mm × 50 mm Scintillators				305 mm × 50 mm Scintillators			
Aluminium container		Glass container		Old		New	
Proton Energy MeV	Lp(E)	Proton Energy MeV	Lp(E)	Proton Energy MeV	Lp(E)	Proton Energy MeV	Lp(E)
1.96 ± 0.08	0.91 ± 0.11	1.92 ± 0.08	0.94 ± 0.11	1.33 ± 0.01	1.01 ± 0.10	1.06 ± 0.01	1.05 ± 0.10
2.17 ± 0.09	1.04 ± 0.14	2.10 ± 0.09	1.12 ± 0.12	1.64 ± 0.01	1.27 ± 0.10	1.33 ± 0.01,	1.16 ± 0.12
2.63 ± 0.11	1.14 ± 0.14	2.17 ± 0.09	1.24 ± 0,12	2.00 ± 0.01	1.57 ± 0.12	1.71 ± 0.01	1.54 ± 0.15
2.74 ± 0.11	1.54 ± 0.15	2.53 ± 0.10	1.27 ± 0.12	2.11 ± 0.01	1.67 ± 0.14	2.01 ± 0.01	1.83 ± 0.15
2.98 ± 0.12	1.66 ± 0.16	2.74 ± 0.11	1.45 ± 0.13	2.39 ± 0.01	1.78 ± 0.14	2.34 ± 0.01	2.02 ± 0.15
3.24 ± 0.13	1.91 ± 0.16	2.98 ± 0.12	1.58 ± 0.13	2.75 ± 0.01	2.22 ± 0.15	3.09 ± 0.02	2.72 ± 0.18
3.40 ± 0.14	2.08 ± 0.18	3.19 ± 0.13	1.70 ± 0.15	2.87 ± 0.01	2.52 ± 0.15	4.29 ± 0.03	4.16 ± 0.24
				3.68 ± 0.02	3.29 ± 0.18		
a) 2.61 ± 0.05	1.58 ± 0.10	- -	- -	2.61 ± 0.05	2.06 ± 0.13	2.61 ± 0.05	2.24 ± 0.13
b) 14.05 ± 0.03	16.97 ± 0.25	- -	- -	13.86 ± 0.04	17.60 ± 0.25	13.58 ± 0.10	17.70 ± 0.25

a) $^{2}H(d,n)^{3}He$ reaction. b) $^{3}H(d,n)^{4}He$ reaction

Fig. 2.6 Relative response of the four NE213 scintillation counters to electrons and protons.

▲	(305mm × 50mm)	New bubbled detector
▽	(305mm × 50mm)	Old detector
○	(50 mm × 50mm)	Glass container
●	(50 mm × 50mm)	Aluminium container
▼	(50 mm × 50mm)	Aluminium container as D2
▌	(305mm × 50mm)	New bubbled detector when used as scatterer D1
◑	(305mm × 50mm)	New bubbled detector; 2.6 MeV $^{2}H(d,n)^{3}He$ reaction
⦶	(305mm × 50mm)	Old detector; 2.6 MeV $^{2}H(d,n)^{3}He$ reaction
0	(50 mm × 50mm)	Aluminium container; 2.6 MeV $^{2}H(d,n)^{3}He$ reaction

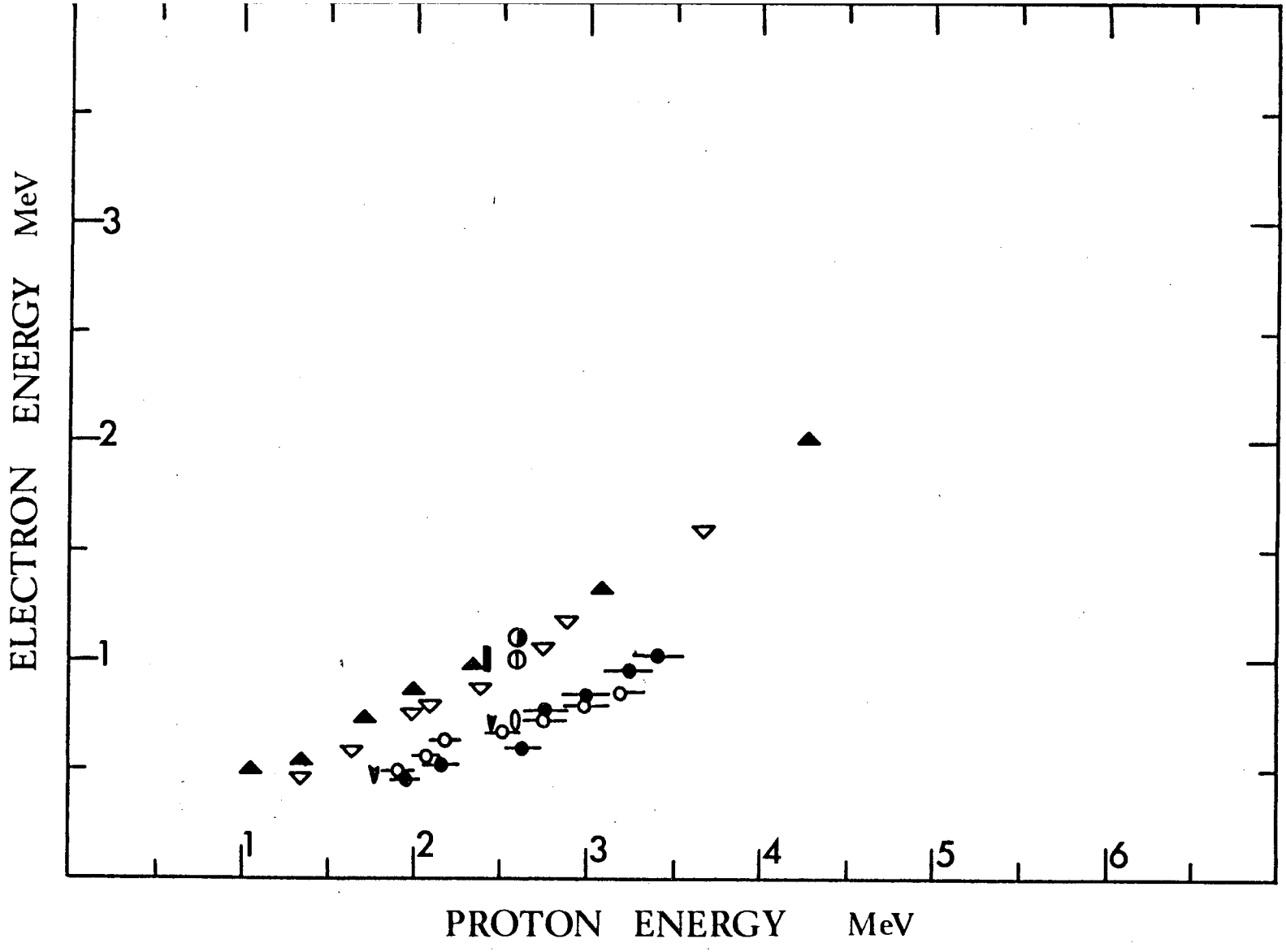

Figure 2.6.

spectrum was expected for the small detector. The results of such measurements which are in good agreement with the other results are also shown in Fig. 2.6.

Finally, to make sure that there is no ambiguity in all of the measurements and calculations, the response of both the large detectors (12" × 2") and the small (2" × 2") metal container scintillator to [$^{2}H(d,n)^{3}He$ + 3.269 MeV] reaction at 82° for 2.61 MeV mono-energetic neutrons, and [$^{3}H(d,n)^{4}He$ + 17.59 MeV] reaction at 95° angle for the small detector with 14.05 MeV, at 105° angle for the old large detector with 13.86 MeV and at 120° angle for the new bubbled large detector with 13.5 MeV mono-energetic neutrons were collected and compared with electron calibration. These results are also in good agreement with the other results and are shown in Figs. 2.6 and 2.7 and Table 2.1.

Since the differentiation of the proton recoil spectrum gives the energy spectrum of the incident neutrons, this approach was used to find the position of pulse height corresponding to 2.61 MeV mono-energetic neutrons from D-D reaction for all detectors.

First the proton recoil spectrum was smoothed by summing groups of 5 channels and then the differentiated spectrum was plotted, as illustrated in Fig. 2.8(a-c), while the spectra obtained from $^{3}H(d,n)^{4}He$ reaction are shown in Fig. 2.9(a-c).

2.6 Analysis of Time-of-Flight Spectrum

The time of flight spectrum of neutrons emitted from an Americium 241/Beryllium source is shown in Fig. 2.10. The time-of-flight spectrum can be converted to an energy spectrum through the following procedure:

Figure 2.7 Comparison of the present and previous measurements

Symbol	Size	Reference
Curve 1	(152 mm × 127 mm × 101 mm)	Rothberg et al. (73)
Curve 2	(50.8 mm × 57.1 mm)	Smith et al. (51)
Curve 3	(50.8 mm × 63.5 mm)	Batchelor et al. (70)
Dashed Curve	(177.8 mm × 101.6 mm)	Alberigi Quaranta et al. (71)
D	(120 mm × 57 mm)	Drosg (67)
0	(46 mm × 46.5 mm)	Verbinsky et al. (72)
▼	(101.6 mm × 25 mm)	Taylor and Kalyna (69)
▮	(50.8 mm × 38.1 mm)	Fowler et al. (47)
■	(127 mm × 101.6 mm)	Bertin et al. (68)
▲	(305 mm × 50 mm)	New bubbled detector
▽	(305 mm × 50 mm)	Old detector
●	(50 mm × 50 mm)	Aluminium container
○	(50 mm × 50 mm)	Glass container

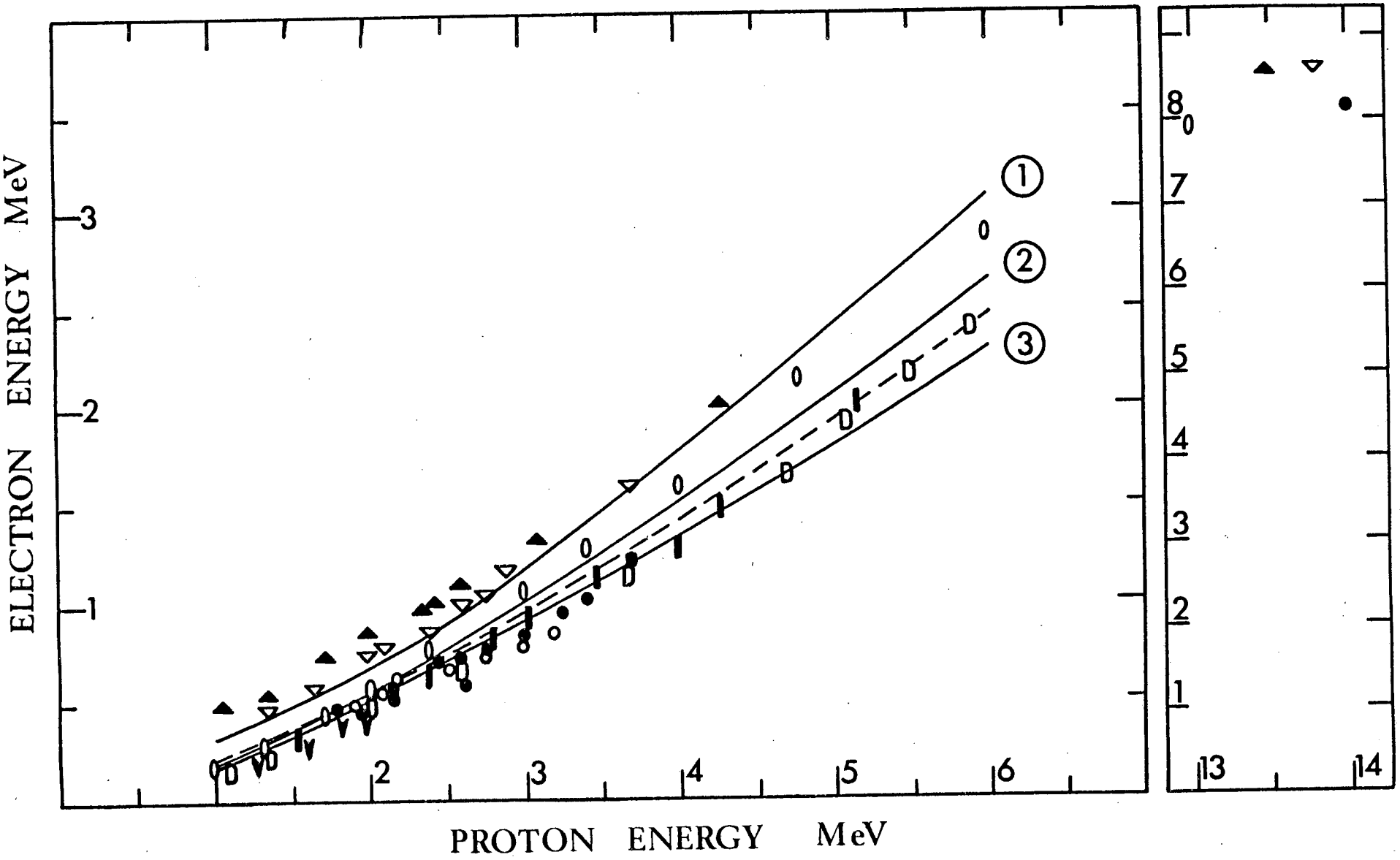

Figure 2.7.

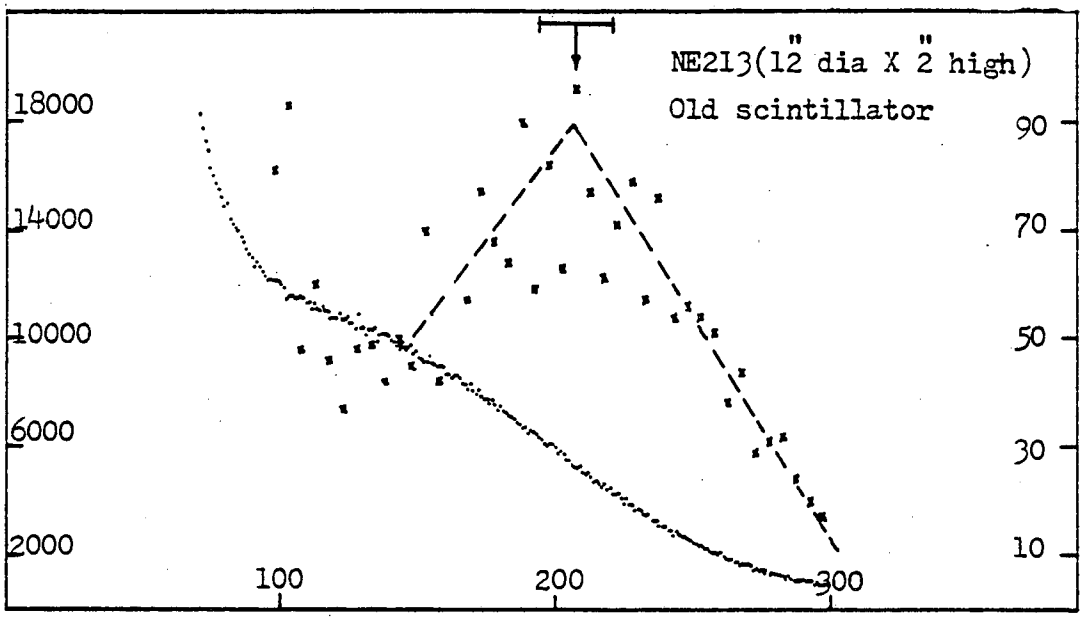

(a)

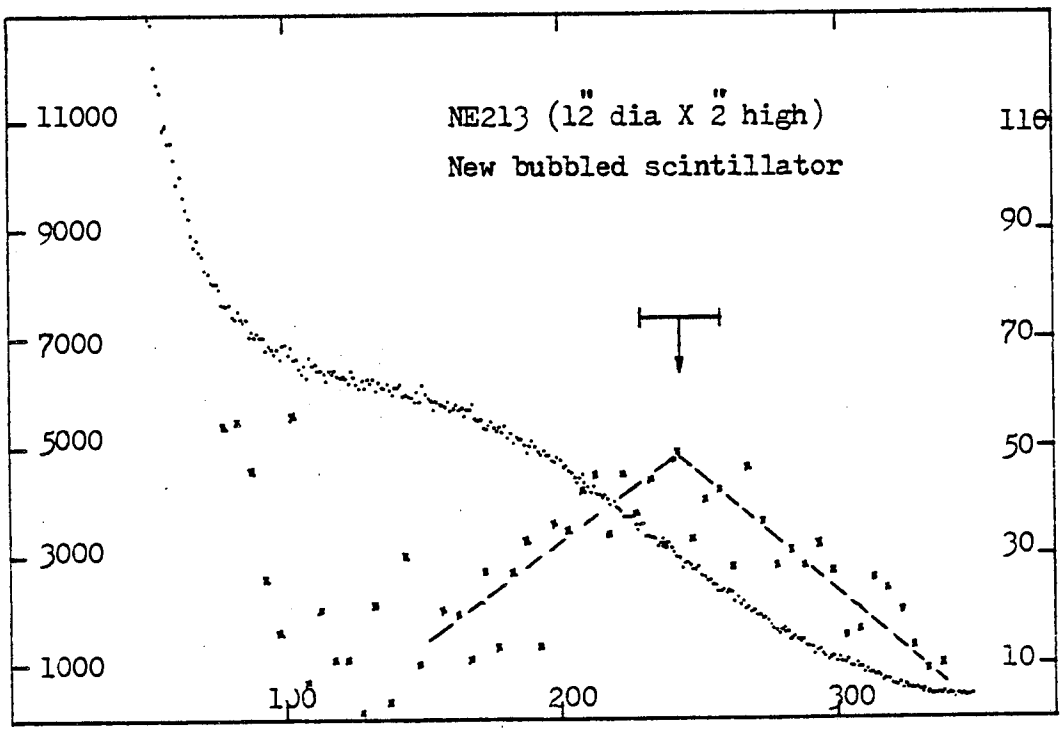

(b)

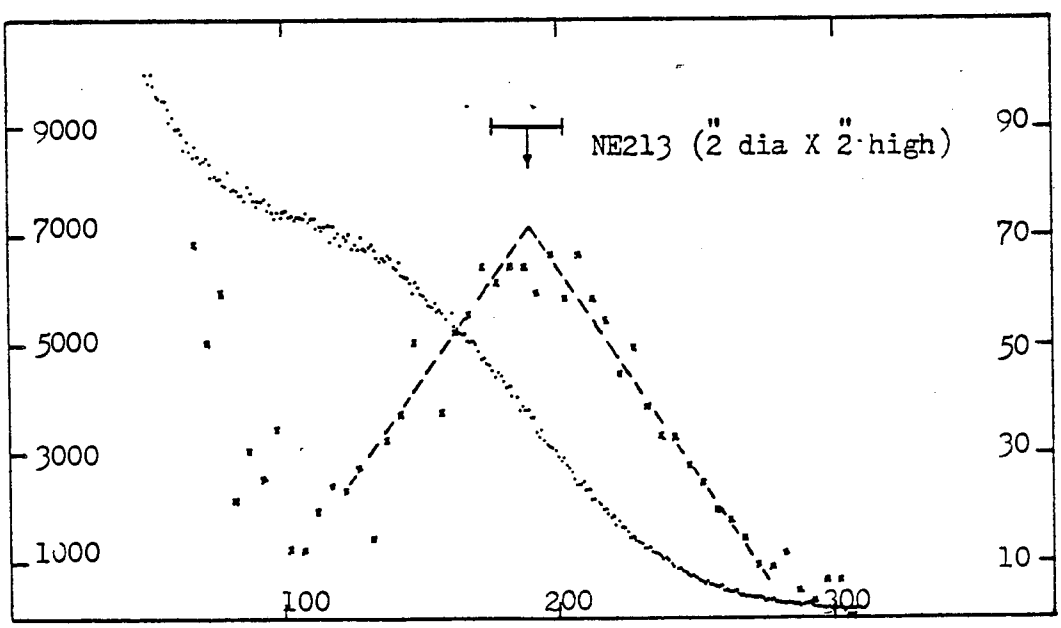

(c)

Figure 2.8. Recoil proton spectra from three different detectors to mono-energetic neutrons of 2.61 MeV. The differentiated spectra are shown with (X) and dashed line shows the position of pe

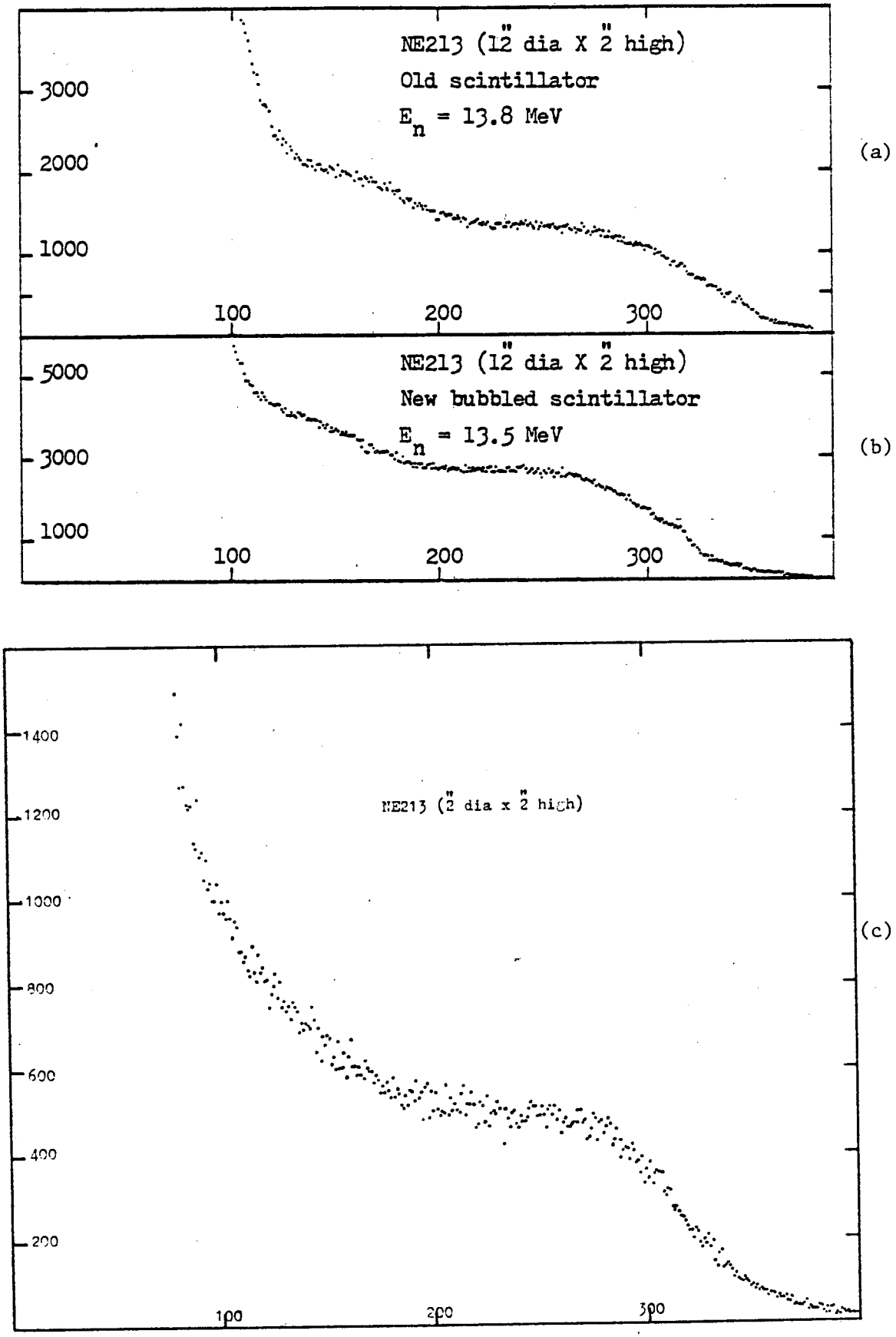

Figure 2.9. Recoil proton spectra from three different detectors to mono-energetic neutrons from $^{3}H(d,n)^{4}He$ reaction.

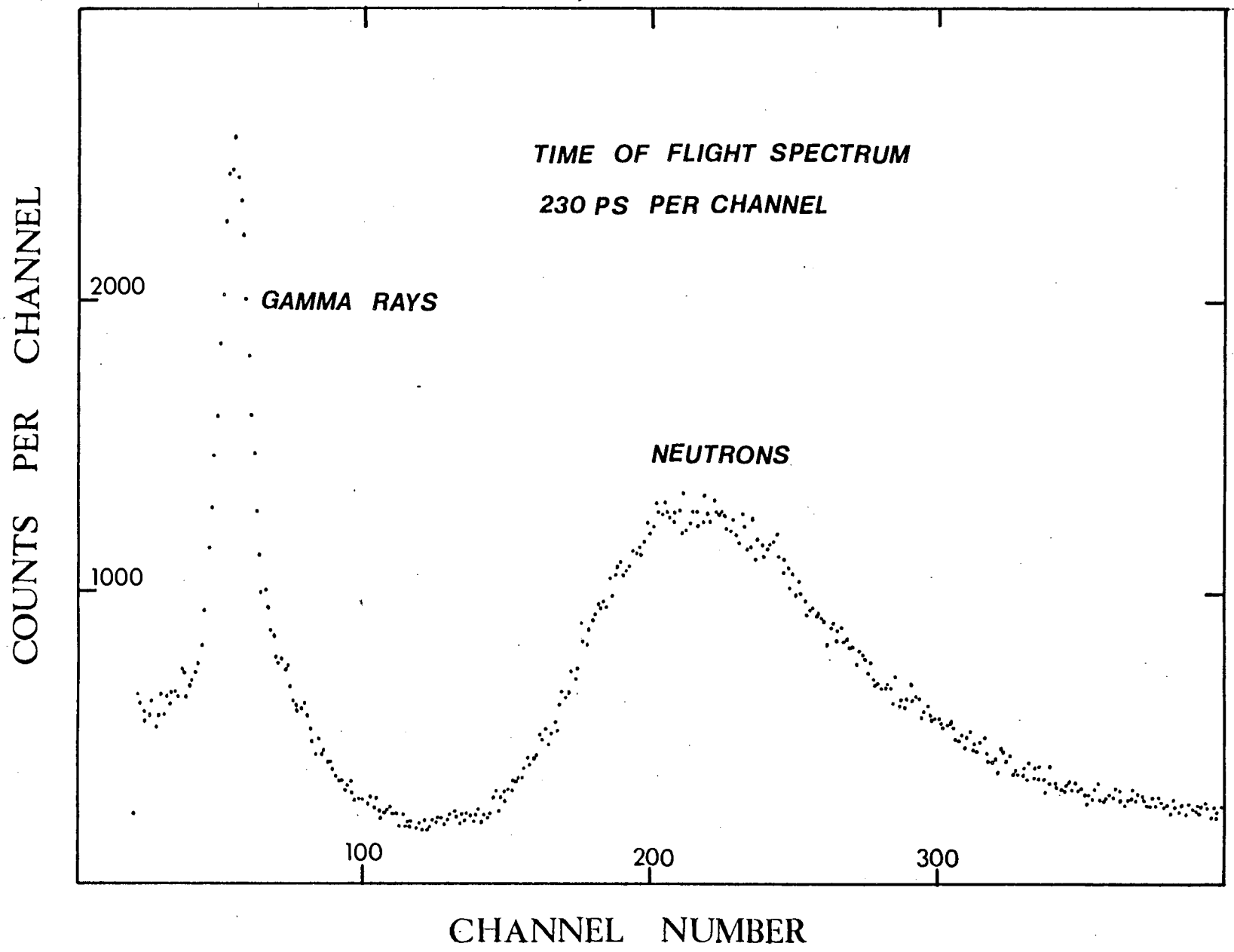

Figure 2.10. A typical time-of-flight spectrum obtained with the experimental arrangement shown in Figure 1.

To determine the incident neutron energy E_i corresponding to each channel i of the time-of-flight spectrum, it is necessary to determine the time of flight t_i corresponding to each channel i of the spectrum.

For this reason the annihilation gamma rays emitted from a ^{22}Na source were used to obtain the time calibration T_c = 230 ps per channel of the analyzer.

The gamma peak occurs at a time $t_\gamma = X/c$ from $t = 0$, where X is the gamma ray flight path (distance between the centre of D1 and D2 detectors, Fig. (2.1) and c is the velocity of light.

The time of flight corresponding to any channel of the spectrum is then

$$t_i = t_\gamma + (i-\gamma)T_c = \frac{X}{c} + (i-\gamma)T_c$$

where γ denotes the gamma peak's channel number.

The kinetic energy E_i' of a scattered neutron corresponding to channel i is expressed by:

$$E_i' = M_n\left[\frac{1}{(1 - \frac{X^2}{c^2 t_i^2})^{\frac{1}{2}}} - 1\right]$$

where M_n is the neutron rest mass in MeV

c is the speed of light

X is the length of the fixed flight path

t_i is the time of flight of the scattered neutron.

Kinematically, the kinetic energy of the incident neutron can be specified in terms of the scattering angle, the flight path, and the

flight time of the scattered neutron.

$$E_i = \frac{2M}{[(1 + \frac{2M}{E_i'})\cos^2\theta - 1]}$$

where M is the nucleon rest mass and θ is the scattering angle.

If the velocity of neutrons is more than 0.1C, the above expressions are suitable for measurement of energy, otherwise a simple formula shown below can be applied:

$$E_i'^{\frac{1}{2}} = 72.3X/t_i$$

where t_i is the flight time in nsec, X is the flight path (metres) and E_i' is the energy in MeV. The latter formula is used in the present work.

Finally, to obtain the incident neutron kinetic energy E_i corresponding to channel i, kinematically it is found to be

$$V_n^2 = V_n'^2 (1 + \tan^2\theta)$$

where V_n is the velocity of neutron before scattering and V_n' is the velocity of the neutron after scattering, therefore

$$E_i = E_i' (1 + \tan^2\theta) \quad .$$

2.7 Background Problems

There are several background sources in a time of flight spectrum, which are discussed briefly in the following lines.

1) Accidental or random coincidences:

If the signal rates in the detectors D1 and D2 are designated N_1 and N_2, respectively, then the number of accidental or chance coincidences, A, observed per second with a steady beam is given by the well known expression

$$A = N_1 N_2 (\tau_1 + \tau_2)$$

where τ_1 and τ_2 represent the time durations of the D1 and D2 logic pulses respectively, or where $(\tau_1 + \tau_2)$ is the time resolution of the system.

Since these uncorrelated D1 and D2 pulses are randomly distributed in time, the resulting background is a level "sea" of events spread over the entire time of flight spectrum.

The rate of accidental coincidences can be reduced by shielding the D2 detector from the source and from stray radiation to reduce the event in this detector.

2) Gamma-ray background

Comparing the flight time of gamma rays over 90 Cm flight path (3.0 nsec) and that of the most energetic neutron emitted by ^{241}Am/Be (24.27 nsec) and taking account of the time resolution of our system ($\sim$ 3.5 nsec) results that gamma rays are easily separated from neutrons by time of flight, hence, subtraction of the gamma ray background using P.S.D. is not required.

3) Carbon background:

Neutron-carbon non-elastic interactions in the D1 scintillator

may produce both a detectable charged particle and a secondary neutron. Such interactions are indistinguishable from the desired n-p interactions. At 90 MeV all neutron-carbon non-elastic interactions produce charged secondaries and about 90% of these interactions produce secondary neutrons[66].

Because the carbon background begins to become significant above about 15 MeV, therefore, this effect is not of importance in this experiment.

2.8 Discussion

In such an experiment one may think that many factors could be involved as a cause of discrepancies between results from different work, that is, the electronics, the purity of the scintillator and some other factors that have already been mentioned in 2.7.1.

The data, Table 2.1 and Fig. 2.6, show no significant difference in response between the two small detectors, a small difference between the two large detectors and a marked difference between the large detectors and the small detectors. The present data is compared with previous measurements in Fig. 2.7. It can be seen that the present small detector data comes close to the data by Fowler et al.[47], Drosg[67], Bertin et al.[68], Taylor and Kalyna[69] and Batchelor et al.[70], while they tend to differ a little from the data of Alberigi Quaranta et al.[71] and Smith et al.[51]. They differ significantly from the trend of the data of Verbinski et al.[72] and markedly from the data of Rothberg et al.[73]. Thus the behaviour of both small detectors is consistent with the general trend of most previous measurements. The response

of both large detectors on the other hand differ significantly from all other measurements, with the sole exception that the curve due to Rothberg et al.[73] and the data on one of the large detectors are consistent. While it is tempting to note that the scintillator studied by Rothberg et al.[73] was the largest of the previously studied scintillators (150 mm × 125 mm × 100 mm), it is not significantly different in size from those studied by Bertin et al.[68] and by Alberigi Quaranta et al.[71].

The present large detectors (305 mm diameter by 50 mm long) are the only cases in which the scintillator is substantially larger than the photomultiplier cathode and in which a light guide is employed. These facts seem more relevant to an explanation of the behaviour than possible contamination of the NE213 in the large scintillators, since one of them was newly filled for these tests while the other has been in use for 10 years. (Contamination may well account for the small difference between their responses.) Suggestions as to a possible explanation can be offered, although without any proof of correctness. An electron induced scintillation in NE213 consists principally of a "fast" component with a decay time constant of 4 ns along with a much less intense component with a decay time constant of 25 ns, whereas for a proton induced scintillation the "fast" 4 ns component is accompanied by a relatively intense "slow" component of decay time constant 47 ns[74]. If the important "slow" component in the proton induced scintillation were of a different wavelength from the "fast" component which is predominant in the electron induced scintillation, then preferential absorption of the proton induced scintillation might occur in the perspex light guide. In this connection it may be

noted that Kalyna and Taylor[75], discussing pulse shape discrimination with scintillators of larger diameter than the photomultiplier cathode, comment on the desirability of keeping the coupling light guide as short as possible. Alternatively, the sensitivity of a photocathode is often more wavelength dependent near the edge[76] and if the action of the light guide were to direct, by total internal reflection for example, a large proportion of the scintillations to the edge of the photocathode a different sensitivity to electron and proton induced scintillations might result compared with a small scintillator mounted without light guide when the photocathode would be more uniformly illuminated. Kalyna and Taylor[75] have commented on the greater importance of the illumination of the edge of the photocathode when a conical light guide is employed, albeit in relation to the poorer quality of zero-cross-over timing pulse shape discrimination.

We conclude that for an NE213 scintillation counter with a large scintillator coupled by a conical light guide to a small photomultiplier there is a significant difference in the electron-proton relative response function from that applicable to a small sample of NE213 mounted directly on a photomultiplier.

In relation to the analysing power studies to be described in the following chapters, these tests indicate the desirability of setting recoil proton discrimination levels with reference to recoil proton spectra rather than using gamma-ray sources and electron-proton relative light output data.

A paper based on the work described in this chapter has been published in Nuclear Instruments and Methods and is included in an appendix.

CHAPTER 3

NEUTRON POLARIMETER

3.1 Introduction

The fast neutron polarimeter, holding 24 detectors, used in the present work is capable of analysing power and cross-section measurements at twelve angles simultaneously. The detectors are sited in pairs at each scattering angle at equal distance from the centre of the scattering sample, for left, right scattering asymmetry measurement.

In order to determine the asymmetry, accurately, any variation in detection efficiency should be cancelled by interchanging left and right detectors. This can be done either by precessing the incident neutron spin through 180° degrees in a magnetic field[40], or by making successive measurements with the roles of the right and left detectors interchanged[77]. Interchanging the detector pair may also cause disturbances. While opinions differ as to which is the better technique, the latter has been used successfully in this laboratory[77,78] and thus was used in this work.

3.2 The Neutron Polarimeter

Fig. 3.1 shows side and top schematic drawings of the polarimeter. In order to make the polarimeter light and to avoid the stray magnetic fields which can be caused with steel components, it is constructed almost entirely of aluminium alloy.

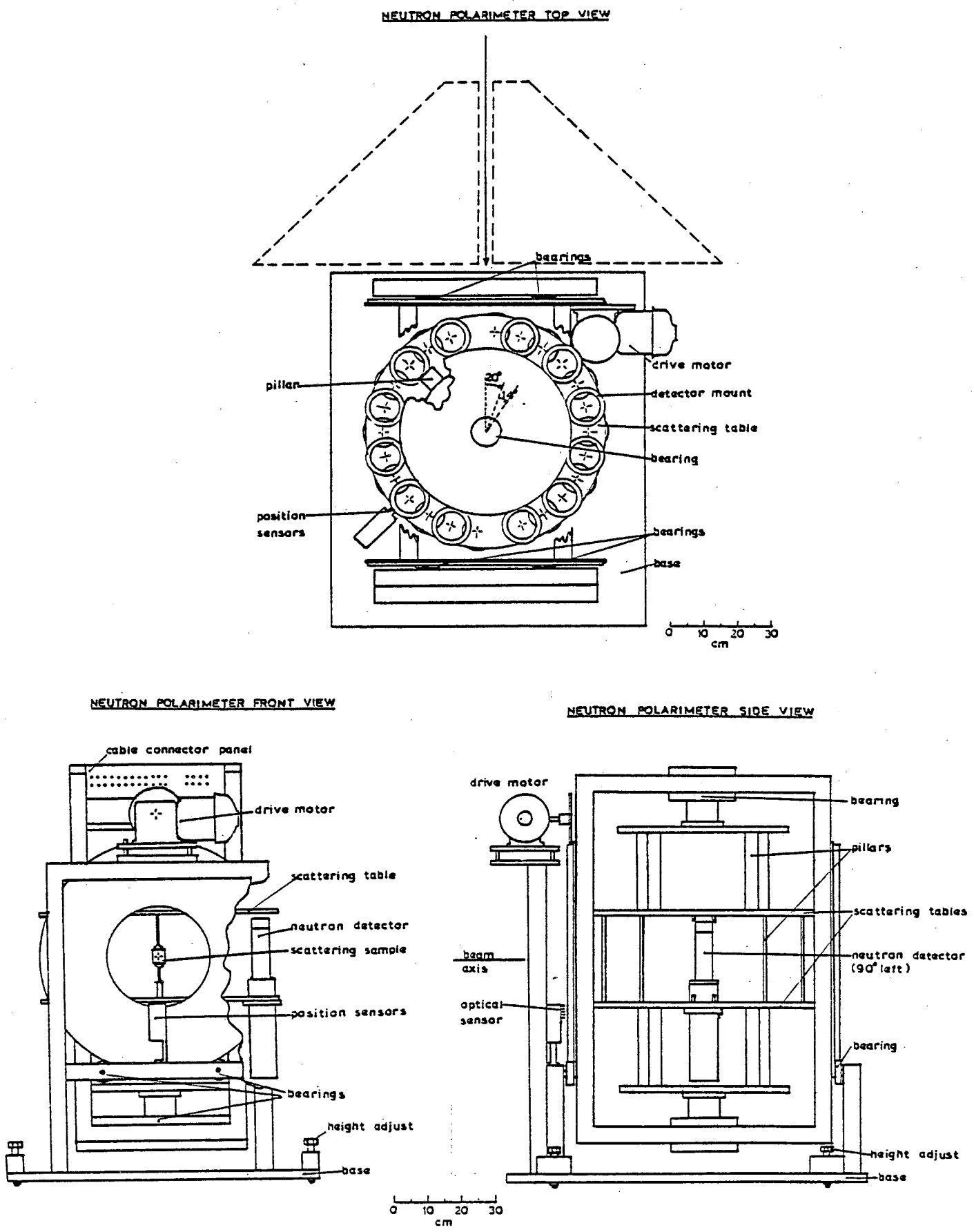
NEUTRON POLARIMETER TOP VIEW
bearings
drive motor
pillar
detector mount
scattering table
bearing
position sensors
bearings
base
0 10 20 30
cm
NEUTRON POLARIMETER FRONT VIEW
cable connector panel
drive motor
scattering table
neutron detector
scattering sample
position sensors
bearings
height adjust
base
NEUTRON POLARIMETER SIDE VIEW
drive motor
bearing
pillars
scattering tables
neutron detector (90° left)
beam axis
optical sensor
bearing
height adjust
base
0 10 20 30
cm

Figure.3.1

The polarimeter holds a maximum of 24 detectors on two scattering tables, which lie parallel to the reaction plane, and they are able to rotate around the vertical axis of the scattering sample. This provides the variation of the scattering angle for the detectors, and also the detectors can be rotated into the neutron beam position to determine their relative efficiencies as required for differential cross-section measurements.

The sample holder is connected to a compressed air cylinder. The sample is fixed to the holder and can be pneumatically retracted remotely from the in-beam position for background measurements. The polarimeter can be set in two positions, one covering 20 - 160 degrees in 14 degree intervals, the other covering 13 - 167 degrees in 14 degree intervals. Therefore overall it can measure 23 angles ranging from 13 to 167 degrees in 7 degree intervals. The frame which holds the scattering tables rotates with respect to the polarimeter base plate which is adjusted so that rotation is about the axis defined by the neutron collimator. Each detector is mounted in a clamp so that the height of the detectors, with their axes perpendicular to the scattering table, can be adjusted.

The rotation of the polarimeter is driven by a motor and four stopping positions, $\phi = 0$, $\phi = \pi$, $\phi = \frac{\pi}{2}$, $\phi = \frac{3\pi}{2}$, are provided. The first two orientations provide the required analysing power and cross-section measurements, while the last two positions provide a test for any instrumental asymmetry, since in this configuration there should not be any left/right asymmetry and any measured is due to a systematic fault.

The polarimeter assembly was placed behind a collimator for neutron collimation and shielding. The collimator was placed in

front of the neutron producing target at the particular emission angle (49°) selected for the experiment. The scattering table can be rotated to twenty seven positions, three counting positions and twenty four in beam detector calibration positions.

Alignment is performed optically, using cylindrical inserts in the collimater and polarimeter end plates. The height of the liquid scintillators were adjusted so that their centres were at the same height as the centre of the scattering sample, while the latter was in line with the collimator axis and with the centre of the neutron producing target.

In addition to 22 neutron detectors for the polarization and cross-section measurements, two more neutron detectors were used for monitoring the yield of the neutrons from the target. One of the monitors was placed very close to the target (to be referred to as the target yield monitor (TYM). It was used for normalization. The other monitor, was positioned directly in the collimated beam behind the polarimeter (to be referred to as the collimated beam monitor (CBM). It was used to monitor the neutron flux in the collimated beam and to measure the transmitted flux when the scattering sample was in the beam position.

3.3 Polarimeter Control CAMAC System

A PDP11/Camac system, which includes some custom built pulse routing and interfacing, was used to control the polarimeter and automatic data collection. It was developed by J.R.M. Annand[16] from one designed and built up by F. McNeil-Watson[79] to control a 12 detector polarimeter. Fig. 3.2 shows block diagram of the system.

POLARIMETER CONTROLL

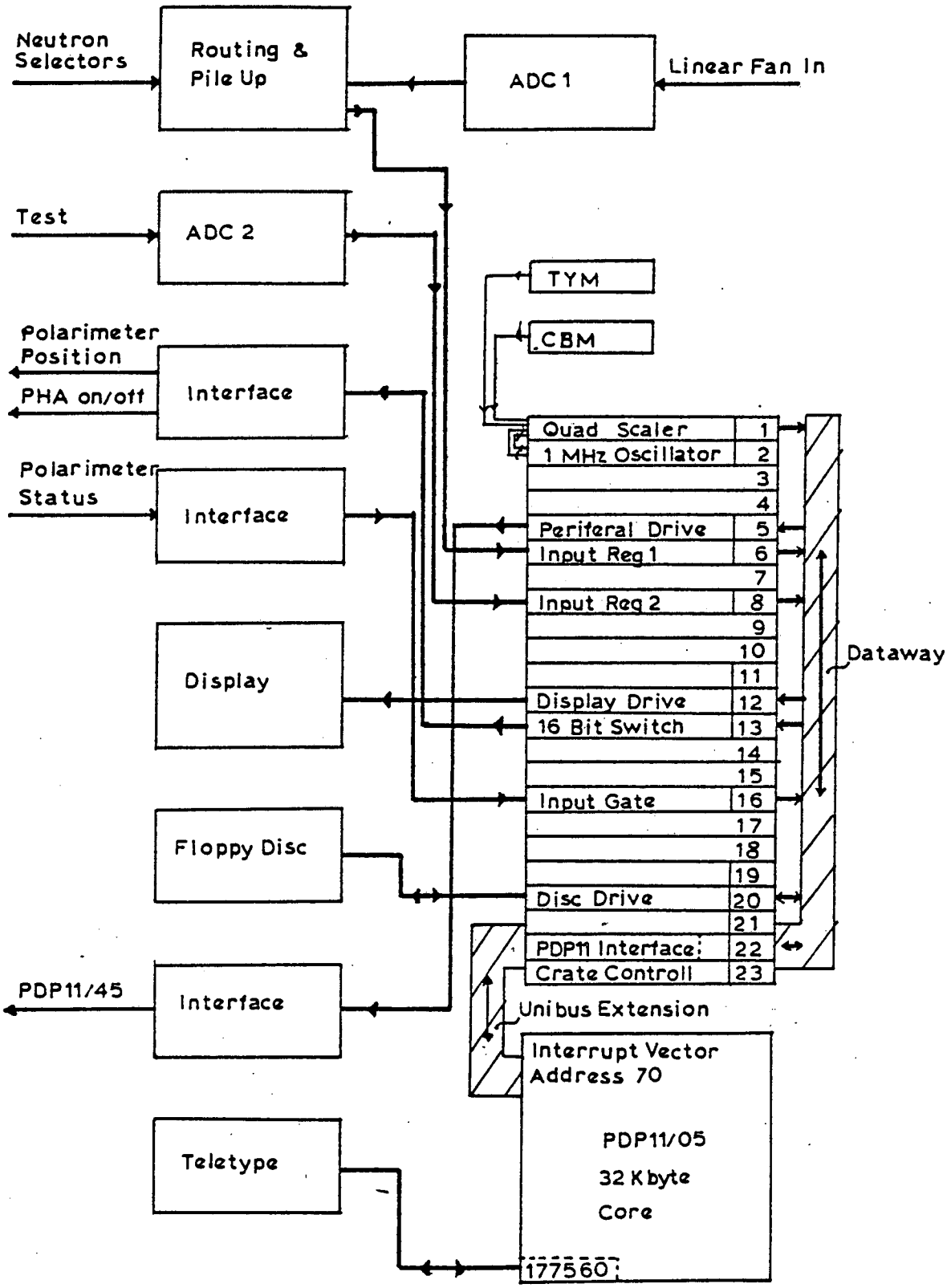

Figure.3.2

The slow coincidence pulses from a maximum of 24 "AND" gate outputs of neutron selectors corresponding to the 24 neutron detectors are fed into the routing and pile up rejection network, Fig. 3.3. Only one ADC (LABEN model 8213) is used to give service to the neutron detectors and so the origins of pulses have to be identified. A network of NAND gates which produces the 5 bit code corresponding to the active "high" input 1 - 24, facilitates this identification, but activation of two or more inputs at the same time, produces a code which is the logical "OR" of the two or more, thus misrouting will occur. In order to detect such pile up events a network of EXCLUSIVE OR gates is used whose output goes low for all combinations of 2 and some combinations of 3 simultaneously active inputs. This is used to gate the conversion start pulse within the ADC, thus pile up events are not counted.

One pile up reject bit and 5 routing bits are latched, as are the 8 bits from conversion of the linear fan-in pulse height.

The total dead time output which switches low signalling a pulse for conversion at the ADC is used, after being suitably delayed, to strobe the latch. The state of the routing information and pile up bit is stored at this instant and does not change until the ADC accepts another input. The "data-ready" signal causes the bits to be transferred to a Camac Parallel Input Register of type NE7014.

A multi scaler mode is also provided for asymmetry tests. In this case ADC bits are ignored and counts stored to double precision (32 bits). The offset (channel number) is incremented after each run so that the number of counts for each run is stored separately.

The pulse height analysing facility for testing and adjustment

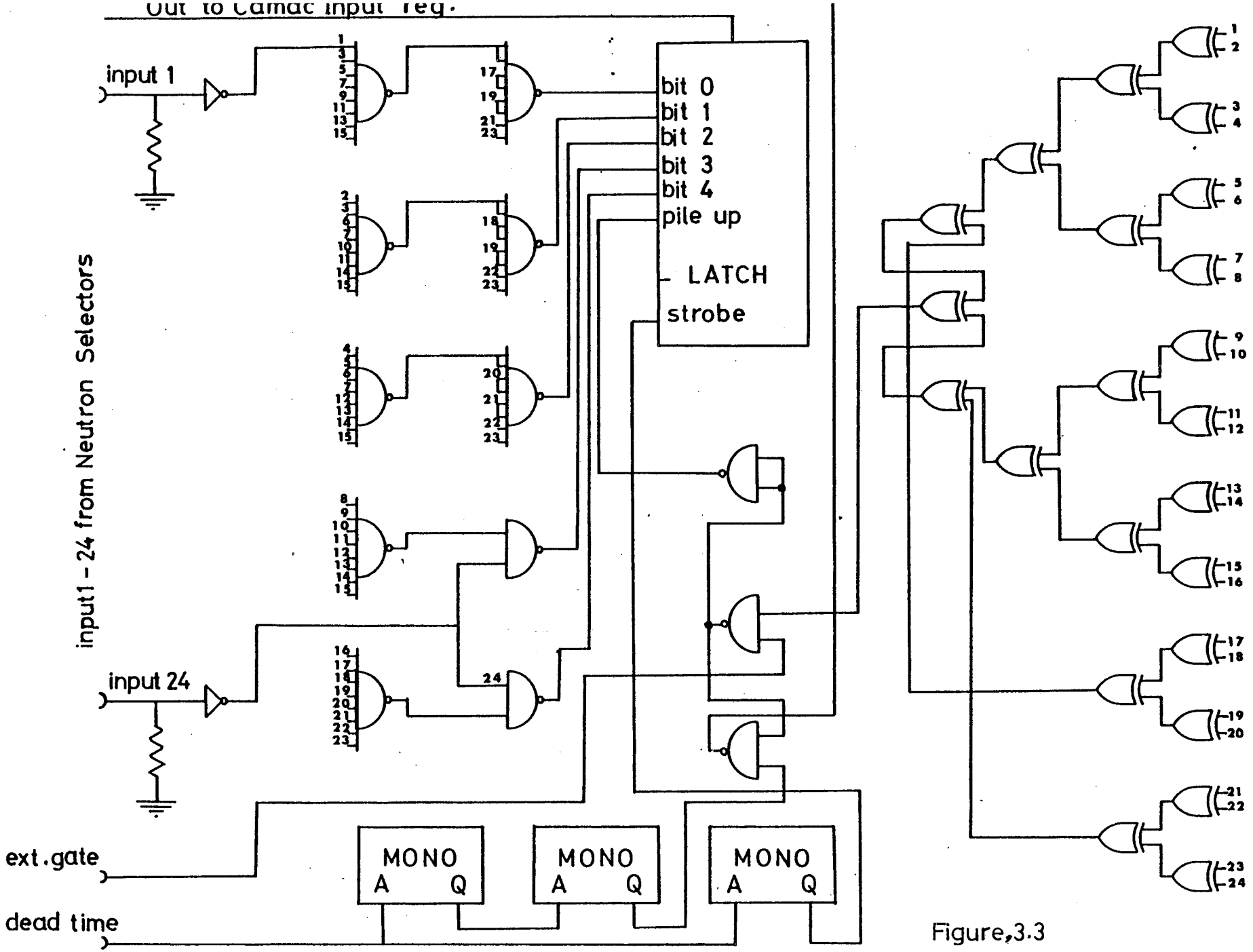
Out to Camac input reg.
input 1
input1 - 24 from Neutron Selectors
input 24
bit 0
bit 1
bit 2
bit 3
bit 4
pile up
LATCH
strobe
ext.gate
dead time
MONO
A
Q
MONO
A
Q
MONO
A
Q

Figure,3.3

of detectors and neutron selectors is provided by another identical ADC feeding directly to a NE7014 register.

A DEC PDP11/05 computer with 16K words of core memory to which is attached a single Camac crate which controls and accumulates data from the 24 detector polarimeter.

A pulse height analysing programme is provided to accumulate the spectra from the 24 neutron detectors as well as monitor counts for each measurement condition of the polarimeter. It also includes facilities for driving the polarimeter to any of the four azimuthal positions, as well as sample changing for each position automatically. Spectra stored in core may be displayed on a 19" screen controlled by a NE7011 display driver. The data blocks of 64, 128, 256 or 1K words may be displayed. An 8" floppy disk unit, using a flexible disk drive, developed by F. McNeil Watson[79] provides an independent extra 256K bytes of data storage space. This is divided into 76 tracks, each track is also divided into two sectors. Data may be read or written in blocks of 2K words, i.e. one data area.

1K of data can be read or written into each sector, therefore the total of 10K data associated with a measurement on one sample occupies 5 tracks. Data could be transferred to the PDP11/45 computer of the Edinburgh Physics Department by a NE7065 peripheral driver and a small custom built interface, while the PDP11/45 was available. The data could be transferred in blocks of 64, 128, 256, 1K or 10K words. A data checking and receiving programme had to be run simultaneously on the PDP11/45. The 11/05 routine would terminate unless a handshake signal was received within 2 seconds of sending data. Alternatively data was taken via a teletype paper punch and thence to the computing network of EMAS for off line analysis.

An NE7066 switch which is extended from 12 to 16 bits by the inclusion of 4 reed relays, switches signals to control the polarimeter orientation and switches the ADC's and scalers on and off. The system clock consists of a 1 MHZ oscillator feeding into one channel of an NE9021 Quad scaler. Neutron target monitors feed the other channels. The crate and PDP11/05 buses are interfaced by a NE9030/9032 controller.

3.4 Polarimeter Movement

The four azimuthal positions of the polarimeter have already been discussed in Section 3.2. For automatic data collection, a remote position command drives the polarimeter to a particular position. The routine first checks if the polarimeter is in the right position or not. If not, it fails and returns to command level. If so, it gives the position change command and waits for the correct position response via the Camac Input Gate. Each of the four positions is entered by an optical switch activated by a small black plastic tab fitted to the rear wheel of the polarimeter. If in 600 seconds the polarimeter does not reach the correct position, the motor drive is switched off, and an error message is given. This is a safety device to protect the drive.

Automatic data collection is provided by giving a sequence of desired positions, each associated with an identified area of computer memory. The measuring time for each position of the scattering sample in and out, and the number of cycles of the selected sequence also should be entered at the start of a run. When the command to start the sequence is typed in, the polarimeter

will be driven to the first position and counting starts for the pre-set time and the system goes through the requested sequence.

In the automatic mode, the polarimeter position is checked on every clock interrupt and an external error input, normally fed from the accelerator control system, is inspected. If a fault in the polarimeter or the accelerator shut down is observed, execution of the sequence will be automatically stopped. It can be restarted from where it stopped after the fault has been removed manually.

3.5 Data Storage

The 10K 16 bit words of data store is divided into five areas of 2K and each of the areas may be sub-divided into sub-areas of 1K, 512, 256, 128 or 64 words. Therefore area or sub-area can be specified for spectrum input, display, output or numerical analysis.

Areas 1 - 4 are specified for the data collection with sample in or out for two different polarimeter positions ($\phi = 0$, $\phi = \pi$). while area 5 is specified for detector efficiency calibration data, for the purpose of the differential cross-section calculation.

If a test run is required, any area with any orientation can be used.

CHAPTER 4

NEUTRON DETECTORS

4.1 Description

The neutron detectors are cylindrical containers made from aluminium of 2 mm thickness, 15.4 cm in length by 5.08 in diameter, filled with NE213 liquid scintillator. The aluminium cylinders are internally painted with titanium dioxide paint (NE562). As an expansion chamber, to keep the sensitive volume of liquid free from the nitrogen expansion bubbles, a small glass chamber with a neck of 2 mm diameter is fixed to the top end of the scintillator container. A fast linear focused type photomultiplier tube is optically coupled, using optical contact grease (NE587), to a glass window which is fitted to the other end of the scintillator container. A mu-metal shield is used round each photomultiplier tube for protection against any possible change in gain of the photomultiplier due to change in orientation in the magnetic field of earth during rotation of the polarimeter.

The photomultiplier, voltage divider chain and preamplifier are all enclosed in a light-tight aluminium tube as shown in Fig. 4.1.

The EMI 9814B type photomultipliers were used for most of the detectors while Mullard 56 AVP photomultipliers were used just to build a few of the detectors.

The carbon resistor dynode chains used with the two types of photomultiplier are shown in Fig. 4.2. Both photomultipliers have similar spectral response and electron transit time spread. Differences in photomultiplier gain, caused by differences in the

LIQUID SCINTILLATION COUNTER

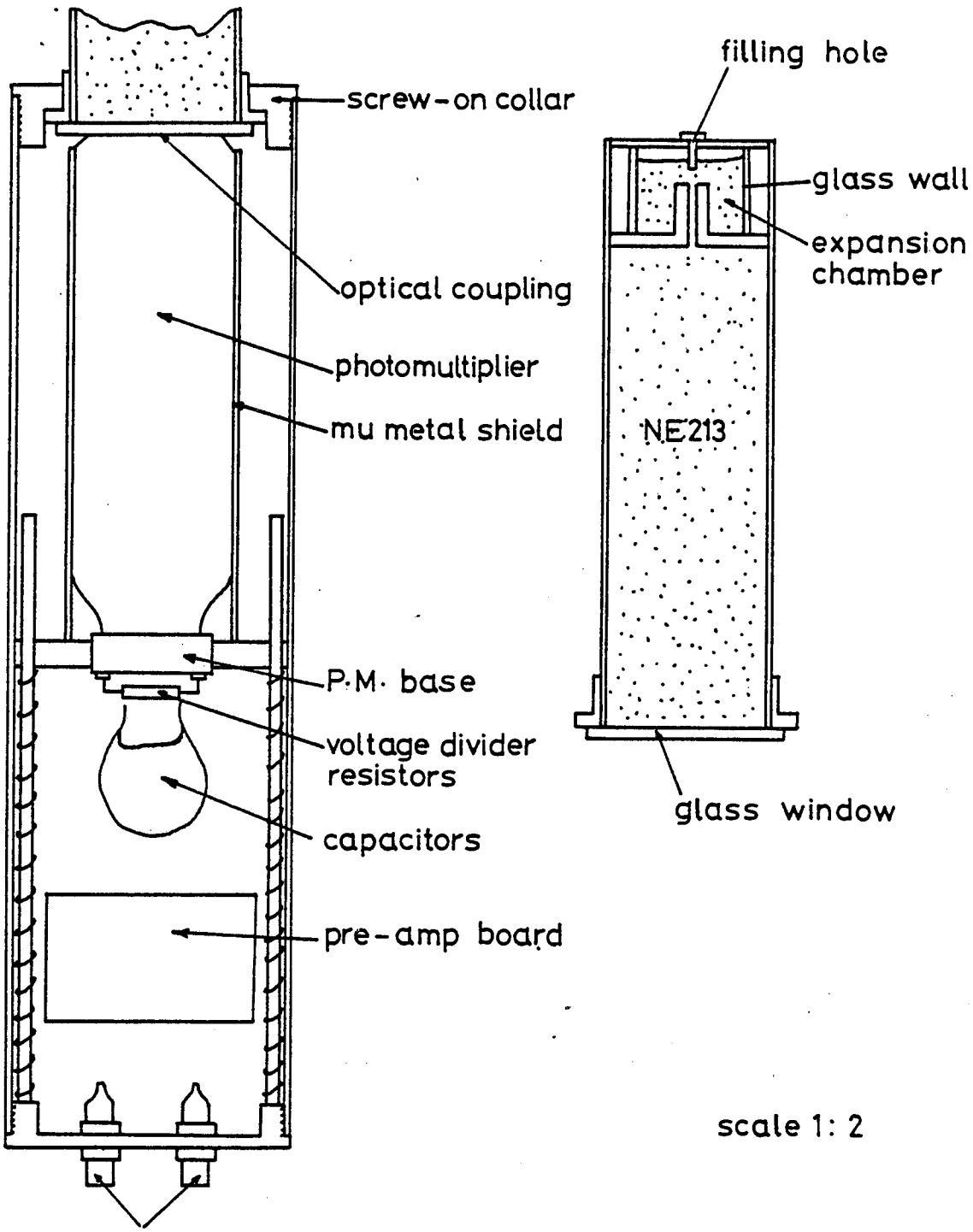

Figure 4.1.

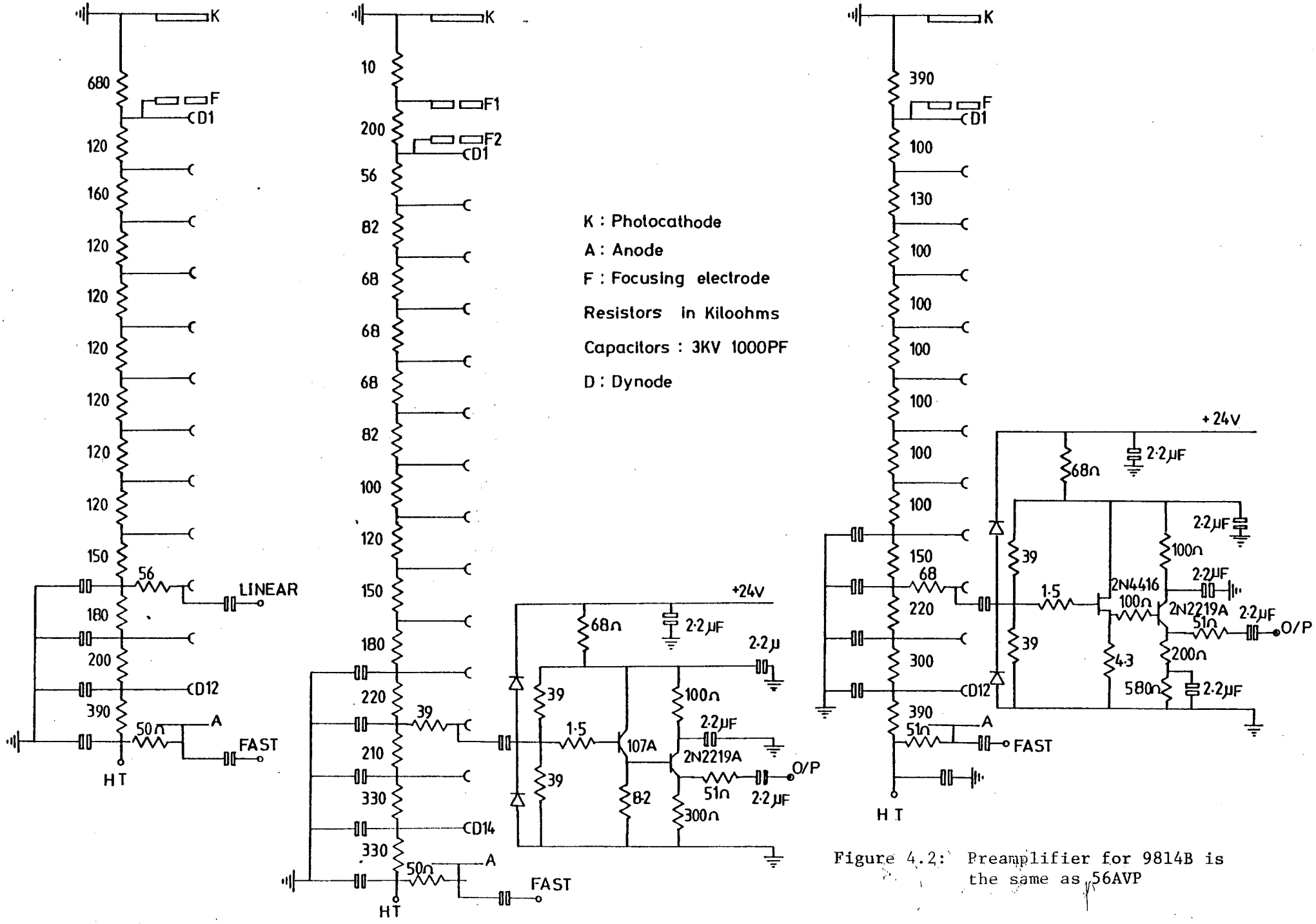

Figure 4.2: Preamplifier for 9814B is the same as 56AVP

quantum efficiency of the photocathode are equalised by a resistor which is added in series with the divider chain, therefore reducing the anode potential.

In order to achieve better results by reducing the background counting rate, a systematic test was carried out on the use of a RCA8575 photomultiplier which has a better quantum efficiency than EMI9814B and 56AVP photomultipliers, in conjunction with a new dynode chain, a preamplifier and a newly designed[80] neutron selector. This test showed satisfactory results, which will be discussed in Section 4. Four new detectors employing RCA8575 photomultipliers and six new neutron selectors[80], which were modified for pulse shaping and delay to be compatible with the other neutron selectors, were built and used in the polarimeter. The dynode chain and preamplifier circuit used with the RCA8575 photomultiplier is also shown in Fig. 4.2.

The H.T. for all detectors was supplied by a 30 mA Fluke Power supply. A common 24V supply was used to power the preamplifiers.

4.2 Pulse Shape Discrimination

The scintillation and the response mechanism of organic scintillators to heavy particles (i.e. protons) and electrons is fully discussed in Chapter 2.

Discrimination between proton recoils and electron recoils from incident neutrons and incident gamma-rays, respectively, is possible by distinguishing the different shapes of current pulses resulting at the output of the photomultiplier from the different intensity ratios of fast and slow scintillation decay times. A considerable

number of methods have been developed for distinguishing particles of differing specific ionization.

The method used in the present work to discriminate neutrons from gammas is referred to as the Zero Cross Over Timing technique. In this technique all the information about particle identification is carried by an integrated and doubly differentiated pulse from a single dynode of the photomultiplier. The time from the start of such a pulse to zero crossing of the amplitude base line is longer for neutrons (recoil protons) than gamma rays (recoil electrons).

The results of the double differentiation is to produce a bipolar voltage pulse which passes through zero at a time which depends only on the input pulse shape and is amplitude independent. This is shown in Fig. 4.3.

4.3 Electronics of the Side Detectors

For each of the side detectors an electronic unit known as a neutron selector, which is a double width NIM module (old arrangement) or a single width NIM module (new arrangement), is used (Fig. 4.4). This unit is an assembly of linear amplifier linear discriminator, neutron/gamma discrimination circuit and a discriminator for gamma rejection. The amplifier is of conventional op-amp based design and the shaping is done by RC differentiation and integration. Pulse Shape Discrimination is by the "zero cross over" technique[81], which has already been discussed in Section 4.2.

The amplifier output is fed into a discriminator for the energy bias setting. The PSD circuit's output is fed into a discriminator for the rejection of gamma-ray events. The logic outputs of two discriminators are then fed into an AND gate whose output, in coincidence with the linear pulse from the amplifier, corresponds to the detection of a proton recoil of energy above the preset value.

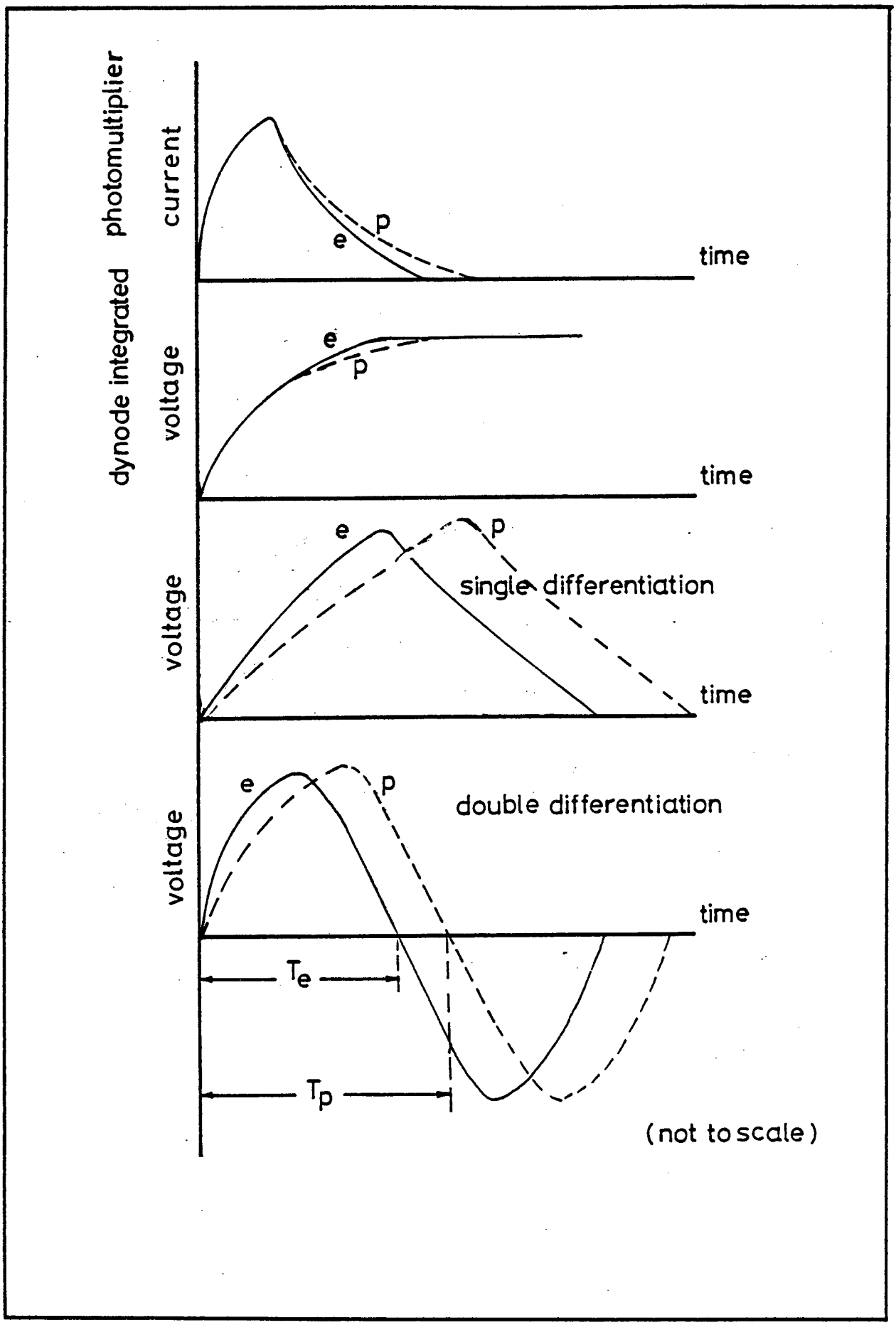

Figure 4.3. Pulse shapes in a zero crossing P.S.D. system.

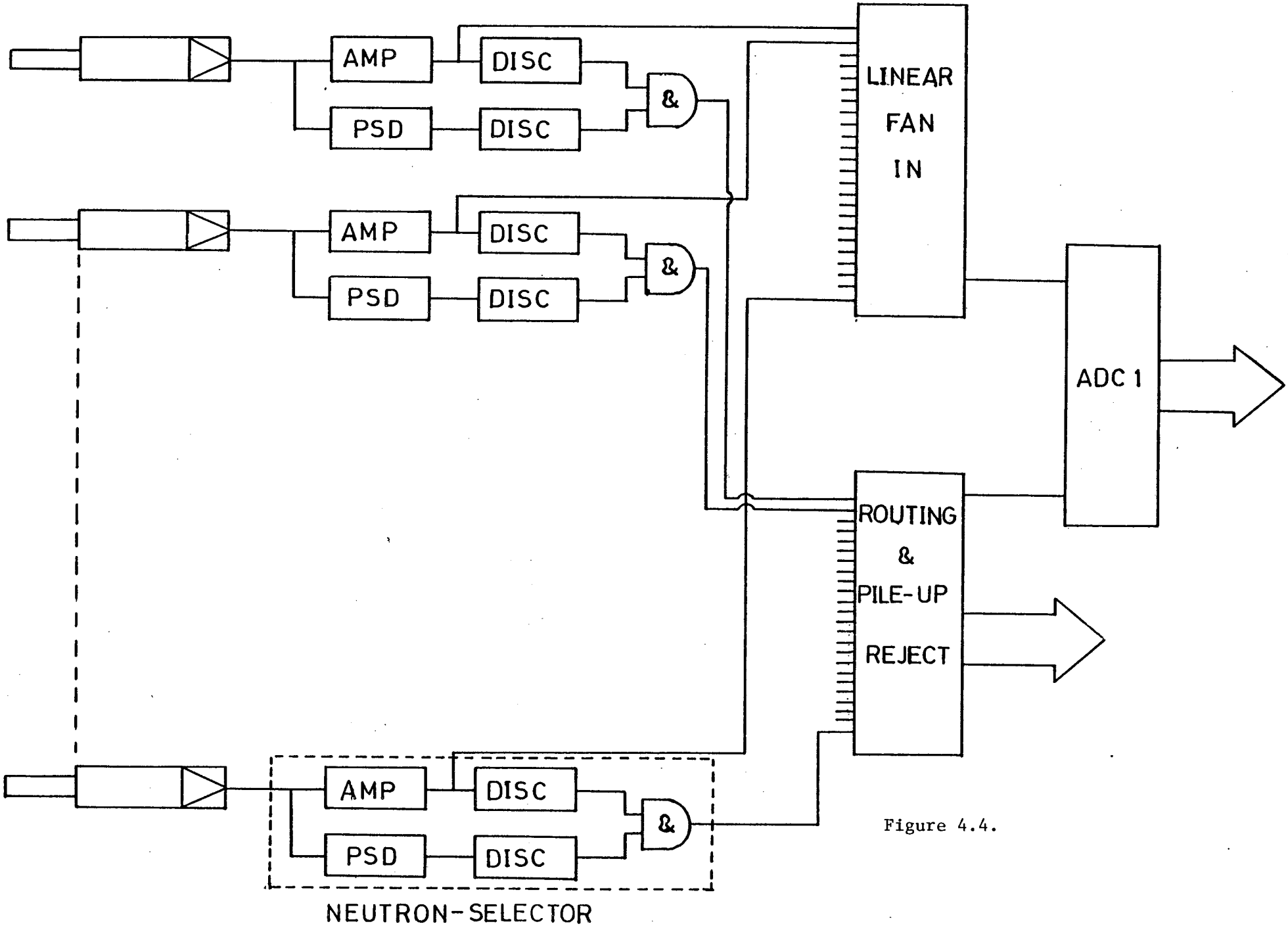
AMP
DISC
PSD
DISC
&
AMP
DISC
PSD
DISC
&
AMP
DISC
PSD
DISC
&
NEUTRON-SELECTOR
LINEAR
FAN
IN
ADC 1
ROUTING
&
PILE-UP
REJECT

Figure 4.4.

The amplifier outputs of all side detectors are fed into a linear fan-in unit, while all the outputs from the AND gates are used with the routing unit.

The output of the linear fan-in unit is used as input for a Laben 256 channel ADC, in coincidence with the output from the routing unit. Therefore pulse height spectra are accumulated in particular sections of the memory selected by the routing pulses as described in Chapter 3.

4.4 Target Yield Monitor; (TYM)

The TYM used to monitor the neutrons from the $^{2}H(d,n)^{3}He$ reaction consists of a 5 cm diameter by 5 cm long cylinder of NE213, coupled to a 56 AVP photomultiplier. The detector views the target through a one inch diameter collimator. The electronics employed with the TYM are similar to the electronics used for the detectors in the polarimeter, with PSD against gamma rays. A pulse height spectrum from the TYM is not collected. The number of events detected for any fixed time is recorded in a Camac scaler by using the discriminator output from the TYM neutron selector.

4.5 Collimated Beam Monitor; (CBM)

The CBM is positioned directly in the collimated beam behind the polarimeter. The distance of the CBM from the target was chosen such that the collimated beam defined by the collimator throat can illuminate the whole area of the scintillator. Also the distance was made sufficient to avoid contribution to the background of the side detectors by neutrons scattered from the monitor.

The CBM consists of a 12 Cm diameter by 5 Cm long cylinder of NE213 coupled to an EMI 9814B photomultiplier.

Similar electronics to those used with the polarimeter detectors are used for the CBM.

4.6 The Neutron producing Target and Shielding

The 3.0 MeV neutrons are obtained from a deuterium impregnated titanium backed by copper target, bombarded by deuterons of 390 keV energy. A strip 3mm by 10 mm of this target material is soft-soldered on to the copper end of a stainless steel, water-cooled target holder in the form of a finger.

The whole of the target assembly is mounted on the end of the beam line. Accurate alignment of target and collimator axis is possible due to flexibility of the target assembly.

A 500 Kv, voltage stabilized Van de Graaf supplies deuterons for bombarding the target. The target is capable of withstanding over 50 μA of DC beam current at 500 keV. Experimental runs were made with maximum beam current available and not less than 30 μA on the target. The vacuum pump oil causes some problems by depositing carbon on the target material, which reduces the efficiency of running time of the experiment seriously.

Using the Ti stopping power data of refs. (82) and (83) and hydrogen stopping power data[84], the target thickness was calculated to be 132 keV at 390 ± 10 keV incident energy. The Q value for the $^{2}H(d,n)^{3}He$ reaction was taken as 3.26 MeV, therefore neutrons of 3.0 ± 0.15 MeV were produced.

To reduce background due to direct neutrons from the source

reaction being detected by the side detectors, and scattered neutrons from the walls, floor and surrounding objects, a massive shielding mostly of paraffin wax and some concrete is deployed around the polarimeter, as shown in Fig. 4.5. The reconstruction and change of some concrete shielding which was used by J.R.M. Annand[16] to paraffin wax, provided much better background achievement which is illustrated in Fig. 4.6(a) and (b) for two detectors at two different angles, and can be compared with the results obtained from the original shielding[16] which is illustrated in Fig. 4.6(c).

A collimator of the form of a trapezium, made of steel and filled with paraffin wax is placed in front of the neutron producing target. A well defined beam is then produced by a circular throat, made of brass and high density polythene. To reduce the energy of the direct neutron flux passing through the shielding by inelastic scattering, a cylindrical block of lead was introduced around the collimator near the target end. The neutrons are then moderated by paraffin wax and subsequently captured and produce gamma-rays. To reduce this gamma-ray flux a 7.6 cm thick wall of lead was constructed at the back of the collimator.

4.7.1 Test for Instrumental Asymmetry

Before starting actual data measurements a test for instrumental asymmetries was needed to make sure that the detectors are stable and the polarimeter system is free from any false asymmetries.

This was done by the use of a strong ^{60}Co source (1 mC_i) which was placed at the centre of polarimeter (sample position). The multiscaler mode of the pulse height analysis system, described in

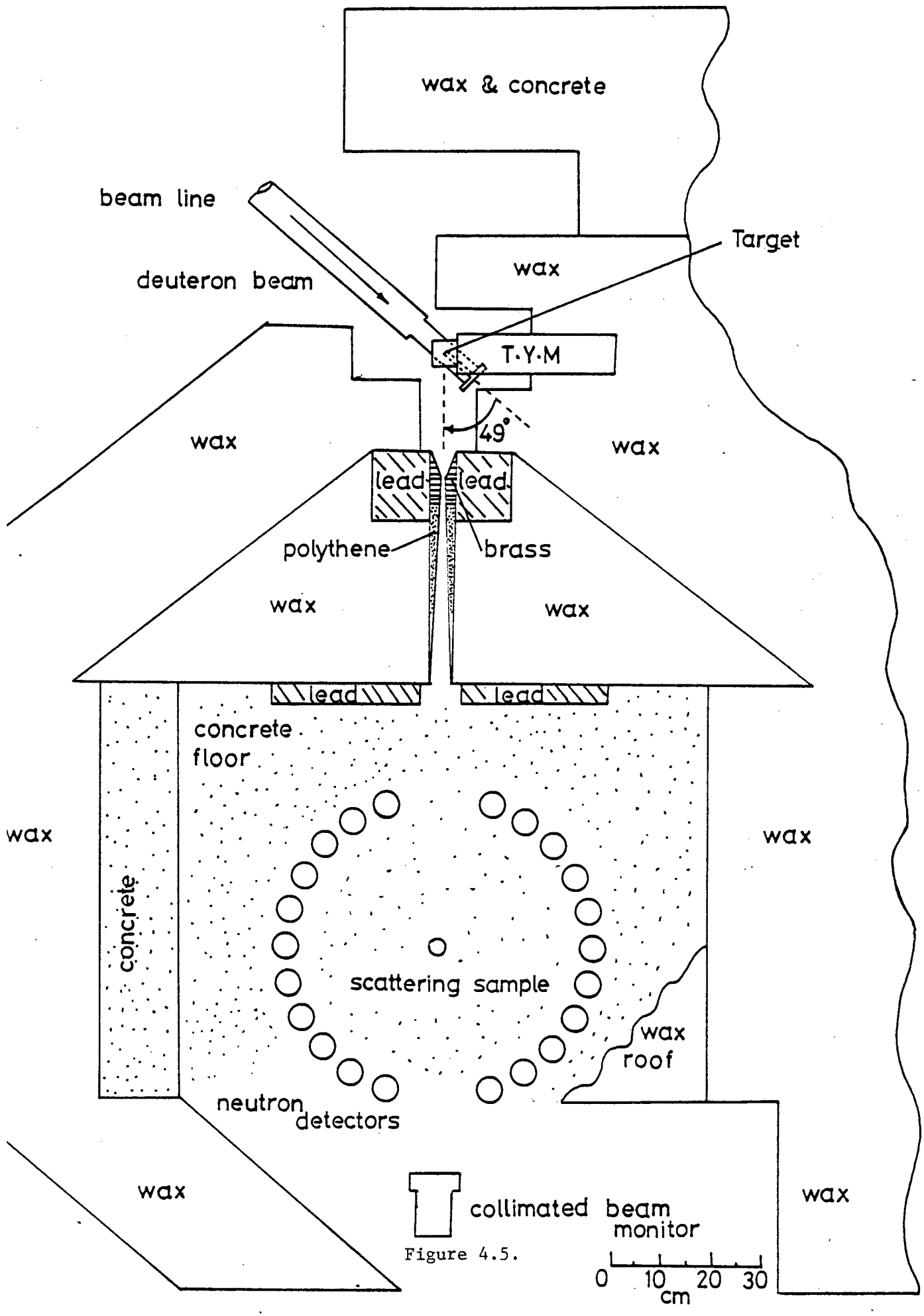
3·0MeV NEUTRON SCATTERING LAYOUT
wax & concrete
beam line
deuteron beam
Target
wax
T·Y·M
49°
wax
wax
lead
lead
polythene
brass
wax
wax
lead
lead
concrete
floor
wax
wax
concrete
scattering sample
wax
roof
neutron
detectors
wax
wax
collimated beam
monitor
0 10 20 30
cm

Figure 4.5.

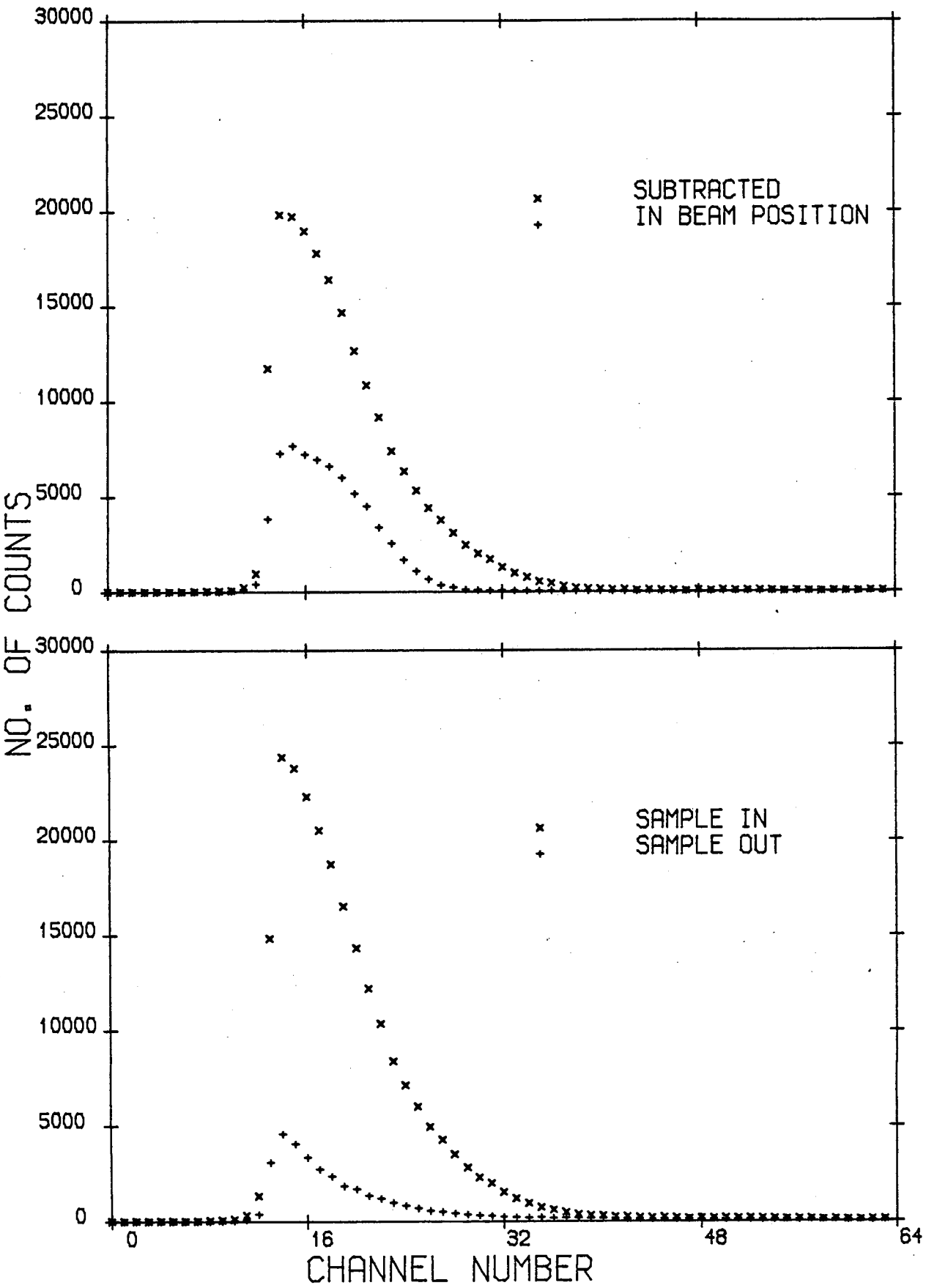
28/04/83 NEUTRON SPECTRA DETECTOR 11
30000
25000
20000
15000
10000
5000
0
SUBTRACTED
IN BEAM POSITION
NO. OF COUNTS
SAMPLE IN
SAMPLE OUT
0
16
32
48
64
CHANNEL NUMBER

Figure 4.6(a).

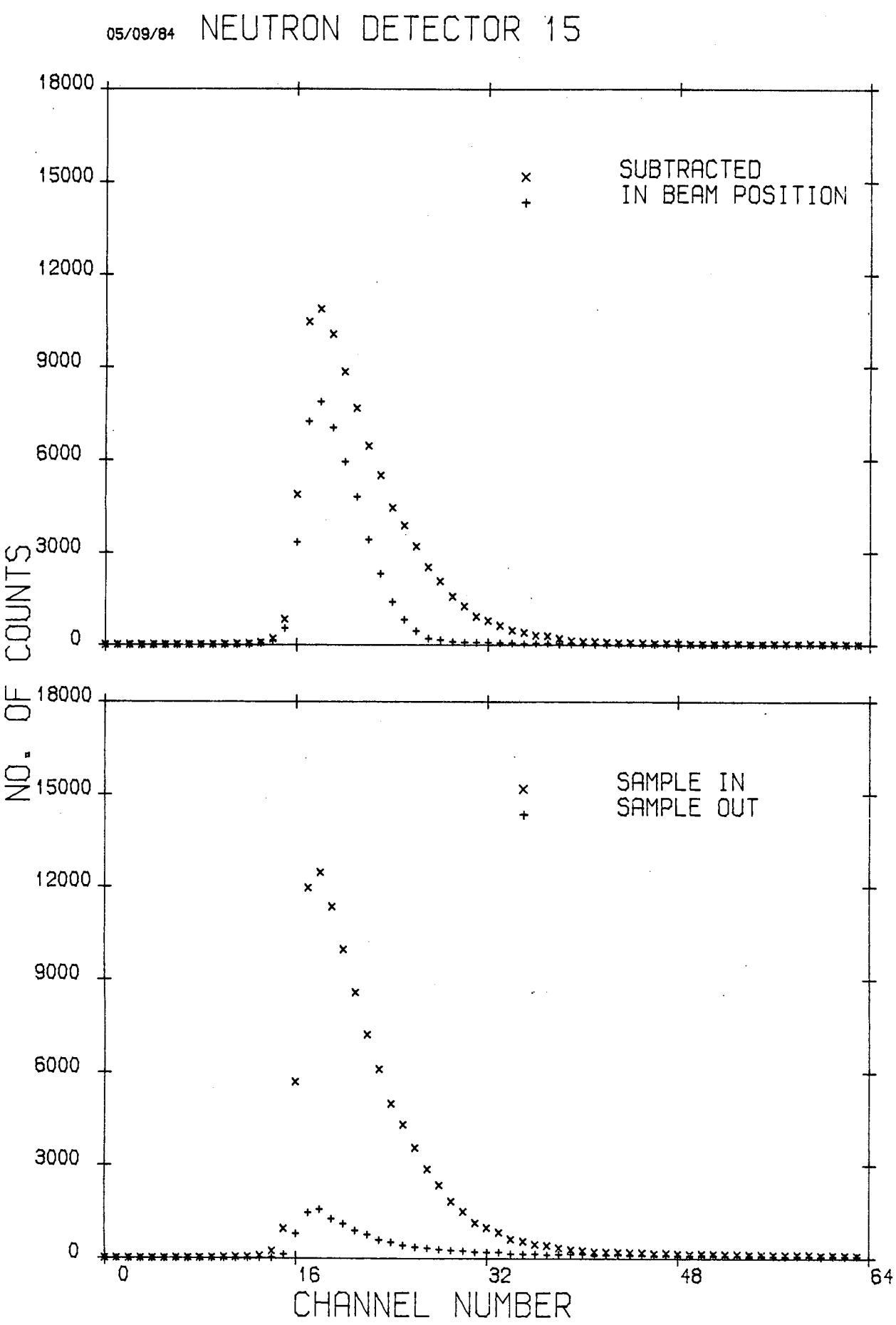
05/09/84 NEUTRON DETECTOR 15
SUBTRACTED
IN BEAM POSITION
SAMPLE IN
SAMPLE OUT
NO. OF COUNTS
CHANNEL NUMBER
18000
15000
12000
9000
6000
3000
0
0
16
32
48
64

Figure 4.6(b)

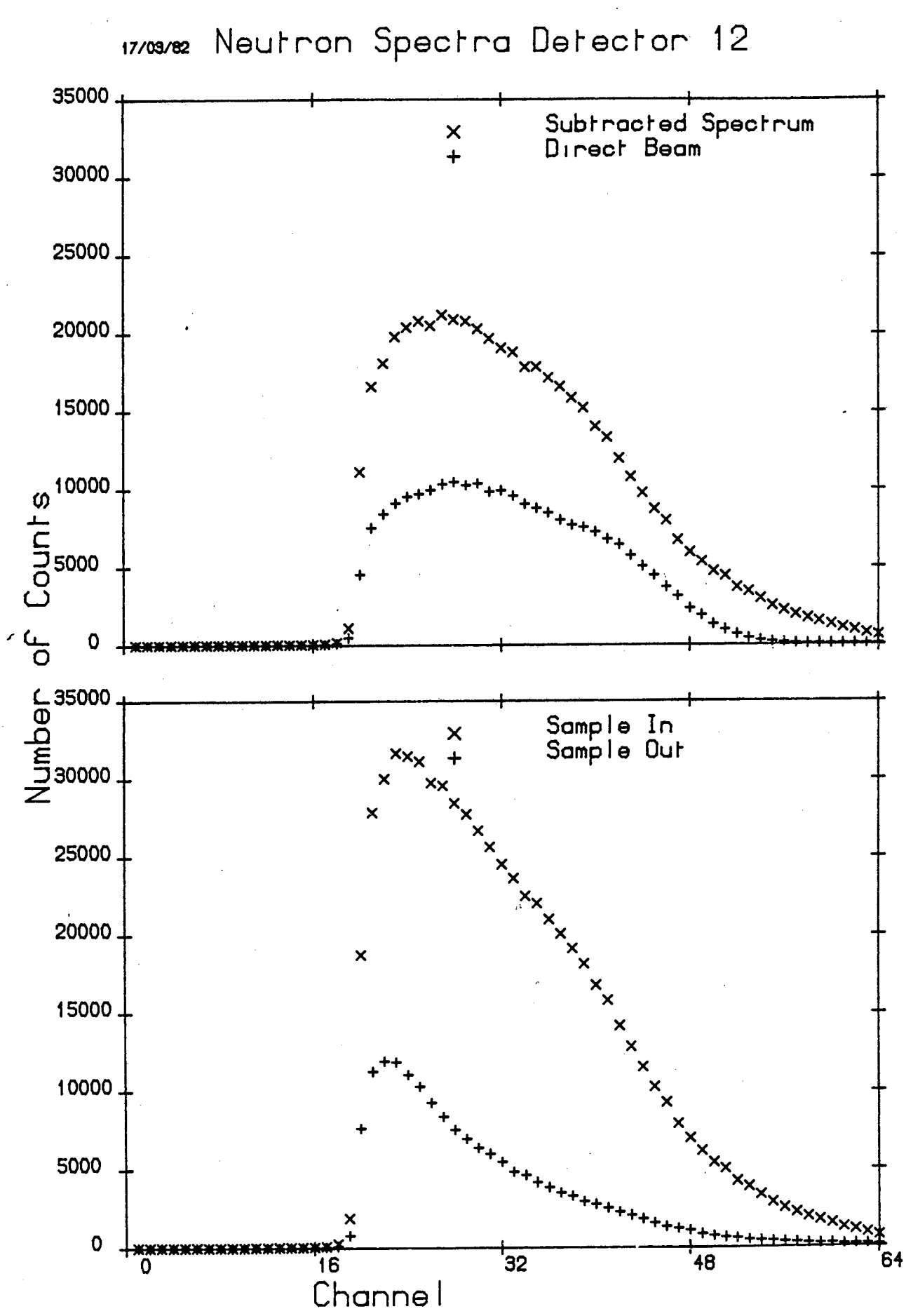
17/09/82 Neutron Spectra Detector 12
Subtracted Spectrum
Direct Beam
Sample In
Sample Out
Number of Counts
35000
30000
25000
20000
15000
10000
5000
0
0
16
32
48
64
Channel

Figure 4.6(c).

Chapter 3, was used.

Having the source fixed, the polarimeter was rotated to two azimuthal positions for $\phi = 0$ and $\phi = \pi$ and recoil events were collected in all the detectors for the same length of time in the two positions. 128 measurements with the polarimeter alternately in orientation $\phi = 0$ and $\phi = \pi$ were made. The measurement time for each individual run was 1000 seconds.

The pulse shape discrimination circuits were disabled to accept the detection of gamma-rays in the scintillators. ^{60}Co produces two gamma-rays of 1.17 and 1.33 MeV, too close in energy to be resolved, but still having a reasonably well defined Compton edge to the recoil electron spectrum at 1.04 MeV.

As a second check for false asymmetry a similar test was repeated with the use of a ^{252}Cf neutron source (0.5μg, 268μCi), positioned at the centre of the polarimeter, while the PSD circuits were incorporated to reject gamma-rays and count only neutrons. ^{252}Cf produces neutrons with a maximum energy of 10 MeV averaging 2.5 MeV and is therefore comparable to the energy of neutrons used from the reaction. The recoil proton spectra are relatively featureless with maximum counts at low energy, tailing off progressively at higher energies.

As a result of different tests on dynode chain, preamplifier and PSD unit[80] with both EMI9814B and RCA8575 photomultipliers, it was found that the peak to valley ratio of the neutron peak in the PSD spectrum improved by a factor of $\approx$ 3.0, when the RCA8575 photomultiplier is used with the new preamplifier and new neutron selector (PSD), while gamma peak and neutron peak are also better separated. Therefore in rejecting the gamma peak, the number of

neutrons which are rejected with the gamma peak is less. Figs. 4.7(a) - (f) show the results obtained during these tests, which are summarized in Table 4.1. No energy bias was applied during these tests.

A gamma leakage test was carried out with the system set up for a neutron scattering measurement, to compare the old and new detector-neutron selector arrangements. The PSD discriminator was set to reject all gamma rays. A ^{60}Co source was set in the sample position and data was collected for 20 hours. The best and the worst examples of the two arrangements are compared in Fig. 4.8. It is obvious that the gamma leakage in the new arrangement is almost half of the old one.

Since in the neutron scattering measurements the lowest count rate with a high background is from 90 to 120 degree angles, so in this range of angles the results have the poorest accuracy. Four detectors made with RCA8575 photomultipliers and associated new electronics, as described in previous sections of this chapter, were devoted in pairs to (104 and 118) and (111 and 125) degree angles. An improvement in reducing the background by a factor of $\sim$ 2 was achieved. Fig. 4.9 illustrates a comparison between the old and new arrangements in this range of angle. The same kind of improvement was also observed at forward angles (20°) although in this case the background is in any case low compared with the scattered neutron intensity.

Fig. 4.10 shows the comparison of recoil proton, electron and PSD spectra. A pulse height discrimination level of about 0.55 of the ^{60}Co Compton edge was set in each case.

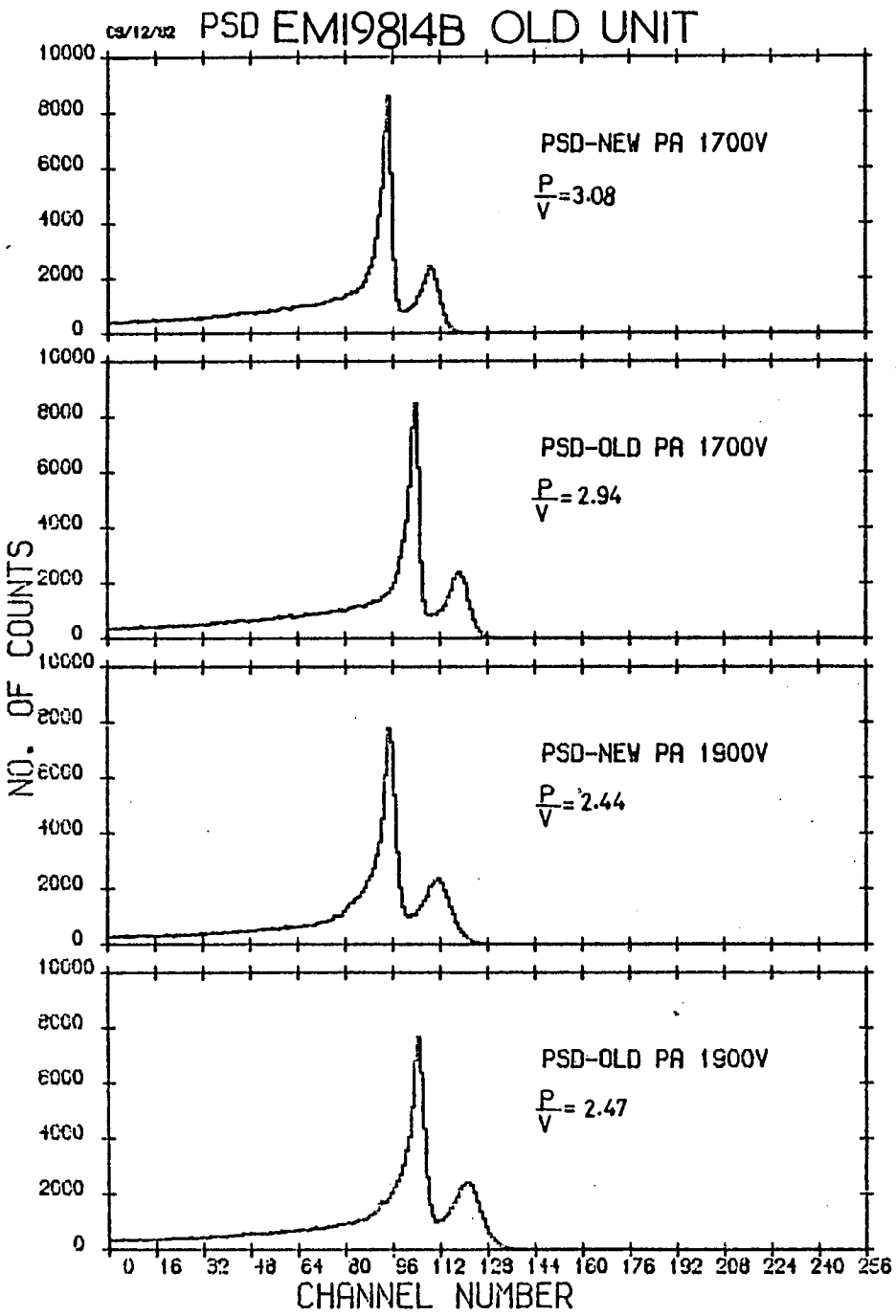

Figure 4.7(a)

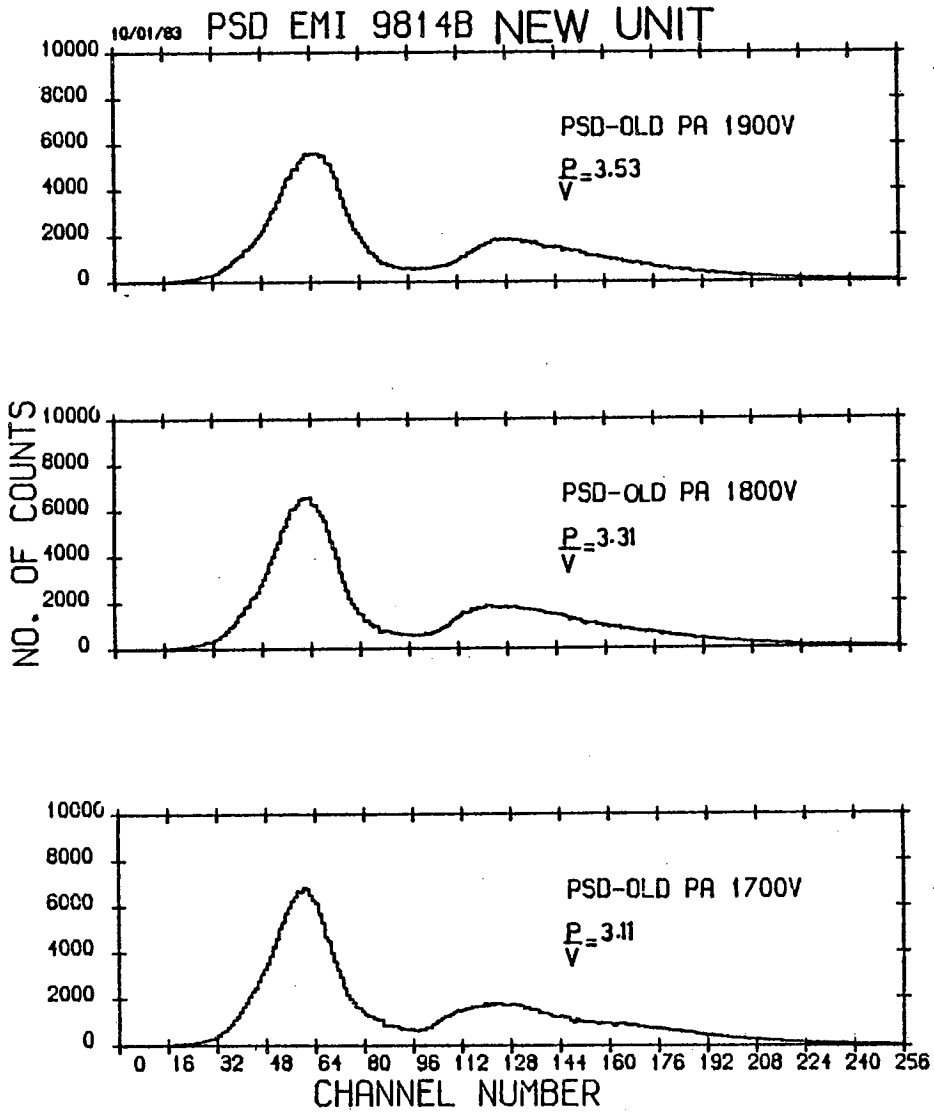

Figure 4.7(b).

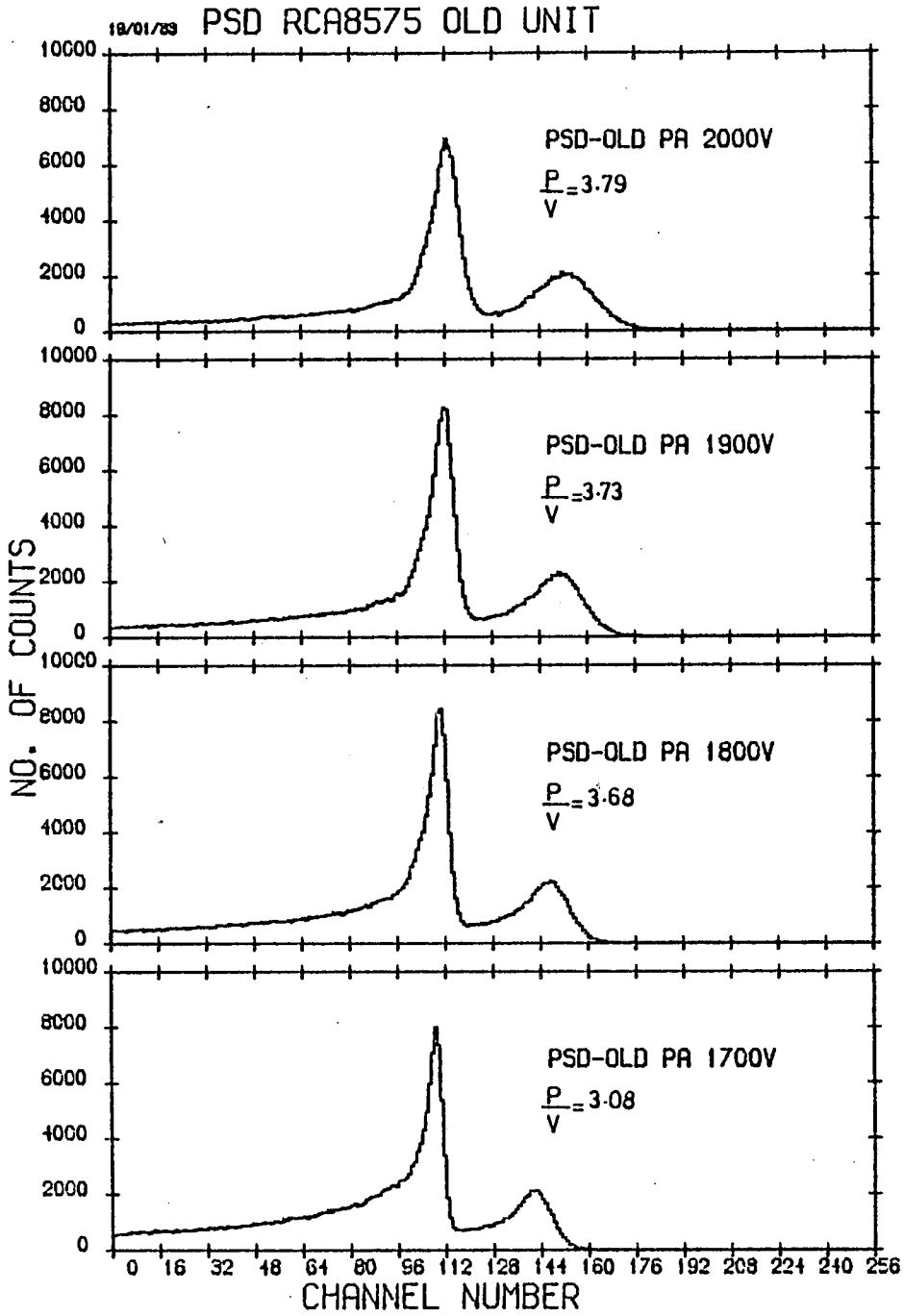

Figure 4.7(c)

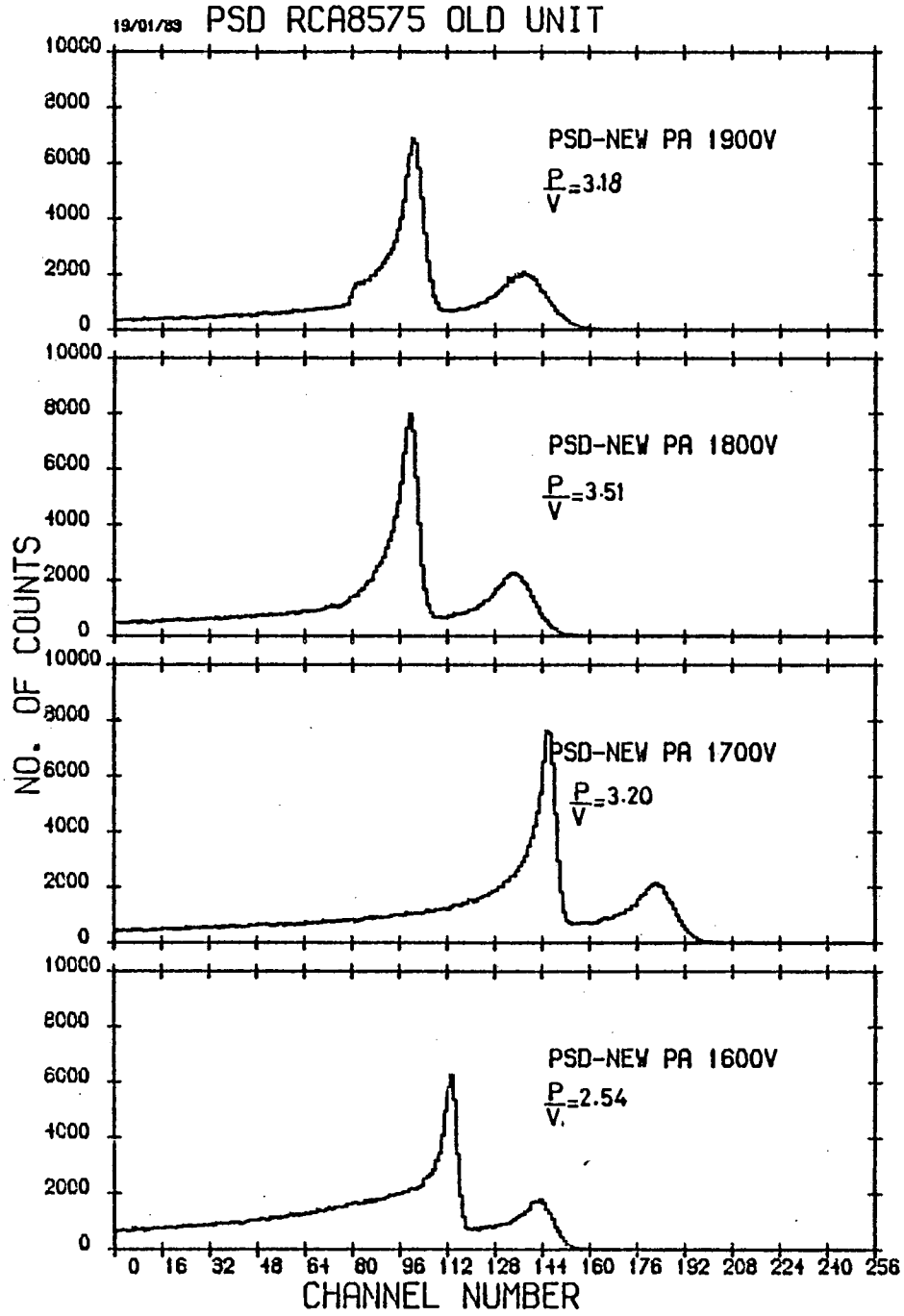

Figure 4.7(d)

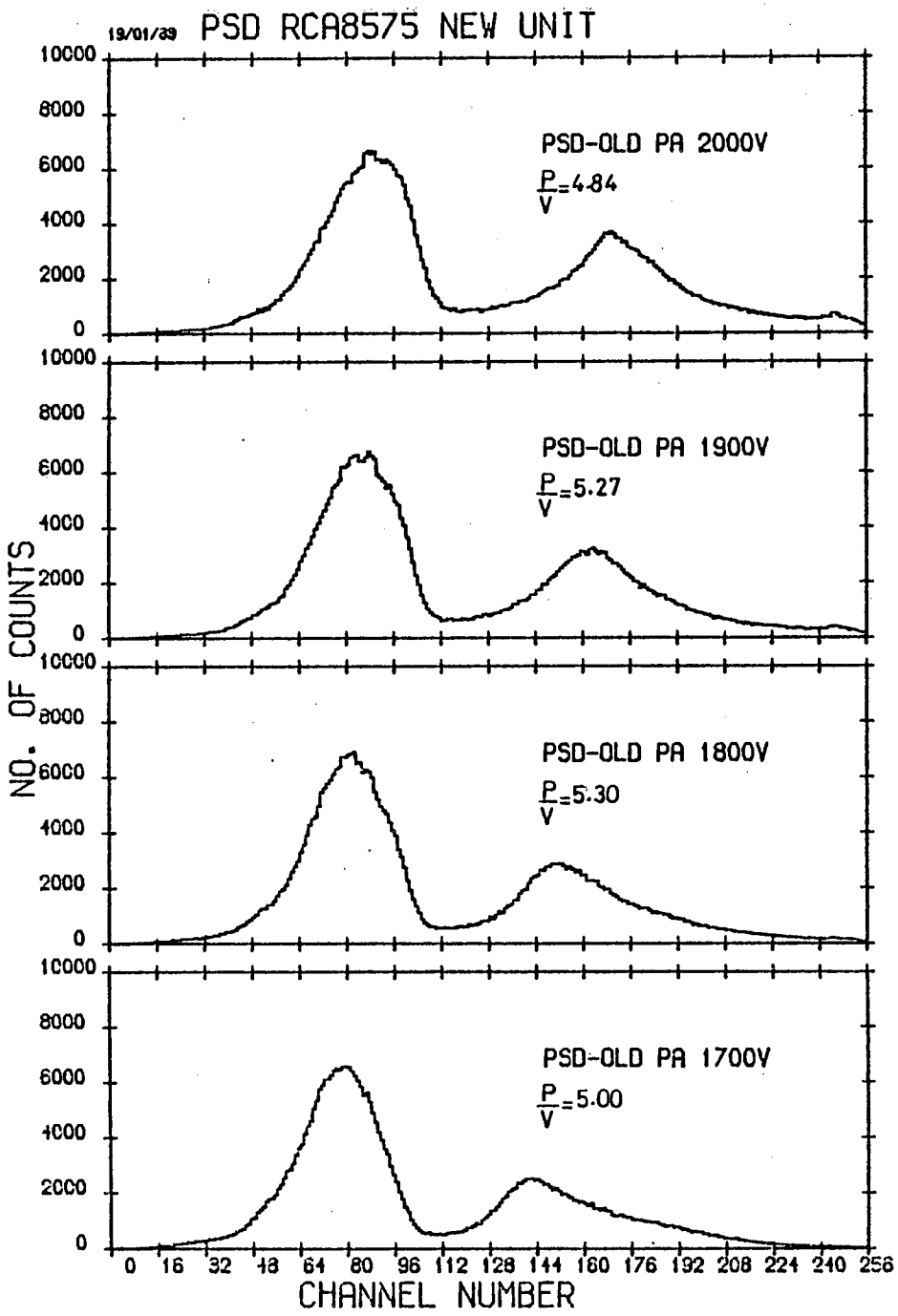

Figure 4.7(e)

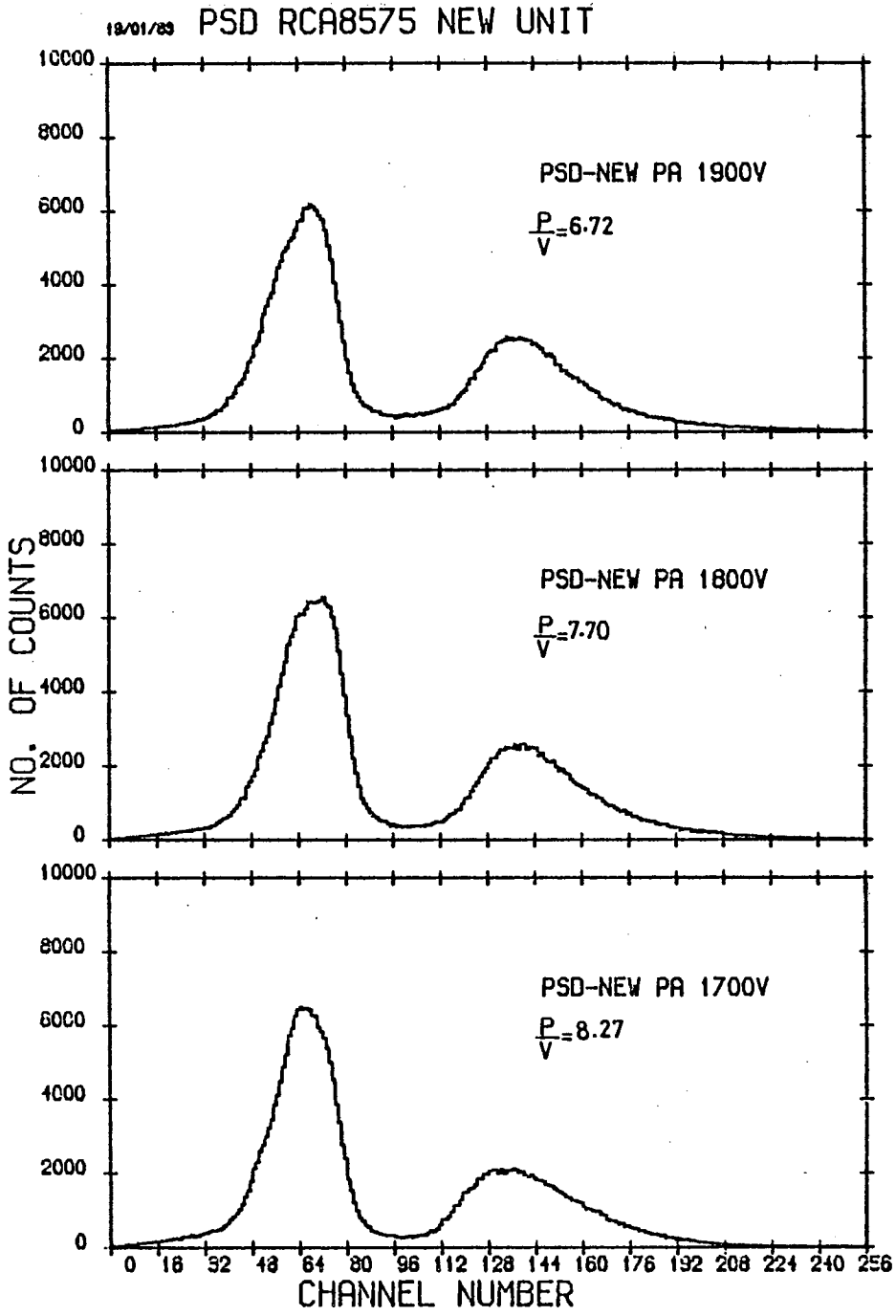

Figure 4.7(f)

TABLE 4.1

Neutron Peak to Valley Ratios from Fig. 4.7

EMI9814B P.M.					RCA8575 P.M.				
H.T. Voltage	Old PSD Unit		New PSD Unit		H.T. Voltage	Old PSD Unit		New PSD Unit	
	Old-P.a.	New-P.a	Old-P.a.	New-P.a.		Old-P.a.	New-P.a.	Old-P.a.	New-P.a.
1700	2.94	3.08	3.11		1600	-	2.54	-	-
1800	-	-	3.31		1700	3.08	3.20	5.0	8.27†
1900	2.47	2.44	3.53		1800	3.68	3.51	5.30	7.70
					1900	3.73	3.18	5.27	6.72
					2000	3.79*	-	4.84	-

* Best performance of Old arrangement

† Best performance of New arrangement

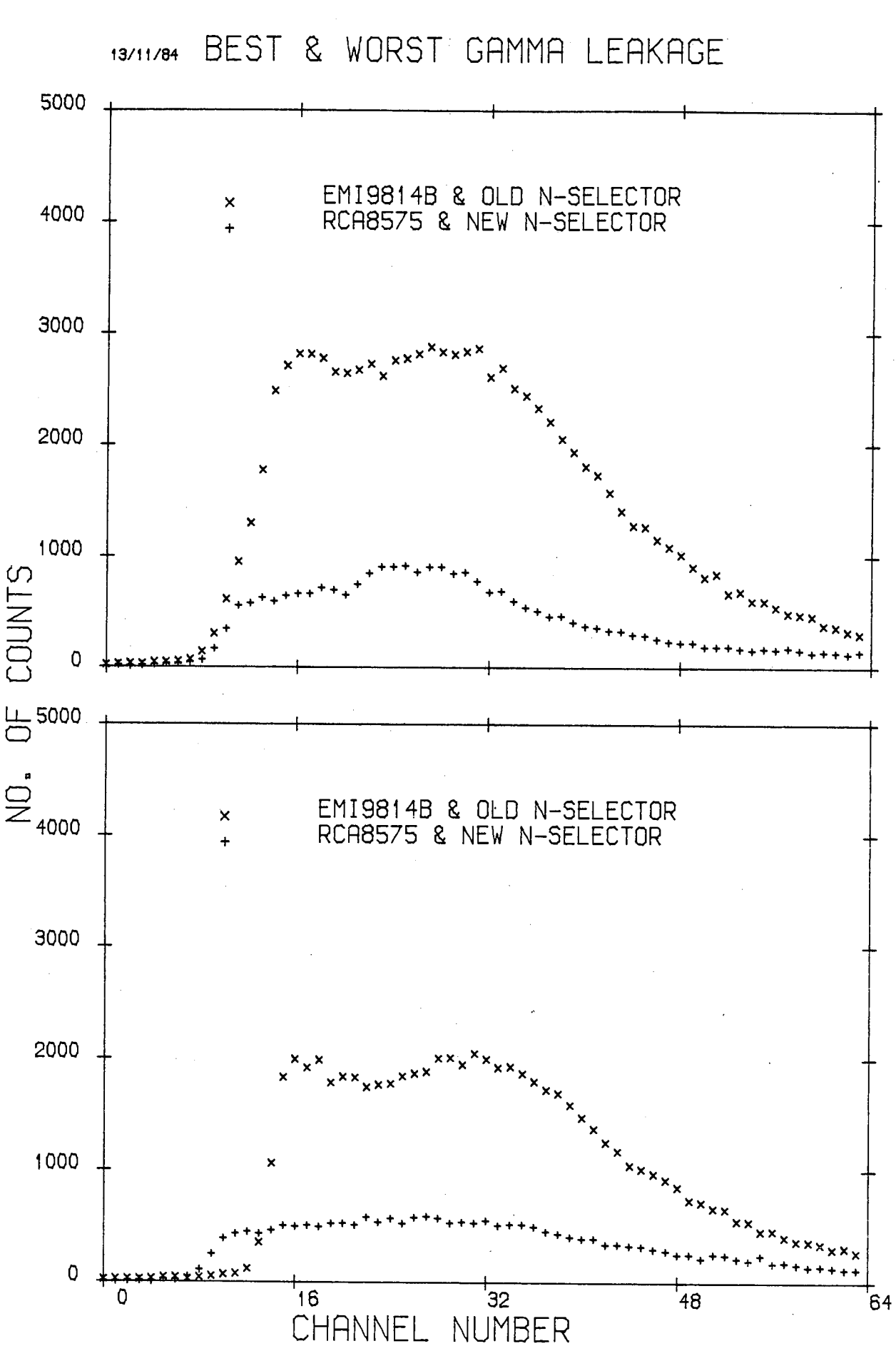
13/11/84 BEST & WORST GAMMA LEAKAGE
EMI9814B & OLD N-SELECTOR
RCA8575 & NEW N-SELECTOR
NO. OF COUNTS
5000
4000
3000
2000
1000
0
EMI9814B & OLD N-SELECTOR
RCA8575 & NEW N-SELECTOR
5000
4000
3000
2000
1000
0
0
16
32
48
64
CHANNEL NUMBER

Figure 4.8.

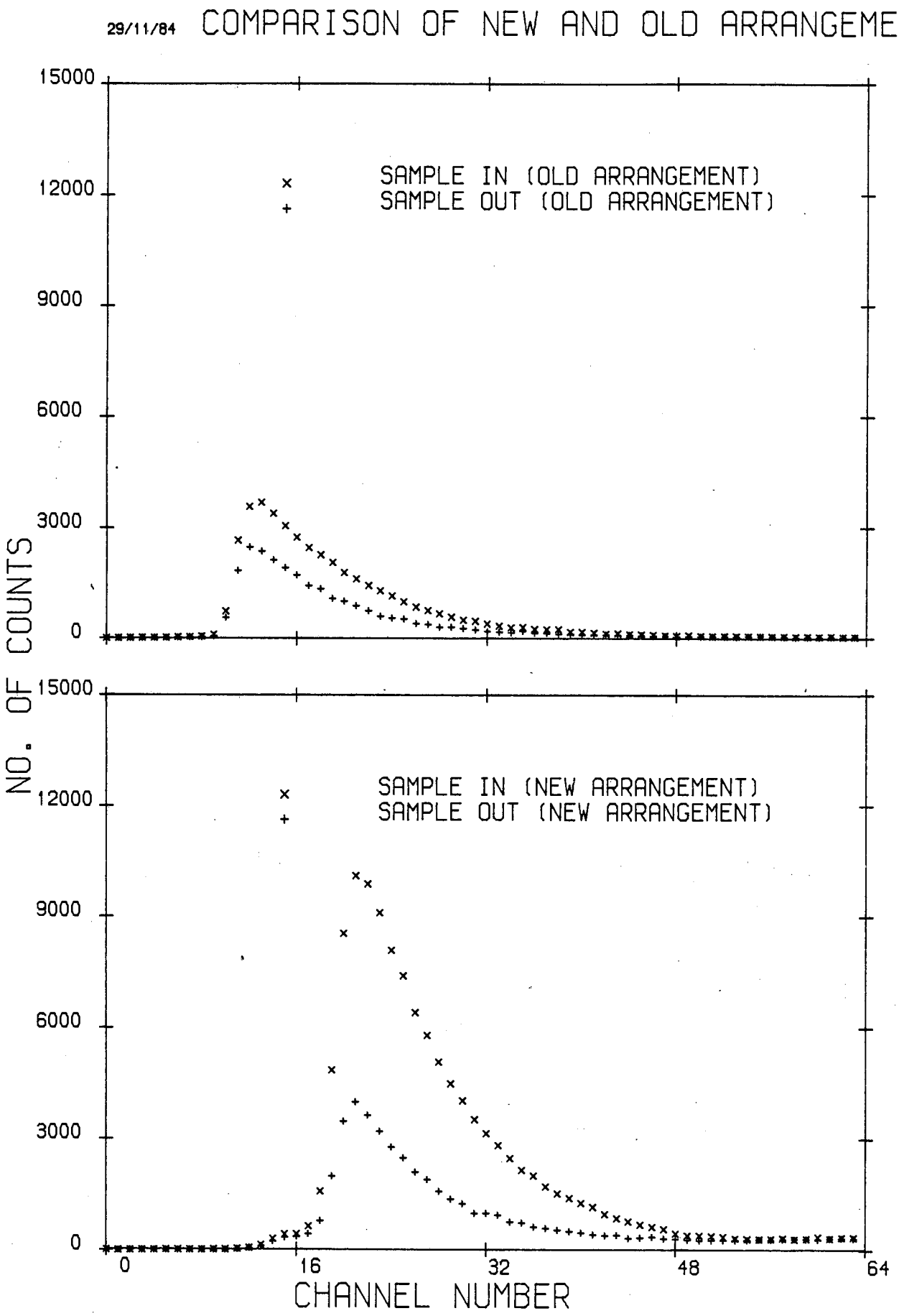
29/11/84 COMPARISON OF NEW AND OLD ARRANGEMENTS
SAMPLE IN (OLD ARRANGEMENT)
SAMPLE OUT (OLD ARRANGEMENT)
SAMPLE IN (NEW ARRANGEMENT)
SAMPLE OUT (NEW ARRANGEMENT)
NO. OF COUNTS
CHANNEL NUMBER
15000
12000
9000
6000
3000
0
16
32
48
64

Figure 4.9.

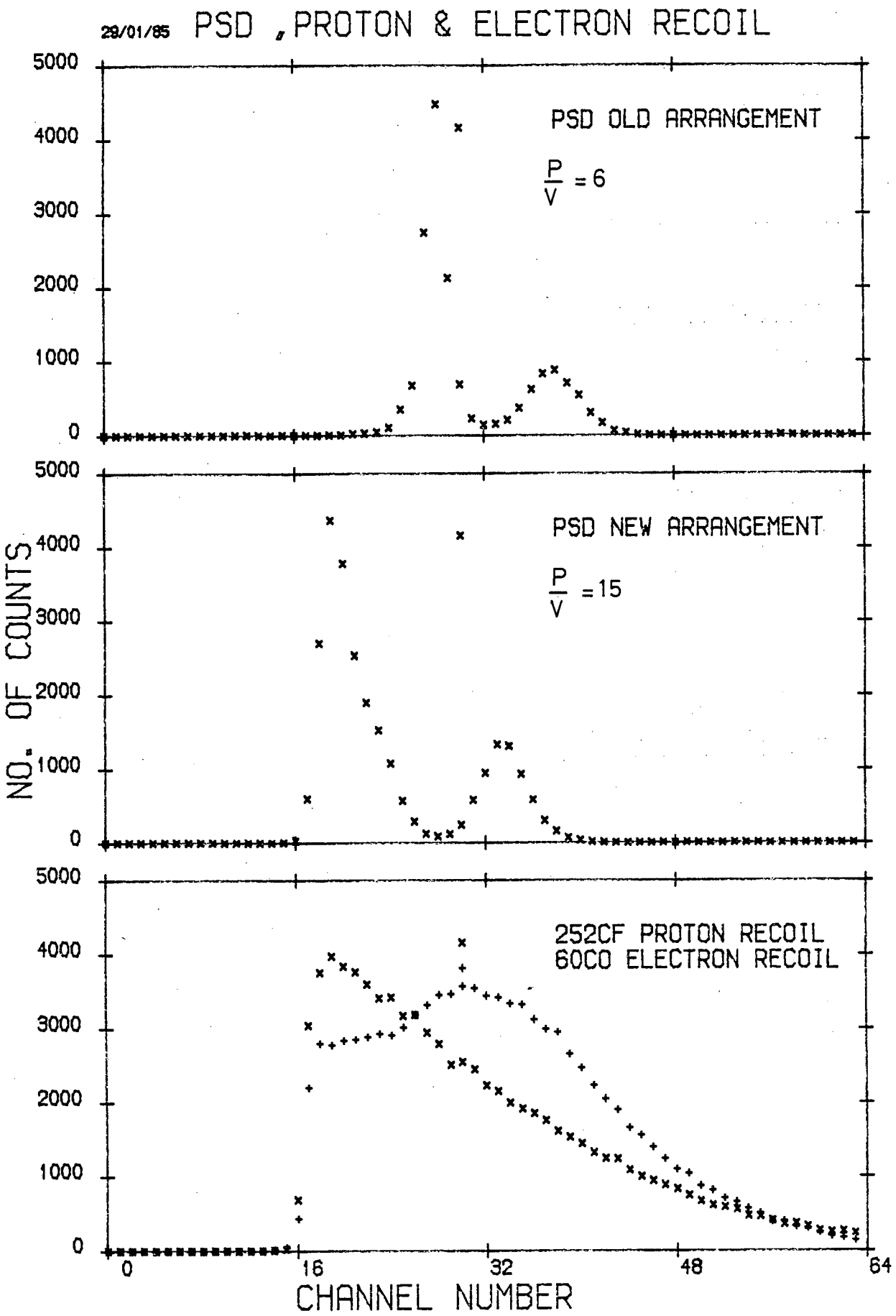
29/01/85 PSD , PROTON & ELECTRON RECOIL
PSD OLD ARRANGEMENT
P/V = 6
PSD NEW ARRANGEMENT
P/V = 15
252CF PROTON RECOIL
60CO ELECTRON RECOIL
NO. OF COUNTS
CHANNEL NUMBER
0
1000
2000
3000
4000
5000
16
32
48
64

Figure.4.10

4.7.2 Results of the Asymmetry Tests

Tables 4.2 and 4.3 give the results of the asymmetry tests obtained with the ^{60}Co gamma source and ^{252}Cf neutron source, respectively. The instrumental asymmetry is not more than 0.3% and 0.7% from tests done with the gamma source and the neutron source, respectively, even for the worst cases. The count rate stability can be judged by comparing the standard error, the standard deviation in the mean of the 1000 seconds counts, with the Poisson error.For detectors 1-11 the asymmetry is calculated as $\left|\frac{N(A) - N(B)}{N(A) + N(B)}\right|$ and for detectors 12-22 as $\left|\frac{N(B) - N(A)}{N(B) + N(A)}\right|$, where $N(A)$ and $N(B)$ are the number of counts in orientations $A(\phi = 0)$ and $B(\phi = \pi)$ respectively. The variation of count rate when the polarimeter is rotated can be obtained with a good measure in this way. The asymmetry tests with both sources were repeated each time before and after the actual data collection. It was decided always to keep the maximum asymmetry less than ± 3%. Any of the detectors which failed to give a satisfactory result were completely stripped down and reassembled carefully. It was observed that bubbles appearing within the scintillator, a loose mu-metal shield or any loose connection in the dynode chain could contribute a remarkable change in the counting rate on rotation.

4.7.3 Final Check on the Polarimeter Stability

As a final check a measurement of analysing power and differential cross section for only one set of angles covering (20° - 160°)

TABLE 4.2

^{60}Co Source 1000 Sec. Counts

Detector	Polarimeter Orientation	Mean Count	Standard Error	Poisson Error	Asymmetry (%)
1	A	249345	182	62	-0.157
	B	248559	171	62	
2	A	221985	174	59	0.185
	B	222811	162	59	
3	A	285841	197	67	-0.098
	B	285281	198	67	
4	A	266189	69	65	-0.024
	B	266056	67	64	
5	A	266013	23	64	0.267
	B	267440	23	65	
6	A	272661	23	65	0.134
	B	273397	67	65	
7	A	259716	67	64	0.368
	B	261638	78	64	
8	A	257349	125	63	-0.064
	B	257017	129	63	
9	A	244664	129	62	0.237
	B	245830	127	62	
10	A	278508	65	66	0.256
	B	279942	43	66	
11	A	258433	56	64	0.178
	B	259358	63	64	
12	A	258941	103	64	0.136
	B	258238	86	64	
13	A	253930	99	63	-0.069
	B	254281	94	63	
14	A	239111	134	61	0.324
	B	237566	117	61	
15	A	273669	95	65	0.361
	B	271698	81	65	
16	A	270350	89	65	0.163
	B	269465	109	65	
17	A	271713	118	65	0.147
	B	270912	104	65	
18	A	258214	65	64	-0.087
	B	258667	69	64	
19	A	279760	96	66	0.101
	B	279193	85	66	
20	A	264136	36	64	0.251
	B	262810	69	64	
21	A	275246	61	66	0.035
	B	275052	69	66	
22	A	266631	98	65	-0.121
	B	267279	81	65	

TABLE 4.3

^{252}Cf Source 1000 Sec. Counts

Detector	Polarimeter Orientation	Mean Counts	Standard Error	Poisson Error	Asymmetry (%)
1	A	32201	35	22	-0.248
	B	32042	31	22	
2	A	29998	24	21	0.238
	B	30141	28	21	
3	A	36692	43	24	-0.013
	B	36682	40	24	
4	A	32777	27	22	-0.321
	B	32566	27	22	
5	A	32700	30	22	0.232
	B	32852	28	22	
6	A	34261	21	23	0.117
	B	34342	20	23	
7	A	31843	23	22	0.549
	B	32195	20	22	
8	A	31077	32	22	-0.039
	B	31052	30	22	
9	A	27650	50	20	-0.426
	B	27415	55	20	
10	A	29908	64	21	0.361
	B	30124	67	21	
11	A	26415	53	20	0.074
	B	26454	53	20	
12	A	33035	25	22	0.242
	B	32875	27	22	
13	A	31707	22	22	0.096
	B	31646	21	22	
14	A	30097	19	21	0.594
	B	29741	22	21	
15	A	34343	28	23	0.702
	B	33864	21	23	
16	A	32862	32	22	0.234
	B	32708	34	22	
17	A	32215	33	22	0.318
	B	32011	36	22	
18	A	29356	23	21	0.391
	B	29127	30	21	
19	A	35090	24	23	-0.213
	B	35241	23	23	
20	A	33751	23	23	0.701
	B	33281	23	22	
21	A	35571	22	23	0.215
	B	35418	23	23	
22	A	31414	21	22	-0.253
	B	31574	22	22	

for a lead (Pb) sample was made.

The lead sample was a cylinder, 4.92 Cm in height by 4.88 Cm diameter, with a density of 10.99 gm Cm^{-3}. The data was collected for a short time, just enough to confirm that the polarimeter is still capable of reproducing the same results as previously measured[16] within the statistical uncertainty.

The data is not corrected. The uncorrected data is compared with those of J.R.M. Annand in Figs. 4.11 and 4.12 and Table 4.4. The present results have the same angular distribution as those of ref. (16), and good agreement is observed.

TABLE 4.4

Lead

Angle	Analysing Power Uncorrected		Differential Cross Section Uncorrected	
	Present Measurement	J.R.M. Annand Ref. (16)	Present Measurement	J.R.M. Annand Ref. (16)
20	-0.096±0.012	-0.066±0.008	1766.5±285.9	1674.4±92.1
34	-0.067±0.022	-0.073±0.012	829.5±255.3	783.7±19.3
48	-0.142±0.030	-0.093±0.019	342.5± 58.2	330.9±18.2
62	-0.020±0.039	-0.061±0.026	200.0± 29.0	193.2±10.6
76	0.055±0.040	0.013±0.024	224.5± 38.5	199.9±11.0
90	0.016±0.036	0.037±0.024	219.1± 38.5	210.1±11.6
104	0.046±0.039	0.041±0.028	195.6± 27.1	175.8± 9.7
118	-0.057±0.045	0.028±0.031	171.1± 25.6	154.6± 8.5
132	-0.119±0.054	-0.074±0.035	147.9± 19.2	137.6± 7.6
146	-0.003±0.052	0.069±0.035	182.7± 28.3	166.4± 9.2
160	0.220±0.048	0.307±0.030	272.3± 40.5	262.8±14.5

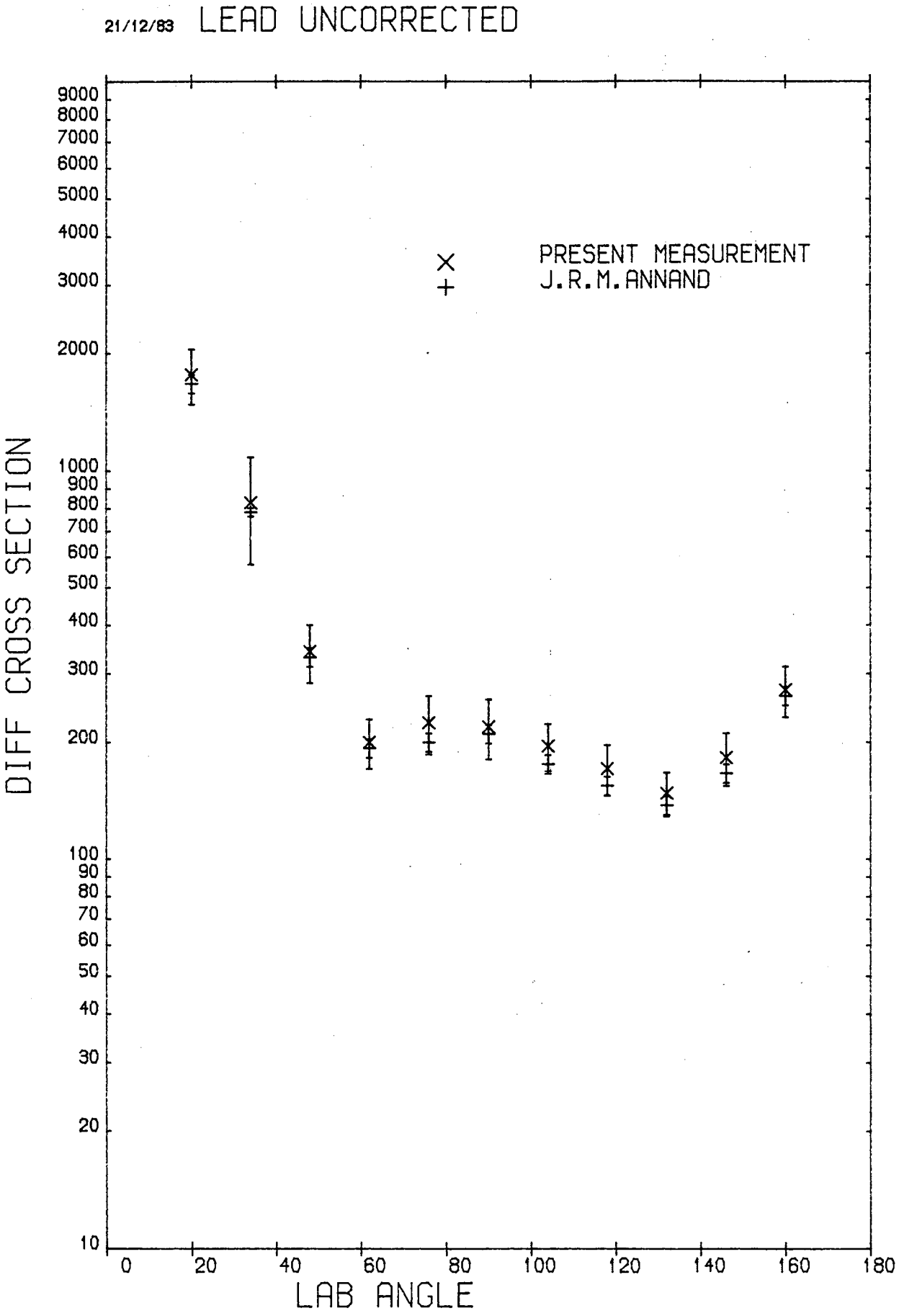
21/12/83 LEAD UNCORRECTED
PRESENT MEASUREMENT
J.R.M.ANNAND
DIFF CROSS SECTION
LAB ANGLE
9000
8000
7000
6000
5000
4000
3000
2000
1000
900
800
700
600
500
400
300
200
100
90
80
70
60
50
40
30
20
10
0
20
40
60
80
100
120
140
160
180

Figure 4.11.

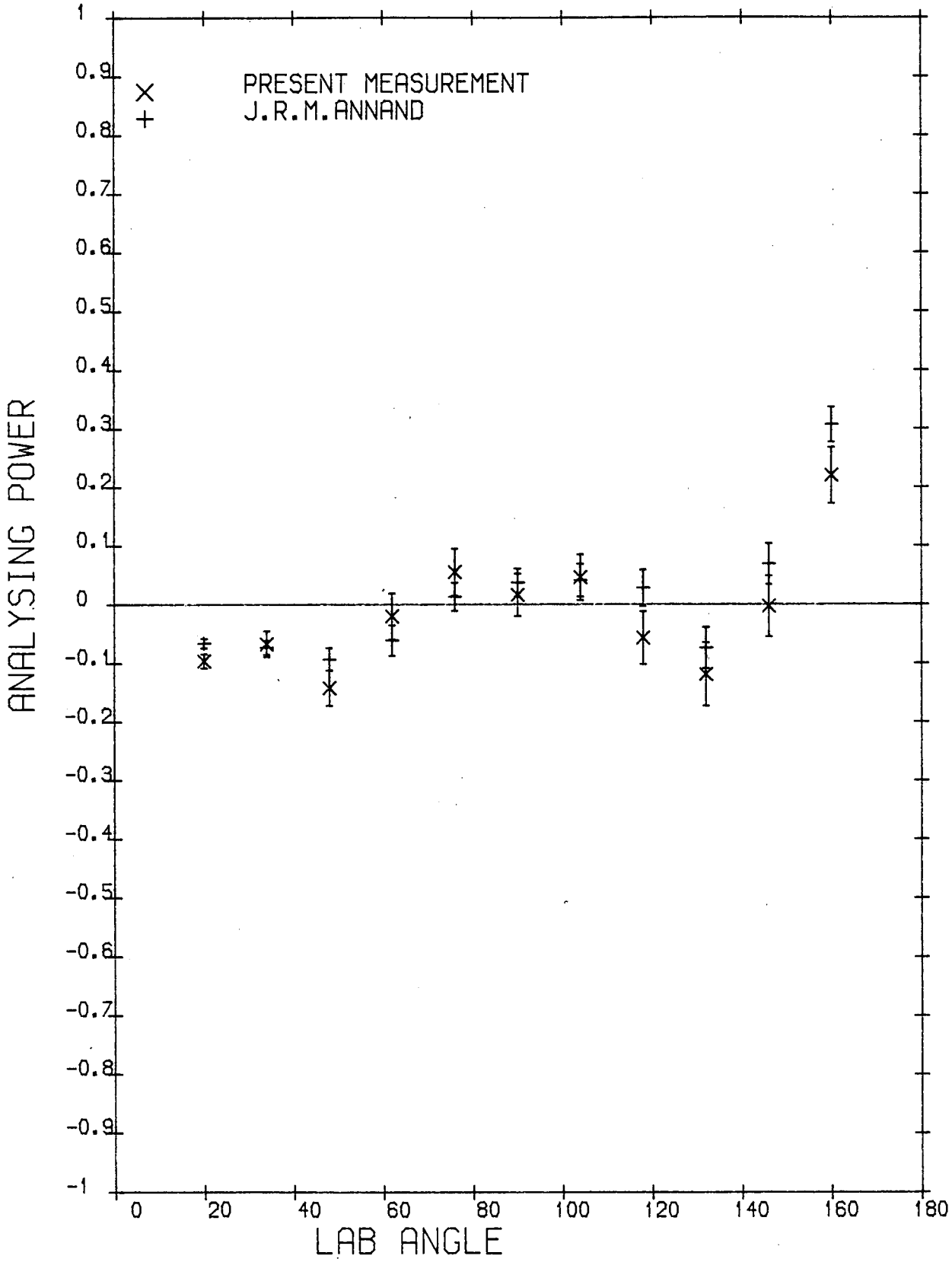
21/12/83 LEAD UNCORRECTED
PRESENT MEASUREMENT
J.R.M.ANNAND
ANALYSING POWER
LAB ANGLE
1
0.9
0.8
0.7
0.6
0.5
0.4
0.3
0.2
0.1
0
-0.1
-0.2
-0.3
-0.4
-0.5
-0.6
-0.7
-0.8
-0.9
-1
0
20
40
60
80
100
120
140
160
180

Figure 4.12.

CHAPTER 5

EXPERIMENTAL DATA

5.1 Data Collection

Having the test runs for false asymmetries satisfactorily completed, the 390 keV deuteron beam accelerated from the 500 kV Van de Graaff accelerator was incident on the deuterium target to produce 3.0 MeV neutrons at 49° angle, for the neutron scattering measurements.

Experimental measurements were made in two stages, one covering the range of angles 20 - 160 degrees in 14 degree intervals and the other covering the range of angles 27 - 167 degrees in 14 degree intervals. The 13 degree angle was not used as in this position detectors were too close to the direct neutron beam, because of the circular cross section of the collimator.

First, data was collected for each sample with the polarimeter in the position covering 20 - 160 degree angles, then the polarimeter was set in the position to cover 27 - 167 degree angles. This way of collecting data gives a useful check on the reproducibility of measurements, since both sets of data are required to mesh together smoothly. Having the angular interval of 7 degrees for the distribution of 22 angles of data in the range of angles 20 - 167 degrees, produces an accurate definition of the shape of angular distribution, especially at backward angles where there are sharp swings from negative to positive values of analysing power.

The samples used were of natural isotopic abundance and made of cylindrical shape. The physical characteristics of the samples are given in Table 5.1. The term MFPR, Mean Free Path Radius, is a

convenient measure of sample size, taken as

$$MFPR = \sigma_T PR$$

where σ_T = total cross section in barns

P = number of nuclei/$A^{\circ 3}$

R = sample radius in Cm .

For experimental measurements, the polarimeter was rotated to the two azimuthal positions, $\phi = 0$ (A orientation) and $\phi = \pi$ (B orientation), and in each position pulse height spectra were collected for sample in and sample out of the collimated neutron beam. The data were collected for 1000 seconds in each position and the sequence was repeated until an accuracy of 3% in analysing power at most of the angles was achieved.

The number of counts for neutrons scattered from the scattering sample is equal to the number of counts when the sample is out subtracted from the number of counts when the sample is in.

$$N(A) = N(A_I) - N(A_O)$$

$$N(B) = N(B_I) - N(B_O)$$

subscripts I and O indicate sample in and sample out of orientations $A(\phi = 0)$ and $B(\phi = \pi)$ respectively. The associated standard deviation in to these numbers of counts are

$$dN(A) = [N(A_I) + N(A_O)]^{\frac{1}{2}}$$

$$dN(B) = [N(B_I) + N(B_O)]^{\frac{1}{2}} \quad .$$

5.2 Experimental Data Analysis

5.2.1 Analysing power calculation

The right left ratio is taken as the geometric mean of the ratios measured with the two detectors at each angle.

$$R_i = \left[\frac{N_j(A)N_i(B)}{N_j(B)N_i(A)}\right]^{\frac{1}{2}}$$

$i = 1 - 11$

$j = 23 - i$

The statistical error in R_i is

$$dR_i = 0.5R_i \left[\left[\frac{dN_i(A)}{N_i(A)}\right]^2 + \left[\frac{dN_i(B)}{N_i(B)}\right]^2 + \left[\frac{dN_j(A)}{N_j(A)}\right]^2 + \left[\frac{dN_j(B)}{N_j(B)}\right]^2\right]^{\frac{1}{2}}.$$

The analysing power can be determined from the scattering asymmetry by,

$$P_i = \frac{(R_i - 1)}{(R_i + 1)} \frac{1}{P_n}$$

where P_n = reaction polarisation.

The error in the analysing power is

$$dP_i = P_i\left[\left[\frac{dR_i}{(R_i-1)} - \frac{dR_i}{(R_i+1)}\right]^2 + \left[\frac{dP_n}{P_n}\right]^2 + D^2\right]^{\frac{1}{2}}$$

dP_n : the error in P_n

D : the systematic error caused by instrumental asymmetries.

The polarisation P_n of the neutrons from the $^2H(d,n)^3He$ reaction for deuteron energies less than 1 MeV has been measured several times[85-93].

The reaction polarisation P_n is only weakly dependent on the energy about 0.5 MeV deuteron energy. The value -0.15 ± 0.01, which was used by J.R.M. Annand[16] using 0.4 MeV deuterons, and Begum and Galloway[43] using 0.315 MeV deuterons, and Zijp and Jonker[40] using 0.65 MeV deuterons was used in the present calculations.

The systematic error D was taken from the result of the instrumental asymmetry tests divided by P_n. The maximum acceptable value for instrumental asymmetry which was measured using the ^{60}Co gamma source with pulse height discrimination set at a level corresponding to 2.0 MeV bias for neutrons of 3.0 MeV energy, as described in Chapter 2, was within 0.003. An average instrumental asymmetry of about 0.001 gives a value of 0.0066 for D. This value is usually equal to or larger than the statistical error in the 20 and 27 degree measurements, but it is much smaller than the statistical uncertainty in measurements at other angles, particularly so at backward angles.

5.2.2 Differential cross section calculation

The differential cross section is expressed as

$$\frac{d\sigma}{d\Omega}(\theta) = \frac{Sr^2}{IN}$$

where S is the scattered neutron flux at the detector at a distance r and at an angle θ to the scatterer, and I is the incident neutron

flux. However for practical evaluation the following substitutions are required

$$S = \frac{n_d}{e_d A_d}$$

n_d = Count rate at the scattered neutron (side) detector

e_d = efficiency of side detector

A_d = area of side detector presented to scattered neutrons

$$I = \frac{n_o}{A_s}$$

A_s = area of the scatterer presented to the incident beam

n_o = number of neutrons incident on the scatterer per unit time

$$n_o = \left(\frac{n_m A_s}{e_m A_m}\right) \cdot \left(\frac{r_m}{r_s}\right)^2$$

n_m : number of neutrons detected/sec by the CBM

e_m : CBM detection efficiency

A_m : CBM area irradiated by the direct beam

r_m : distance from CBM to neutron producing target

r_s : distance from scatterer to neutron producing target

Therefore by substitution

$$\sigma(\theta) = \frac{\left(\frac{e_m}{e_d}\right) \cdot \left(\frac{r_s r}{r_m}\right)^2 \cdot \left(\frac{n_d}{n_m}\right) \cdot \left(\frac{A_m}{A_d}\right)}{N}$$

n_d and $\left(\frac{e_m}{e_d}\right)$ refer to measurement at each angle which has two detectors so that

$$n_d = [N_i(A)N_j(A)N_i(B)N_j(B)]^{\frac{1}{4}}$$

$$dn_d = \frac{n_d}{4}\left[\left(\frac{dN_i(A)}{N_i(A)}\right)^2 + \left(\frac{dN_j(A)}{N_j(A)}\right)^2 + \left(\frac{dN_i(B)}{N_i(B)}\right)^2 + \left(\frac{dN_j(B)}{N_j(B)}\right)^2\right]^{\frac{1}{2}}$$

$$e_i = \frac{e_m}{e_d} \qquad \text{for one detector}$$

$$e = (e_i \cdot e_j)^{\frac{1}{2}}$$

$$de = \frac{e}{2}\left[\left(\frac{de_i}{e_i}\right)^2 + \left(\frac{de_j}{e_j}\right)^2\right]^{\frac{1}{2}}$$

the ratio of detection efficiencies, $\frac{e_m}{e_d}$, is determined by the in-beam calibration runs, with the ratio taken as

$$\frac{e_m}{e_d} = \frac{n'_m M_d}{n'_d M_m}$$

where n'_m and n'_d are the count rates in the CBM and a particular side detector in-beam position, and M_m and M_d are the count rates in TYM when measuring n'_m and when the side detector is in-beam position, respectively.

5.3 Finite Geometry and Multiple Scattering Correction

Due to the restrictions on the intensity of available neutron sources, neutron scattering measurements have to be performed with relatively large scattering samples. Therefore the finite size of the scattering sample makes it necessary to correct the experimental angular distributions of polarisation and cross section for flux

attenuation, multiple scattering and the finite angular spread of target-scatterer and scatterer-detector geometry.

Analytical methods for this kind of calculation have been attempted by J.Blochand C.C. Jonker[94] and developed by Cox[95] and Kinney[96], who used a combination of the speed of the analytic methods with much freedom from approximation of the Monte Carlo Methods. A comparison of analytic methods with Monte Carlo calculations is investigated by Velkley[97] and agreement within $\lesssim$ 1% is quoted when the sample size is not too large. Zijp and Jonker[40] used a combined analytical/Monte Carlo method for analysing power correction, and one involving successive volume integrations by Stinson et al.[98].

Programmes due to Holmqvist et al.[99] have been used for this kind of correction in the Edinburgh Neutron Physics laboratory, until J.R.M. Annand[16] in 1982 developed a method for a combined calculation of cross section and analysing power considering recoil proton spectra, rather than time-of-flight spectra, in which elastic and inelastic neutrons are not conveniently separated.

The experimental data is first corrected by a semi-analytical method of Kinney and Cox, which is in fact a combined analytical/ Monte Carlo approach because some of the parameters are difficult to calculate accurately from analytical formulae. The result of this method provides the initial "guess" at the corrected distributions for feeding into a Monte Carlo correction which provides the final correction to the distributions.

5.3.1 Analytical Method

The correction for flux attenuation is separated from the correction for multiple scattering for the sake of convenience of calculation. The effect of flux attenuation on the analysing power measurement, follows the ratio

$$R_f(\theta) = \frac{F_R(\theta)}{F_L(\theta)}$$

where subscripts R and L denote to Right and Left and

$$F(\theta) = \frac{\int_v \{\sigma_d(E_d,\theta_o)\exp - [\sigma_T(E_o)\rho\ell + \sigma_T(E)\rho\ell']\}\frac{dv}{r^2}}{\int_v \{\sigma_d(E_d,\theta_o)\}\frac{dv}{r^2}} \qquad (1)$$

is the flux attenuation for each angle, to the left and right of the scattering sample, where

σ_d : source reaction cross section

E_d : charged particle energy

θ_o : angle at which source neutrons selected

ρ : nuclear density in scattering sample

σ_T : total neutron cross section

ℓ : distance in sample before first collision

ℓ' : distance in sample before exit from sample

r : distance from neutron source to collision point

E_o : source neutron energy

E : neutron energy after collision.

In order to perform multiple scattering correction, the experimental

differential cross section is least squares fitted by a Legendre Polynomial expansion in the cosine of the lab. angle, μ.

$$U_{exp} = \sum_{\ell} a_{\ell} P_{\ell}(\mu) \quad .$$

The correction is then made on the coefficients a_{ℓ} which are normalised to a_o equal to unity.

The analysing power is corrected assuming that processes other than single shape elastic scattering cause complete depolarisation, that is where compound inelastic scattering dominates and multiple shape elastic events produce neutrons which are substantially depolarised. The correction, therefore, is presented in the form

$$R_c(\theta) = \frac{\{\sigma_{exp}(\theta)[1 + P_1 P_{exp}(\theta)] - \sigma_m(\theta)\}}{\{\sigma_{exp}(\theta)[1 - P_1 P_{exp}(\theta)] - \sigma_m(\theta)\}}$$

where

P_1 : polarization of neutrons from reaction

$P_{exp}(\theta)$: uncorrected experimental analysing power

$\sigma_m(\theta)$: multiple scattering and inelastic correction to the experimental differential cross section.

5.3.2 The Monte Carlo Method

The averaged form of Eq. (1) over angular range accepted by the detector is utilized for the flux attenuation calculation, as angle dependence is absorbed into the MC routine in which the effects

of multiple scattering and finite geometry are calculated.

Detector size effects were considered small enough to approximate analytically. The MC routine follows closely the method introduced by Holmqvist et al.[99] but is extended to take into account the depolarisation due to multiple elastic scattering. Therefore a multiplicative factor (equal to 1 for unpolarised neutrons) on the neutron weight scattered in the sample or to each detector, is introduced. It is calculated by the Aspelund and Gustavson formulae[100] and depends on orientations of the current and previous reaction planes as well as polar angle and energy.

Since proton recoil spectra are collected, the open channel inelastic scattering channel must be considered as well as elastic scattering. The particular channel is randomly sampled with weighting proportional to the angle integrated cross sections, at each collision in the sample. The weights scattered to the detectors are multiplied by the calculated energy dependent detection efficiency.

The cross section is proportional to $(W_R\ W_L)^{\frac{1}{2}}$ and the right - left scattering ratio is $\frac{W_R}{W_L}$ where W_R and W_L are the accumulated weights at the left and right detectors suitably normalised at a given angle. Uncertainties in accumulated detector neutron weights are the standard deviation of the results of several sub-runs.

Differential cross sections and right left scattering ratios are corrected using the approximation

$$f_C(\theta) = f_I(\theta)\ f_{exp}(\theta)/f_{MC}(\theta)$$

where C denotes the corrected value, I the initial "guess",

exp the experimental value and MC the simulated value. The error in the corrected distribution takes into account both the experimental and Monte Carlo errors. $f_I(\theta)$ should be reasonably close to $f_C(\theta)$ for a successful calculation otherwise the whole process must be iterated and so the initial analytical calculation is made to save computer time.

5.4 Spectrum Integration

In Chapter 4, Figs. 4(a) and (b) the proton recoil spectra of detector in-beam position, sample in and sample out positions, as well as the subtracted spectrum, are illustrated. The energy calibration of each detector was obtained by using the spectra recorded individually with the direct neutrons (this is discussed in more detail in Chapter 2). Counting times are 30 or 40 seconds for the direct beam spectrum, depending on the yield of neutrons obtained from the target due to the accelerator's conditions and a total of more than 60000 second (sample in and sample out) for the scattered neutron spectra.

To determine the number of neutrons elastically scattered through a particular angle the appropriate proton recoil pulse height spectrum is integrated above a chosen energy level. A lower limit of 1.5 MeV was chosen to perform Spectrum Integration and the limit raised in 0.1 MeV steps up to 2.9 MeV. After each integration, differential cross section and polarisation were calculated. As the lower limit to the integration is increased, less inelastic scattering should be included and the analysing power should increase towards the value due to elastic

scattering as illustrated in Fig. 5.

A lower limit of 2.2 MeV in most cases was found to be the limit above which calculated values ceased to change significantly.

The upper integration limit was set at 3.1 MeV to exclude any possible gamma-ray leakage due to neutrons captured in the shielding.

The numerical results obtained for differential cross sections and analysing powers for Cadmium, Tin, Antimony, Telerium and Iodine are quoted in Tables 5.1 - 5.10.

The uncorrected values are those obtained through the above-mentioned procedure. The corrected values are calculated by the methods given in Section 5.3.

The statistical error is denoted as, "stat", the instrumental asymmetry is denoted as, "Inst", and "syst" denotes errors in uncorrected differential cross section due to uncertainty in distances and areas. The uncertainty in the corrected distribution due to uncertainties in the simulated Monte Carlo distribution is given as "M.C.".

All the nuclei for which measurements are performed in this work have low lying levels from which inelastically scattered contributions to the data can not be excluded completely by raising the lower integration limit, as this would seriously effect the accuracy of the analysing power data. Therefore the data is corrected for the inelastic scattering contribution, either using available experimental data or by calculation using "CINDY" or "ELIESE3" programmes-see Chapter 6. In the following figures the corrected and uncorrected data are compared. Uncorrected data contain only statistical errors, while corrected data contain the

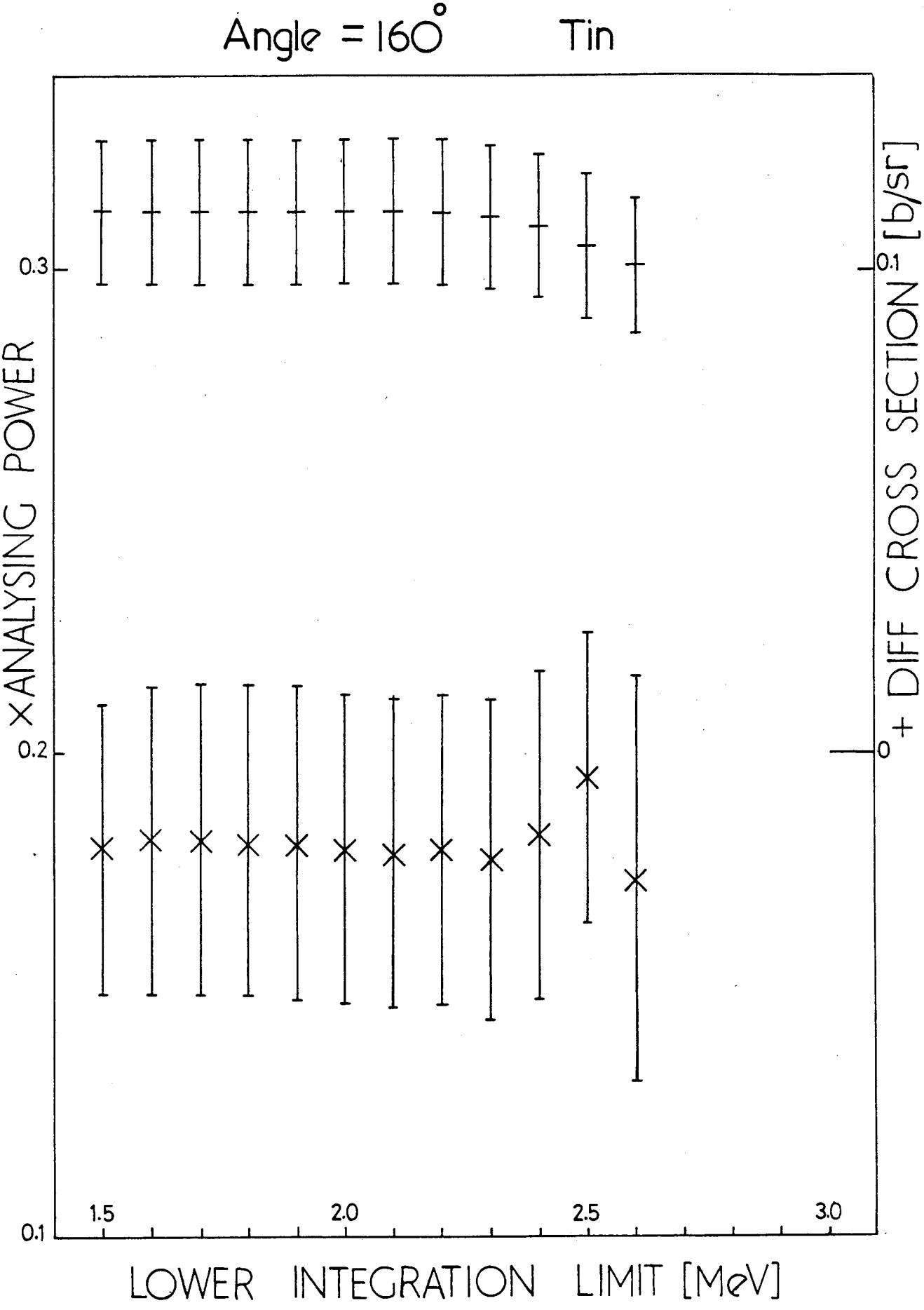
Angle = 160°
Tin
0.3
0.2
0.1
× ANALYSING POWER
0.1
0
+ DIFF CROSS SECTION [b/sr]
1.5
2.0
2.5
3.0
LOWER INTEGRATION LIMIT [MeV]

Figure . 5

total estimated errors. Comparison of the corrected data with previous measurements is also included.

The inelastic differential cross section correction, applied to the observed differential cross section was assumed to be $\Sigma\ \varepsilon\ \sigma_{in}$, where the summation is over relevant excited states. The efficiency factor ε is obtained from a Monte Carlo calculation [16 and 101] by assigning 3.0 MeV to the edge ($\frac{1}{2}$ height) of the 3.0 MeV neutron distribution and assuming a linear channel energy relationship.

TABLE 5.1

Scattering Sample Characteristics

Element	Isotopes and Isotopic Abundances %		Height (mm)	Diameter (mm)	Density (g. Cm^{-3})	MFPR	Comments
Cadmium	^{106}Cd	1.22	53.30	50.71	8.50	0.51	cylindrical, cast 4 discs glued to each other
	^{108}Cd	0.88					
	^{110}Cd	12.39					
	^{111}Cd	12.75					
	^{112}Cd	24.07					
	^{113}Cd	12.26					
	^{114}Cd	28.86					
	^{116}Cd	7.58					
Tin	^{112}Sn	0.96	51.70	50.80	7.12	0.41	cylindrical, cast
	^{114}Sn	0.66					
	^{115}Sn	0.35					
	^{116}Sn	14.30					
	^{117}Sn	7.61					
	^{118}Sn	24.03					
	^{119}Sn	8.58					
	^{120}Sn	32.85					
	^{122}Sn	4.72					
	^{124}Sn	5.94					

TABLE 5.1 (Contd.)

Element	Isotopes and Isotopic Abundances %		Height (mm)	Diameter (mm)	Density (g. Cm^{-3})	MFPR	Comments
Antimony	^{121}Sb	57.25	53.35	48.70	6.63	0.40	cylindrical, cast
	^{123}Sb	42.75					
Tellurium	^{120}Te	0.09	47.4	51.25	6.02	0.36	cylindrical, cast 3 discs glued to each other
	^{122}Te	2.48					
	^{123}Te	0.87					
	^{124}Te	4.16					
	^{125}Te	6.99					
	^{126}Te	18.7					
	^{128}Te	31.8					
	^{130}Te	34.5					
Iodine	^{127}I	100	51.88	48.44	4.16	0.25	Iodine powder pressed into a glass container. identical glass container used for background measurement.
Lead	^{204}Pb	1.5	49.2	4.87	11.05	0.62	cylindrical, cast
	^{206}Pb	23.6					
	^{207}Pb	22.6					
	^{208}Pb	52.3					

5.5 The Data

5.5.1 Cadmium

The scattering sample is a cast cylinder of natural cadmium 5.33 Cm high by 5.07 Cm diameter, made of four discs, with a density of 8.50 gm/cm^3, 98.3% of the accepted value. Natural cadmium consists of eight isotopes ^{106}Cd, ^{108}Cd, ^{110}Cd, ^{111}Cd, ^{112}Cd, ^{113}Cd, ^{114}Cd and ^{116}Cd with percentage abundances of 1.22, 0.88, 12.39, 12.75, 24.07, 12.26, 28.86 and 7.58 respectively. The first two isotopes with 1.22% and 0.88% abundances were not considered in the calculations. The total cross section of 5.1b and 4.5b at 2.5 and 3.0 MeV given by Foster and Glasgow [41] results in MFPR of 0.58 and 0.51 respectively. Having set the lower integration limit at 2.2 MeV, a set of data results, which should be corrected for the inelastic differential cross sections of the following excitation levels.

Isotope	Inelastic levels	No. of Excitation levels up to 3.0 MeV
^{110}Cd	0.657 (2^+)	30 levels [102]
^{111}Cd	0.245 ($5/2^+$)	41 levels [103]
	0.342 ($3/2^+$)	
	0.396 ($3/2^+$)	
	0.416 ($7/2^+$)	
	0.620 ($5/2^+$)	
	0.700 ( )*	where spin and parity are not indicated, they have not been established.
	0.736 ( )	
	0.752 ($5/2^+$)	
	0.754 ($3/2^+$)	
^{112}Cd	0.617 (2^+)	30 levels [104]

Isotope	Inelastic levels	No. of Excitation levels up to 3.0 MeV
^{113}Cd	0.27 $(^{11}/_{2}^{-})$	55 levels (105)
	0.299 $(^{3}/_{2}^{+})$	
	0.316 $(^{5}/_{2}^{+})$	
	0.460 $(^{7}/_{2}^{+})$	
	0.530 $(^{7}/_{2}^{+})$	
	0.583 $(^{5}/_{2}^{+})$	
	0.680 $(^{3}/_{2}^{+})$	
	0.689 ( )	
	0.760 $(^{1}/_{2}^{+})$	
^{114}Cd	0.558 (2^{+})	41 levels (106)
^{116}Cd	0.513 (2^{+})	28 levels (107)

There is no inelastic differential cross section data available for this kind of correction. Therefore ELIESE-3 was used to calculate the inelastic differential cross section. The results from different sets of optical model parameters were similar and the results were also checked by the programme CINDY. The calculated inelastic differential cross sections were then weighted for fractional abundances and relative detection efficiency to the elastic scattering at 3.0 MeV. Data is given in Tables 5.1 and 5.2 and illustrated in Figures 5.1 and 5.2.

Figure 5.3 compares the present analysing powers with those of Zijp and Jonker[40]. The agreement at 30° and 45° is poor, while at 60° and 75° there is a quantitative agreement within the experimental error.

The present differential cross sections are compared with two sets

of available data in Fig. 5.4. The present measurements are in very good agreement with those of Smith et al.[44] in the regions (46° - 97°) and (118° - 167°), while they incline to lower cross sections at forward angles and higher values at the minimum The differential cross sections of Becker et al.[31] at 3.2 MeV show a little inconsistency at backward angles with the present measurements and with those of Smith et al., while they suffer from poor accuracy as well.

TABLE 5.1

CADMIUM

Analysing Power

Angle	Uncorrected P(θ)	Stat.	Inst.	M.C.	Corrected P(θ)
20	-0.091	0.006	0.001	0.017	-0.100 ± 0.018
27	-0.085	0.005	0.001	0.018	-0.097 ± 0.019
34	-0.088	0.007	0.009	0.019	-0.114 ± 0.019
41	-0.115	0.008	0.001	0.021	-0.144 ± 0.019
48	0.085	0.009	0.007	0.021	-0.083 ± 0.023
55	-0.063	0.010	0.012	0.018	0.015 ± 0.021
62	-0.065	0.013	0.011	0.014	-0.018 ± 0.020
69	-0.210	0.013	0.018	0.013	-0.232 ± 0.017
76	-0.204	0.015	0.009	0.013	-0.280 ± 0.019
83	-0.341	0.016	0.011	0.014	-0.445 ± 0.021
90	-0.363	0.021	0.015	0.016	-0.427 ± 0.026
97	-0.320	0.026	0.001	0.018	-0.242 ± 0.032
104	-0.255	0.038	0.006	0.019	-0.066 ± 0.043
111	-0.124	0.041	0.009	0.020	0.044 ± 0.045
118	0.007	0.037	0.011	0.021	0.072 ± 0.043
125	0.116	0.038	0.006	0.024	-0.007 ± 0.044
132	-0.084	0.030	0.001	0.026	-0.172 ± 0.040
139	-0.122	0.025	0.005	0.022	-0.247 ± 0.035
146	-0.039	0.025	0.003	0.022	0.021 ± 0.033
153	0.041	0.021	0.012	0.022	0.137 ± 0.030
160	0.068	0.027	0.001	0.022	0.144 ± 0.035
167	-0.001	0.033	0.011	0.022	0.087 ± 0.039

TABLE 5.2

CADMIUM

Differential Cross Section

Angle	Uncorrected $\sigma(\theta)$	Stat.	Syst.	M.C.	Inelastic $\sigma(\theta)$	Corrected $\sigma(\theta)$
20	781.1	27.6	63.5	3.3	12.1	1055.4 ± 91.2
27	607.0	14.4	49.3	2.4	12.0	797.5 ± 63.7
34	450.1	11.1	33.1	1.7	11.9	558.7 ± 44.2
41	320.4	10.2	21.2	1.5	11.9	370.9 ± 31.2
48	272.3	9.8	18.3	1.0	11.5	245.8 ± 28.0
55	185.2	6.4	13.1	0.7	11.1	175.0 ± 19.2
62	172.8	4.9	4.0	0.5	10.7	139.1 ± 8.9
69	109.7	2.5	7.7	0.4	10.6	117.4 ± 10.1
76	100.9	2.7	6.5	0.3	10.6	96.3 ± 9.2
83	69.4	2.0	5.6	0.3	10.6	72.0 ± 7.6
90	53.2	1.9	3.0	0.3	10.6	47.7 ± 4.9
97	40.1	1.0	3.3	0.3	10.6	29.5 ± 4.3
104	30.3	0.9	2.5	0.3	10.6	21.1 ± 3.4
111	25.1	1.8	2.0	0.3	10.6	21.6 ± 3.8
118	37.6	1.4	2.2	0.3	10.6	27.0 ± 3.6
125	39.9	1.4	2.5	0.3	10.7	32.9 ± 3.9
132	50.7	2.2	4.1	0.3	11.1	37.7 ± 5.3
139	56.3	1.3	3.8	0.3	11.5	43.8 ± 5.1
146	68.3	2.8	5.8	0.3	11.9	54.9 ± 8.6
153	68.1	2.0	5.6	0.3	11.9	74.3 ± 7.6
160	95.5	3.4	7.8	0.4	12.0	100.0 ± 11.1
167	94.4	3.5	7.0	0.4	12.1	126.6 ± 10.5

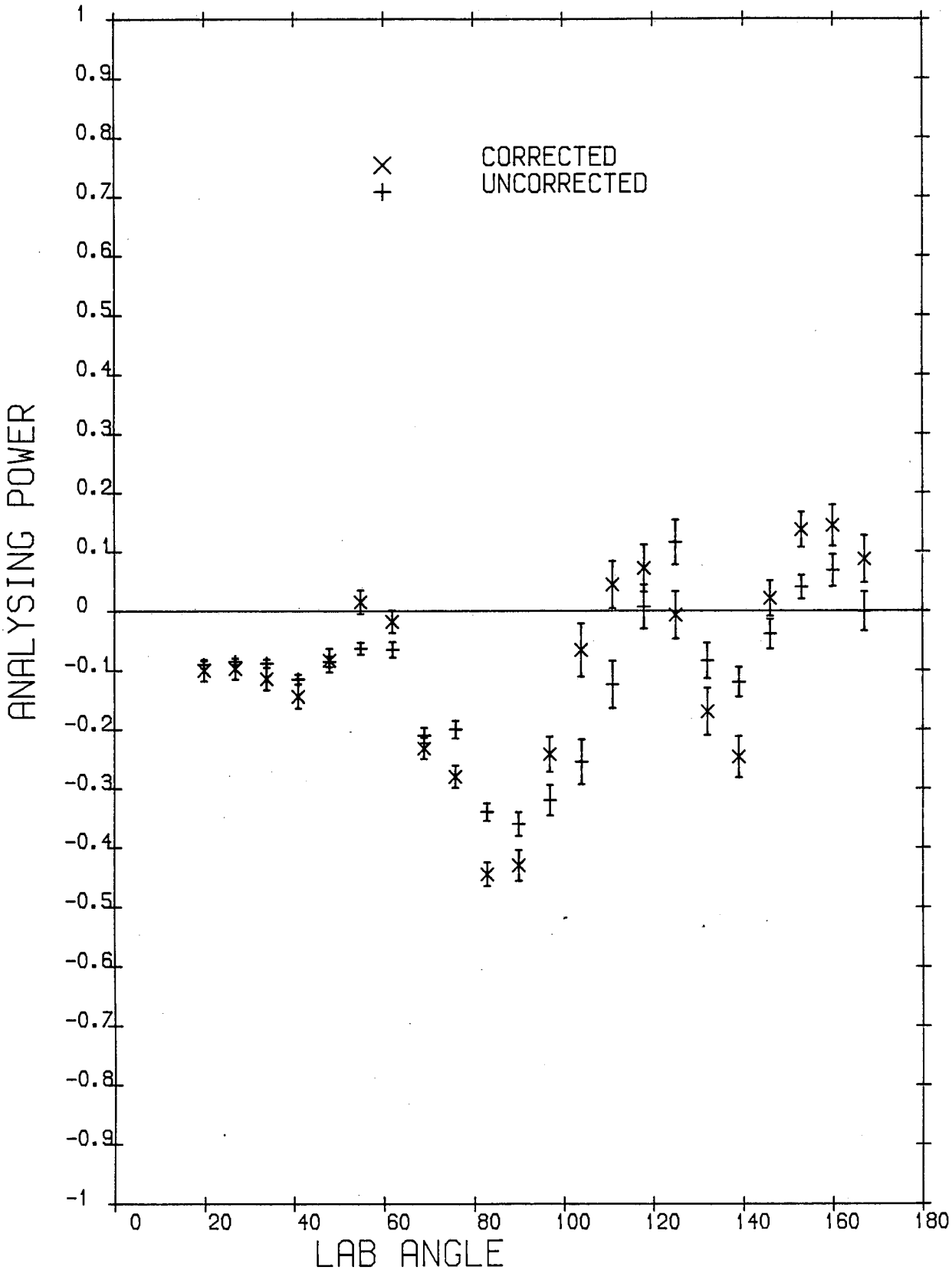
11/01/85 CADMIUM
CORRECTED
UNCORRECTED
ANALYSING POWER
LAB ANGLE
1
0.9
0.8
0.7
0.6
0.5
0.4
0.3
0.2
0.1
0
-0.1
-0.2
-0.3
-0.4
-0.5
-0.6
-0.7
-0.8
-0.9
-1
0
20
40
60
80
100
120
140
160
180

Figure 5.1.

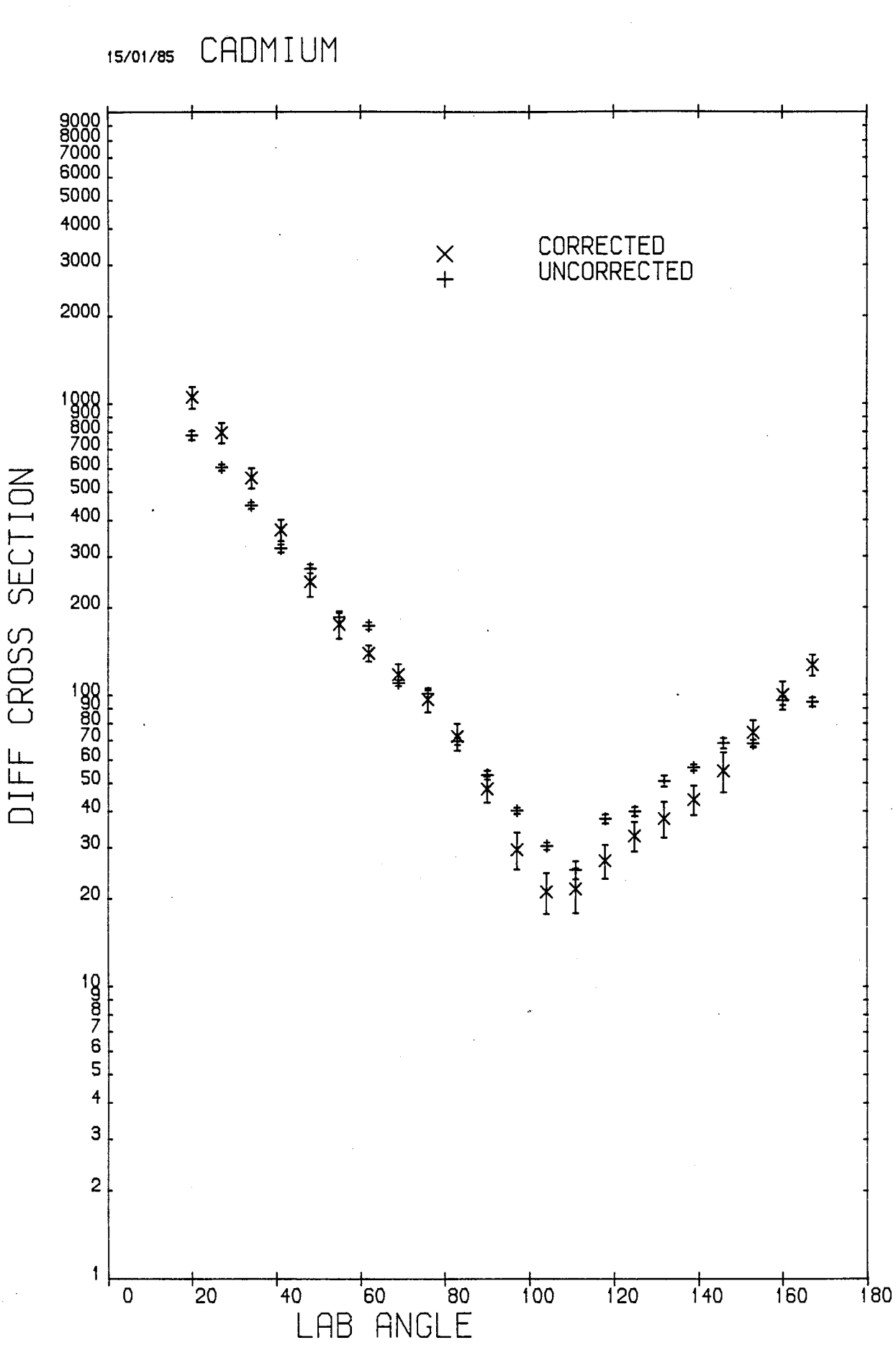
15/01/85
CADMIUM
CORRECTED
UNCORRECTED
DIFF CROSS SECTION
LAB ANGLE
9000
8000
7000
6000
5000
4000
3000
2000
1000
900
800
700
600
500
400
300
200
100
90
80
70
60
50
40
30
20
10
9
8
7
6
5
4
3
2
1
0
20
40
60
80
100
120
140
160
180

Figure 5.2.

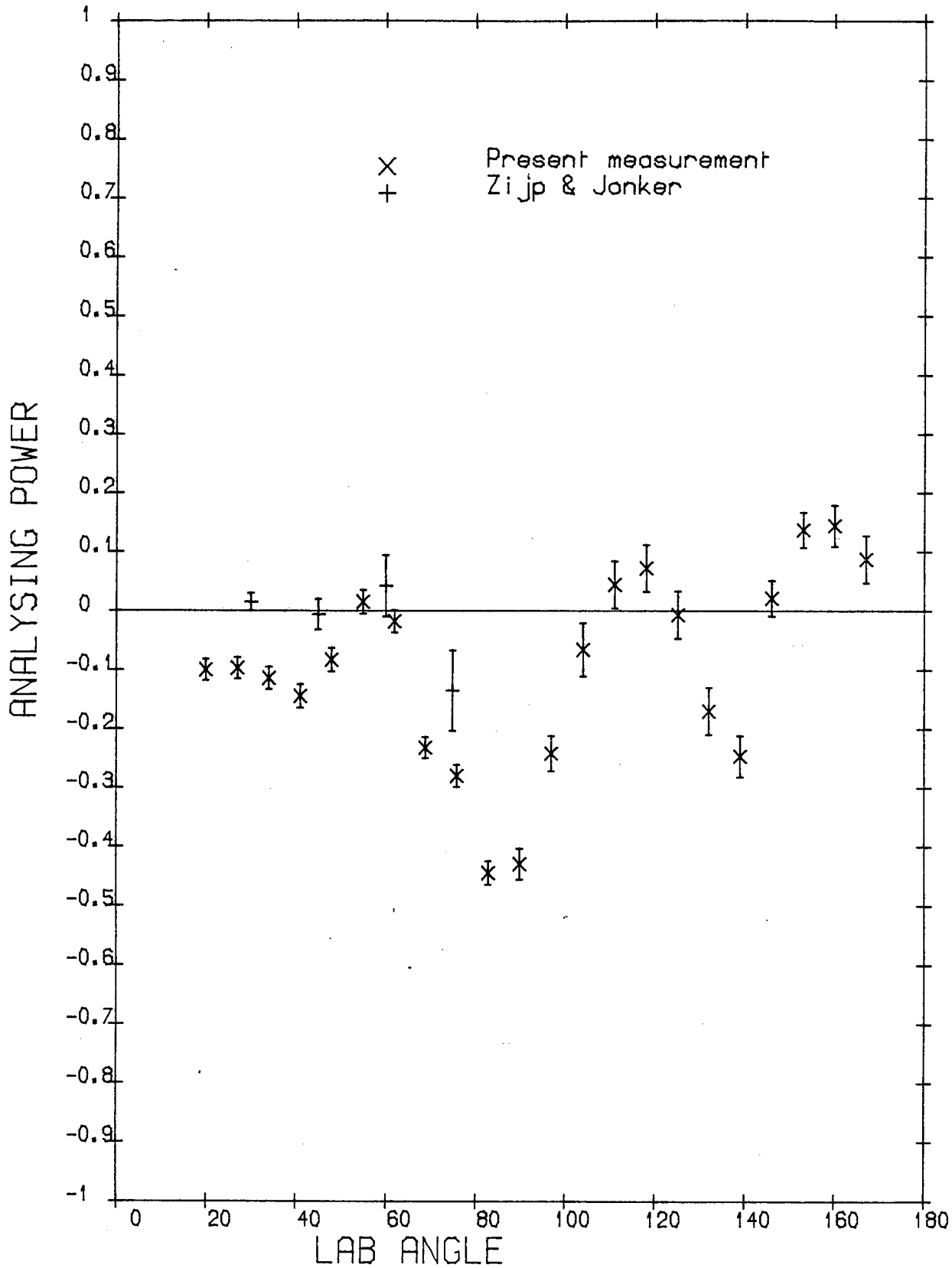
11/01/85 CADMIUM
Present measurement
Zijp & Jonker
ANALYSING POWER
LAB ANGLE
1
0.9
0.8
0.7
0.6
0.5
0.4
0.3
0.2
0.1
0
-0.1
-0.2
-0.3
-0.4
-0.5
-0.6
-0.7
-0.8
-0.9
-1
0
20
40
60
80
100
120
140
160
180

Figure 5.3.

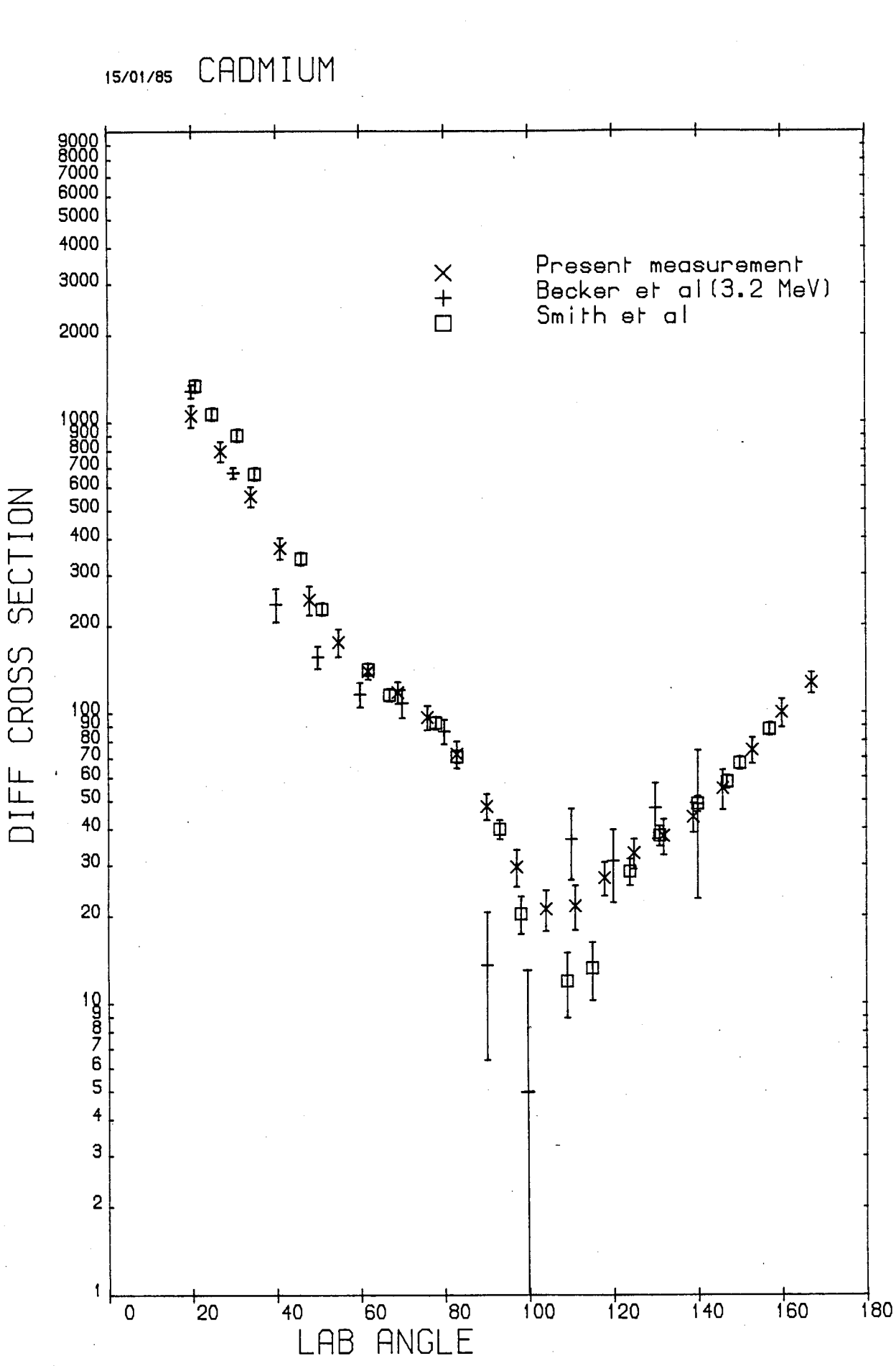
15/01/85 CADMIUM
Present measurement
Becker et al (3.2 MeV)
Smith et al
DIFF CROSS SECTION
LAB ANGLE
9000
8000
7000
6000
5000
4000
3000
2000
1000
900
800
700
600
500
400
300
200
100
90
80
70
60
50
40
30
20
10
9
8
7
6
5
4
3
2
1
0
20
40
60
80
100
120
140
160
180

Figure 5.4.

5.5.2 Tin

A scattering sample of natural Tin of 5.17 Cm high by 5.08 Cm diameter with a density of 7.12 gm/cm^3 was utilized for this measurement. Natural Tin consists of ten isotopes, ^{112}Sn, ^{114}Sn, ^{115}Sn, ^{116}Sn, ^{117}Sn, ^{118}Sn, ^{119}Sn, ^{120}Sn, ^{122}Sn and ^{124}Sn with percentage abundances of 0.96, 0.66, 0.35, 14.30, 7.61, 24.03, 8.58, 32.85, 4.72 and 5.94 respectively. The first three isotopes, having less than 1% abundances were not considered in the calculations. The total cross sections of 5.3b and 4.6b at 2.2 and 3.0 MeV are given by Foster and Glasgow[41] which result in MFPR's of 0.48 and 0.41 respectively.

The lower integration limit was set to 2.2 MeV, thus inelastic scattering of three excitation levels of 0.1585, 0.3145 and 0.711 MeV of ^{117}Sn and three excitation levels of 0.0238, 0.0895 amd 0.787 MeV of ^{119}Sn must be considered. Since there is no experimental inelastic differential cross section data for this kind of correction, corrections were calculated in the same way as for Cadmium.

The information about the Isotopic excitation levels is given below.

Isotope	Inelastic levels	No. of excitation levels up to 3.0 MeV
^{116}Sn	-	19 levels (108)
^{117}Sn	0.158 ($^{3}/_{2}^{+}$)	36 levls (109)
	0.314 ($^{11}/_{2}^{-}$)	
	0.711 ($^{7}/_{2}^{+}$)	
^{118}Sn	-	27 levels (110)
^{119}Sn	0.023 ($^{3}/_{2}^{+}$)	30 levels (111)
	0.089 ($^{11}/_{2}^{-}$)	
	0.787 ($^{7}/_{2}^{+}$)	
^{120}Sn	-	22 levels (112)
^{122}Sn	-	14 levels (113)
^{124}Sn	-	12 levels (114)

Since the fractional abundances of ^{117}Sn and ^{119}Sn are 7.61% and 8.58% respectively, it was found that their effect on the inelastic scattering correction is very small. The effect of the contribution of all six excitation levels of ^{117}Sn and ^{119}Sn is between 2 and 3 mb/sr.

Data is listed in Tables 5.3 and 5.4 and illustrated in Figures 5.5 and 5.6. The comparison of present analysing powers with those of Zijp and Jonker[40] at 3.2 MeV and Gorlov et al.[34] at 4.0 MeV are illustrated in Figure 5.7. The present measurements are in agreement with those of Gorlov et al.[34] at very backward angles, between 150° and 170°. The present analysing powers are also in good agreement with those of Zijp and Jonker on the whole, apart from the data at 90°, while the present measurements incline to higher analysing powers in this region. The zero axis is crossed in the same way as that observed by Zijp and Jonker, almost at the same angles.

The present differential cross section data is compared with those of Gupta et al.[39] at 10° forward angle and at 180° backward angle and with the data of Budtz et al.[45] and Tanaka et al.[46] in Figure 5.8. Although the present measurement covers the region between 20° and 167°, Gupta's data at 10° and 180° nicely fit on the distribution obtained in this work. The present measurement is in good agreement with those of Budtz et al. and Tanaka et al. overall, apart from a region between 90° - 110° (minimum). The differential cross sections of Becker et al.[31] at 3.2 MeV follows the same distribution with a poorer accuracy.

TABLE 5.3

TIN

Analysing Power

Angle	Uncorrected P(θ)	Stat.	Inst.	M.C.	Corrected P(θ)
20	-0.031	0.007	0.008	0.007	-0.025 ± 0.010
27	-0.040	0.007	0.010	0.008	-0.026 ± 0.011
34	0.045	0.011	0.001	0.010	0.053 ± 0.015
41	-0.027	0.009	0.005	0.011	-0.006 ± 0.014
48	0.025	0.012	0.012	0.012	0.054 ± 0.017
55	0.039	0.013	0.006	0.013	0.057 ± 0.019
62	-0.014	0.016	0.009	0.014	0.010 ± 0.021
69	-0.010	0.016	0.005	0.014	-0.005 ± 0.022
76	-0.100	0.023	0.005	0.016	-0.252 ± 0.029
83	-0.193	0.023	0.001	0.019	-0.361 ± 0.030
90	-0.299	0.032	0.013	0.023	-0.410 ± 0.039
97	-0.089	0.038	0.003	0.027	-0.214 ± 0.046
104	-0.094	0.046	0.006	0.028	-0.150 ± 0.053
111	0.085	0.040	0.011	0.025	0.097 ± 0.048
118	0.060	0.044	0.008	0.021	0.073 ± 0.049
125	0.103	0.037	0.002	0.017	0.106 ± 0.041
132	0.018	0.038	0.010	0.015	0.004 ± 0.041
139	0.015	0.029	0.006	0.014	0.010 ± 0.032
146	0.139	0.035	0.002	0.013	0.184 ± 0.037
153	0.104	0.024	0.004	0.013	0.133 ± 0.028
160	0.197	0.033	0.006	0.013	0.265 ± 0.036
167	0.162	0.027	0.005	0.013	0.208 ± 0.030

TABLE 5.4

TIN

Differential Cross Section

Angle	Uncorrected $\sigma(\theta)$	Stat.	Syst.	M.C.	inelastic $\dot{\sigma}(\theta)$	Corrected $\sigma(\theta)$
20	893.4	45.2	58.1	1.6	2.8	1232.7 ± 103.5
27	771.8	23.5	40.1	1.5	2.7	980.2 ± 81.0
34	465.3	31.3	30.2	1.3	2.7	735.5 ± 77.6
41	441.4	23.9	28.6	1.0	2.6	528.8 ± 59.0
48	301.5	25.7	19.5	0.8	2.4	374.0 ± 50.0
55	265.7	16.2	17.7	0.7	2.2	268.8 ± 37.8
62	174.9	5.9	11.4	0.5	2.2	200.7 ± 17.9
69	137.0	3.4	8.9	0.4	2.1	154.8 ± 12.5
76	110.4	3.7	7.2	0.4	2.1	119.4 ± 11.0
83	84.0	2.6	5.5	0.3	2.0	89.3 ± 8.0
90	64.0	2.2	4.2	0.3	2.0	64.7 ± 6.0
97	50.3	1.2	3.3	0.2	2.0	48.1 ± 4.0
104	43.7	1.3	2.8	0.2	2.0	41.1 ± 3.7
111	44.1	1.2	2.9	0.2	2.1	42.6 ± 3.8
118	49.9	1.5	3.2	0.2	2.1	49.7 ± 4.0
125	53.0	1.6	3.4	0.2	2.2	59.8 ± 4.8
132	63.5	2.7	4.2	0.2	2.2	72.1 ± 6.8
139	77.3	2.6	4.0	0.2	2.4	88.1 ± 7.7
146	83.5	3.1	5.4	0.2	2.6	110.0 ± 9.0
153	117.4	3.8	7.6	0.2	2.7	138.7 ± 11.9
160	116.5	7.0	7.6	0.2	2.7	171.4 ± 15.5
167	160.8	6.9	11.4	0.2	2.8	202.2 ± 18.5

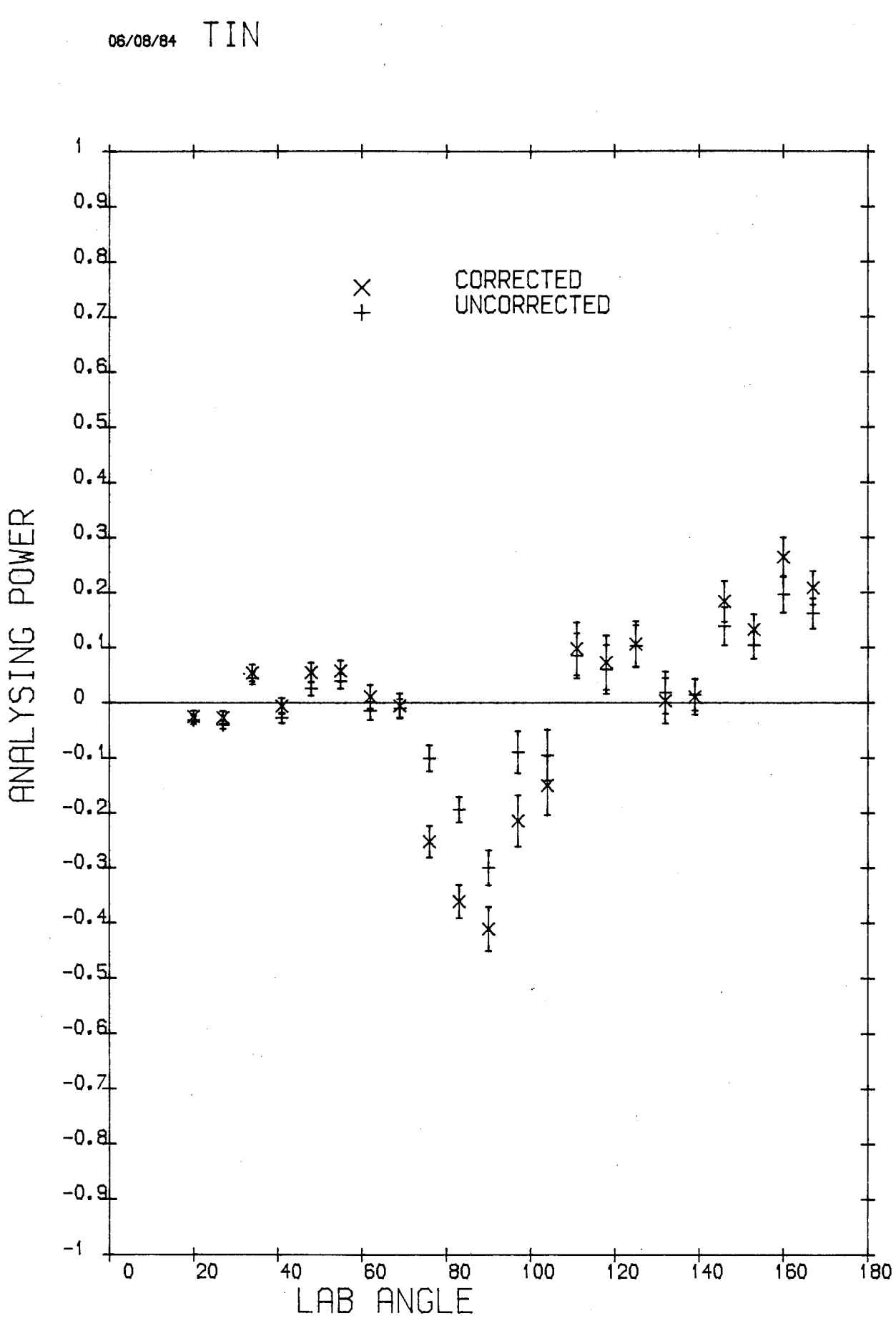
06/08/84 TIN
CORRECTED
UNCORRECTED
ANALYSING POWER
LAB ANGLE
1
0.9
0.8
0.7
0.6
0.5
0.4
0.3
0.2
0.1
0
-0.1
-0.2
-0.3
-0.4
-0.5
-0.6
-0.7
-0.8
-0.9
-1
0
20
40
60
80
100
120
140
160
180

Figure 5.5.

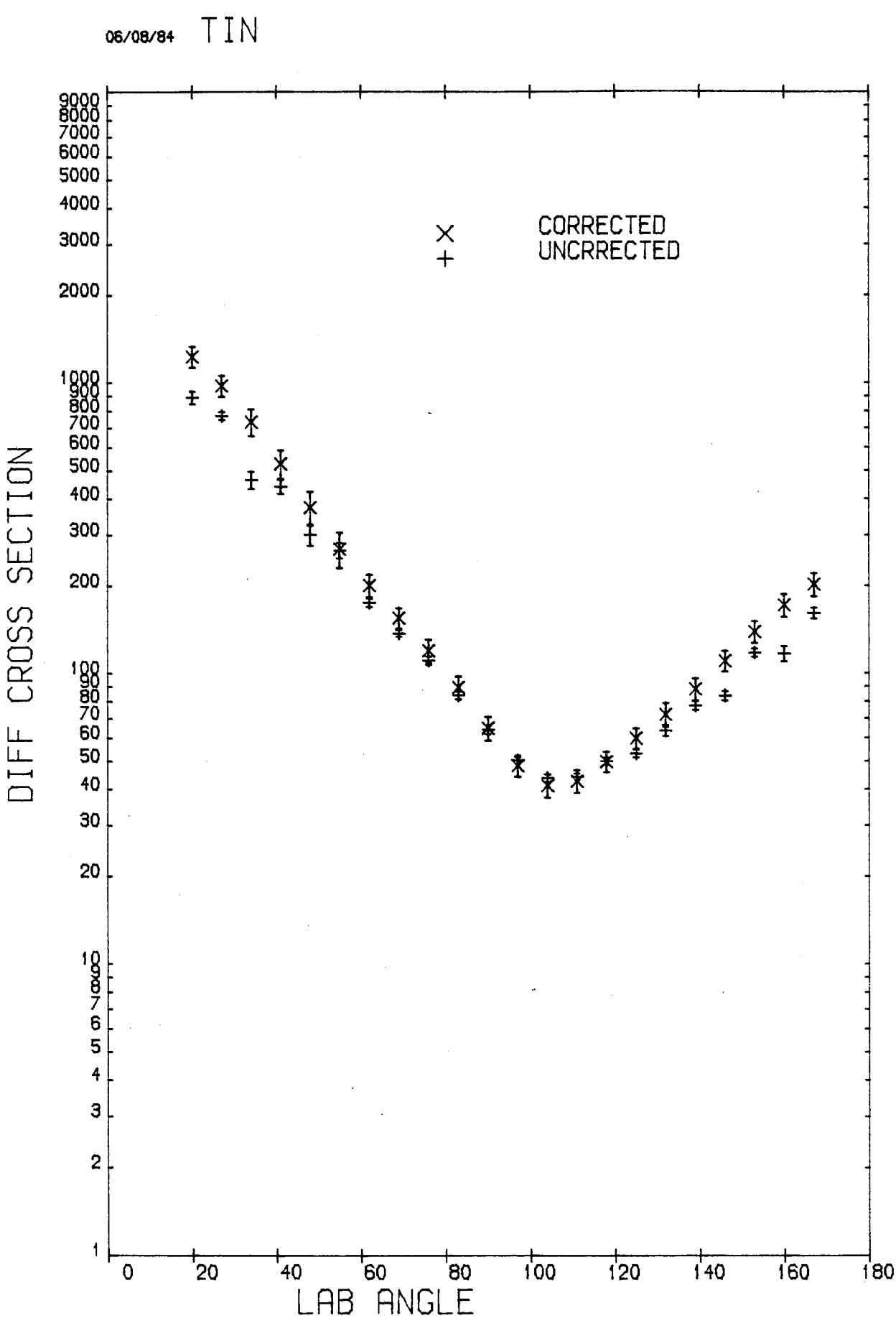
06/08/84 TIN
CORRECTED
UNCRRECTED
DIFF CROSS SECTION
LAB ANGLE
9000
8000
7000
6000
5000
4000
3000
2000
1000
900
800
700
600
500
400
300
200
100
90
80
70
60
50
40
30
20
10
9
8
7
6
5
4
3
2
1
0
20
40
60
80
100
120
140
160
180

Figure 5.6.

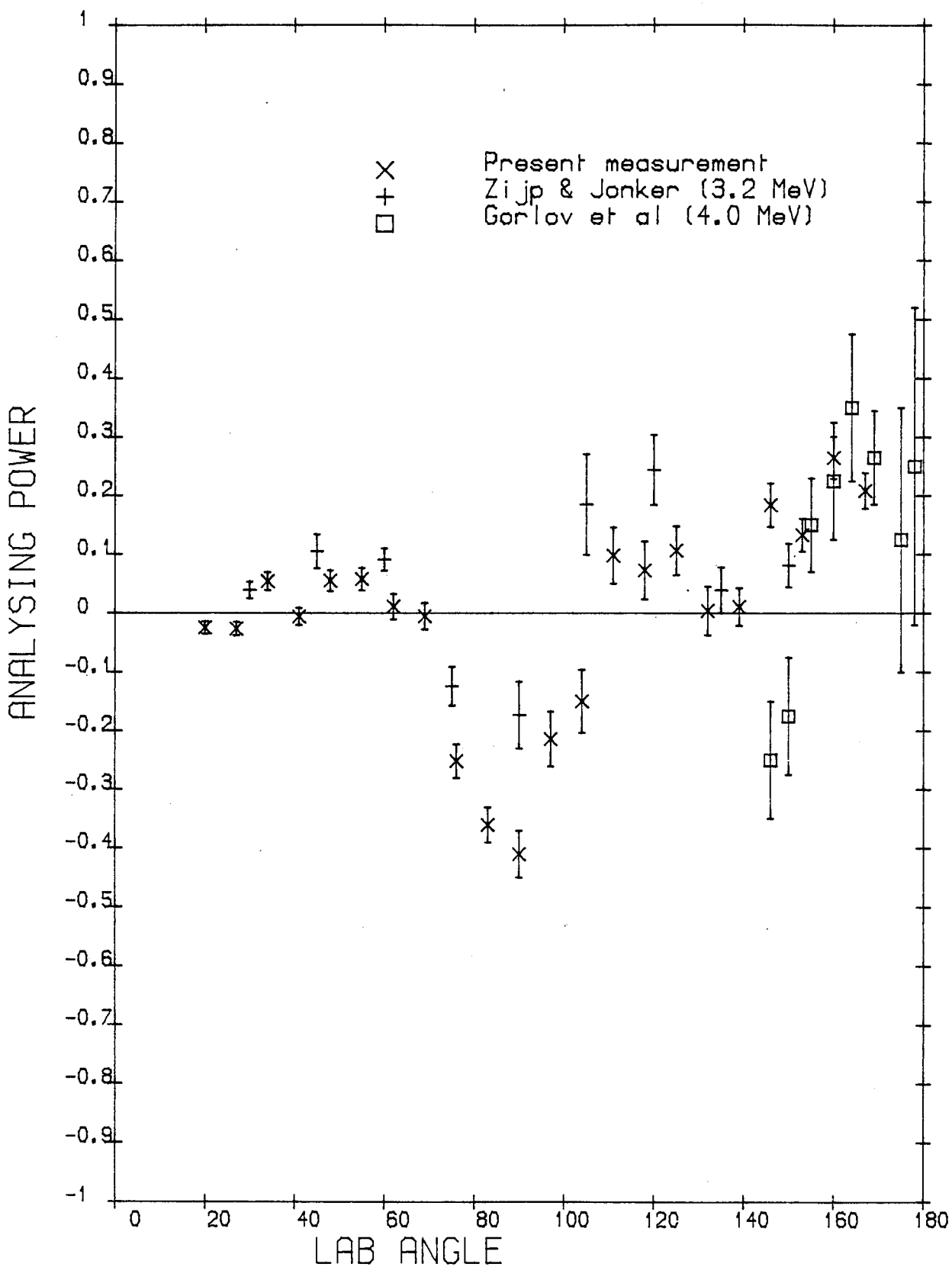
07/08/84 TIN
Present measurement
Zijp & Jonker (3.2 MeV)
Gorlov et al (4.0 MeV)
ANALYSING POWER
LAB ANGLE
1
0.9
0.8
0.7
0.6
0.5
0.4
0.3
0.2
0.1
0
-0.1
-0.2
-0.3
-0.4
-0.5
-0.6
-0.7
-0.8
-0.9
-1
0
20
40
60
80
100
120
140
160
180

Figure 5.7.

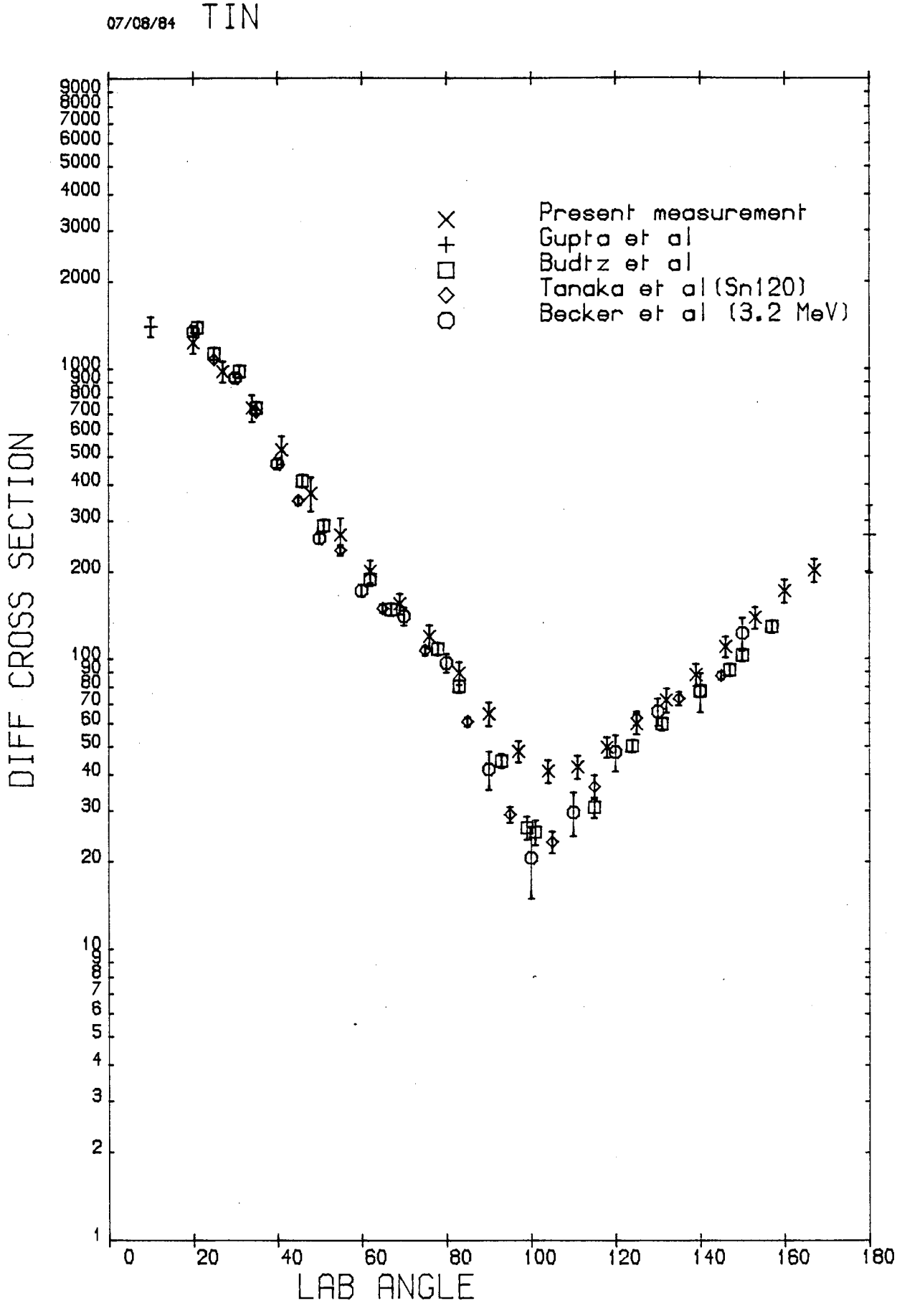
07/08/84 TIN
DIFF CROSS SECTION
LAB ANGLE
Present measurement
Gupta et al
Budtz et al
Tanaka et al (Sn120)
Becker et al (3.2 MeV)
9000
8000
7000
6000
5000
4000
3000
2000
1000
900
800
700
600
500
400
300
200
100
90
80
70
60
50
40
30
20
10
9
8
7
6
5
4
3
2
1
0
20
40
60
80
100
120
140
160
180

Figure 5.8.

5.5.3 Antimony

The scattering sample is cast of natural Antimony 5.33 Cm high by 4.87 Cm diameter with density of 6.63 gm./cm^3. Natural Antimony consists principally of two isotopes, ^{121}Sb and ^{123}Sb in percentage abundances of 52.25% and 42.25% respectively. The lower integration limit was chosen to be 2.20 MeV, hence the inelastic scattering corrections should be performed for the following levels:

Isotope	Inelastic levels	No. of Excitation levels up to 3.0 MeV
^{121}Sb	0.037 ($^7/_2^+$)	39 levels (115)
	0.507 ($^3/_2^+$)	
	0.573 ($^1/_2^+$)	
^{123}Sb	0.160 ($^5/_2^+$)	37 levels (116)
	0.541 ($^3/_2^+$)	
	0.712 ($^1/_2^+$)	

No experimental differential inelastic data exists, therefore corrections were calculated using the same procedure given previously.

A total cross section of 5.4b and 5.0b at 2.2 and 3.0 MeV are given by Smith et al.[44] which result in MFPR's of 0.43 and 0.40 respectively. Tables 5.5 and 5.6 and Figs. 5.9 and 5.10 present the data.

The present differential cross section data is compared with those of Smith et al.[44] and Becker et al.[31] in Fig. 5.12. The present data is in good agreement with those of Smith et al.[44] overall, while those of Becker et al. at forward angles up to 110° show smaller values with poor accuracy. Smith's results include the elastic cross section and inelastic-neutron components due to 0.037 MeV ($^7/_2^+$) and

0.160 MeV ($5/2^+$) levels, while the present measurement is corrected for these inelastic contributions. The inelastic cross sections due to the excitation of these two levels is calculated and given in Table 5.6 column 7. A better agreement between Smith et al. and the present measurements could be obtained, if the calculated cross sections for these two levels in column 7 are subtracted from Smith's results.

The analysing power data is compared with those of Zijp and Jonker[40] at 3.2 MeV and Kazakova et al.[29] at 3.25 MeV in Figure 5.11. The latter has a very poor accuracy and the accuracy of the former is also poor in comparison with present measurements. The present measurements disagree with Kazakova et al. and Zijp and Jonker at 35°, 45° and 75°.

TABLE 5.5

ANTIMONY

Analysing Power

Angle	Uncorrected P(θ)	Stat.	Inst.	M.C.	Corrected P(θ)
20	-0.023	0.007	0.003	0.016	-0.020 ± 0.017
27	-0.076	0.004	0.002	0.015	-0.063 ± 0.016
34	-0.020	0.008	0.002	0.015	-0.061 ± 0.017
41	-0.090	0.007	0.000	0.014	-0.088 ± 0.016
48	-0.095	0.012	0.005	0.014	-0.069 ± 0.017
55	-0.055	0.008	0.010	0.014	-0.021 ± 0.016
62	-0.098	0.013	0.013	0.014	-0.077 ± 0.019
69	-0.160	0.012	0.007	0.014	-0.192 ± 0.019
76	-0.233	0.022	0.007	0.016	-0.344 ± 0.027
83	-0.292	0.017	0.013	0.021	-0.449 ± 0.027
90	-0.291	0.029	0.016	0.030	-0.430 ± 0.041
97	-0.169	0.030	0.010	0.043	-0.396 ± 0.052
104	0.036	0.033	0.004	0.053	0.059 ± 0.063
111	-0.002	0.034	0.012	0.051	0.198 ± 0.062
118	0.053	0.030	0.009	0.042	0.101 ± 0.052
125	0.061	0.030	0.012	0.034	0.044 ± 0.045
132	-0.175	0.029	0.010	0.029	-0.219 ± 0.041
139	-0.101	0.024	0.001	0.026	-0.143 ± 0.036
146	0.013	0.023	0.002	0.023	0.029 ± 0.033
153	0.030	0.023	0.000	0.020	0.079 ± 0.030
160	0.096	0.025	0.003	0.017	0.146 ± 0.031
167	0.028	0.030	0.001	0.014	0.111 ± 0.034

TABLE 5.6

Antimony

Differential Cross Section

Angle	Uncorrected σ(θ)	Stat.	Syst.	M.C.	inelastic σ(θ)*	inelastic σ(θ)†	Corrected σ(θ)
20	1108.7	30.5	80.0	3.9	14.5	11.6	1447.6 ± 128.6
27	951.3	37.0	77.3	3.0	14.5	11.6	1136.2 ± 123.4
34	710.5	18.2	57.8	2.2	14.5	11.4	833.9 ± 80.1
41	432.6	26.4	35.1	1.5	14.1	11.1	578.9 ± 64.4
48	367.9	13.6	29.9	1.0	13.9	10.9	388.2 ± 45.5
55	281.8	15.7	22.9	0.7	13.5	10.6	260.3 ± 40.0
62	202.6	7.2	23.7	0.5	13.2	10.3	179.9 ± 24.0
69	139.9	8.2	16.5	0.4	12.9	10.0	128.1 ± 19.1
76	102.1	1.8	8.3	0.3	12.8	9.9	89.7 ± 9.7
83	79.0	5.9	6.5	0.3	12.8	9.9	57.5 ± 11.0
90	62.7	2.4	5.1	0.3	12.8	9.8	31.4 ± 6.9
97	42.4	1.1	3.5	0.3	12.8	9.8	14.2 ± 3.9
104	33.9	0.9	2.7	0.3	12.8	9.9	8.2 ± 3.0
111	35.2	1.5	2.9	0.3	12.8	9.9	12.3 ± 3.3
118	49.8	1.3	4.1	0.3	12.9	10.0	22.3 ± 5.0
125	49.7	2.8	4.1	0.3	13.2	10.3	33.4 ± 6.0
132	57.9	3.0	4.7	0.3	13.5	10.6	42.9 ± 7.0
139	61.2	2.1	5.0	0.3	13.9	10.9	50.6 ± 6.6
146	78.0	1.9	6.3	0.3	14.1	11.1	59.0 ± 8.1
153	82.6	5.4	6.7	0.3	14.5	11.4	69.7 ± 11.5
160	101.6	5.5	8.3	0.3	14.5	11.6	83.6 ± 13.6
167	101.5	6.8	8.3	0.3	14.5	11.6	97.9 ± 14.8

* Inelastic correction cross sections for present measurement due to six levels mentioned in the text.

† Inelastic correction cross sections due to 0.037 ($^{7}/_{2}^{+}$) and 0.160 ($^{5}/_{2}^{+}$)

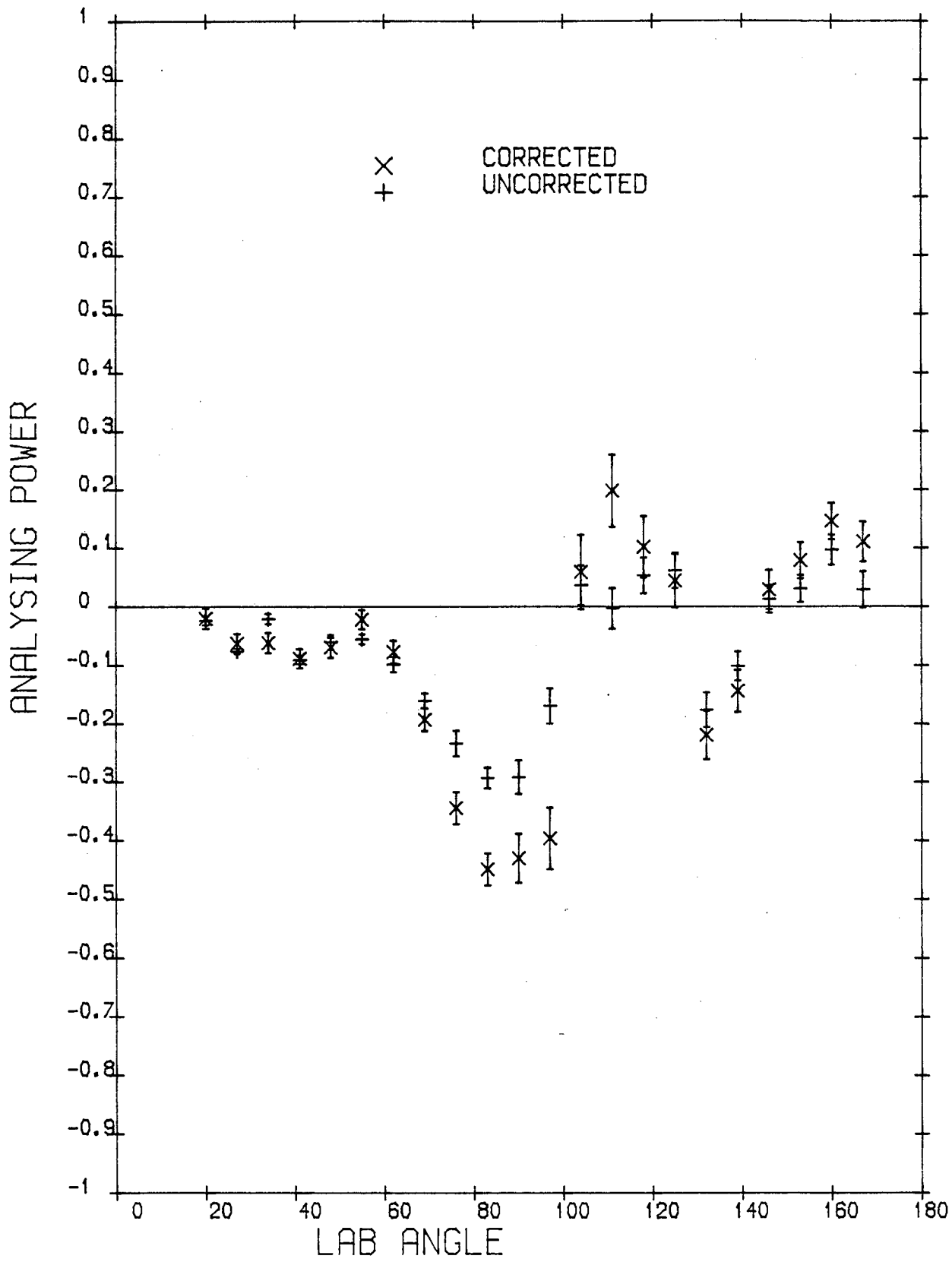
06/08/84 ANTIMONY
CORRECTED
UNCORRECTED
ANALYSING POWER
LAB ANGLE
1
0.9
0.8
0.7
0.6
0.5
0.4
0.3
0.2
0.1
0
-0.1
-0.2
-0.3
-0.4
-0.5
-0.6
-0.7
-0.8
-0.9
-1
0
20
40
60
80
100
120
140
160
180

Figure 5.9.

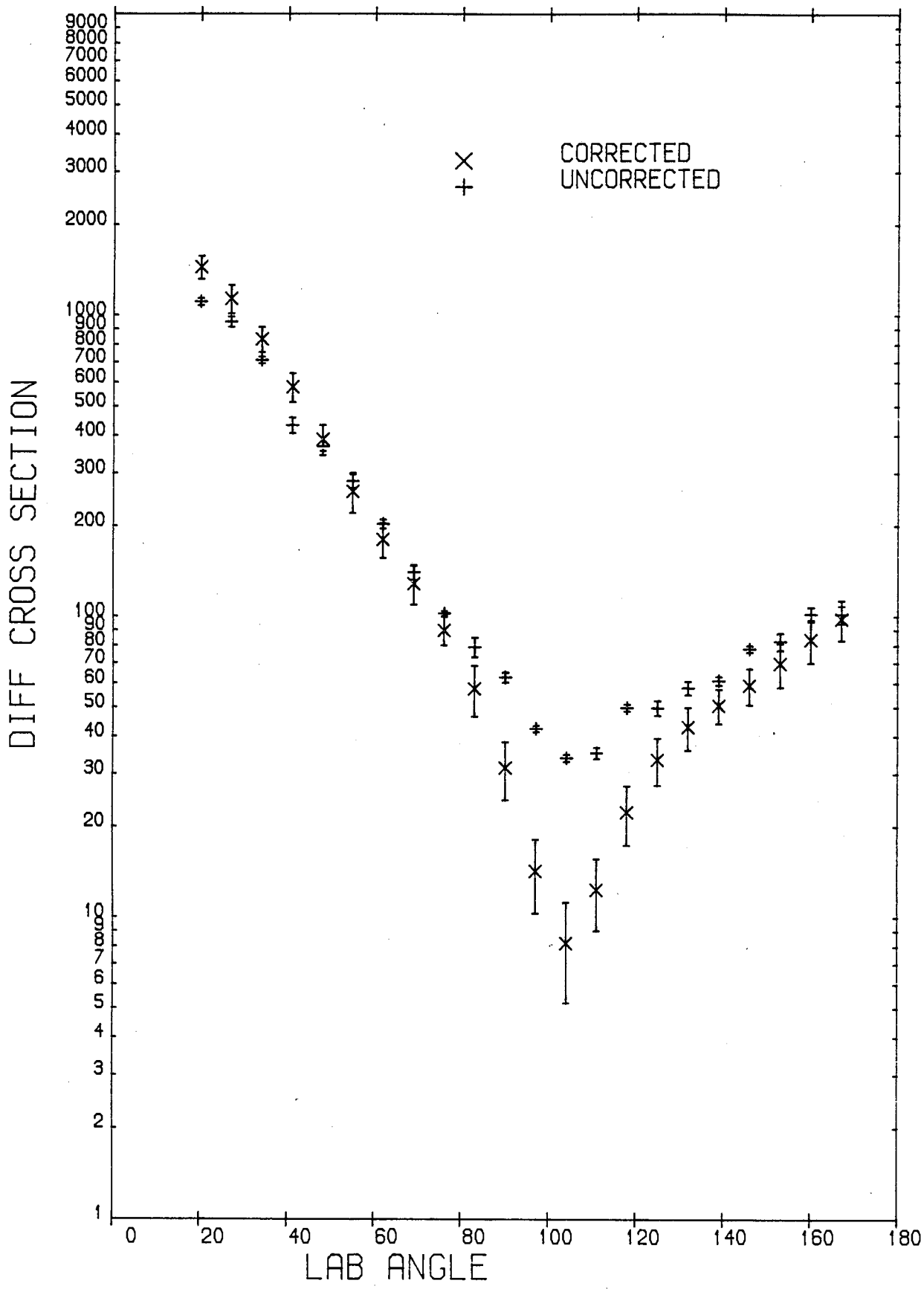
15/01/85 ANTIMONY
CORRECTED
UNCORRECTED
DIFF CROSS SECTION
LAB ANGLE
9000
8000
7000
6000
5000
4000
3000
2000
1000
900
800
700
600
500
400
300
200
100
90
80
70
60
50
40
30
20
10
9
8
7
6
5
4
3
2
1
0
20
40
60
80
100
120
140
160
180

Figure 5.10.

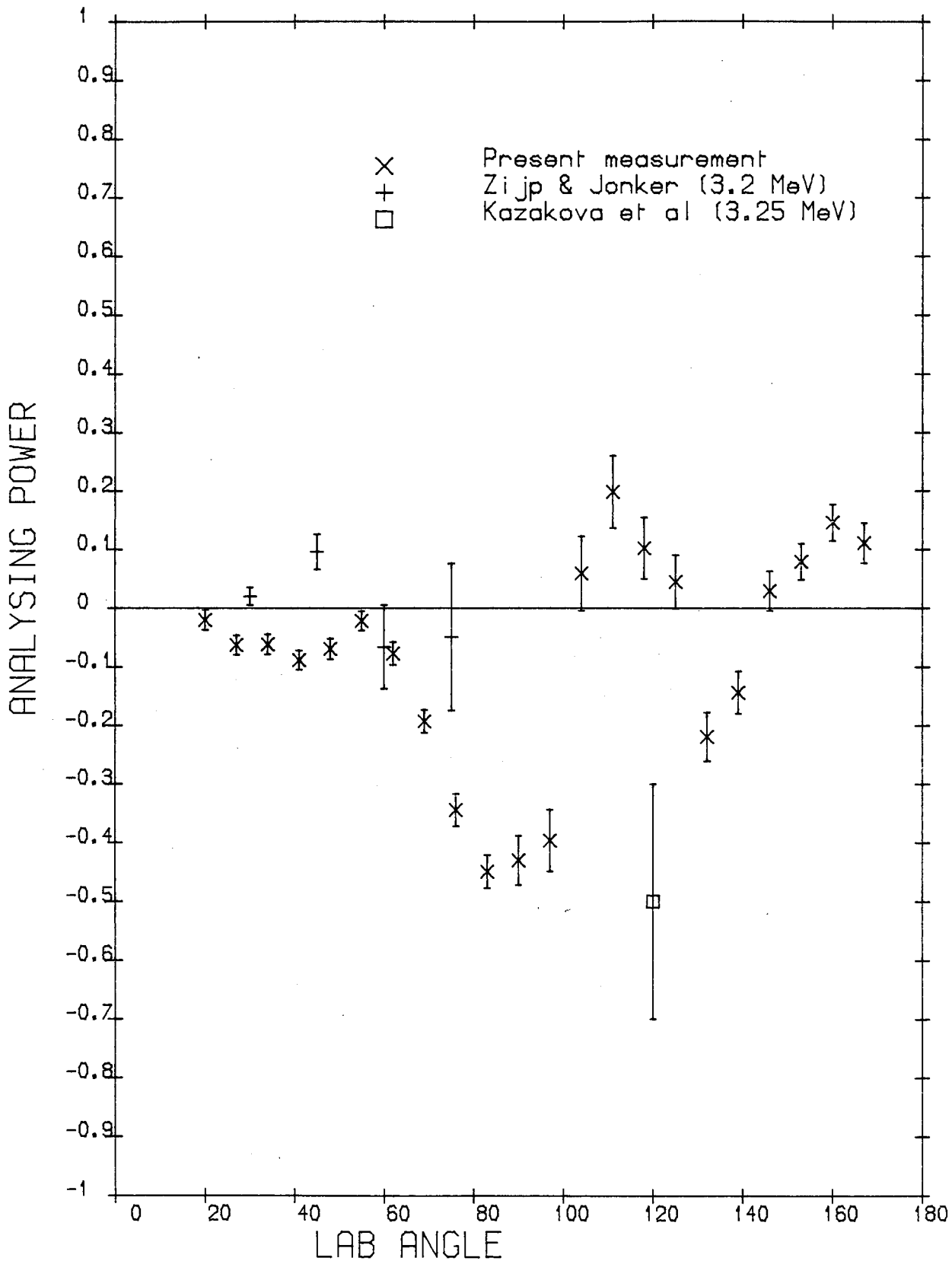
08/08/84 ANTIMONY
Present measurement
Zijp & Jonker (3.2 MeV)
Kazakova et al (3.25 MeV)
ANALYSING POWER
LAB ANGLE
1
0.9
0.8
0.7
0.6
0.5
0.4
0.3
0.2
0.1
0
-0.1
-0.2
-0.3
-0.4
-0.5
-0.6
-0.7
-0.8
-0.9
-1
0
20
40
60
80
100
120
140
160
180

Figure 5.11.

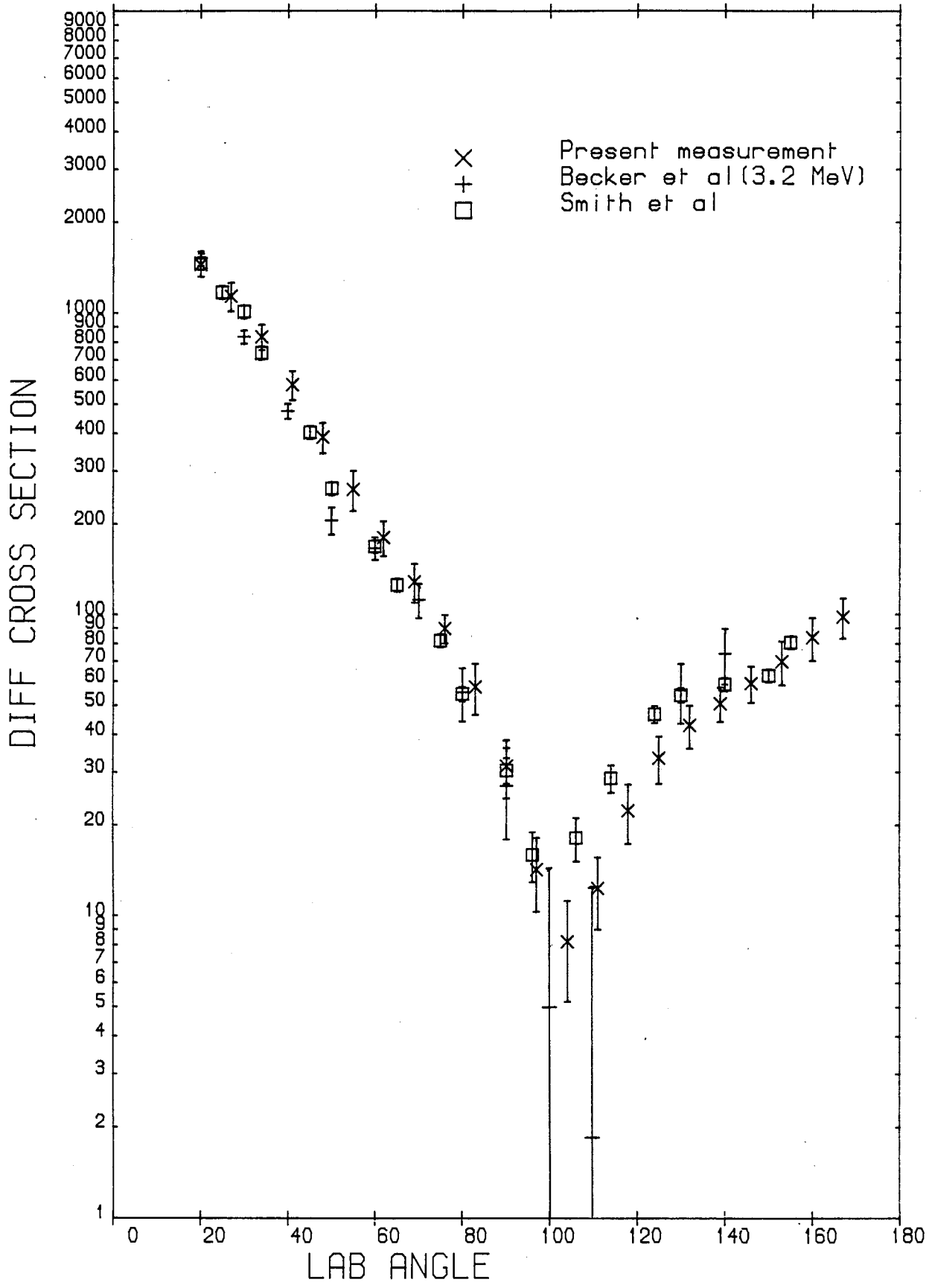
15/01/85 ANTIMONY
Present measurement
Becker et al (3.2 MeV)
Smith et al
DIFF CROSS SECTION
LAB ANGLE
9000
8000
7000
6000
5000
4000
3000
2000
1000
900
800
700
600
500
400
300
200
100
90
80
70
60
50
40
30
20
10
9
8
7
6
5
4
3
2
1
0
20
40
60
80
100
120
140
160
180

Finger 5.12.

5.5.4 Tellurium

The scattering sample is a cast cylinder of natural Tellurium, made of three discs, overall 4.76 Cm high by 5.13 Cm diameter, and its density is 6.02 gm/Cm^3. Natural Tellurium consists of eight isotopes ^{120}Te, ^{122}Te, ^{123}Te, ^{124}Te, ^{125}Te, ^{126}Te, ^{128}Te, and ^{130}Te in percentage abundances of 0.09, 2.48, 0.87, 4.16, 6.99, 18.7, 31.8 and 34.5 respectively. The first three isotopes with low abundances were not considered in the calculations. The lower integration limit was set at 2.2 MeV so that inelastic scattering involving the excitation of the following levels must be considered.

Isotope	Inelastic levels	No. of Excitation levels up to 3.0 MeV
^{124}Te	0.602 (2^+)	59 levels (117)
^{125}Te	0.035 ($3/2^+$)	57 levels (118)
	0.144 ($11/2^-$)	
	0.321 ($9/2^+$)	
	0.443 ($3/2^+$)	
	0.463 ($5/2^+$)	
	0.525 ($7/2^-$)	
	0.636 ($7/2^+$)	
	0.642 ($7/2^+$)	
	0.671 ($5/2^+$)	
	0.729 ($3/2^\pm$)	
	0.786 ( )	
^{126}Te	0.666 (2^+)	32 levels (119)
^{128}Te	0.743 (2^+)	32 levels (120)
^{130}Te	-	18 levels (121)

Foster and Glasgow[41] give total cross sections of 5.5b and 5.0b at energies of 2.5 and 3.0 MeV respectively, which result in sample MFPR's of 0.39 and 0.36.

As before neutron inelastic differential cross sections were calculated using the statistical model, then weighted according to the fractional isotopic abundances and relative detection efficiency to the elastic scattering at 3.0 MeV. The results are given in Table 5.8. Data is listed in Tables 5.7 and 5.8 and illustrated in Figures 5.13 and 5.14. The present analysing powers are compared with those of Zijp and Jonker[40] in Fig. 5.15. The present measurements are lower than those of Zijp and Jonker at 30°, 45°, 60° and 75°. No experimental differential cross sections are available for comparison.

TABLE 5.7

TELLERIUM

Analysing Power

Angle	Uncorrected P(θ)	Stat.	Inst.	M.C.	Corrected P(θ)
20	-0.120	0.046	0.003	0.015	-0.123 ± 0.047
27	-0.110	0.045	0.002	0.015	-0.130 ± 0.048
34	-0.136	0.048	0.002	0.015	-0.136 ± 0.050
41	-0.152	0.048	0.002	0.015	-0.204 ± 0.050
48	-0.125	0.049	0.014	0.015	-0.141 ± 0.050
55	-0.092	0.040	0.014	0.017	-0.108 ± 0.043
62	-0.069	0.043	0.012	0.018	-0.098 ± 0.047
69	-0.151	0.015	0.020	0.020	-0.217 ± 0.025
76	-0.183	0.020	0.018	0.022	-0.312 ± 0.031
83	-0.216	0.021	0.013	0.025	-0.345 ± 0.032
90	-0.191	0.027	0.016	0.026	-0.232 ± 0.037
97	-0.067	0.028	0.005	0.026	-0.098 ± 0.038
104	-0.002	0.036	0.005	0.027	0.012 ± 0.045
111	-0.042	0.030	0.011	0.028	0.005 ± 0.041
118	-0.053	0.029	0.006	0.027	-0.055 ± 0.040
125	-0.092	0.027	0.009	0.025	-0.209 ± 0.037
132	-0.239	0.029	0.016	0.023	-0.365 ± 0.036
139	-0.144	0.024	0.001	0.021	-0.253 ± 0.032
146	-0.136	0.028	0.001	0.021	-0.220 ± 0.035
153	-0.060	0.025	0.011	0.021	-0.077 ± 0.032
160	0.079	0.034	0.003	0.022	0.102 ± 0.039
167	0.128	0.032	0.001	0.023	0.186 ± 0.039

TABLE 5.8

TELLERIUM

Differential Cross Section

Angle	Uncorrected $\sigma(\theta)$	Stat.	Syst.	M.C.	Inelastic $\sigma(\theta)$	Corrected $\sigma(\theta)$
20	1105.0	37.5	89.7	4.4	6.5	1709.5 ± 127.3
27	1122.1	29.6	91.2	3.7	6.4	1430.3 ± 120.9
34	1014.1	26.1	81.9	3.0	6.4	1128.7 ± 107.8
41	618.5	25.0	40.3	2.3	6.4	838.3 ± 65.3
48	508.4	16.2	38.0	1.7	6.2	585.7 ± 54.0
55	344.6	19.4	28.0	1.3	6.2	386.6 ± 47.0
62	227.1	9.1	18.4	0.9	6.2	246.0 ± 27.5
69	156.0	9.8	12.7	0.7	6.2	157.8 ± 22.7
76	117.4	3.3	9.6	0.6	6.3	109.6 ± 12.9
83	101.3	4.3	7.3	0.5	6.3	86.4 ± 11.7
90	98.9	2.3	8.1	0.4	6.3	75.5 ± 10.5
97	79.5	3.0	6.5	0.4	6.3	68.7 ± 9.5
104	56.8	2.7	4.6	0.4	6.3	63.4 ± 7.1
111	67.3	2.8	5.1	0.4	6.3	60.5 ± 7.5
118	82.8	2.6	6.7	0.4	6.2	62.9 ± 9.0
125	80.2	3.5	5.6	0.4	6.2	71.7 ± 9.3
132	91.5	3.1	7.4	0.4	6.2	86.2 ± 10.5
139	101.6	4.4	8.2	0.4	6.2	103.0 ± 12.5
146	103.9	4.1	8.5	0.5	6.4	117.8 ± 12.5
153	118.7	5.1	9.6	0.5	6.4	127.8 ± 14.8
160	119.9	5.8	9.8	0.5	6.4	132.0 ± 14.7
167	136.4	7.1	10.9	0.6	6.5	131.9 ± 18.2

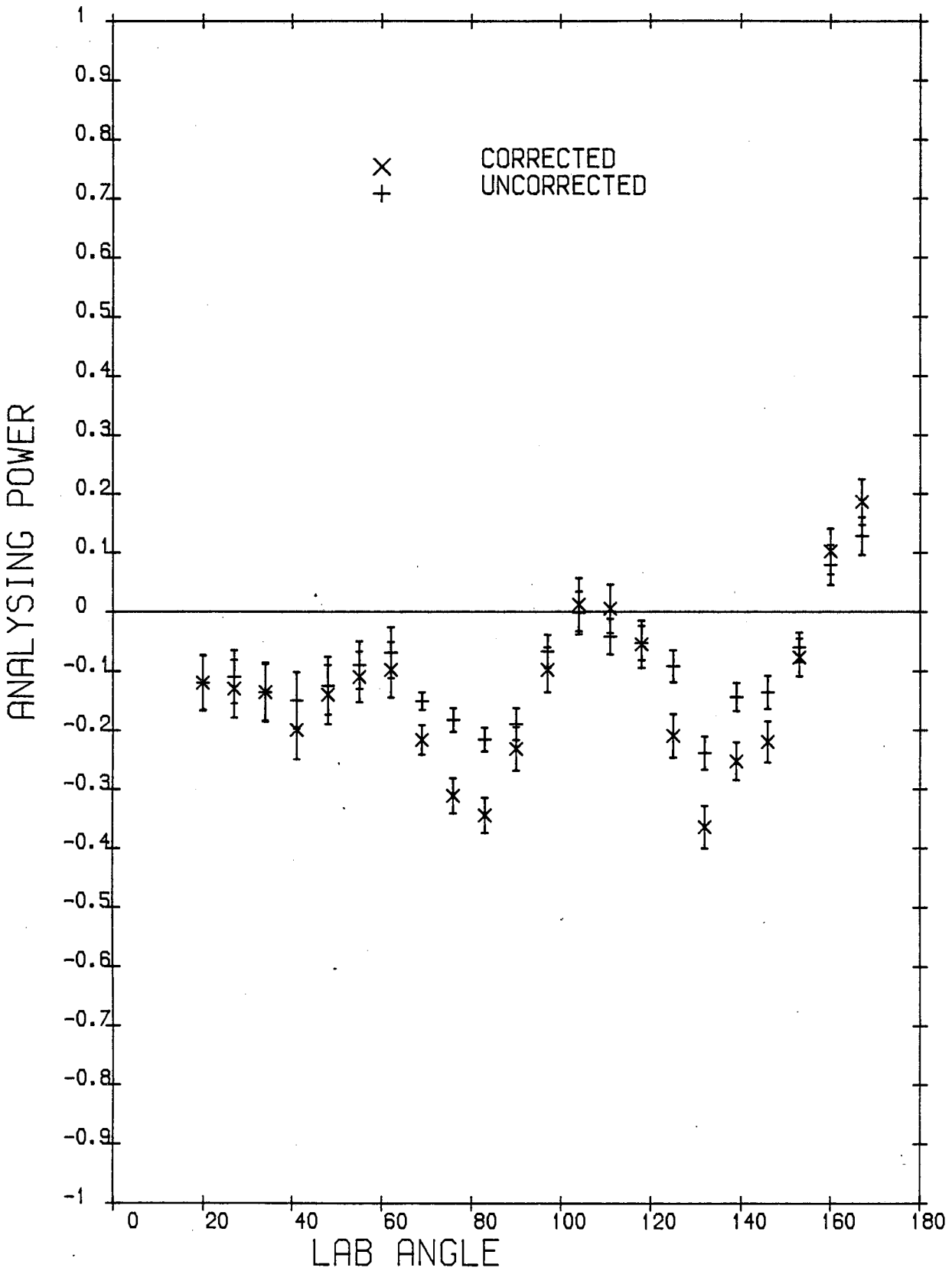
11/01/85 TELLURIUM
CORRECTED
UNCORRECTED
ANALYSING POWER
LAB ANGLE
1
0.9
0.8
0.7
0.6
0.5
0.4
0.3
0.2
0.1
0
-0.1
-0.2
-0.3
-0.4
-0.5
-0.6
-0.7
-0.8
-0.9
-1
0
20
40
60
80
100
120
140
160
180

Figure 5.13.

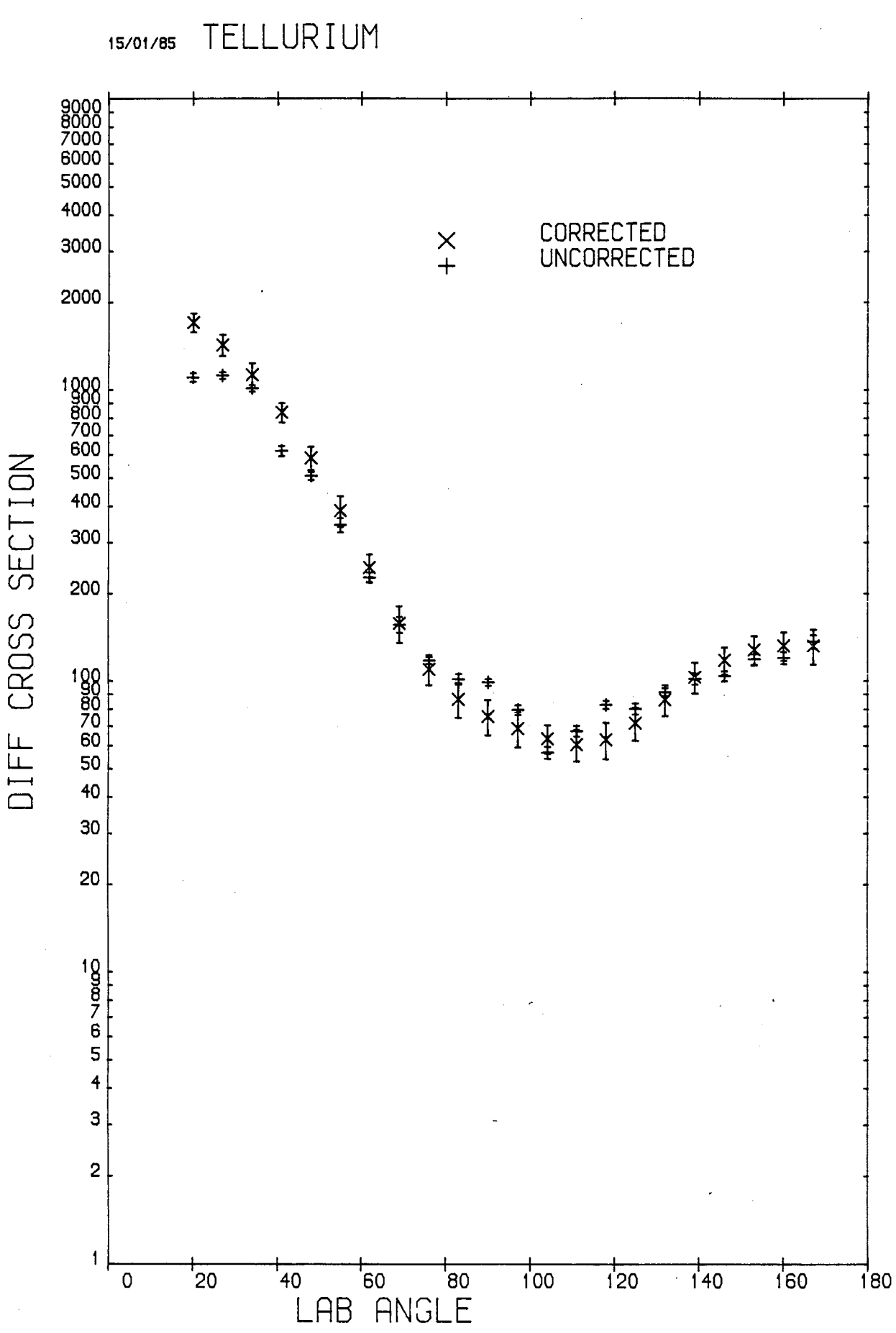
15/01/85 TELLURIUM
CORRECTED
UNCORRECTED
DIFF CROSS SECTION
LAB ANGLE
9000
8000
7000
6000
5000
4000
3000
2000
1000
900
800
700
600
500
400
300
200
100
90
80
70
60
50
40
30
20
10
9
8
7
6
5
4
3
2
1
0
20
40
60
80
100
120
140
160
180

Figure 5.14.

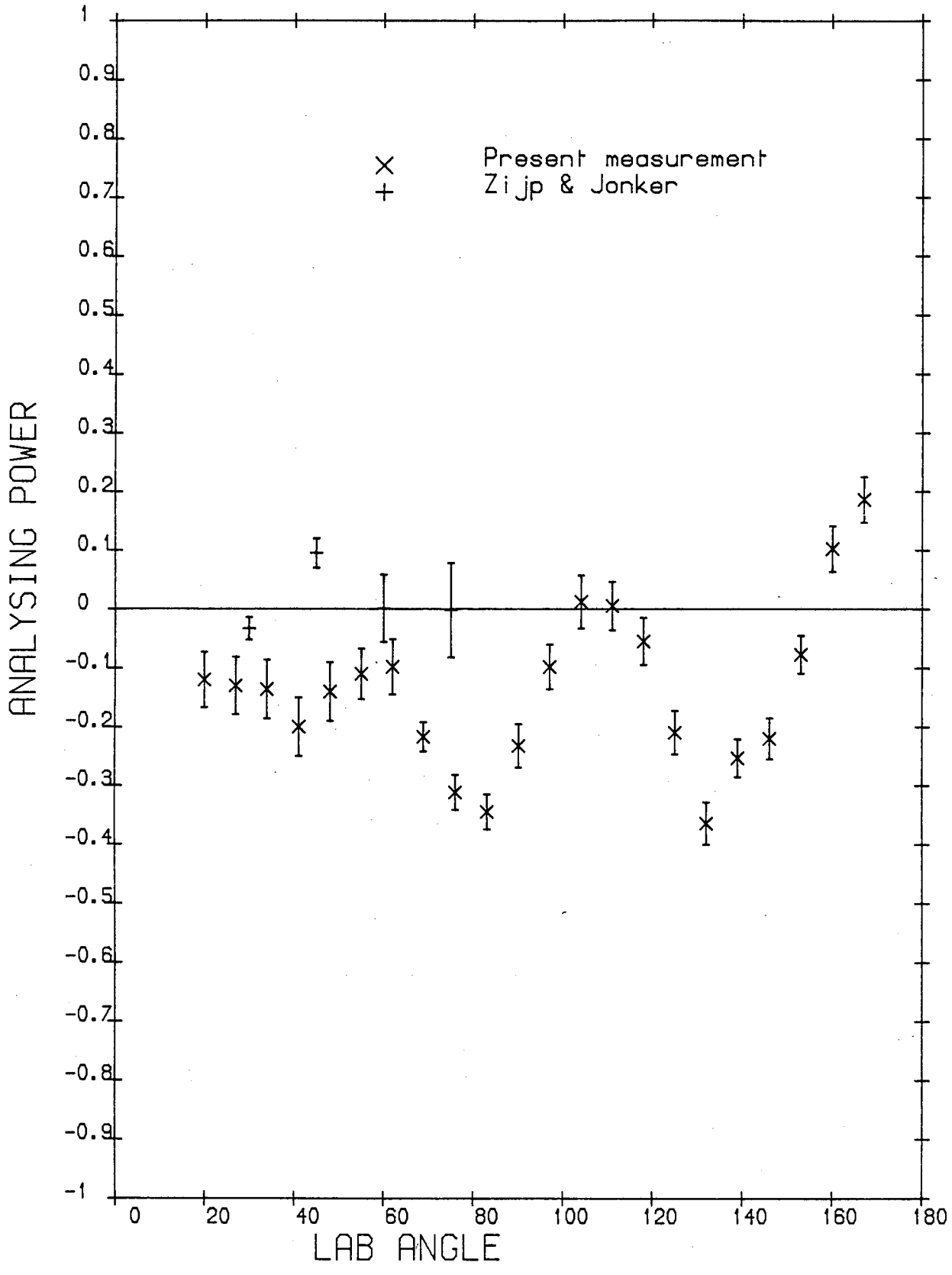
15/01/85 TELLURIUM
Present measurement
Zijp & Jonker
ANALYSING POWER
LAB ANGLE
1
0.9
0.8
0.7
0.6
0.5
0.4
0.3
0.2
0.1
0
-0.1
-0.2
-0.3
-0.4
-0.5
-0.6
-0.7
-0.8
-0.9
-1
0
20
40
60
80
100
120
140
160
180

Figure 5.15.

5.5.5 Iodine

The scattering sample is composed of crystals and is contained in a glass cylinder 5.18 Cm high by 4.84 Cm inner diameter with 2 mm wall thickness. The final density obtained, by pressing the fine Iodine crystals into the glass container, is 4.16 gm/Cm^3, very close to the accepted value 4.94 gm/Cm^3. An identical empty container was used for background measurement. Foster and Glasgow[41] give total cross sections of 5.6b and 5.2b at energies of 2.5 and 3.0 MeV respectively, which result in sample MFPR's of 0.27 and 0.25.

Although Iodine is mono-isotopic, the analysis was complicated by sixty seven excitation levels up to 3.0 MeV. Therefore continuum band calculations were performed using the programme CINDY, and the inelastic differential cross sections were calculated and weighted according to the relative detection efficiency to the elastic scattering at 3.0 MeV for the following excitation levels. The lower integration limit was set at 2.2 MeV.

Isotope	Inelastic levels	No. of Excitation levels up to 3.0 MeV
^{127}I	0.057 $(^{7}/_{2}^{+})$	67 levels (122)
	0.202 $(^{3}/_{2}^{+})$	
	0.374 $(^{1}/_{2}^{+})$	
	0.417 $(^{5}/_{2}^{+})$	
	0.473 ( )	
	0.618 $(^{3}/_{2}^{+})$	
	0.628 $(^{7}/_{2}^{+})$	
	0.651 $(^{9}/_{2}^{+})$	
	0.716 $(^{11}/_{2}^{+})$	
	0.744 $(^{9}/_{2}^{+})$	

Data is listed in Tables 5.9 and 5.10 and illustrated in Figures 5.16 and 5.17.

Figures 5.18 and 5.19 compare present analysing powers and differential cross sections with the only available data by Galloway and Waheed[42] at 3.0 MeV.

The present analysing powers are in quantitative agreement with those of Galloway and Waheed at backward angles, while those of Galloway and Waheed show opposite sign to the present measurement at forward angles.

The present differential cross sections disagree with those of Galloway and Waheed apart from those up to 62°, probably because they were not corrected for inelastic contamination.

TABLE 5.9

IODINE

Analysing Power

Angle	Uncorrected P(θ)	Stat.	Inst.	M.C.	Corrected P(θ)
20	-0.063	0.007	0.003	0.011	-0.075 ± 0.013
27	-0.083	0.009	0.001	0.011	-0.064 ± 0.014
34	-0.099	0.010	0.007	0.011	-0.082 ± 0.015
41	-0.097	0.013	0.009	0.012	-0.075 ± 0.018
48	-0.124	0.013	0.002	0.013	-0.095 ± 0.018
55	-0.108	0.021	0.001	0.014	-0.083 ± 0.025
62	-0.013	0.023	0.014	0.015	-0.109 ± 0.028
69	-0.175	0.034	0.009	0.016	-0.206 ± 0.038
76	-0.249	0.034	0.006	0.018	-0.350 ± 0.039
83	-0.402	0.059	0.001	0.022	-0.551 ± 0.063
90	-0.360	0.060	0.011	0.030	-0.583 ± 0.067
97	-0.276	0.108	0.001	0.040	-0.558 ± 0.114
104	0.134	0.083	0.013	0.042	0.245 ± 0.093
111	0.076	0.092	0.003	0.034	0.321 ± 0.098
118	0.094	0.051	0.002	0.025	0.142 ± 0.057
125	0.143	0.077	0.012	0.020	0.140 ± 0.079
132	-0.206	0.043	0.006	0.017	-0.158 ± 0.046
139	-0.308	0.071	0.017	0.017	-0.411 ± 0.072
146	-0.131	0.047	0.002	0.018	-0.224 ± 0.050
153	-0.167	0.077	0.005	0.018	-0.217 ± 0.080
160	-0.075	0.056	0.006	0.018	-0.070 ± 0.060
167	0.039	0.114	0.001	0.018	0.080 ± 0.120

TABLE 5.10

IODINE

Differential Cross Section

Angle	Uncorrected $\sigma(\theta)$	Stat.	Syst.	M.C.	Inelastic $\sigma(\theta)$	Corrected $\sigma(\theta)$
20	1438.5	28.0	116.9	3.4	12.7	1955.8 ± 145.0
27	1481.7	30.8	120.4	2.8	12.3	1534.5 ± 150.0
34	1058.0	28.8	76.0	2.2	11.9	1121.8 ± 94.0
41	755.3	16.2	61.4	1.7	11.6	768.7 ± 77.5
48	509.9	12.3	41.4	1.2	11.4	500.4 ± 53.4
55	316.4	9.9	25.7	0.9	11.5	316.8 ± 25.9
62	209.6	6.3	16.0	0.6	11.8	200.3 ± 22.5
69	140.4	2.9	11.6	0.4	12.0	127.7 ± 14.4
76	102.0	2.0	8.2	0.3	12.3	79.0 ± 10.3
83	76.4	2.8	6.2	0.3	12.6	43.5 ± 9.0
90	66.9	2.2	5.4	0.2	12.6	19.2 ± 7.6
97	36.5	0.9	3.0	0.2	12.6	7.4 ± 3.6
104	36.3	0.8	3.0	0.2	12.6	8.5 ± 3.9
111	34.9	1.1	2.8	0.2	12.3	20.1 ± 4.0
118	70.0	2.3	5.7	0.2	12.0	35.6 ± 8.1
125	74.8	1.4	5.0	0.2	11.7	49.3 ± 6.5
132	82.5	4.9	6.7	0.2	11.5	56.8 ± 11.6
139	75.5	1.5	5.0	0.2	11.4	59.1 ± 6.3
146	79.6	2.1	6.5	0.2	11.6	59.6 ± 8.7
153	80.4	2.0	5.4	0.2	11.9	62.6 ± 7.4
160	88.0	1.9	7.0	0.2	12.3	69.8 ± 9.0
167	92.2	2.6	6.2	0.2	12.7	79.3 ± 8.9

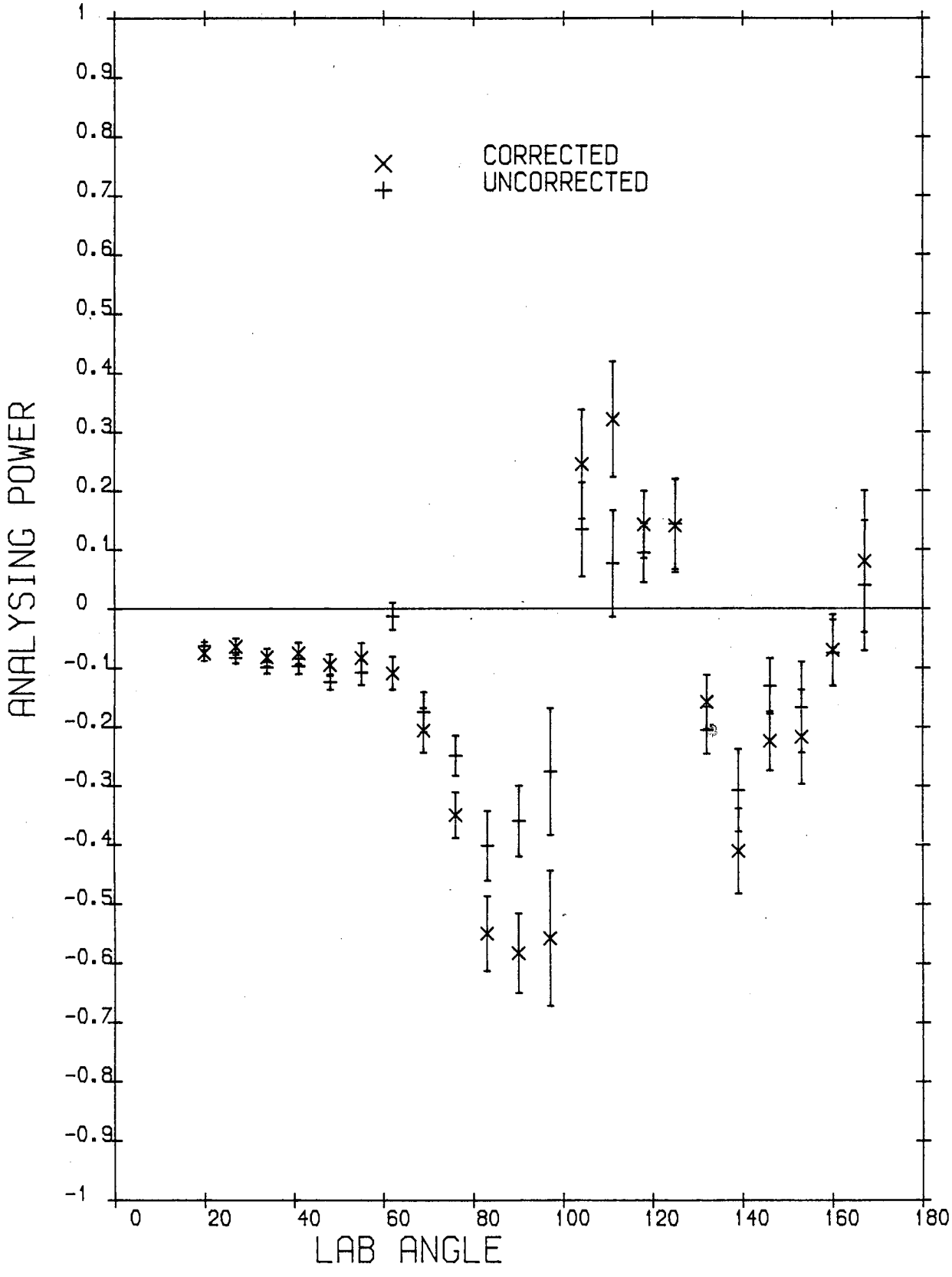
15/01/85 IODINE
CORRECTED
UNCORRECTED
ANALYSING POWER
LAB ANGLE
1
0.9
0.8
0.7
0.6
0.5
0.4
0.3
0.2
0.1
0
-0.1
-0.2
-0.3
-0.4
-0.5
-0.6
-0.7
-0.8
-0.9
-1
0
20
40
60
80
100
120
140
160
180

Figure 5.16.

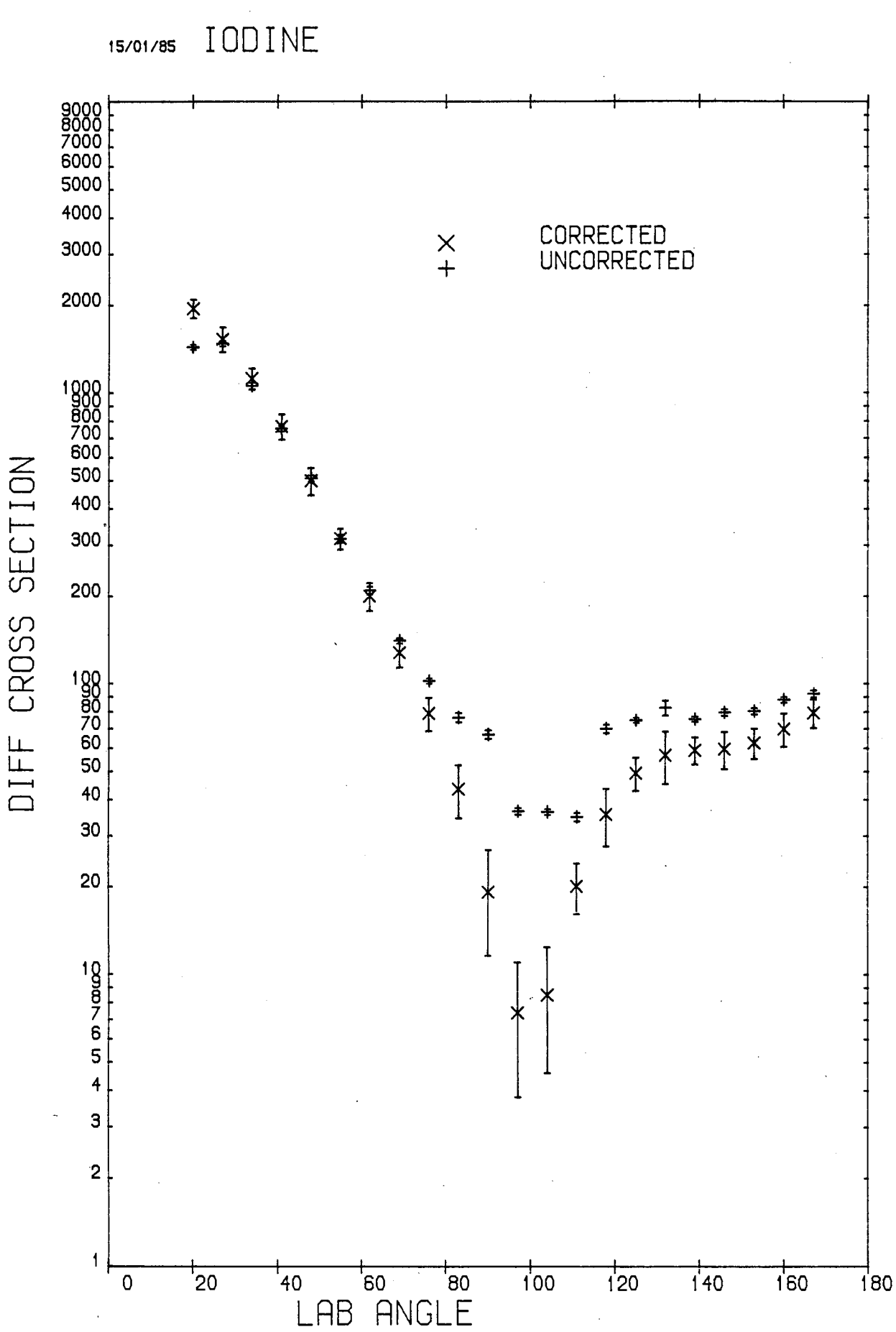
15/01/85 IODINE
CORRECTED
UNCORRECTED
DIFF CROSS SECTION
LAB ANGLE
9000
8000
7000
6000
5000
4000
3000
2000
1000
900
800
700
600
500
400
300
200
100
90
80
70
60
50
40
30
20
10
9
8
7
6
5
4
3
2
1
0
20
40
60
80
100
120
140
160
180

Figure 5.17.

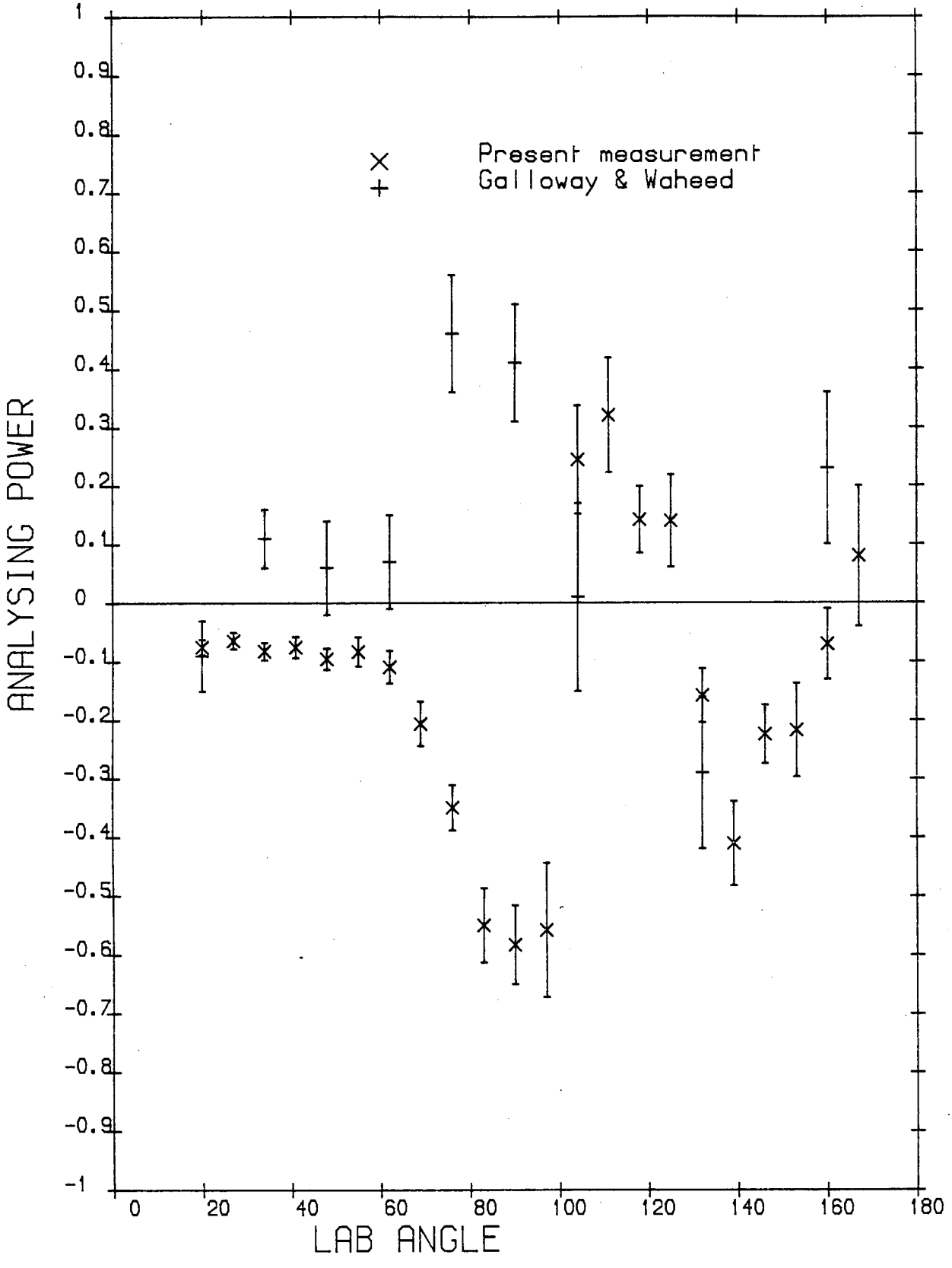
15/01/85 IODINE
Present measurement
Galloway & Waheed
ANALYSING POWER
LAB ANGLE
1
0.9
0.8
0.7
0.6
0.5
0.4
0.3
0.2
0.1
0
-0.1
-0.2
-0.3
-0.4
-0.5
-0.6
-0.7
-0.8
-0.9
-1
0
20
40
60
80
100
120
140
160
180

Figure 5.18.

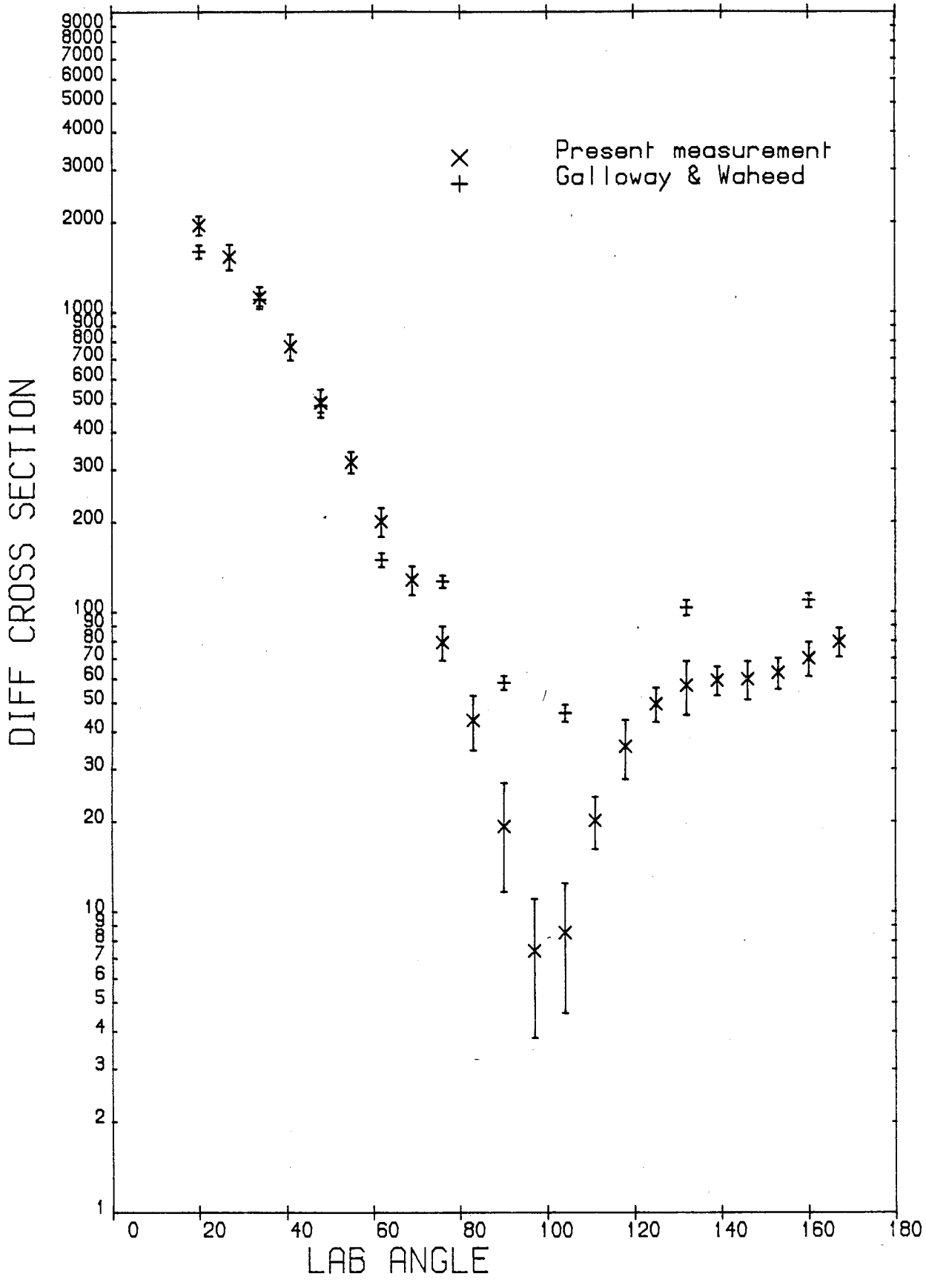
15/01/85 IODINE
Present measurement
Galloway & Waheed
DIFF CROSS SECTION
LAB ANGLE
9000
8000
7000
6000
5000
4000
3000
2000
1000
900
800
700
600
500
400
300
200
100
90
80
70
60
50
40
30
20
10
9
8
7
6
5
4
3
2
1
0
20
40
60
80
100
120
140
160
180

Figure 5.19.

CHAPTER 6

OPTICAL MODEL CALCULATION

6.1 Introduction

The optical model for the scattering of nucleons by nuclei was introduced by Feshbach, Porter and Weisskopf in 1954[4] to explain regular variations in the measured average total neutron cross sections when either the target mass number or the neutron energy is varied. For example, to explain the monotonic decrease of the total cross section with energy as found by Barschall in 1952[123] for neutron energies up to 3.0 MeV.

In the following years this optical model has been applied with remarkable success to analyse a wide body of neutron scattering data, and several global parameter sets have been introduced that give generally excellent fits over a range of neutron energies and target nuclei. The non-local potential of Perey and Buck[24] and its local equivalent of Wilmore and Hodgson[11] and the global potentials of Becchetti and Greenlees[10] are some of the most successful optical potentials. When the optical potential is inserted into the Schrödinger equation which is describing the scattering process, it gives the measured total and reaction cross-sections, together with the differential elastic cross sections and polarisations. The optical model is further of great importance to the applied problems of correlating and estimating neutron cross sections for use in the design of nuclear reactors.

6.2 The Spherical Optical Potential

The central potential of the spherical optical potential in the ELIESE-3[124] program is given as

$$V_c(r) = V_{cr}(r) + i\, W_{ci}(r) \tag{6.1}$$

where $V_{cr}(r)$ is the real part and $W_{ci}(r)$ the imaginary part. The real potential $V_{cr}(r)$ is assumed to have a Woods-Saxon form factor and is represented as

$$V_{cr}(r) = \frac{2\mu}{\hbar^2} V_c \; f_{cr}(r) \tag{6.2}$$

where $f_{cr}(r)$ is the Woods-Saxon form factor and is defined as

$$f_{cr}(r) = \frac{1}{1 + \exp\left(\frac{r - R_o}{a_o}\right)} \tag{6.3}$$

and V_c is the potential strength (or potential well depth) parameter.

The Imaginary potential $W_{ci}(r)$ consists of a nuclear surface part and nuclear interior part, and is expressed as

$$W_{ci}(r) = \frac{2\mu}{\hbar^2} \{W_s f_{cs}(r) + W_i f_{ci}(r)\} \tag{6.4}$$

The form factor of the surface part, $f_{cs}(r)$, is assumed to be derivative Woods-Saxon type and is given as

$$f_{cs}(r) = \frac{4 \exp\left[\frac{(r - R_s)}{b}\right]}{\left[1 + \exp\left[\frac{(r - R_s)}{b}\right]\right]^2} \tag{6.5}$$

The form factor of the interior part, $f_{ci}(r)$, is negligible for neutrons of only a few MeV energy, but it is assumed to be Woods-Saxon form in ELIESE-3 if the interior part of the Imaginary Potential should be taken into account

$$f_{ci}(r) = \frac{1}{1 + \exp\left(\frac{r - R_I}{a_I}\right)} \tag{6.6}$$

The Spin-Orbit potential is assumed to be Thomas-Fermi type and is expressed as

$$V_{so}(r) = \frac{2\mu}{\hbar^2} C_{so} \frac{1}{r} (V_{so} + iW_{so}) \frac{1}{a_{so}} \frac{\exp\left[\frac{r - R_{so}}{a_{so}}\right]}{\left[1 + \exp\left(\frac{r - R_{so}}{a_{so}}\right)\right]^2} \tag{6.7}$$

where C_{so} is given by using the π-meson mass m_π and the velocity of light c:

$$C_{so} = \left(\frac{h}{m_\pi c}\right)^2$$

Radial parameters R_o, R_I, R_s and R_{so} are defined as

$$R_o = r_o A^{1/3} \quad \text{or} \quad r_o(A^{1/3} + A'^{1/3})$$

$$R_I = r_I A^{1/3} \quad \text{or} \quad r_I(A^{1/3} + A^{1/3})$$

$$R_s = r_s A^{1/3} \quad \text{or} \quad r_s(A^{1/3} + A'^{1/3})$$

$$R_{so} = r_{so} A^{1/3} \quad \text{or} \quad r_{so}(A^{1/3} + A'^{1/3})$$

The additional term $(r_i A'^{1/3})$ means radius of the incident particle.

The Imaginary Spin-Orbit term W_{so} is usually taken to be negligible, although an investigation on the effect of this term on the polarisation and cross section is given in Section 6.6

Solution of the Schrödinger equation, using the optical potential leads to the elements of the scattering Matrix (S Matrix), and from these elements the following characteristics can be calculated; total, integrated elastic, integrated absorption, differential shape elastic cross sections and differential polarisations.

In order to establish an energy-averaged behaviour consistent with the concept of the Optical Model, detailed observations, with relatively broad resolutions, extending over the first several MeV of incident-neutron energy is required. Since the apparatus described in the previous chapters has relatively poor energy resolution and the neutron beam has sufficient energy spread, therefore the above requirement is fulfilled for the data collected in this work, which is effectively energy averaged, compared with the average spacing of compound nuclear states at 3.0 MeV neutron energy for the nuclei under investigation in this work. Discrete-level properties of the mass-region studied in this work are reasonably well known to excitations of up to 2 MeV, and occasionally to higher energies[102-122]. The compound nucleus processes can often be explicitly evaluated to several MeV, but recourse must be made to statistical level representations if the calculations are extended to higher energies. The ELIESE-3 programme is capable of calculating compound nucleus cross sections based on the Hauser-Feshbach[125] formalism up to 30 discrete levels. When it was needed to include more than 30 levels, the continuum Band calculation was applied using the programme CINDY[126]. Moldauer level width fluctuation (MLF) correction is included in both

programmes. Therefore inclusion of spins, parities and excitation energies of open reaction channels to the experimental data and optical potential parameters are required in calculations for each isotope of the natural samples. The number of excitation levels involved in calculations for each isotope is already given in Chapter 5.

6.3 The Programme Investigation and Optical Model Analysis of the Data

Although in the previous section the formulation of ELIESE-3 was discussed, there were two programmes available for Optical Model calculation. A combined version of Code SCAT[127] for Optical Model calculation and code CINDY[126] for compound elastic calculation, which will be referred to as ELAST 1B used by J.R.M. Annand[16], and the ELIESE-3[124] programme which performs Optical Model calculations as well as compound elastic. Both programmes are capable of automatic search iterations. A comparison of results from the two programmes was made to find whether one or other is to be preferred.

A set of parameters obtained as giving a Best fit to the differential elastic cross section and analysing power data for the Tin sample, using the ELAST1B programme is given in Table 6.1, set A. This set of parameters were also used with ELIESE-3. The expectation was to observe the same results from both programmes, Figures 6.1 and 6.2 illustrate differential cross sections and analysing powers obtained from the two programmes. A marked difference in analysing power and compound elastic cross sections is observed. The slight difference between the two differential elastic cross section curves is due to a difference in prediction of compound elastic cross section by the two programmes. In fact, both programmes

reproduced exactly the same results for shape elastic cross section and polarisation, which are not included in Figures 6.1 and 6.2. Therefore, since the shape elastic cross sections show no difference it could be suggested that the compound elastic cross section, which is calculated including a continuum band in ELAST1B and for discrete levels in ELIESE-3 is the cause of the discrepancy which is observed.

TABLE 6.1

Parameters	V_c	W_s	V_{so}	r_o	r_s	r_{so}	a_o	b	a_{so}
Set (A)	52.88	2.51	3.99	1.108	1.025	1.279	0.725	0.993	0.589
Set (B)	53.51	2.42	2.98	1.095	1.022	1.292	0.719	0.977	0.559

In order to investigate this effect, a set of parameters (set B, Table 6.1), which was obtained as giving a best fit to the results for the Tin sample using ELIESE-3, was used to calculate for ^{120}Sn compound elastic cross sections due to 23 discrete levels up to 3.0 MeV with three programmes, ELIESE-3, ELAST 1B and CINDY. The same calculation was also performed for 17 discrete levels plus one continuum-band using the ELAST 1B programme. The results for polarisation and elastic differential cross sections are shown in Figures 6.3 and 6.4 respectively. Curves 1 and 2 show the result from the ELAST 1B programme for 23 discrete levels and for 17 levels and a continuum band, respectively. The difference between these two curves might be explained, due to uncertainty in the continuum band calculation. A more striking point is the difference between curve 1 and curve 4 in Fig. 6.4. Curve 4 is the compound elastic

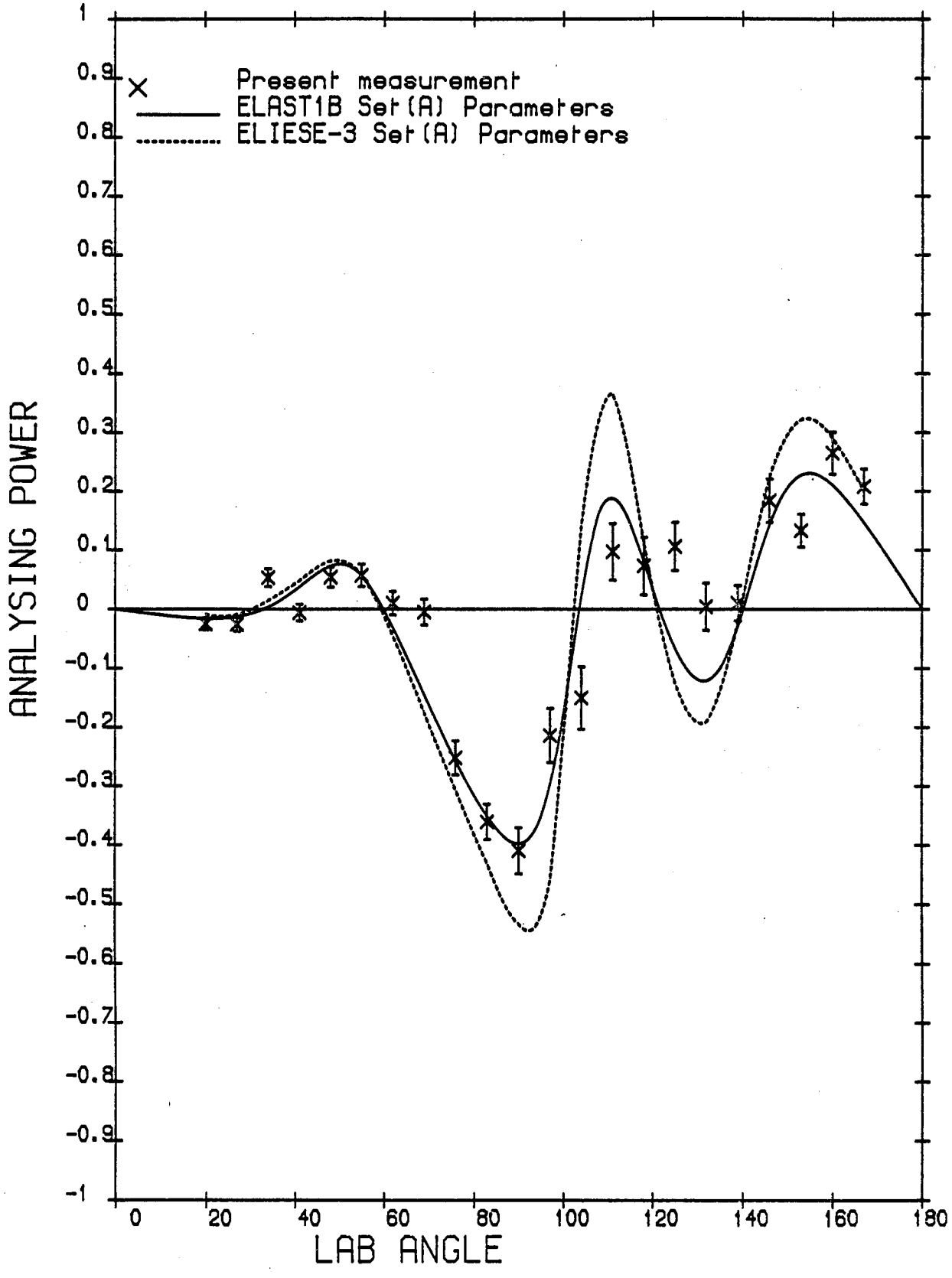
21/01/85 Tin
Present measurement
ELAST1B Set(A) Parameters
ELIESE-3 Set(A) Parameters
ANALYSING POWER
LAB ANGLE
1
0.9
0.8
0.7
0.6
0.5
0.4
0.3
0.2
0.1
0
-0.1
-0.2
-0.3
-0.4
-0.5
-0.6
-0.7
-0.8
-0.9
-1
0
20
40
60
80
100
120
140
160
180

Figure 6.1.

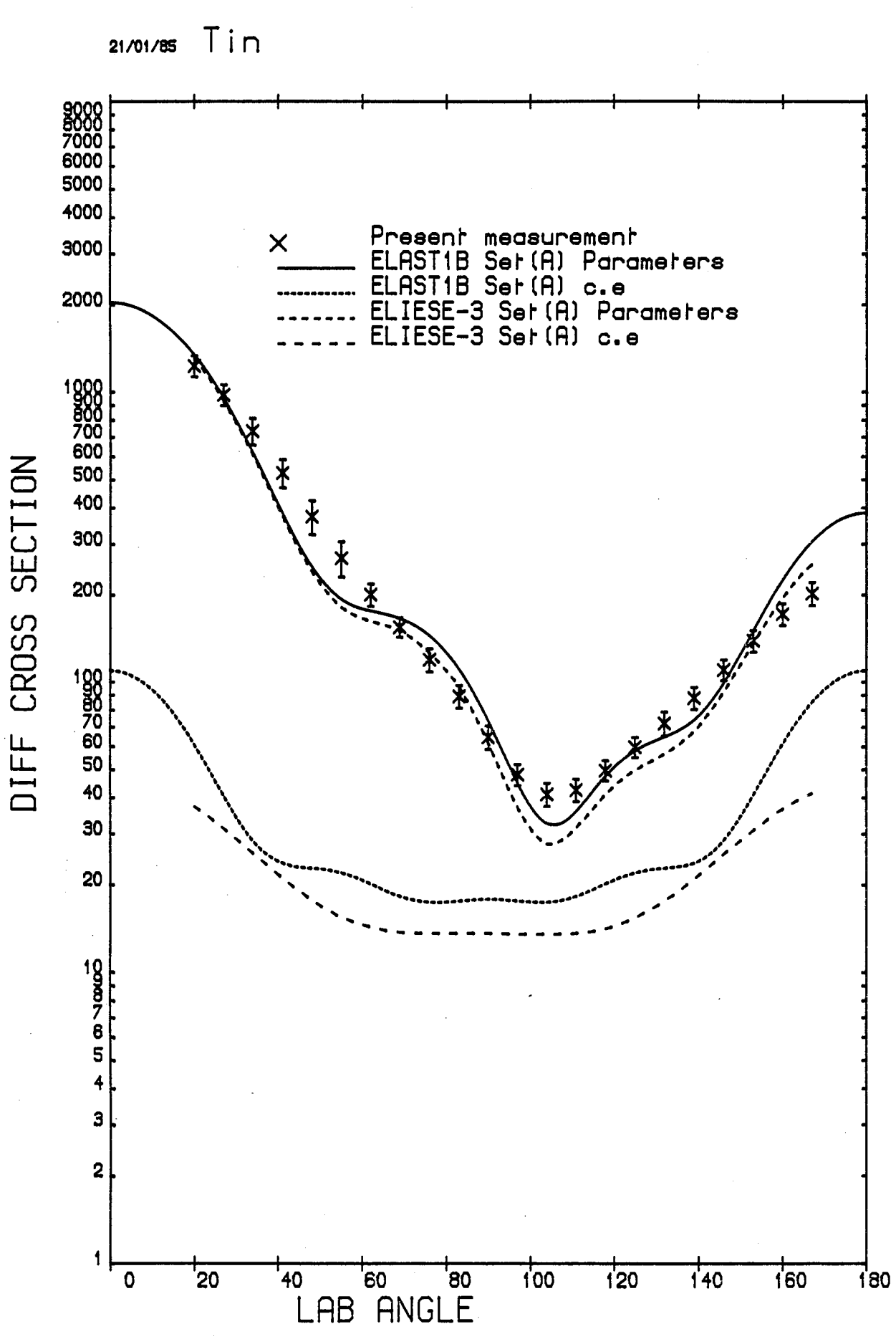
21/01/85 Tin
Present measurement
ELAST1B Set(A) Parameters
ELAST1B Set(A) c.e
ELIESE-3 Set(A) Parameters
ELIESE-3 Set(A) c.e
DIFF CROSS SECTION
LAB ANGLE
0
20
40
60
80
100
120
140
160
180

Figure 6.2.

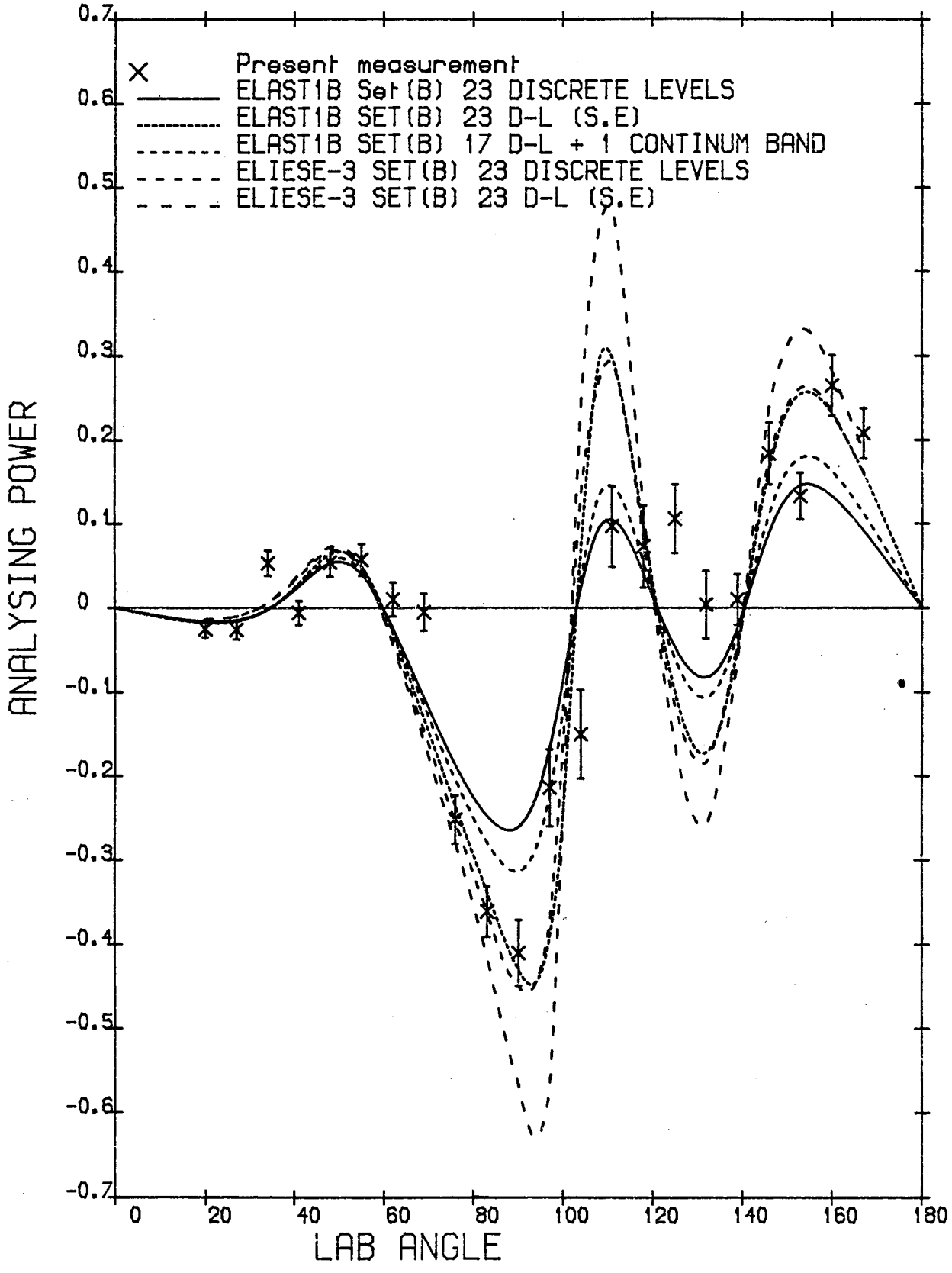
22/01/85 Tin
Present measurement
ELAST1B Set(B) 23 DISCRETE LEVELS
ELAST1B SET(B) 23 D-L (S.E)
ELAST1B SET(B) 17 D-L + 1 CONTINUM BAND
ELIESE-3 SET(B) 23 DISCRETE LEVELS
ELIESE-3 SET(B) 23 D-L (S.E)
ANALYSING POWER
LAB ANGLE
0.7
0.6
0.5
0.4
0.3
0.2
0.1
0
-0.1
-0.2
-0.3
-0.4
-0.5
-0.6
-0.7
0
20
40
60
80
100
120
140
160
180

Figure 6.3.

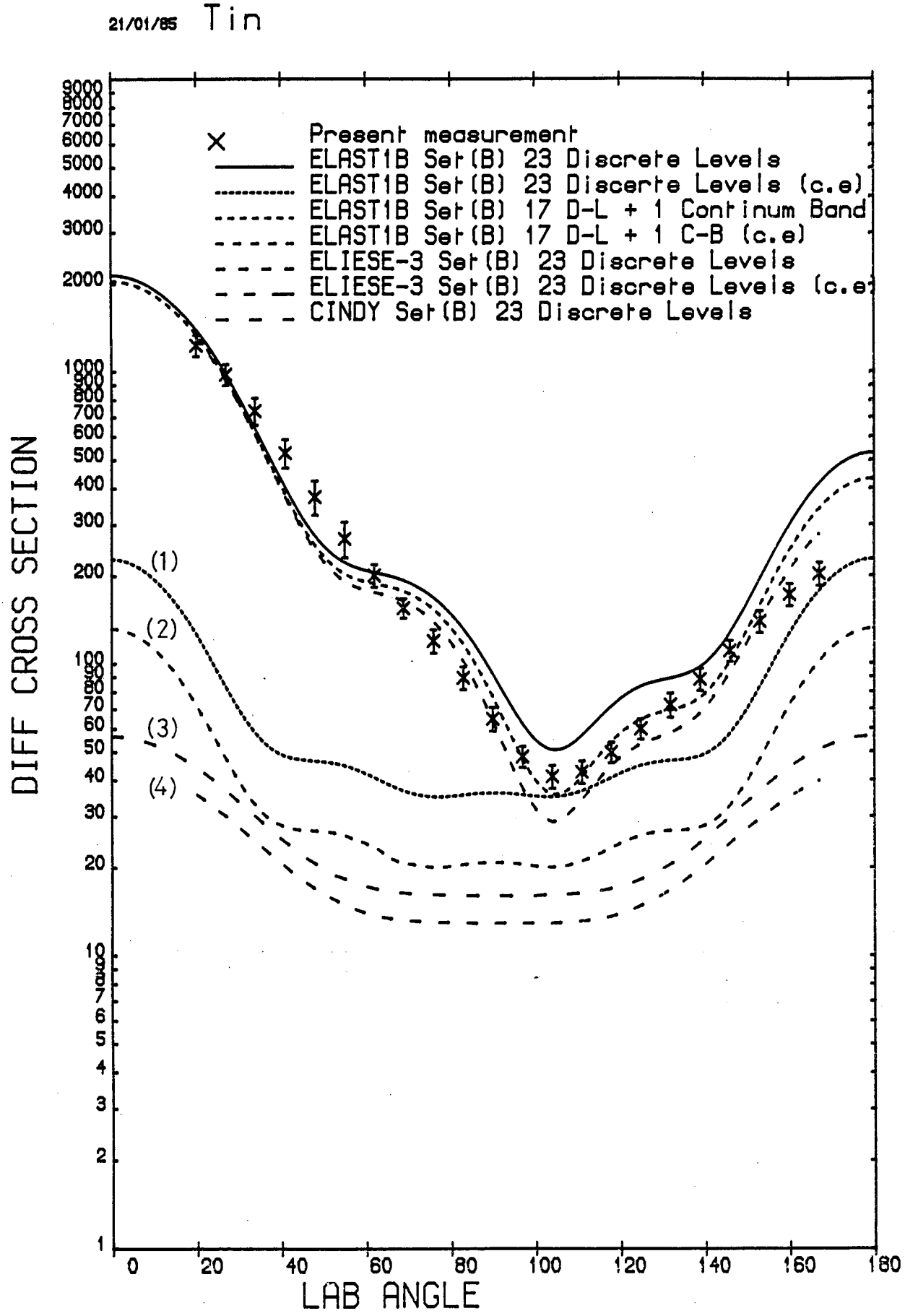
21/01/85 Tin
Present measurement
ELAST1B Set(B) 23 Discrete Levels
ELAST1B Set(B) 23 Discrete Levels (c.e)
ELAST1B Set(B) 17 D-L + 1 Continum Band
ELAST1B Set(B) 17 D-L + 1 C-B (c.e)
ELIESE-3 Set(B) 23 Discrete Levels
ELIESE-3 Set(B) 23 Discrete Levels (c.e
CINDY Set(B) 23 Discrete Levels
DIFF CROSS SECTION
LAB ANGLE
(1)
(2)
(3)
(4)

Figure 6.4.

cross section taking account of 23 discrete levels obtained from the ELIESE-3 programmes, curve 1 being the comparable ELAST 1B result. Curve 3 is the result from the CINDY programme for 23 discrete levels. Curve 3 is very close to curve 4, but curve 1 for the same kind of calculation is far from being acceptable, either quantitatively or regarding the shape of the compound elastic cross section distribution.

It is concluded that the combined (SCAT + CINDY) ELAST 1B programme is not capable of calculating reasonable results for compound elastic cross sections, whether including a continuum band or only discrete levels. In the CINDY programme the assumption is made that $a_o = a_{so}$ and $r_o = r_{so}$, while there is no such assumption in ELIESE-3.

Introducing the same assumption in ELIESE-3, did not produce a considerable change in the results. Therefore it might be concluded that the difference between curves 3 and 4 in Fig. 6.4 be due to different formulations used in the ELIESE-3[128] and CINDY[126] programmes.

In order to make sure that the ELIESE-3 programme is capable of calculating correct values for shape elastic cross sections, compound elastic cross sections and inelastic cross sections due to decay of the compound nucleus, the following calculations are made.

Elastic and inelastic cross sections for Vanadium (^{51}V) for 2.47, 3.0, 3.49 and 4.0 MeV neutrons are calculated according to the Hauser-Feshbach Formalism, corrected for the Moldauer level fluctuations, utilizing Holmqvist et al.[129] parameters given in Table 6.2 and compared with Holmqvist et al.[129] results. Figures 2, 3 and 5 of reference (129). The ELIESE-3 programme produced

exactly the same results as reported by Holmqvist et al.[129]. Figures 6.5 - 6.9 illustrate these results.

TABLE 6.2

E_n(MeV)	2.47	3.00	3.49	4.0
V_c	5.13	47.4	48.6	48.1
W_s	8.40	8.40	8.41	8.30
r_o	1.19	1.26	1.24	1.25
r_s	1.21	1.23	1.22	1.21
a_o	0.65	0.66	0.66	0.66
b	0.48	0.48	0.48	0.48
V_{so}	8.0	8.0	8.0	8.0

Therefore being convinced that ELIESE-3 is the programme which produces correct results for all kind of cross sections and polarisation, a systematic search was performed to obtain the best fit parameters for each sample. The search was carried out first for single parameters, then groups of three, including depth, radius and diffuseness of each part of the Optical Model Potential, then groups of three, including (V_c, W_s, V_{so}), (R_o, R_s, R_{so}) and (a_o, b, a_{so}). Then different groups of six parameters and finally all parameters were searched together to trim the results.

The above mentioned procedure of obtaining the optimum fit of the experimental data to the prediction of the theory was carried out by allowing an automatic search routine to vary the parameters

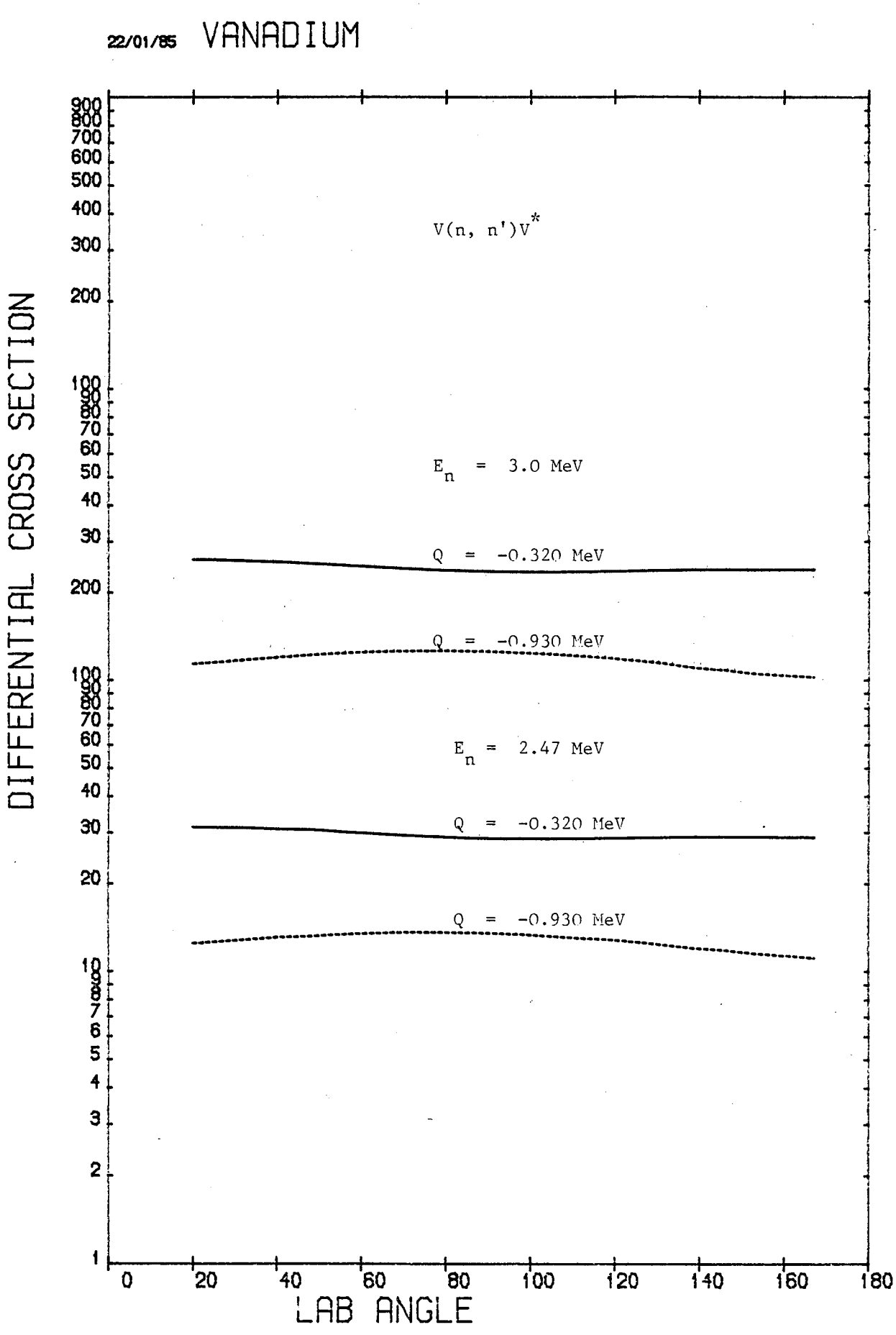
22/01/85 VANADIUM
DIFFERENTIAL CROSS SECTION
LAB ANGLE
V(n, n')V*
E_n = 3.0 MeV
Q = -0.320 MeV
Q = -0.930 MeV
E_n = 2.47 MeV
Q = -0.320 MeV
Q = -0.930 MeV
900
800
700
600
500
400
300
200
100
90
80
70
60
50
40
30
20
10
9
8
7
6
5
4
3
2
1
0
20
40
60
80
100
120
140
160
180

Figure 6.5.

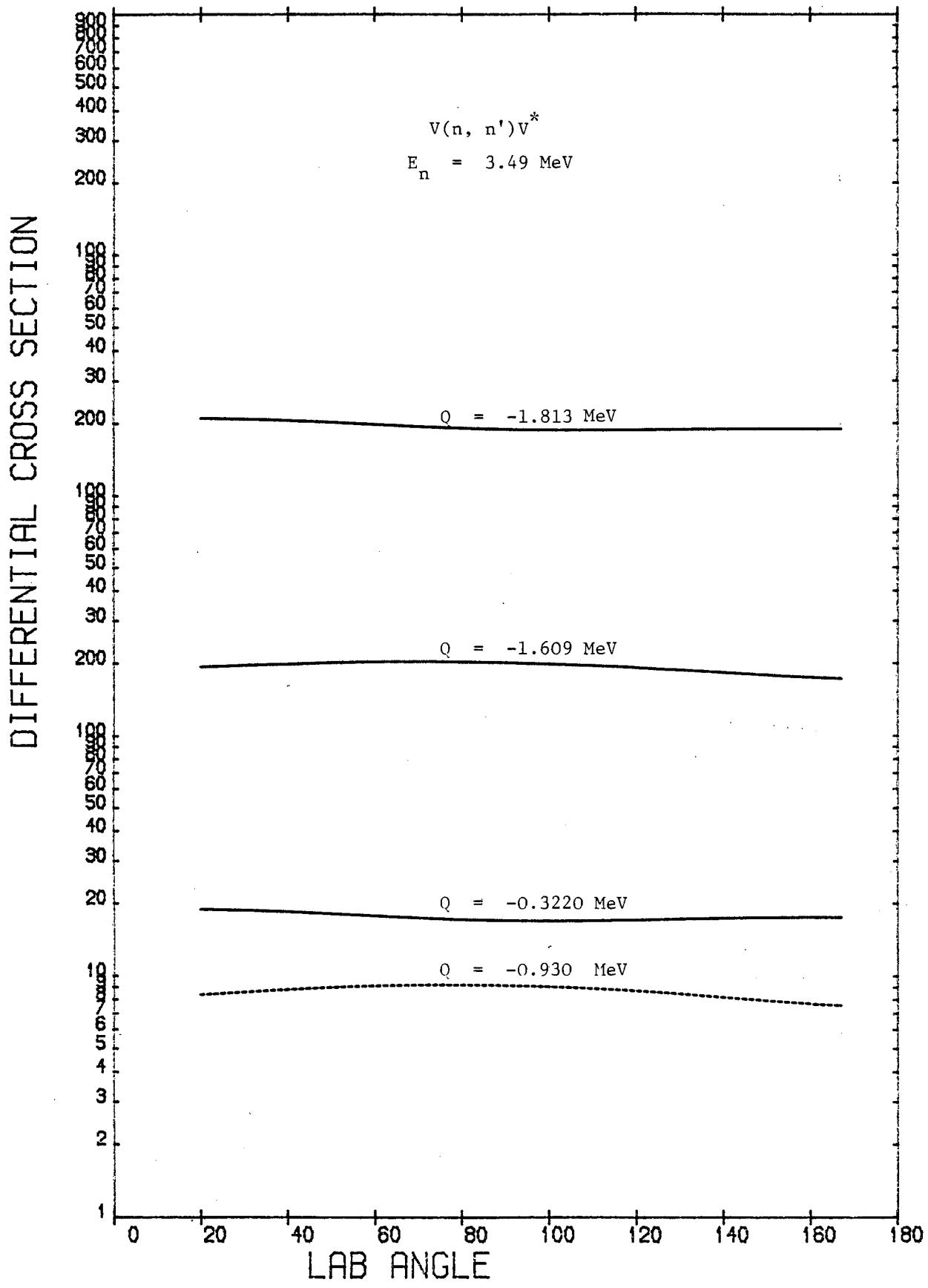
22/01/85 VANADIUM
V(n, n')V*
E_n = 3.49 MeV
Q = -1.813 MeV
Q = -1.609 MeV
Q = -0.3220 MeV
Q = -0.930 MeV
DIFFERENTIAL CROSS SECTION
LAB ANGLE
0
20
40
60
80
100
120
140
160
180

Figure 6.6.

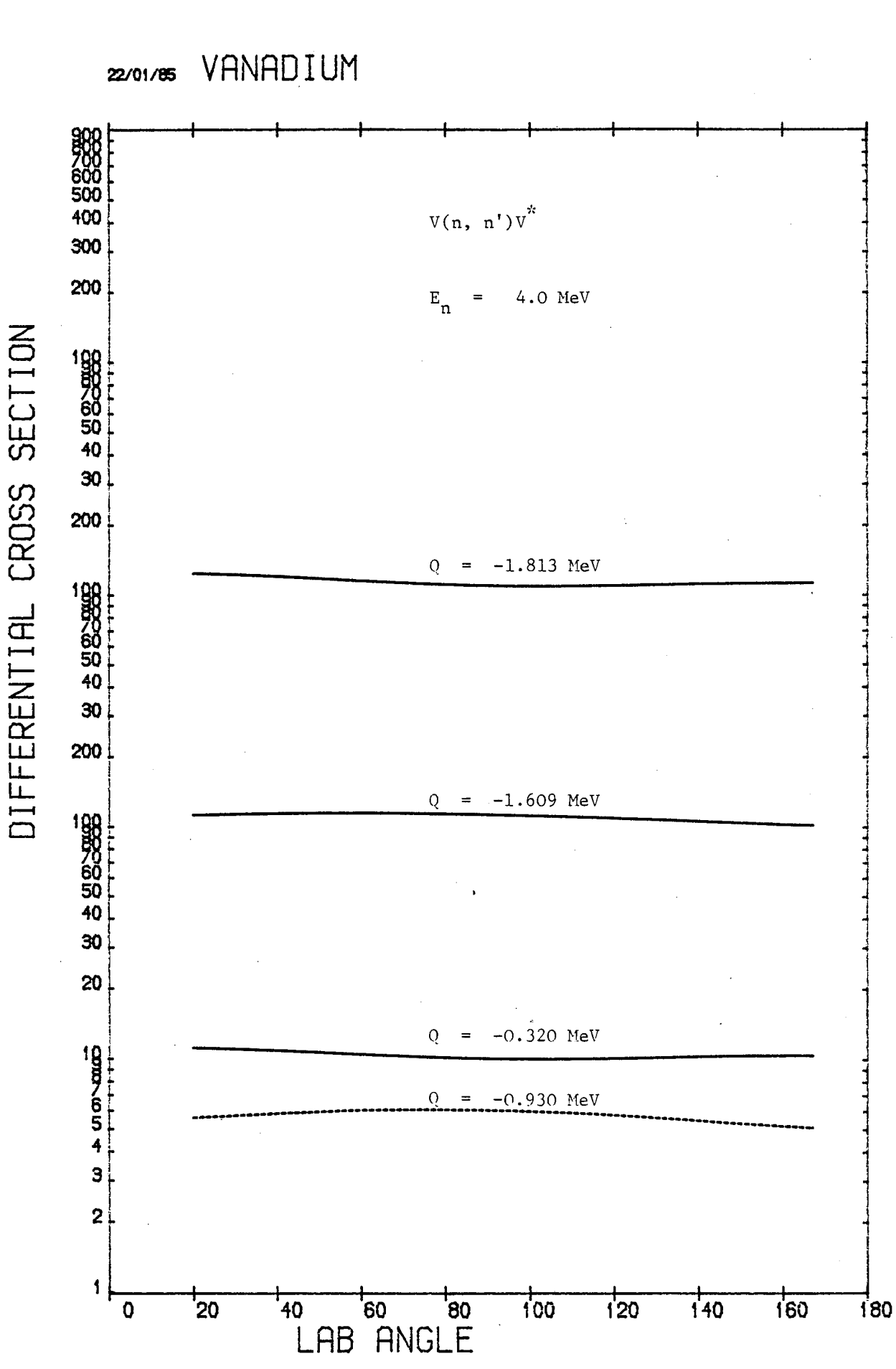
22/01/85 VANADIUM
V(n, n')V*
E_n = 4.0 MeV
Q = -1.813 MeV
Q = -1.609 MeV
Q = -0.320 MeV
Q = -0.930 MeV
DIFFERENTIAL CROSS SECTION
LAB ANGLE
0
20
40
60
80
100
120
140
160
180

Figure 6.7.

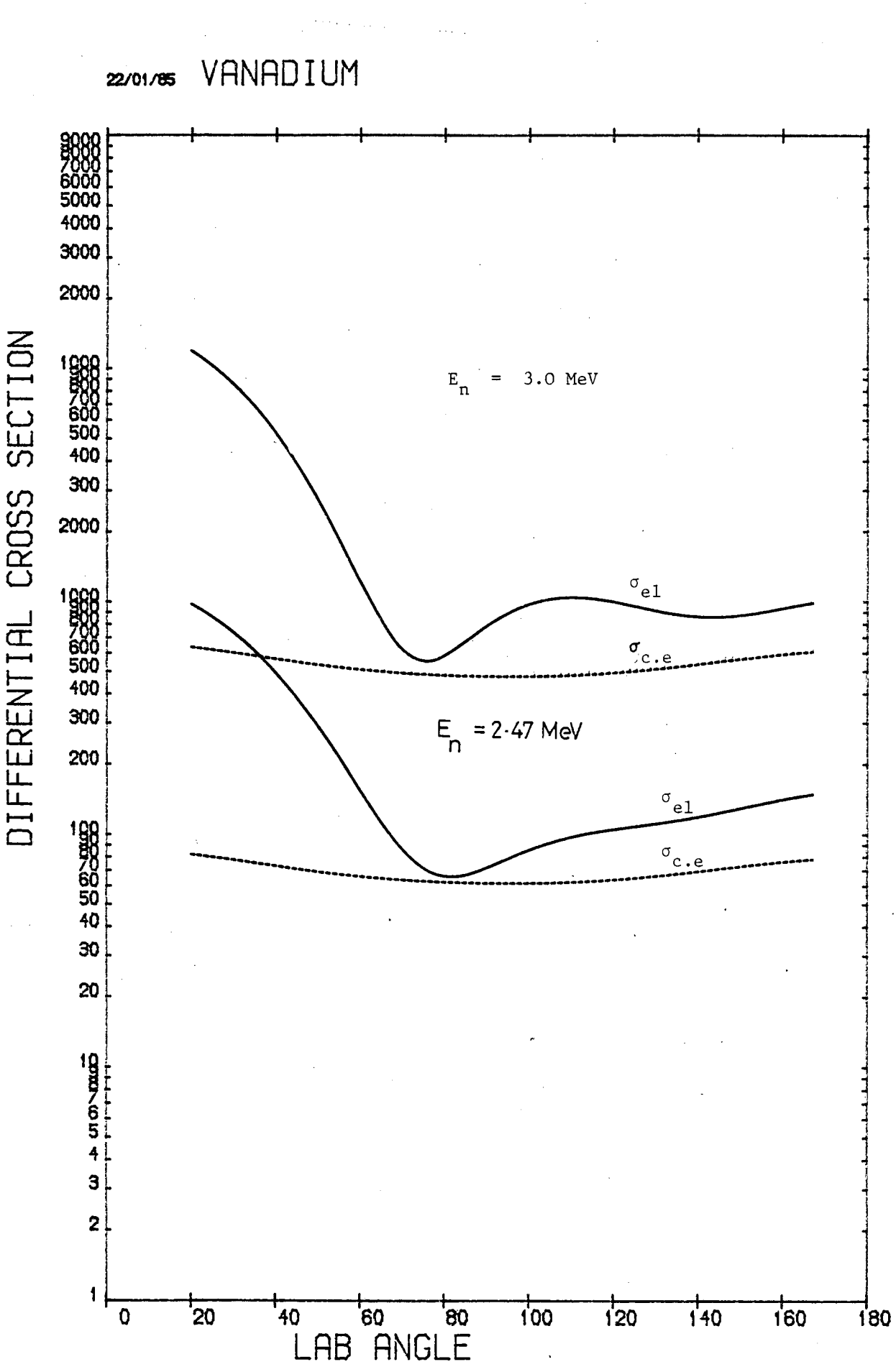
22/01/85 VANADIUM
DIFFERENTIAL CROSS SECTION
LAB ANGLE
E_n = 3.0 MeV
σ_el
σ_c.e
E_n = 2·47 MeV
σ_el
σ_c.e
0
20
40
60
80
100
120
140
160
180

Figure 6.8.

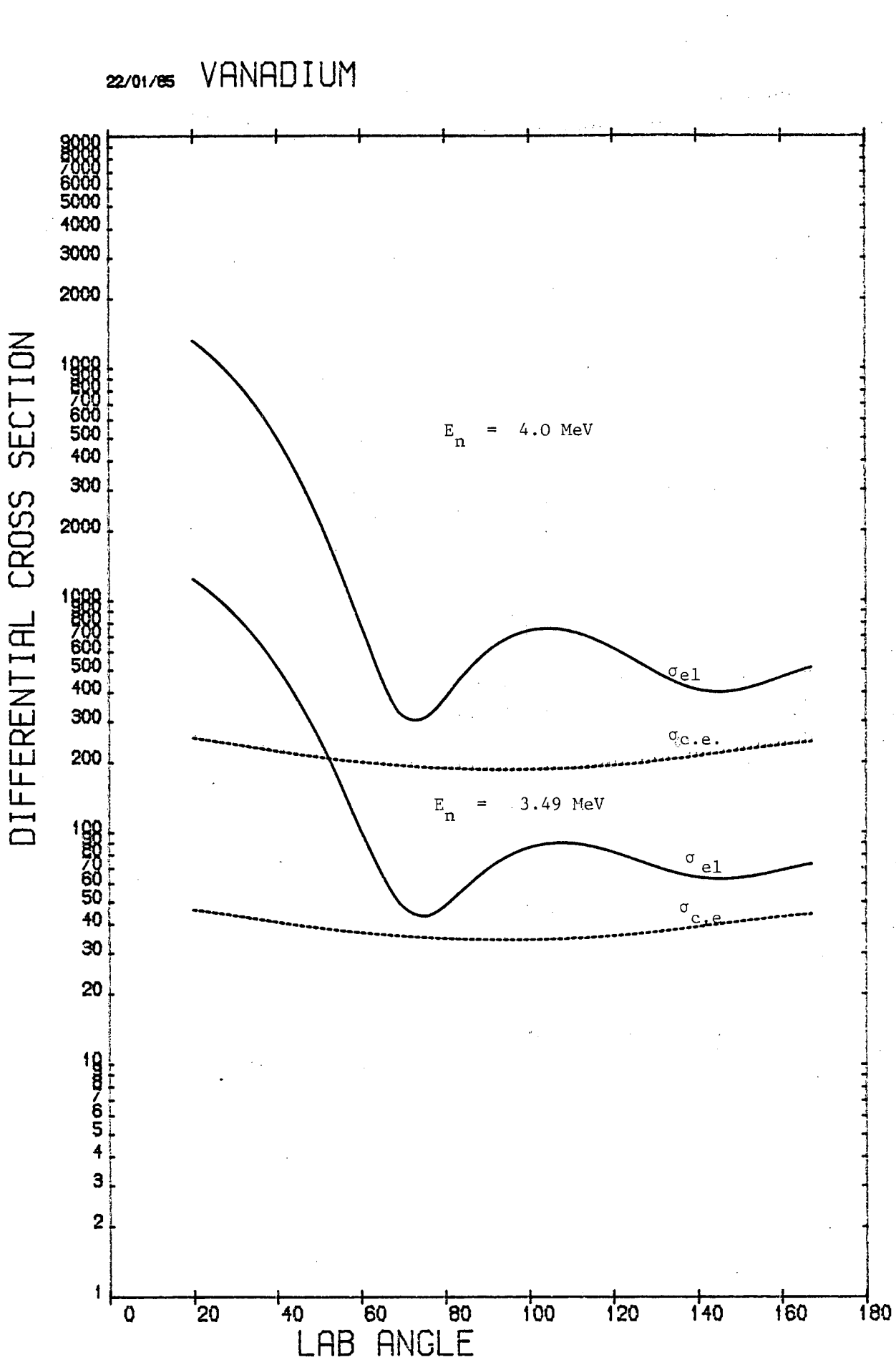
22/01/85 VANADIUM
DIFFERENTIAL CROSS SECTION
LAB ANGLE
E n = 4.0 MeV
σel
σc.e.
E n = 3.49 MeV
σ el
σ c.e
0
20
40
60
80
100
120
140
160
180

Figure 6.9.

so as to minimize the quantity

$$X_{\sigma}^{2} = \frac{1}{n} \sum_{n} \left[\frac{(\sigma_{exp} - \sigma_{cal})}{\Delta\sigma_{exp}} \right]^{2}$$

or

$$X_{P}^{2} = \frac{1}{n} \sum_{n} \left[\frac{(P_{exp} - P_{cal})}{\Delta P_{exp}} \right]^{2}$$

or

$$X_{Comb}^{2} = \left[\frac{(X_{P}^{2} + X_{\sigma}^{2})}{2} \right]$$

where σ_{exp} and P_{exp} are the measured cross sections and polarisations at angle θ_i, $\Delta\sigma_{exp}$ and ΔP_{exp} are the corresponding errors associated with σ_{exp} and P_{exp}, respectively, and σ_{cal} and P_{cal} are the theoretical predicted cross sections and polarisations. Comparison of X^2 for a set of experimental data shows the relative success of different optical potentials introduced to calculate cross sections and polarisation. A summary of global potentials and parameters suggested previously for particular nuclei used in the present work are presented in Table 6.3. The potential well depths are in MeV and radius and diffuseness parameters in fm.

There are well known ambiguities in optical potential searches relating V_c and r_o and also W_s and b in the forms $V_c \cdot r_o^n$ (n usually equal to 2) $\approx$ constant and $W_s \cdot b \approx$ constant. Because of these ambiguities of the optical model potential, it is difficult to make systematic investigations of the potential depths with different geometric parameters. This can be avoided by studying the energy variation of the volume integrals per nucleon of the real and imaginary potential parts as well as the r.m.s. radius[131].

TABLE 6.3

Optical Potential Parameters

Rosen et al. (32)	V_c: 49.03-0.33E	W_s: 5.75	V_{so}: 5.5
	r_o: 1.25	r_s: 1.25	r_{so}: 1.2
	a_o: 0.65	b : 0.75	a_{so}: 0.65
Becchetti and Greenlees (10)	V_c: 56.3-0.32E -24(N-Z)/A	W_s: 13-0.25E -12(N-Z)/A	V_{so}: 6.2
	r_o: 1.17	r_s: 1.26	r_{so}: 1.01
	a_o: 0.75	b : 0.58	a_{so}: 0.75
Tanaka (46)	V_c: 51.85-0.33E -24(N-Z)/A	W_s: $2.55\sqrt{E}$	V_{so}: 7.0
	r_o: 1.25	r_s: 1.25	r_{so}: 1.25
	a_i: 0.65	b : 0.48	a_{so}: 0.65
Smith et al. (44)	V_c: 52.58-0.3E -30(N-Z)/A	W_s: 11.7-25(N-Z)/A $-1.8\cos(\frac{2\pi(A-90)}{29})$	V_{so}: 6.0
	r_o: 1.131+0.00107A	r_s: 2.028-0.00683A	r_{so}: r_o
	a_o: 1.203-0.00511A	b : -0.1061 +0.005551A	a_{so}: a_o
Zijp and Jonker (40)	V_c: 44.5 (Cd)	W_s: 10.1 (Cd)	V_{so}: 8.0
	: 47.2 (Sn)	: 10.5 (Sn)	
	: 45.8 (Sb)	: 11.4 (Sb)	
	: 46.8 (Te)	: 7.9 (Te)	
	r_o: 1.25	r_s: 1.25	r_{so} : 1.12
	a_o: 0.65	b : 0.48	a_{so} : 0.65

Gupta et al. (39)	V_c : 46.0	W_s : 7.6	V_{so}: 7.2
	r_o : 1.265	r_s : 1.24	r_{so}: 1.265
	a_o : 0.66	b : 0.48	a_{so}: 0.66
Strizhak et al. (130)	V_c : 47.5 (Cd)	W_s : 14.8 (Cd)	V_{so}: 10.0
	: 44.8 (Sn)	: 4.2 (Sn)	
	: 50.0 (Sb)	: 7.0 (Sb)	
	: 49.0 (Te)	: 4.5 (Te)	
	r_o : 1.25	r_s : 1.25	r_{so}: 1.25
	a_o : 0.65	b : 0.98	a_{so}: 0.65
Gorlov et al. (34)	V_c : $50(1 - \frac{N-Z}{3A})$	W_s : 8.5	V_{so}: ≈ 0.17
	r_o : 1.25	r_s : 1.25	r_{so}: 1.25
	a_o : 0.65	b : 0.98	a_{so}: 0.65
Galloway and Waheed (I) (42)	V_c : 47.06	W_s : 7.43	V_{so}: 5.50
	r_o : 1.25	r_s : 1.25	r_{so}: 1.25
	a_o : 0.62	b : 0.56	a_{so}: 0.31

The volume integral per nucleon is defined by

$$\left(\frac{J}{A}\right) = -\frac{1}{A}\int V(r)\, d^3r$$

and the r.m.s. radius given by

$$\langle r^2 \rangle = \frac{\int V(r) r^2 d^3r}{\int V(r) d^3r}$$

these integrals can be simplified as

$$\left(\frac{J}{A}\right)_V = \frac{4}{3}\pi\, r_o^3\, V_c \left[1 + \left(\frac{ra_o}{R_o}\right)^2\right]$$

$$\left(\frac{J}{A}\right)_W = \frac{16\pi R_s^2}{A}\, b\, W_s \left[1 + \frac{1}{3}\left(\frac{\pi b}{R_s}\right)^2\right]$$

$$\langle r_o^2 \rangle^{\frac{1}{2}} = \left[\frac{1}{5}\left(3R_o^2 + 7\pi^2 a_o^2\right)\right]^{\frac{1}{2}}$$

The values calculated for these integrals are given in Table 6.10.

The observed elastic polarisation $P_{el}(\theta)$ at each angle can be represented by

$$P_{el}(\theta) = \frac{[\sigma^{(+)}_{s.e}(\theta) + \sigma^{(+)}_{c.e}(\theta)] - [\sigma^{(-)}_{s.e}(\theta) + \sigma^{(-)}_{c.e}(\theta)]}{[\sigma_{s.e}(\theta) + \sigma_{c.e}(\theta)]}$$

An important characteristic of angular distributions calculated with the statistical model is the symmetry about 90° scattering angle. The symmetry is a consequence of the independent hypothesis for the formation and decay of the compound nucleus in the Hauser-Feshbach model. Therefore if this assumption is valid, the compound elastic scattering is unpolarised so that the above equation reduces to

$$P_{el}(\theta) = \frac{\overset{(+)}{\sigma}_{se}(\theta) - \overset{(-)}{\sigma}_{se}(\theta)}{(\sigma_{se}(\theta) + \sigma_{ce}(\theta))}$$

the model calculations predict the shape elastic polarisation $P_{se}(\theta)$ which is represented by

$$P_{s.e}(\theta) = \frac{\overset{(+)}{\sigma}_{se}(\theta) - \overset{(-)}{\sigma}_{se}(\theta)}{\sigma_{se}(\theta)}$$

Hence, the relation between observed and shape elastic polarisation is as follows

$$P_{el}(\theta) = \left[\frac{\sigma_{se}(\theta)}{\sigma_{se}(\theta) + \sigma_{ce}(\theta)}\right] P_{se}(\theta)$$

Therefore, in general, the observed polarisation is less than the pure shape elastic polarisation.

6.4 The Optical Model Calculations

6.4.1 Cadmium

The optical potentials of Becchetti and Greenlees, Rosen et al., Smith et al. and Zijp and Jonker were tried for Cadmium. The relative success of these potentials and the Best Fit parameters obtained are summarised in Table 6.4, and the predictions of the most successful are compared with the present data in Figures 6.10 (analysing power) and 6.12 (differential cross section). The Best fit parameters are compared with present measurement in Figures 6.11 and 6.13. The Best fit parameters reproduce the shape of differential cross section and analysing power quite well, although they tend to underestimate the analysing power at forward angles.

TABLE 6.4

Cadmium: Quality of Optical Model Fit

Potential	X^2_{comb}	X^2_P	X^2_σ
Best Fit	9.42	13.73	5.12
Becchetti and Greenless	34.19	56.24	12.14
Rosen et al.	34.31	54.73	13.90
Smith et al.	59.18	112.95	5.41
Zijp and Jonker	76.34	148.15	4.53

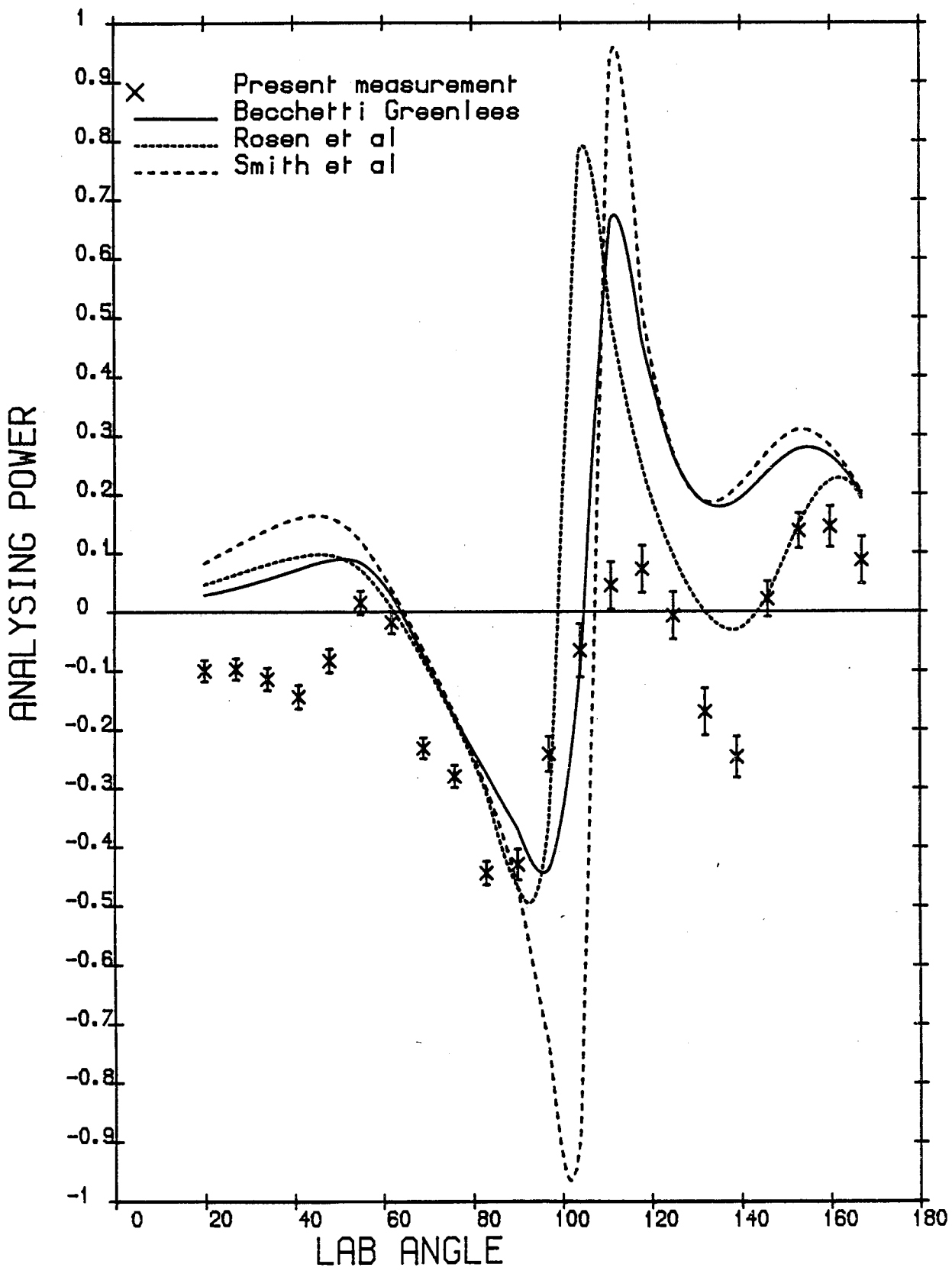
18/01/85 CADMIUM
Present measurement
Becchetti Greenlees
Rosen et al
Smith et al
ANALYSING POWER
LAB ANGLE
1
0.9
0.8
0.7
0.6
0.5
0.4
0.3
0.2
0.1
0
-0.1
-0.2
-0.3
-0.4
-0.5
-0.6
-0.7
-0.8
-0.9
-1
0
20
40
60
80
100
120
140
160
180

Figure 6.10.

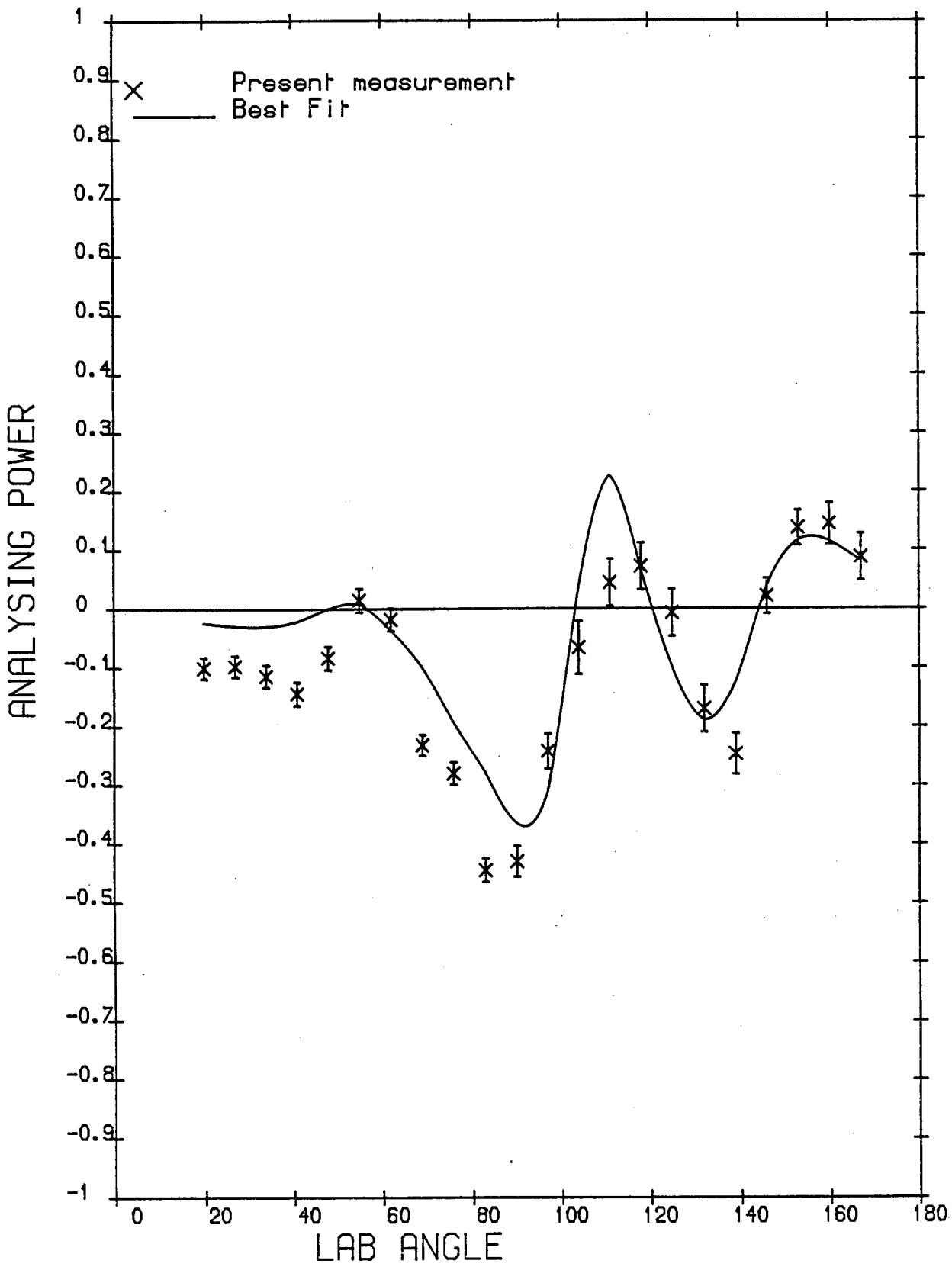
18/01/85 CADMIUM
Present measurement
Best Fit
ANALYSING POWER
LAB ANGLE
1
0.9
0.8
0.7
0.6
0.5
0.4
0.3
0.2
0.1
0
-0.1
-0.2
-0.3
-0.4
-0.5
-0.6
-0.7
-0.8
-0.9
-1
0
20
40
60
80
100
120
140
160
180

Figure 6.11.

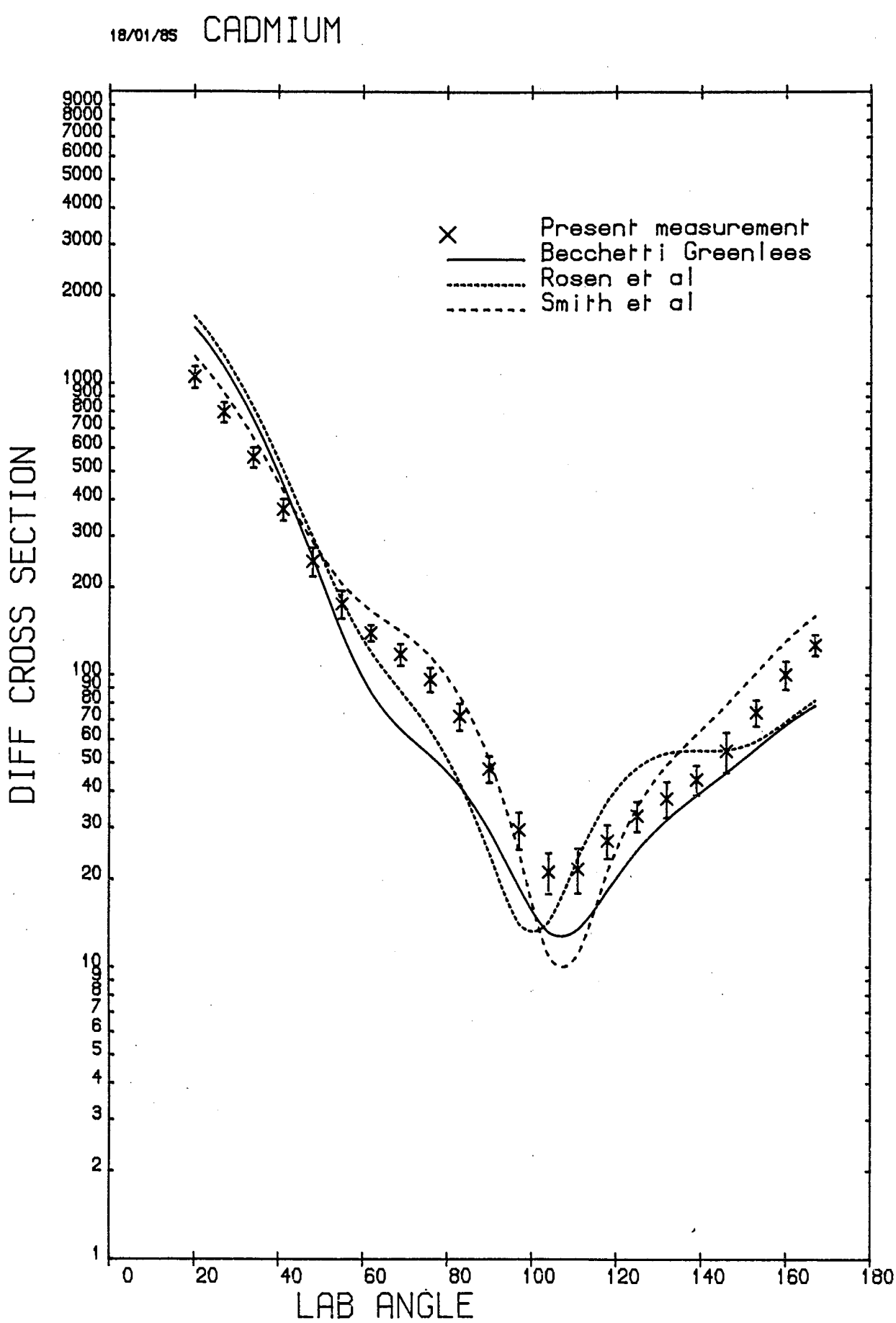
18/01/85 CADMIUM
DIFF CROSS SECTION
LAB ANGLE
Present measurement
Becchetti Greenlees
Rosen et al
Smith et al
9000
8000
7000
6000
5000
4000
3000
2000
1000
900
800
700
600
500
400
300
200
100
90
80
70
60
50
40
30
20
10
9
8
7
6
5
4
3
2
1
0
20
40
60
80
100
120
140
160
180

Figure 6.12.

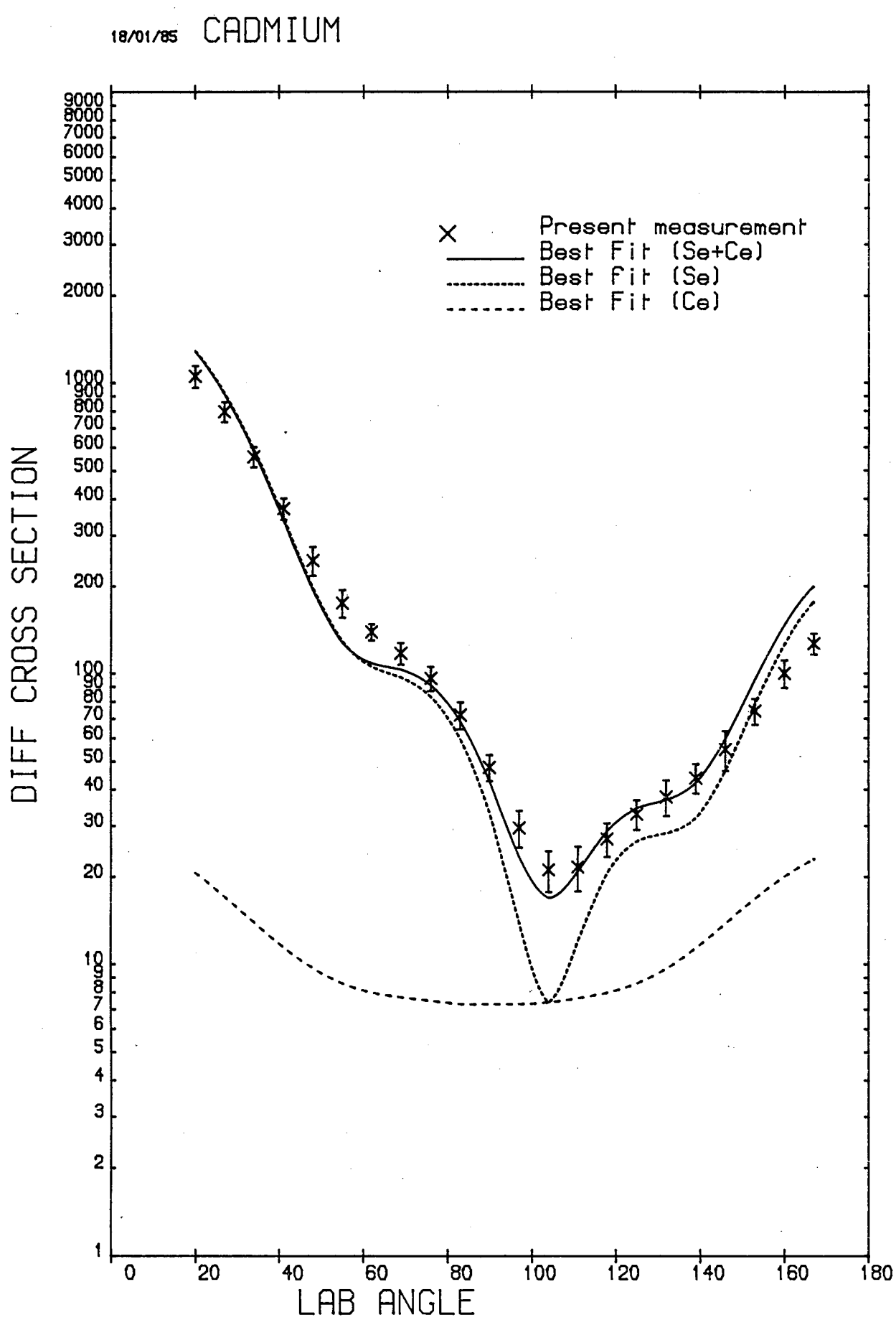
18/01/85 CADMIUM
DIFF CROSS SECTION
LAB ANGLE
Present measurement
Best Fit (Se+Ce)
Best Fit (Se)
Best Fit (Ce)
9000
8000
7000
6000
5000
4000
3000
2000
1000
900
800
700
600
500
400
300
200
100
90
80
70
60
50
40
30
20
10
9
8
7
6
5
4
3
2
1
0
20
40
60
80
100
120
140
160
180

Figure 6.13.

6.4.2 Tin

A summary of the quality of fit for various potentials used with Tin is presented in Table 6.5. Figures 6.14 and 6.15 show the predictions of the most successful potential parameters with the present analysing power data, while the predictions of the most successful are compared with the present differential cross section data in Figures 6.16 and 6.17. The potentials of Strizhak, Gupta et al. and Zijp and Jonker reproduce the shape of analysing power and differential cross section rather poorly, and overestimate the magnitude of analysing power at most angles. None of the potentials tried give the same sign for the forward angles. The Best fit potential reproduces the analysing power and the differential cross section quite well.

TABLE 6.5

Tin: Quality of Optical Model Fit

Potential	X^2_{Comb}	X^2_P	X^2_σ
Best Fit	7.20	9.85	4.55
Smith et al.	21.90	26.88	17.04
Rosen et al.	22.97	29.18	16.76
Zijp and Jonker	29.70	44.70	14.70
Strizhak et al.	32.13	51.95	12.32
Gupta et al.	42.36	76.90	7.83
Tanaka	52.42	101.09	3.75
Becchetti and Greenlees	79.41	123.44	35.39

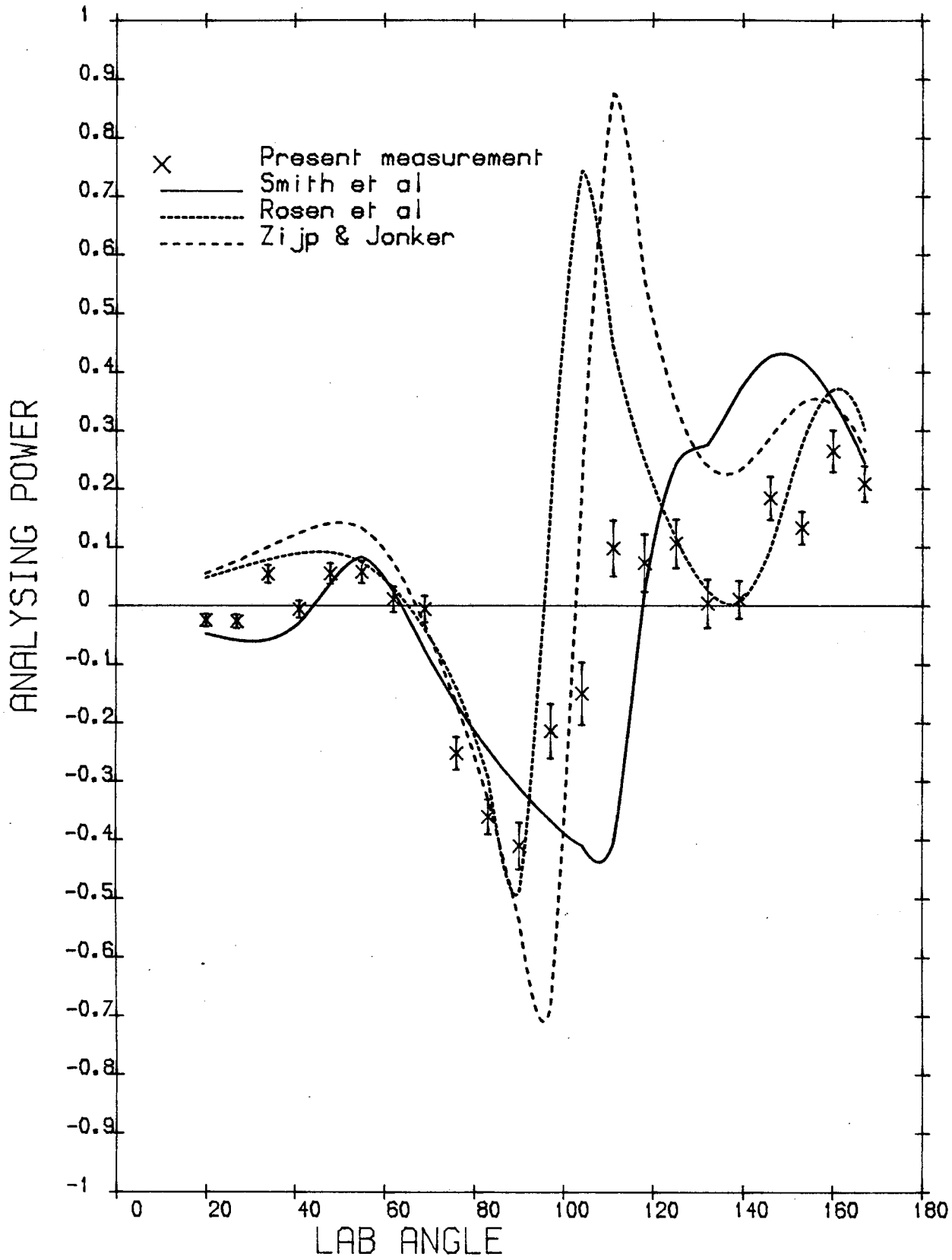
30/08/84 TIN
Present measurement
Smith et al
Rosen et al
Zijp & Jonker
ANALYSING POWER
LAB ANGLE
1
0.9
0.8
0.7
0.6
0.5
0.4
0.3
0.2
0.1
0
-0.1
-0.2
-0.3
-0.4
-0.5
-0.6
-0.7
-0.8
-0.9
-1
0
20
40
60
80
100
120
140
160
180

Figure 6.14.

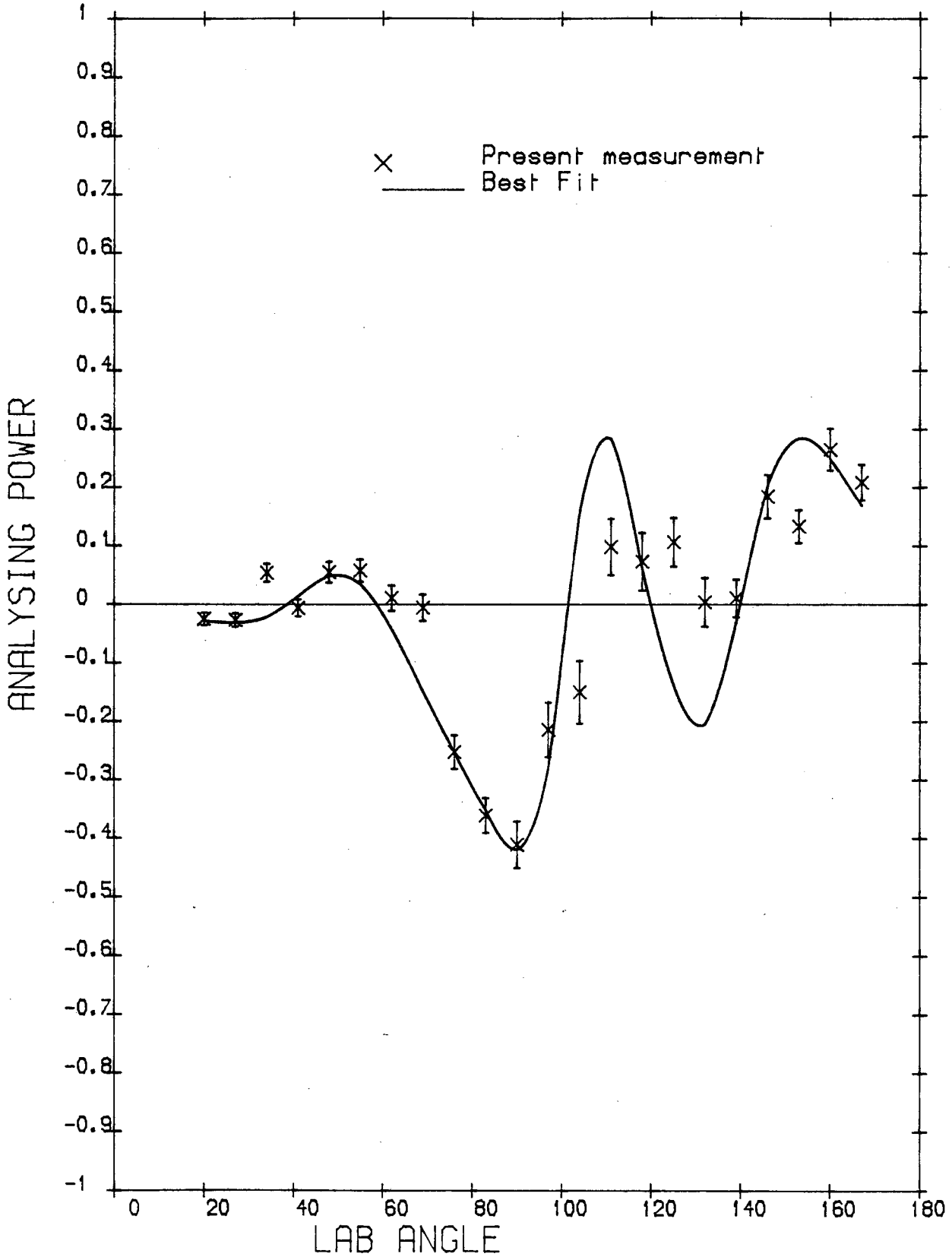
07/08/84 TIN
Present measurement
Best Fit
ANALYSING POWER
LAB ANGLE
1
0.9
0.8
0.7
0.6
0.5
0.4
0.3
0.2
0.1
0
-0.1
-0.2
-0.3
-0.4
-0.5
-0.6
-0.7
-0.8
-0.9
-1
0
20
40
60
80
100
120
140
160
180

Figure 6.15.

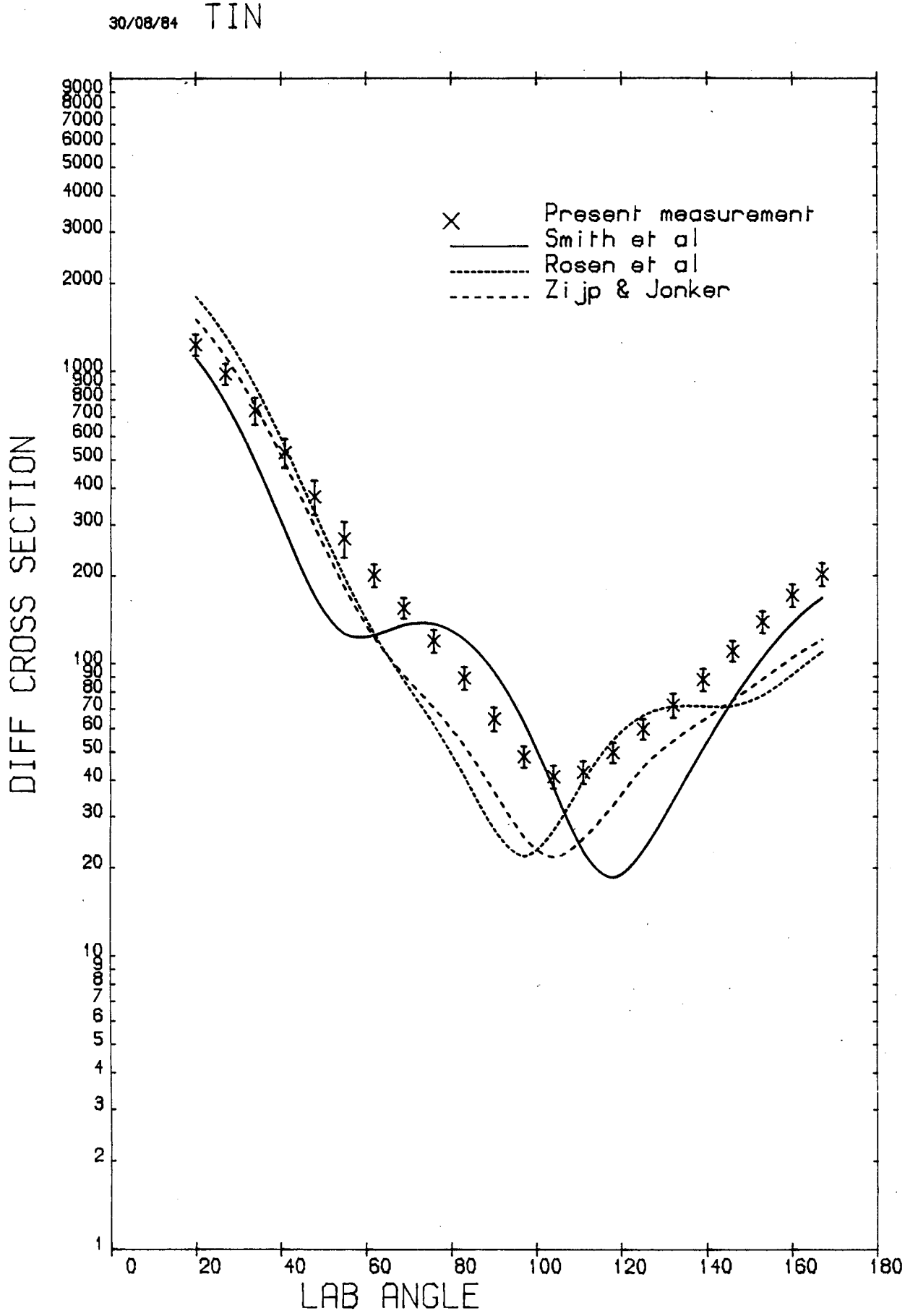
30/08/84 TIN
DIFF CROSS SECTION
LAB ANGLE
Present measurement
Smith et al
Rosen et al
Zijp & Jonker
9000
8000
7000
6000
5000
4000
3000
2000
1000
900
800
700
600
500
400
300
200
100
90
80
70
60
50
40
30
20
10
9
8
7
6
5
4
3
2
1
0
20
40
60
80
100
120
140
160
180

Figure 6.16.

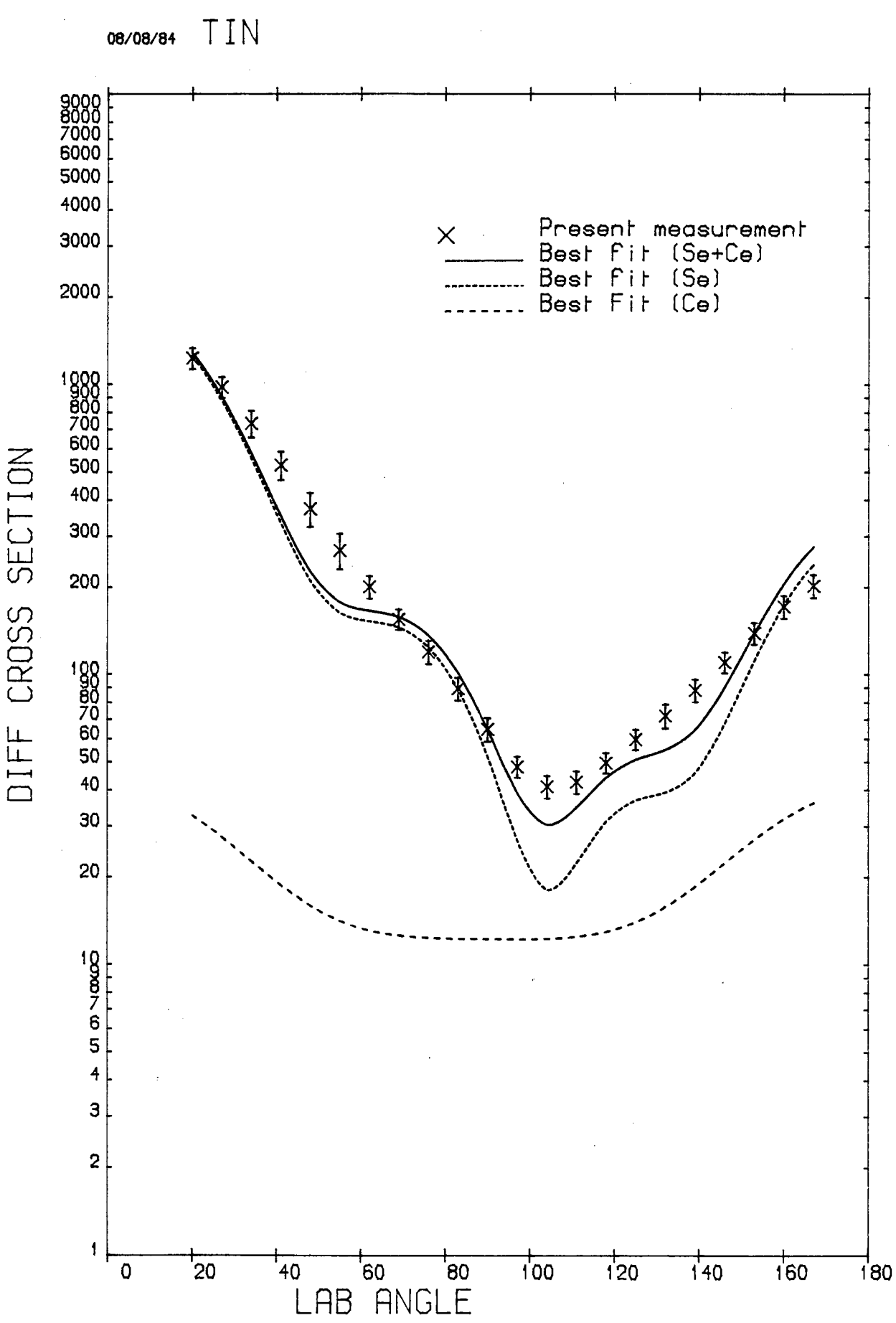
08/08/84 TIN
Present measurement
Best Fit (Se+Ce)
Best Fit (Se)
Best Fit (Ce)
DIFF CROSS SECTION
LAB ANGLE
9000
8000
7000
6000
5000
4000
3000
2000
1000
900
800
700
600
500
400
300
200
100
90
80
70
60
50
40
30
20
10
9
8
7
6
5
4
3
2
1
0
20
40
60
80
100
120
140
160
180

Figure 6.17.

6.4.3 Antimony

The optical model parameters for Antimony were obtained by the following procedure.

The fractional abundances of the two isotopes of Antimony are reasonably close (i.e. 50%), but the spin and parity for the levels over 1.659 MeV in ^{121}Sb are not known, while the level structure (i.e. excitation energies) of two isotopes are very similar. Therefore the decision was made to find the best fit optical model parameters for ^{123}Sb and then apply the best fit parameters to ^{121}Sb and after weighting on abundancy, sum and compare with the experimental results

The ELIESE-3 programme is not capable of handling more than 30 levels, while there are 37 levels up to 3.0 MeV, therefore it was necessary to omit the seven highest levels and search with 30 levels up to 2.580 MeV level. The parameters obtained are given in Table 6.6, set (A) and Fig. 6.18, and 6.19, illustrate the comparison between experimental results and calculated values for ^{121}Sb and ^{123}Sb. Figures 6.20 and 6.21 show the calculated results weighted on abundances compared with the experimental results. The a_{so} in this set of parameters show irregularity with most of the optical model parameter sets discussed in Chapter 6, Section 3.

In order to investigate the effect of higher levels in the calculations, those levels with $\lesssim$ 1 mb/str. inelastic cross section were omitted and instead the higher levels were substituted. These levels which were omitted are

1.729	$1/2^-$
1.740	$3/2^-$
1.884	$1/2^-$
2.10	$3/2^+$
2.235	$1/2^-$
2.520	$1/2^+$

and six higher levels up to 2.915 MeV were substituted. The set of optical model parameters resulting from this kind of calculation are given in Table 6.6, set (B), which were obtained by fixing $a_{so} = 0.37$ and searching for eight other parameters. In Table 6.6, (a) indicates 30 levels up to 2.580 MeV and (b) indicates 30 levels up to 2.915 MeV when six levels are exchanged. It is obvious that there is no considerable difference between the two kinds of calculations, comparing the quality of fit parameter (X^2). Figures 6.22 and 6.23 show the results from set (B) parameters compared with experimental data.

TABLE 6.6

	V_c	r_o	a_o	W_s	r_s	b	V_{so}	r_{so}	a_{so}	X^2_P	X^2_σ	$X^2_{Combined}$
Set (A)	56.56	1.069	0.752	5.38	1.006	0.722	2.42	1.176	0.082	4.41	7.40	5.90 (^{123}Sb)
	-	-	-	-	-	-	-	-	-	3.57	6.33	4.95 (^{121}Sb)
Set (B)	60.71	1.025	0.556	2.27	1.252	0.96	1.91	1.101	0.371	7.11	6.10	6.60 (a)
	-	-	-	-	-	-	-	-	-	7.10	6.26	6.68 (b)

The relative success of several potentials is given in Table 6.7, and the experimental results are compared with calculations using the most successful potentials in Fig. 6.24 (analysing power) and Fig. 6.25 (differential cross section). After the Best fit parameters - Becchetti and Greenlees are the most successful, while Zijp and Jonker parameters and those of Smith et al. reproduce the differential cross section as well as the Best Fit parameters, the analysing power prediction is too poor.

TABLE 6.7

Antimony: Quality of OM Fit

Potential	X^2_{Comb}	X^2_P	X^2_σ
Best Fit (set A)	5.25	3.86	6.65
Best Fit (set B)	6.68	7.10	6.26
Becchetti and Greenlees	14.56	21.67	7.45
Zijp and Jonker	34.45	65.06	3.84
Rosen et al.	38.17	57.79	18.54
Smith et al.	41.61	76.59	6.63
Tanaka et al.	71.06	124.79	17.34
Strizhak et al.	119.97	209.43	30.51

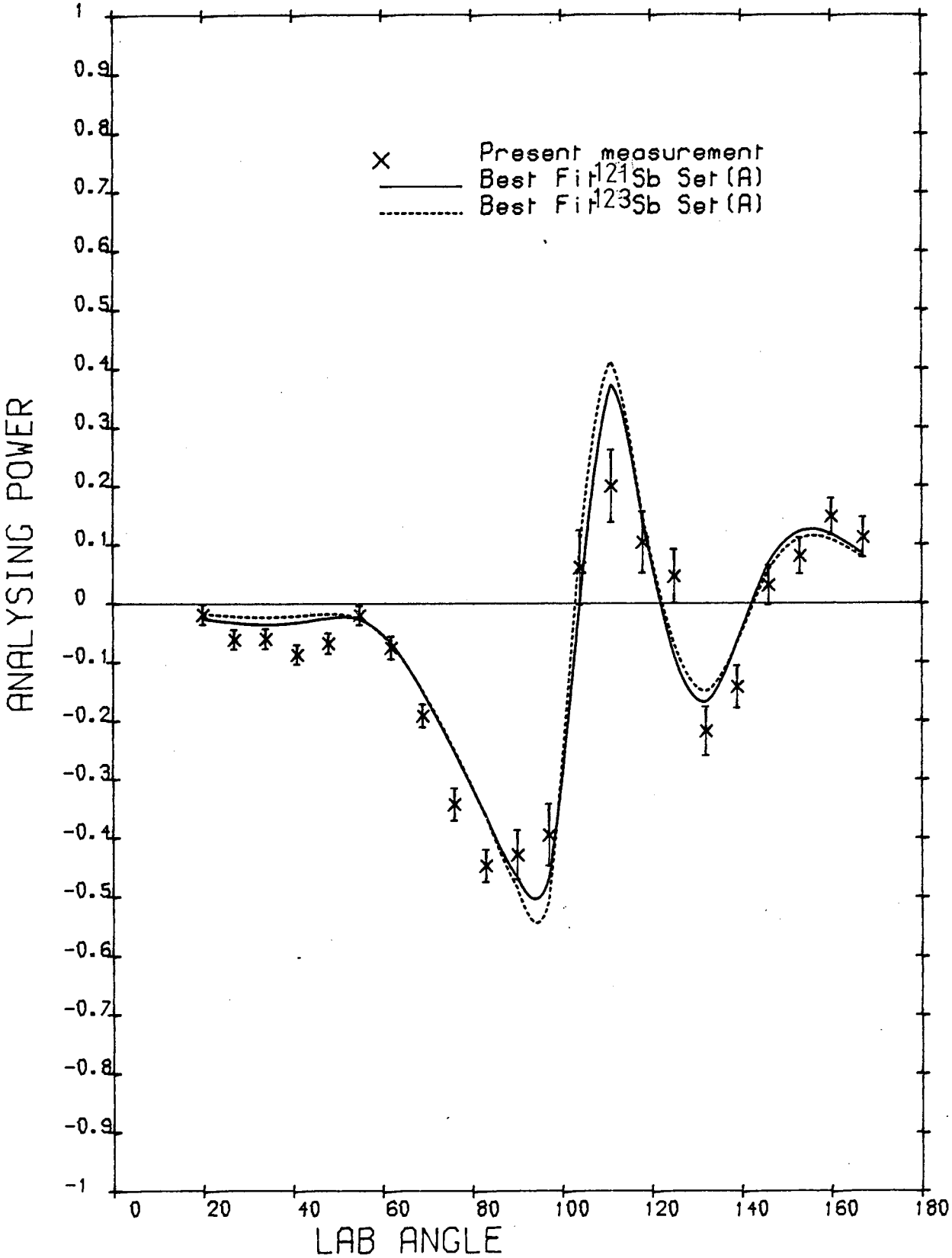
24/08/84 ANTIMONY
Present measurement
Best Fit 121Sb Set (A)
Best Fit 123Sb Set (A)
ANALYSING POWER
LAB ANGLE
1
0.9
0.8
0.7
0.6
0.5
0.4
0.3
0.2
0.1
0
-0.1
-0.2
-0.3
-0.4
-0.5
-0.6
-0.7
-0.8
-0.9
-1
0
20
40
60
80
100
120
140
160
180

Figure 6.18.

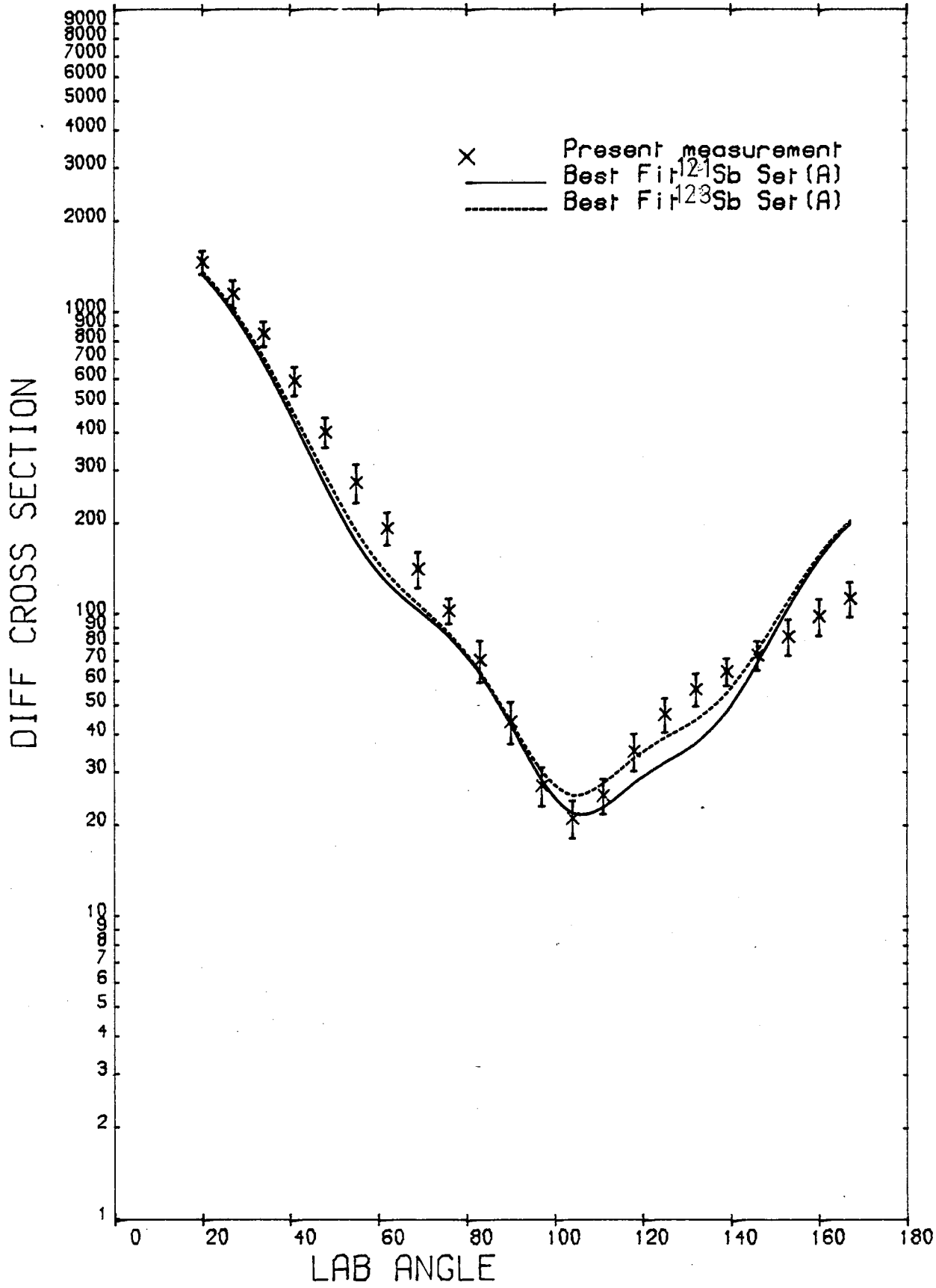
24/08/84 ANTIMONY
Present measurement
Best Fit 121Sb Set (A)
Best Fit 123Sb Set (A)
DIFF CROSS SECTION
LAB ANGLE
9000
8000
7000
6000
5000
4000
3000
2000
1000
900
800
700
600
500
400
300
200
100
90
80
70
60
50
40
30
20
10
9
8
7
6
5
4
3
2
1
0
20
40
60
80
100
120
140
160
180

Figure 6.19.

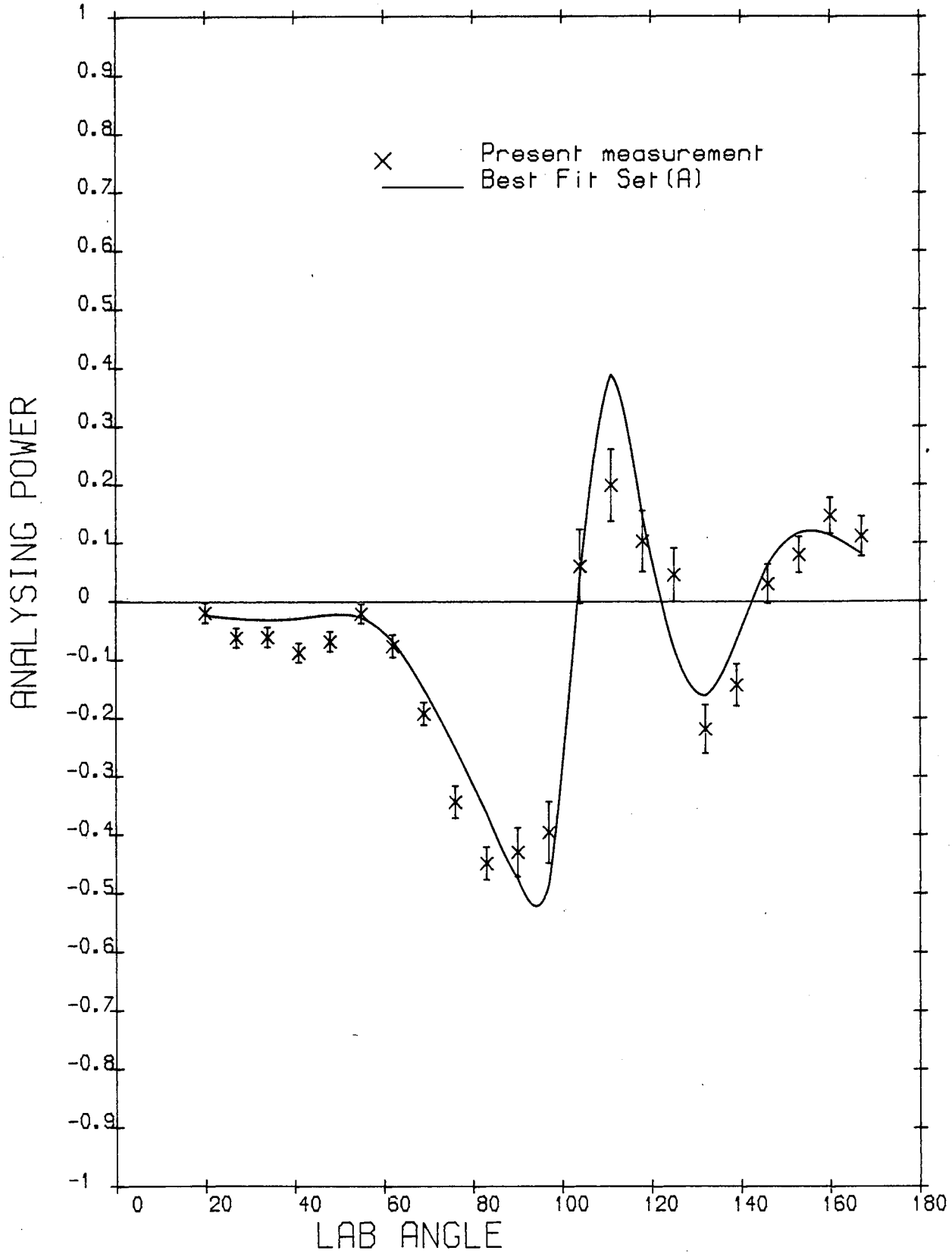
24/08/84 ANTIMONY
Present measurement
Best Fit Set(A)
ANALYSING POWER
LAB ANGLE
1
0.9
0.8
0.7
0.6
0.5
0.4
0.3
0.2
0.1
0
-0.1
-0.2
-0.3
-0.4
-0.5
-0.6
-0.7
-0.8
-0.9
-1
0
20
40
60
80
100
120
140
160
180

Figure 6.20.

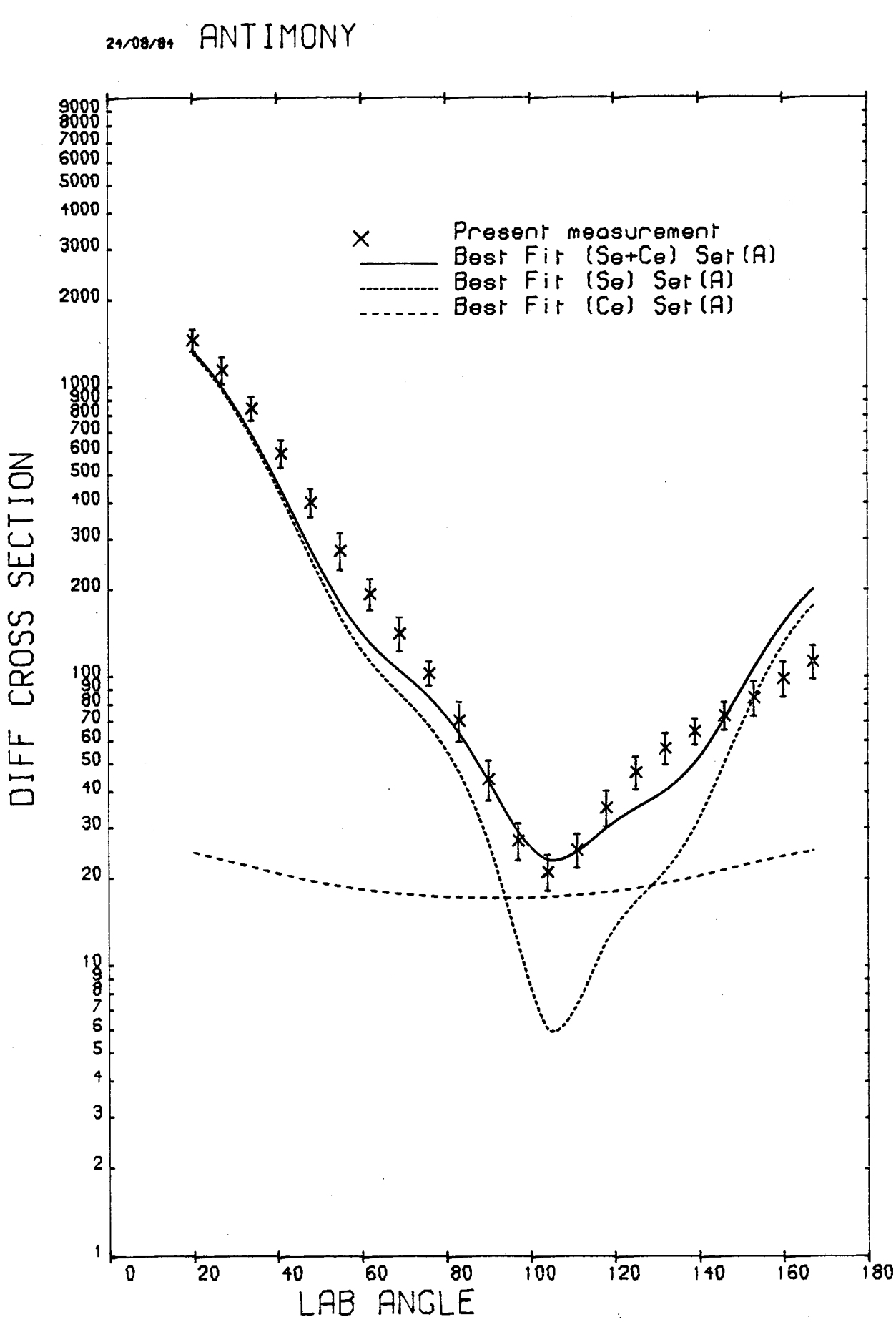
24/08/84 ANTIMONY
DIFF CROSS SECTION
LAB ANGLE
Present measurement
Best Fit (Se+Ce) Set(A)
Best Fit (Se) Set(A)
Best Fit (Ce) Set(A)
9000
8000
7000
6000
5000
4000
3000
2000
1000
900
800
700
600
500
400
300
200
100
90
80
70
60
50
40
30
20
10
9
8
7
6
5
4
3
2
1
0
20
40
60
80
100
120
140
160
180

Figure 6.21.

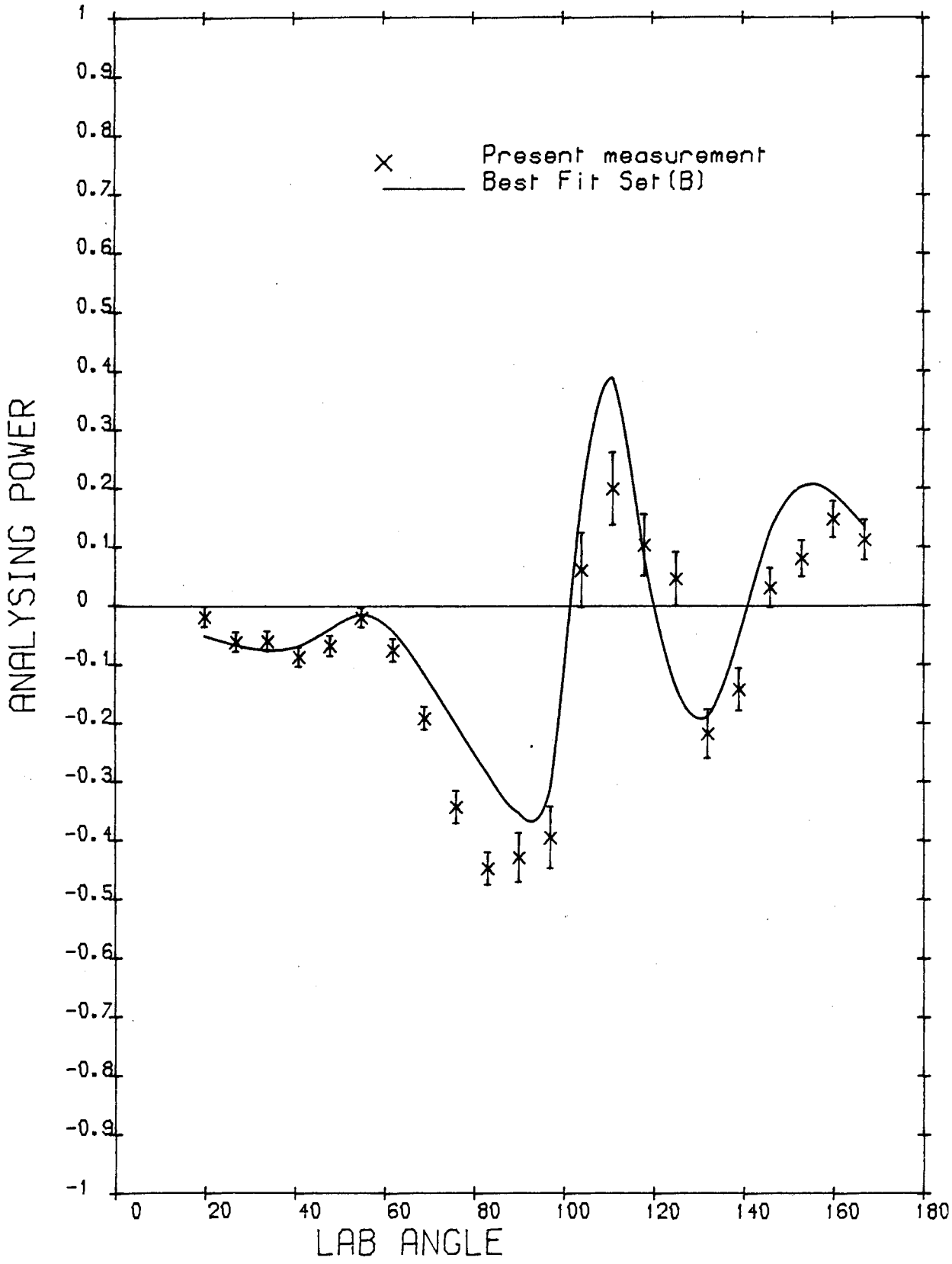
24/08/84 ANTIMONY
Present measurement
Best Fit Set(B)
ANALYSING POWER
LAB ANGLE
1
0.9
0.8
0.7
0.6
0.5
0.4
0.3
0.2
0.1
0
-0.1
-0.2
-0.3
-0.4
-0.5
-0.6
-0.7
-0.8
-0.9
-1
0
20
40
60
80
100
120
140
160
180

Figure 6.22.

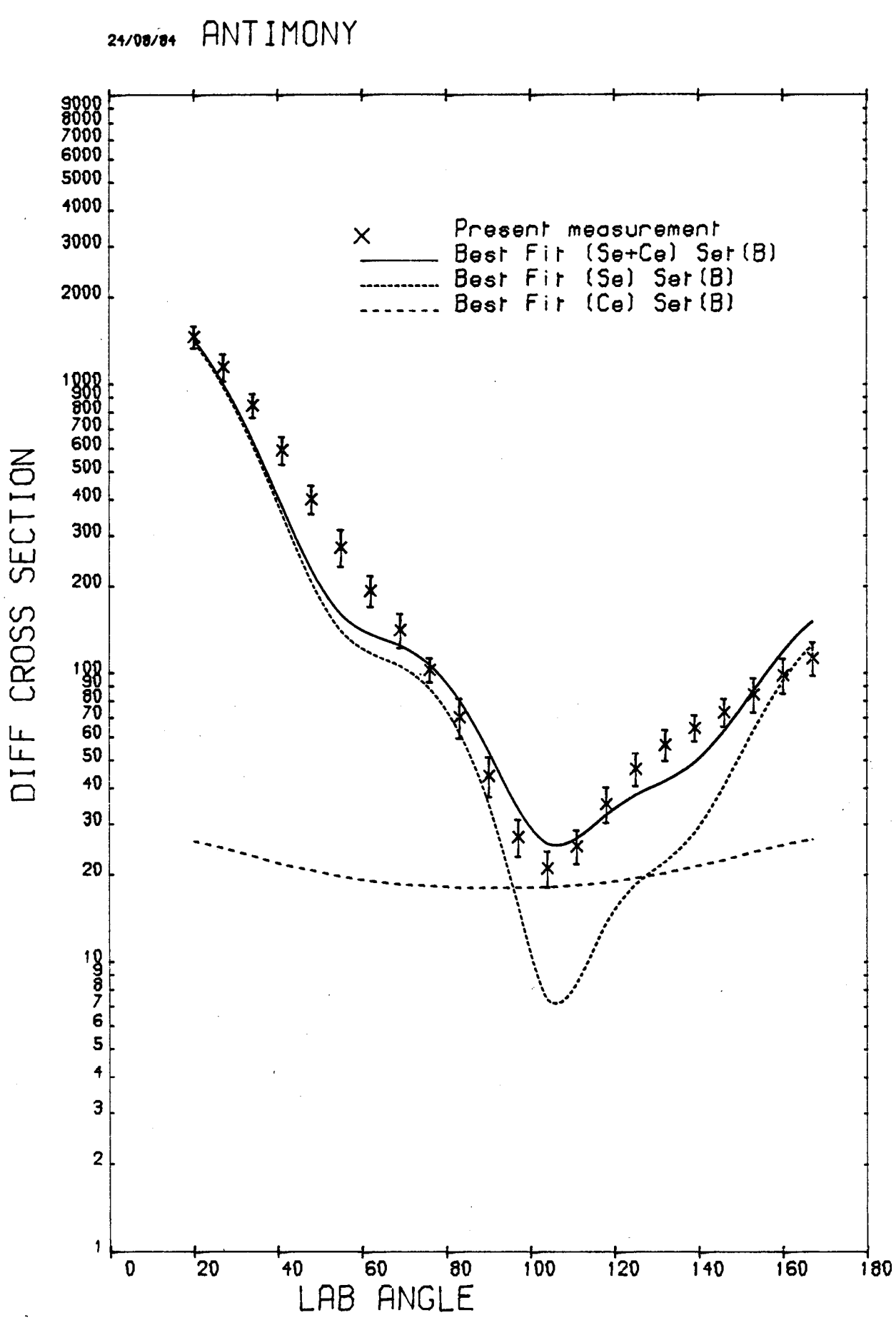
24/08/84 ANTIMONY
Present measurement
Best Fit (Se+Ce) Set(B)
Best Fit (Se) Set(B)
Best Fit (Ce) Set(B)
DIFF CROSS SECTION
LAB ANGLE
9000
8000
7000
6000
5000
4000
3000
2000
1000
900
800
700
600
500
400
300
200
100
90
80
70
60
50
40
30
20
10
9
8
7
6
5
4
3
2
1
0
20
40
60
80
100
120
140
160
180

Figure 6.23.

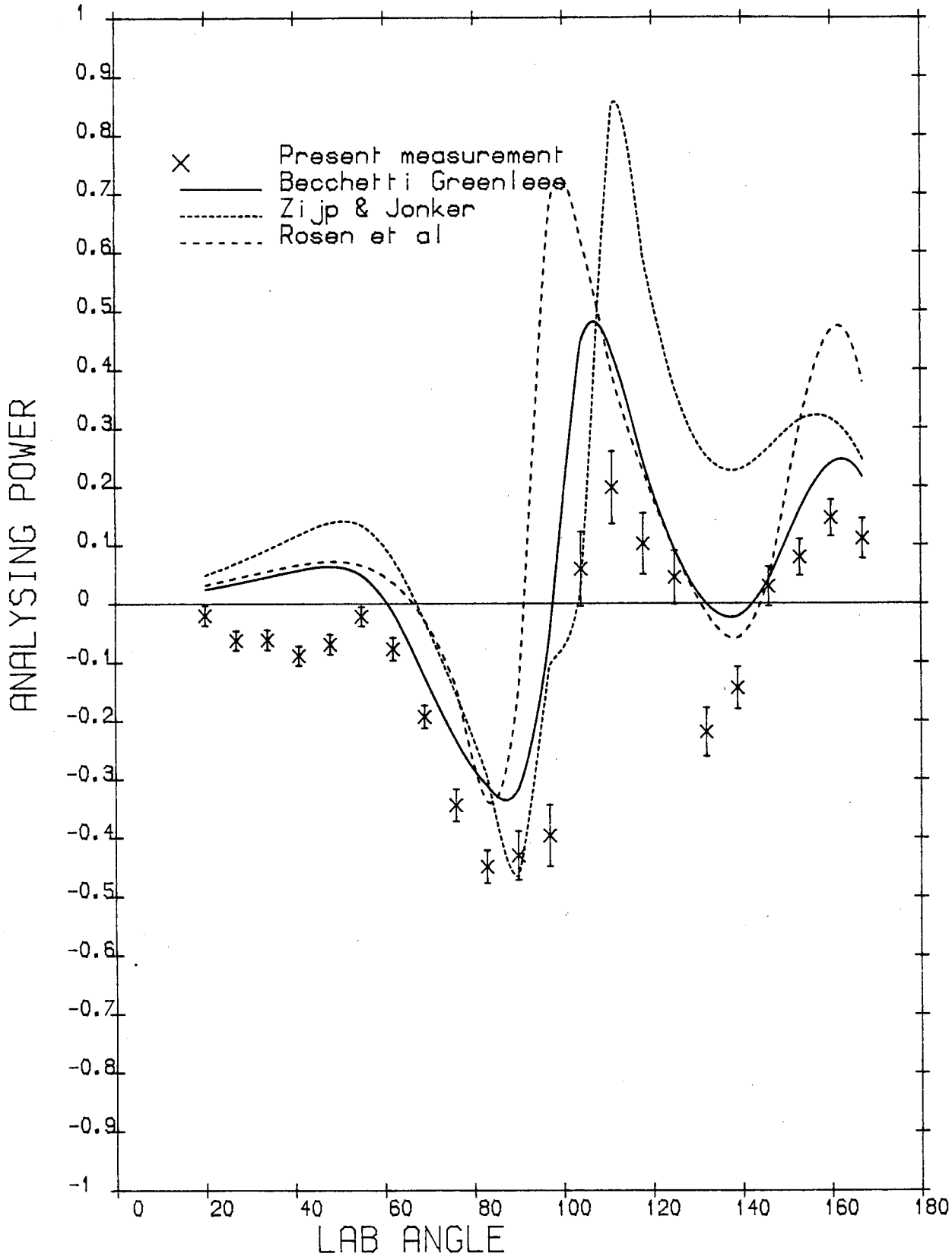
31/08/84 ANTIMONY
Present measurement
Becchetti Greenlees
Zijp & Jonker
Rosen et al
ANALYSING POWER
LAB ANGLE
1
0.9
0.8
0.7
0.6
0.5
0.4
0.3
0.2
0.1
0
-0.1
-0.2
-0.3
-0.4
-0.5
-0.6
-0.7
-0.8
-0.9
-1
0
20
40
60
80
100
120
140
160
180

Figure 6.24.

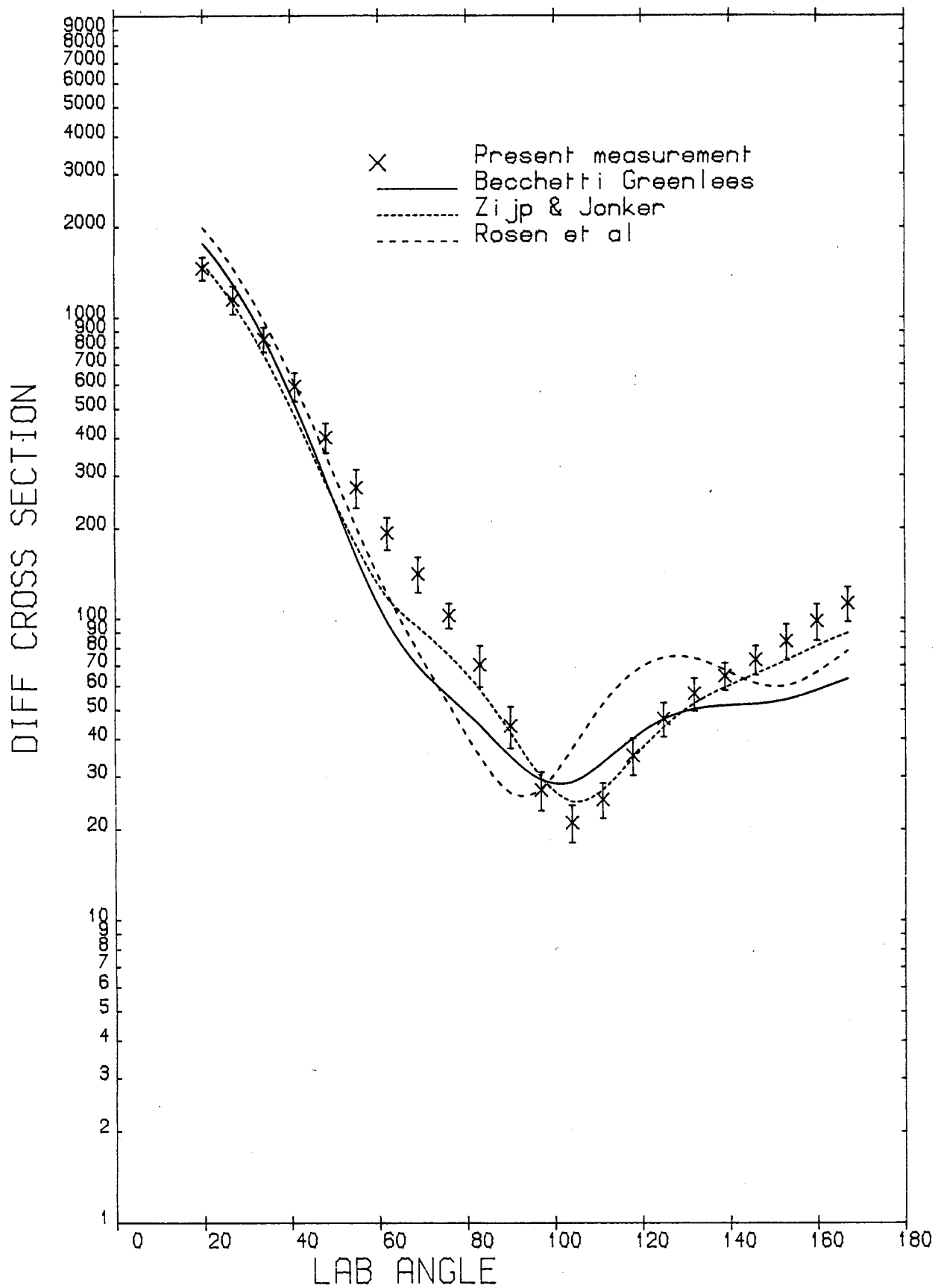
31/08/84 ANTIMONY
Present measurement
Becchetti Greenlees
Zijp & Jonker
Rosen et al
DIFF CROSS SECTION
LAB ANGLE
9000
8000
7000
6000
5000
4000
3000
2000
1000
900
800
700
600
500
400
300
200
100
90
80
70
60
50
40
30
20
10
9
8
7
6
5
4
3
2
1
0
20
40
60
80
100
120
140
160
180

Figure 6.25.

6.4.4 Tellurium

The relative success of various optical potential parameters is summarised in Table 6.8. The predictions of the most successful are compared with the present data in Figures 6.26 and 6.27 (analysing power) and 6.28 and 6.29 (differential cross section). None of the potentials used reproduce the cross section well, even the Best Fit parameters are not capable of reproducing the cross section and analysing power distribution well. They predict the shape of the analysing power distribution. While they tend to overestimate the magnitude at some angles, and at forward angles the prediction of the theory has the opposite sign to the experimental data.

Since the level structure of the most abundant isotopes of Tellurium (i.e. ^{130}Te and ^{128}Te and ^{126}Te) are not very well known, it might be possible that the lack of knowledge about spin and parity of the excitation levels of these isotopes, leads to unacceptable results.

TABLE 6.8

Tellurium: Quality of OM Fit

Potential	X^2_{Comb}	X^2_P	X^2_σ
Best Fit	13.61	16.01	11.20
Becchetti and Greenlees	22.68	23.85	21.51
Rosen et al.	39.17	61.06	17.27
Zijp and Jonker	54.51	96.30	12.72
Smith et al.	67.37	126.03	8.72
Tanaka	71.98	136.01	7.94

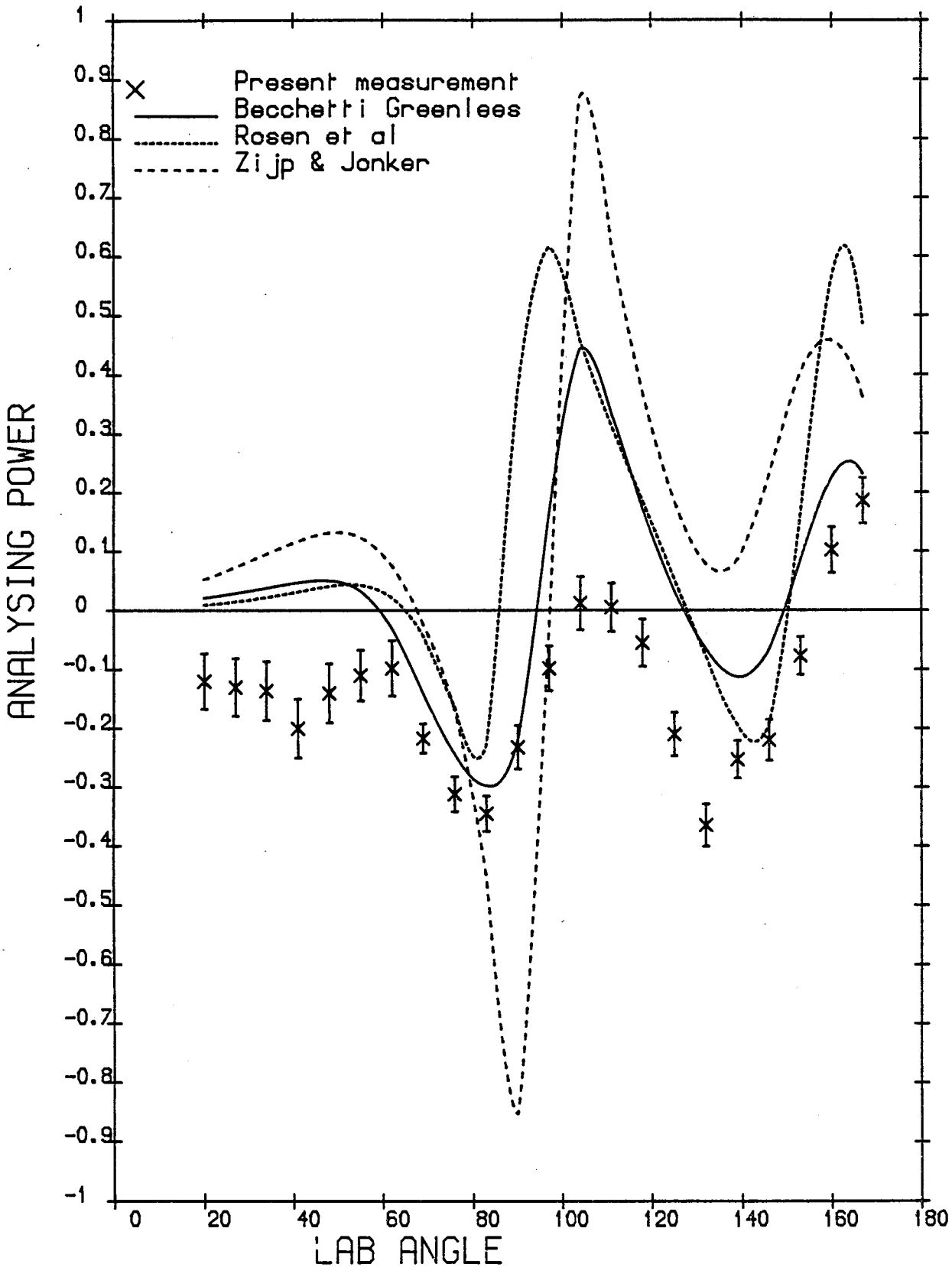
18/01/85 TELLURIUM
Present measurement
Becchetti Greenlees
Rosen et al
Zijp & Jonker
ANALYSING POWER
LAB ANGLE
1
0.9
0.8
0.7
0.6
0.5
0.4
0.3
0.2
0.1
0
-0.1
-0.2
-0.3
-0.4
-0.5
-0.6
-0.7
-0.8
-0.9
-1
0
20
40
60
80
100
120
140
160
180

Figure 6.26.

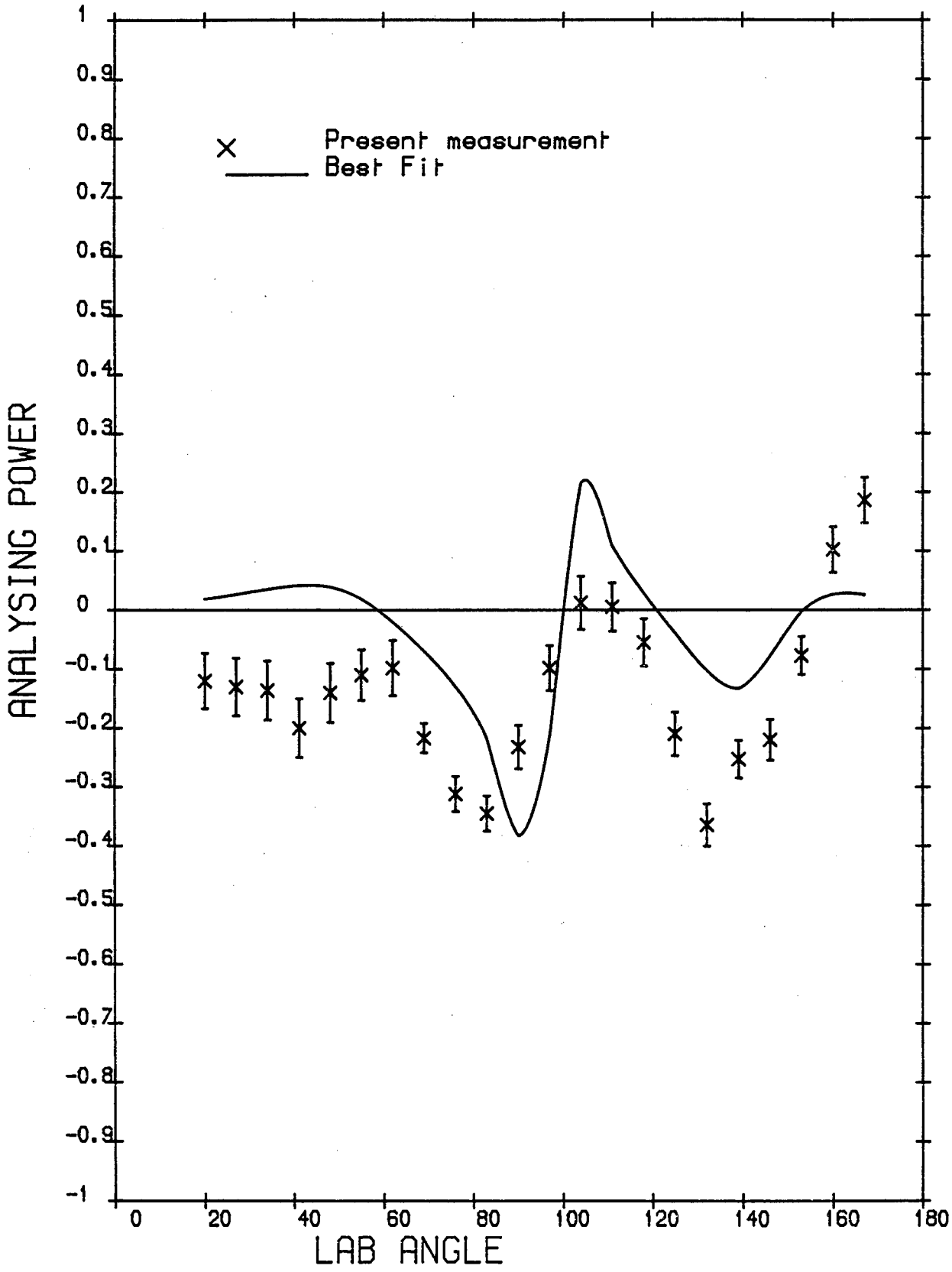
18/01/85 TELLURIUM
Present measurement
Best Fit
ANALYSING POWER
LAB ANGLE
1
0.9
0.8
0.7
0.6
0.5
0.4
0.3
0.2
0.1
0
-0.1
-0.2
-0.3
-0.4
-0.5
-0.6
-0.7
-0.8
-0.9
-1
0
20
40
60
80
100
120
140
160
180

Figure 6.27.

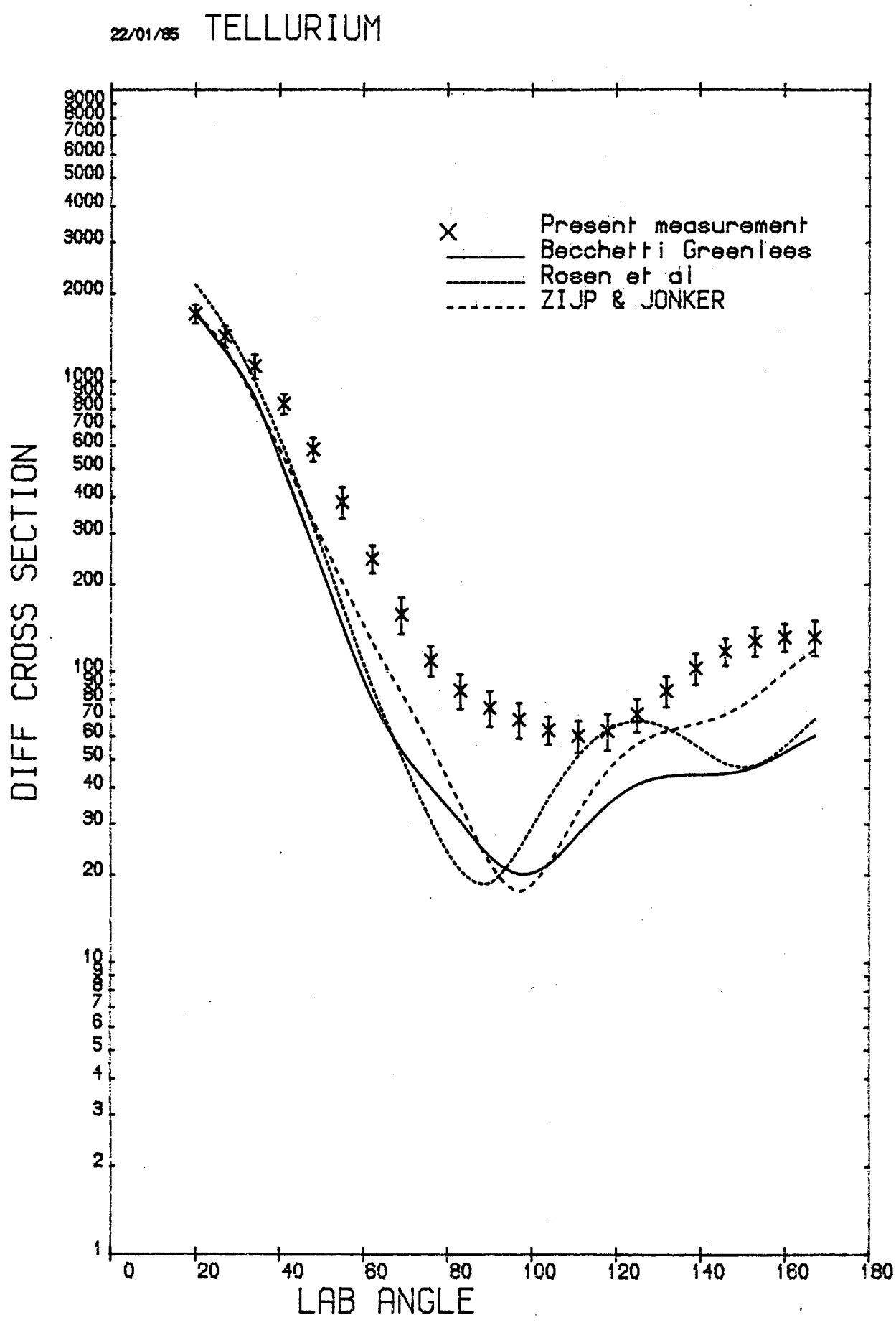
22/01/85 TELLURIUM
Present measurement
Becchetti Greenlees
Rosen et al
ZIJP & JONKER
DIFF CROSS SECTION
LAB ANGLE
0
20
40
60
80
100
120
140
160
180

Figure 6.28.

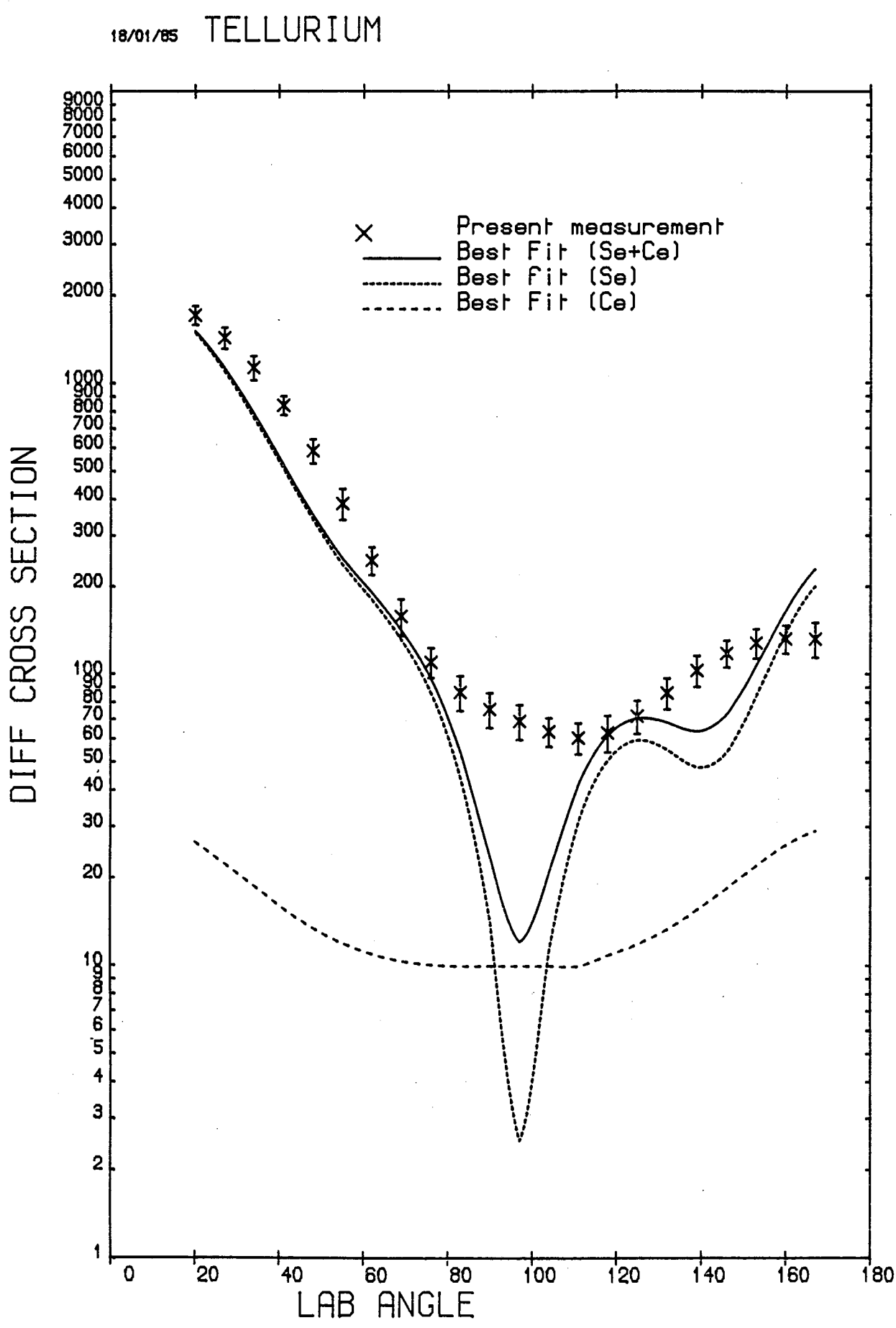
18/01/85 TELLURIUM
DIFF CROSS SECTION
LAB ANGLE
Present measurement
Best Fit (Se+Ce)
Best Fit (Se)
Best Fit (Ce)
9000
8000
7000
6000
5000
4000
3000
2000
1000
900
800
700
600
500
400
300
200
100
90
80
70
60
50
40
30
20
10
9
8
7
6
5
4
3
2
1
0
20
40
60
80
100
120
140
160
180

Figure 6.29.

6.4.5 Iodine

Table 6.9 summarises the relative success of optical potentials used for Iodine. The predictions of the most successful are plotted against the present data in Figures 6.30 and 6.31 (analysing power) and 6.32 and 6.33 (differential cross section). The Best Fit parameters reproduce both analysing power and differential cross section quite well. Galloway and Waheed's parameters and those of Becchetti and Greenlees reproduce a good fit to the present cross section data, but all of the parameters tried fail to reproduce the shape of the analysing power as successfully as the cross section.

TABLE 6.9

Iodine: Quality of OM Fit

Potential	X^2_{Comb}	X^2_P	X^2_σ
Best Fit	6.28	7.06	5.50
Galloway and Waheed	14.40	24.47	4.34
Becchetti and Greenlees	19.10	32.38	5.82
Rosen et al.	26.40	40.50	12.29
Tanaka	40.99	71.75	10.23
Smith et al.	83.93	74.86	92.99

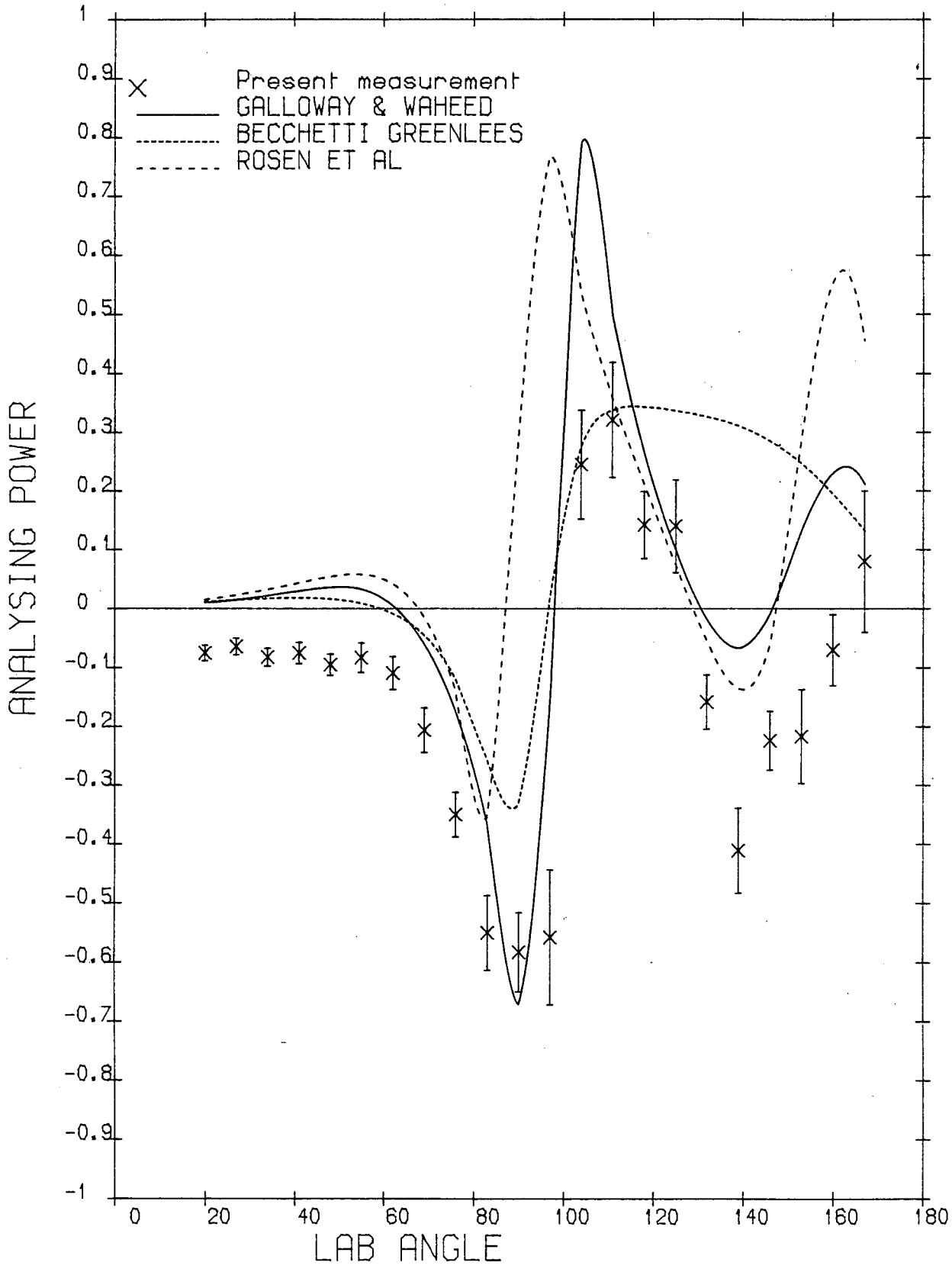
22/01/85 IODINE
Present measurement
GALLOWAY & WAHEED
BECCHETTI GREENLEES
ROSEN ET AL
ANALYSING POWER
LAB ANGLE
1
0.9
0.8
0.7
0.6
0.5
0.4
0.3
0.2
0.1
0
-0.1
-0.2
-0.3
-0.4
-0.5
-0.6
-0.7
-0.8
-0.9
-1
0
20
40
60
80
100
120
140
160
180

Figure 6.30.

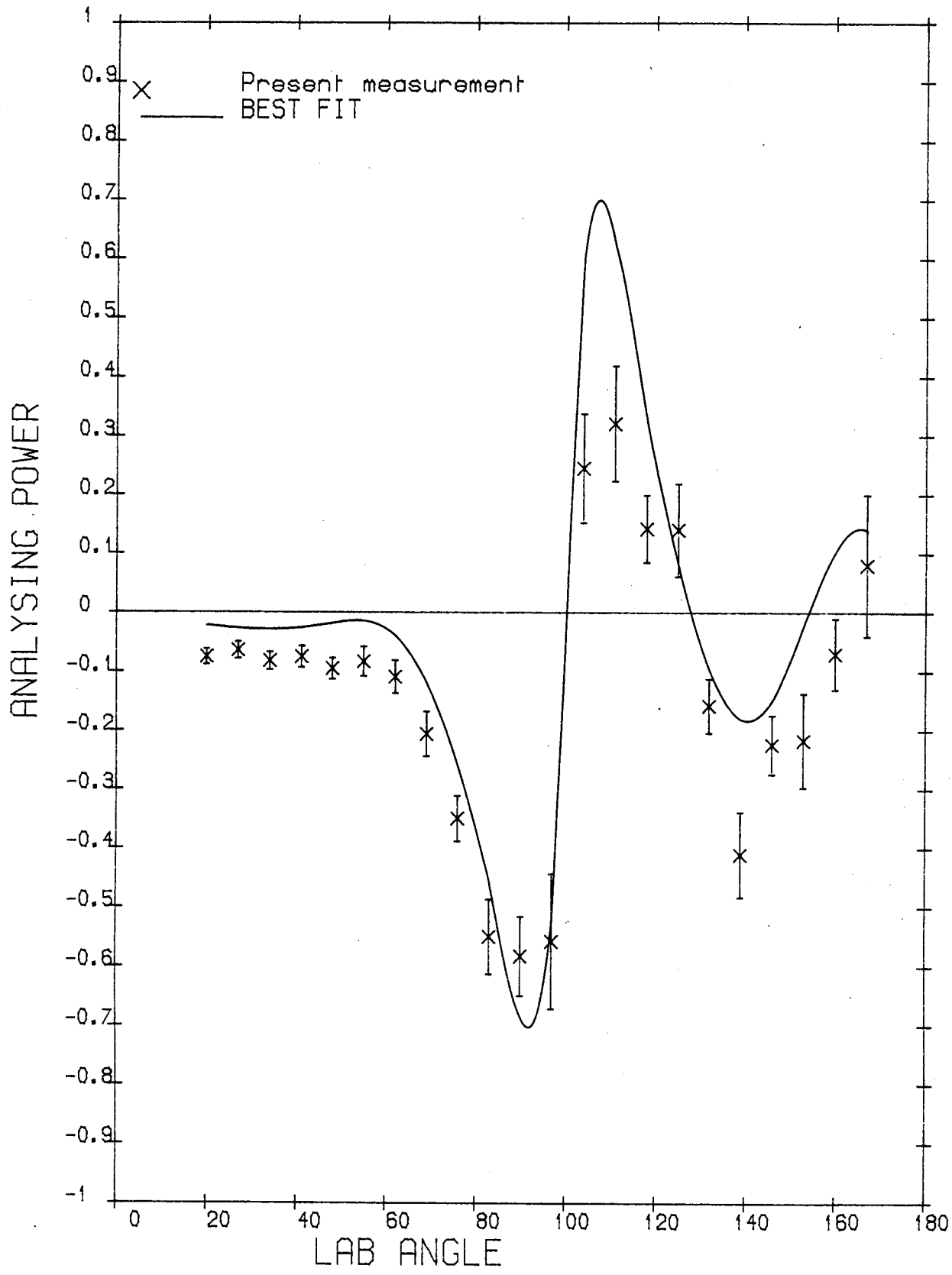
22/01/85 IODINE
Present measurement
BEST FIT
ANALYSING POWER
LAB ANGLE
1
0.9
0.8
0.7
0.6
0.5
0.4
0.3
0.2
0.1
0
-0.1
-0.2
-0.3
-0.4
-0.5
-0.6
-0.7
-0.8
-0.9
-1
0
20
40
60
80
100
120
140
160
180

Figure 6.31.

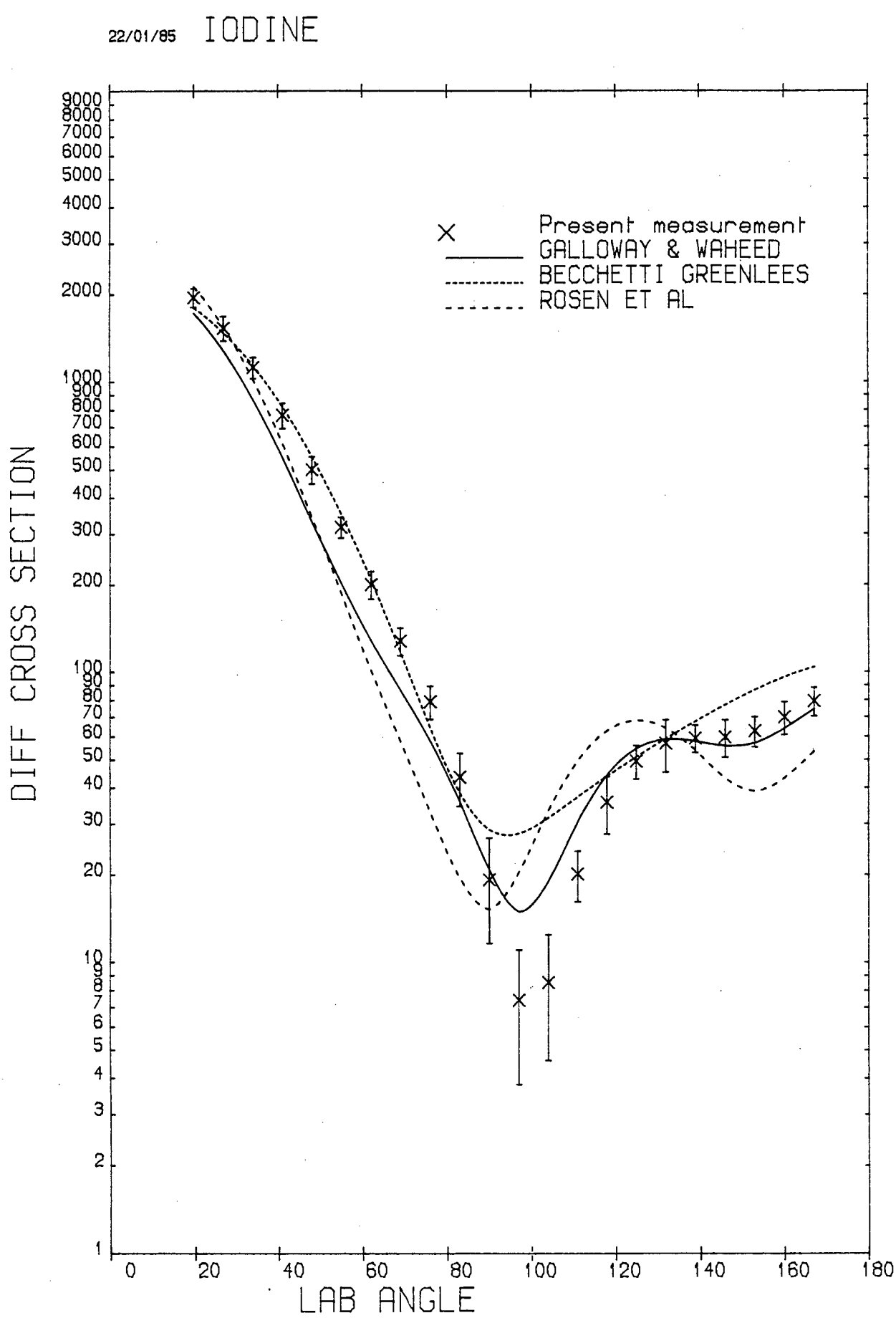
22/01/85 IODINE
Present measurement
GALLOWAY & WAHEED
BECCHETTI GREENLEES
ROSEN ET AL
DIFF CROSS SECTION
LAB ANGLE
9000
8000
7000
6000
5000
4000
3000
2000
1000
900
800
700
600
500
400
300
200
100
90
80
70
60
50
40
30
20
10
9
8
7
6
5
4
3
2
1
0
20
40
60
80
100
120
140
160
180

Figure 6.32.

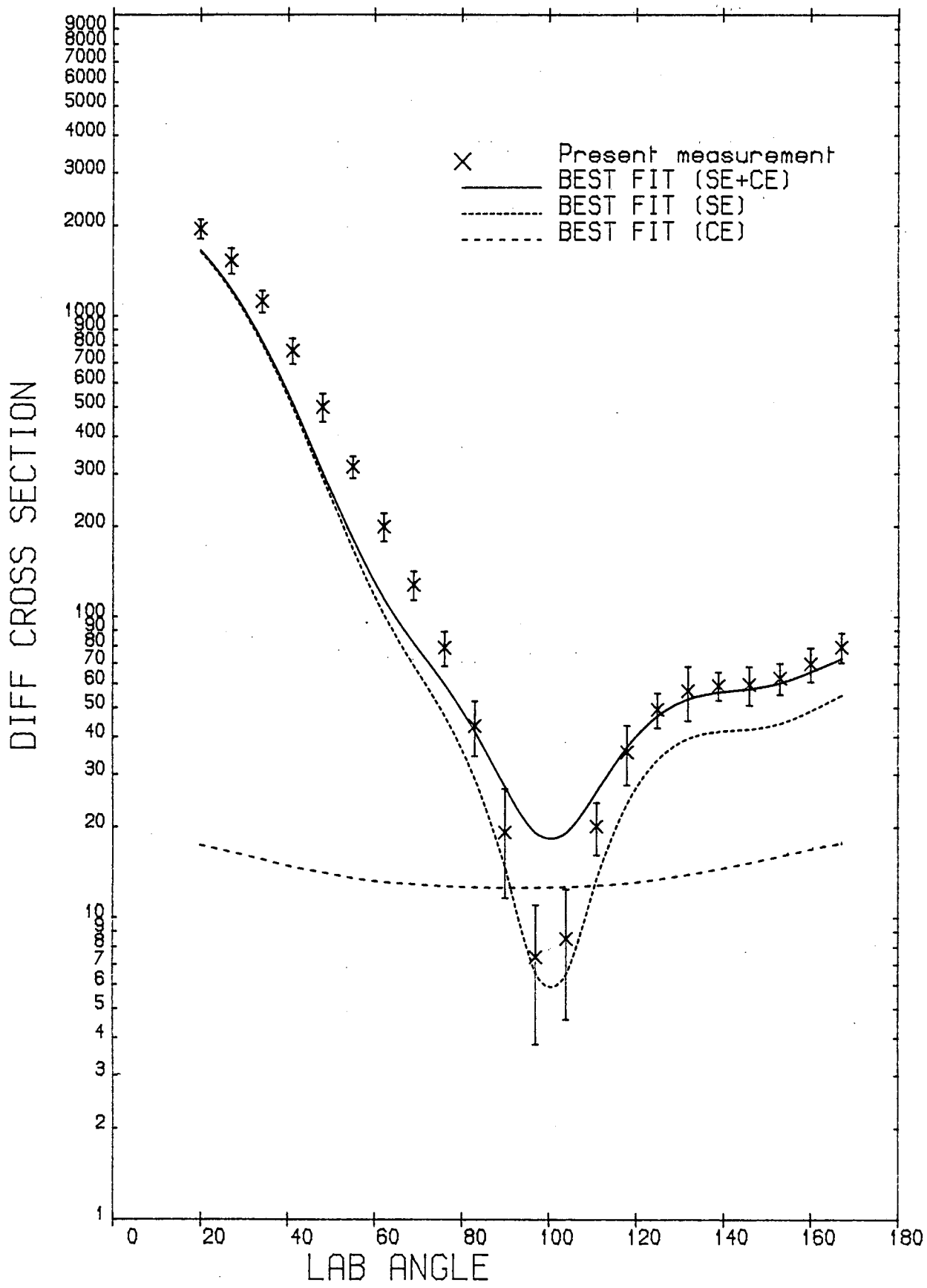
22/01/85 IODINE
DIFF CROSS SECTION
LAB ANGLE
Present measurement
BEST FIT (SE+CE)
BEST FIT (SE)
BEST FIT (CE)
9000
8000
7000
6000
5000
4000
3000
2000
1000
900
800
700
600
500
400
300
200
100
90
80
70
60
50
40
30
20
10
9
8
7
6
5
4
3
2
1
0
20
40
60
80
100
120
140
160
180

Figure 6.33.

6.5 Optical Model Analysis of the Polarisation Data

Since the objective of this work is to find out whether the optical model potential can be applied successfully to describe the polarisation due to scattering by medium weight nuclei, as Ellgehausen et al.[13] illustrated this aspect for lighter nuclei (e.g. Ti to Zn nuclei), it was therefore of interest to search for optimum optical model parameters on the polarisation data alone.

The polarisation, for example, is quite sensitive to the strength of the spin-orbit coupling in the interaction.

Table 6.10 gives the parameters obtained to fit only polarisation data, ignoring the cross sections data, compared with those obtained for simultaneous fit to polarisation and cross sections in the previous section. The quality of fit, X^2, is also compared. Figures 6.34, 6.36, 38, 40 and 6.42 show an illustrated comparison of the experimental polarisation data with calculated values obtained from both sets of parameters given in Table 6.10. The cross sections resulting from this analysis are also compared with the result of simultaneous fit to analysing power and cross section in Figures 6.35, 37, 39, 41 and 6.43.

Generally only a modest improvement in the fit to the polarisation data is achieved and a small worsening of the fit to the differential cross section results.

TABLE 6.10

Optimum Values of the Optical Potential Parameters for 3.0 MeV Neutrons

	V_c	r_o	a_o	W_s	r_s	b	V_{so}	r_{so}	a_{so}	X^2_P	X^2_σ	X^2_{Comb}	$(J/A)_V$	$(J/A)_W$
Cd	50.35	1.150	0.714	8.52	1.01	0.464	2.34	1.223	0.310	6.65*	9.46*	8.05	373	43
	50.23	1.160	0.744	8.02	1.01	0.548	2.00	1.240	0.310	13.73†	5.12†	9.42	385	48
Sn	52.30	1.110	0.699	4.17	1.071	0.752	3.01	1.137	0.679	4.23*	9.59*	6.91	348	39
	53.51	1.095	0.719	2.42	1.022	0.977	2.98	1.292	0.559	9.85†	4.55†	7.20	346	28
Sb	53.41	1.090	0.703	10.76	1.049	0.254	2.80	1.160	0.242	1.68*	35.41*	18.54	338	31
(set B)	60.71	1.025	0.556	2.27	1.252	0.960	1.91	1.101	0.371	7.10†	6.26†	6.68	306	37
(set A)	56.56	1.069	0.752	5.38	1.006	0.722	2.42	1.176	0.101	3.86†	6.65†	5.25	347	43
Te	60.50	1.010	0.800	1.45	1.290	0.907	1.23	1.100	0.290	14.30*	11.98*	13.14	324	24
	58.80	1.030	0.800	1.76	1.290	0.907	1.10	1.100	0.290	16.01†	11.20†	13.61	332	28
I	45.11	1.293	0.507	16.51	1.030	0.450	8.20	1.241	0.245	2.25*	6.98*	4.61	433	80
	45.03	1.278	0.539	12.13	1.030	0.523	6.63	1.240	0.245	7.06†	5.50†	6.28	421	69

(*) only polarisation

(†) polarisation and cross section.

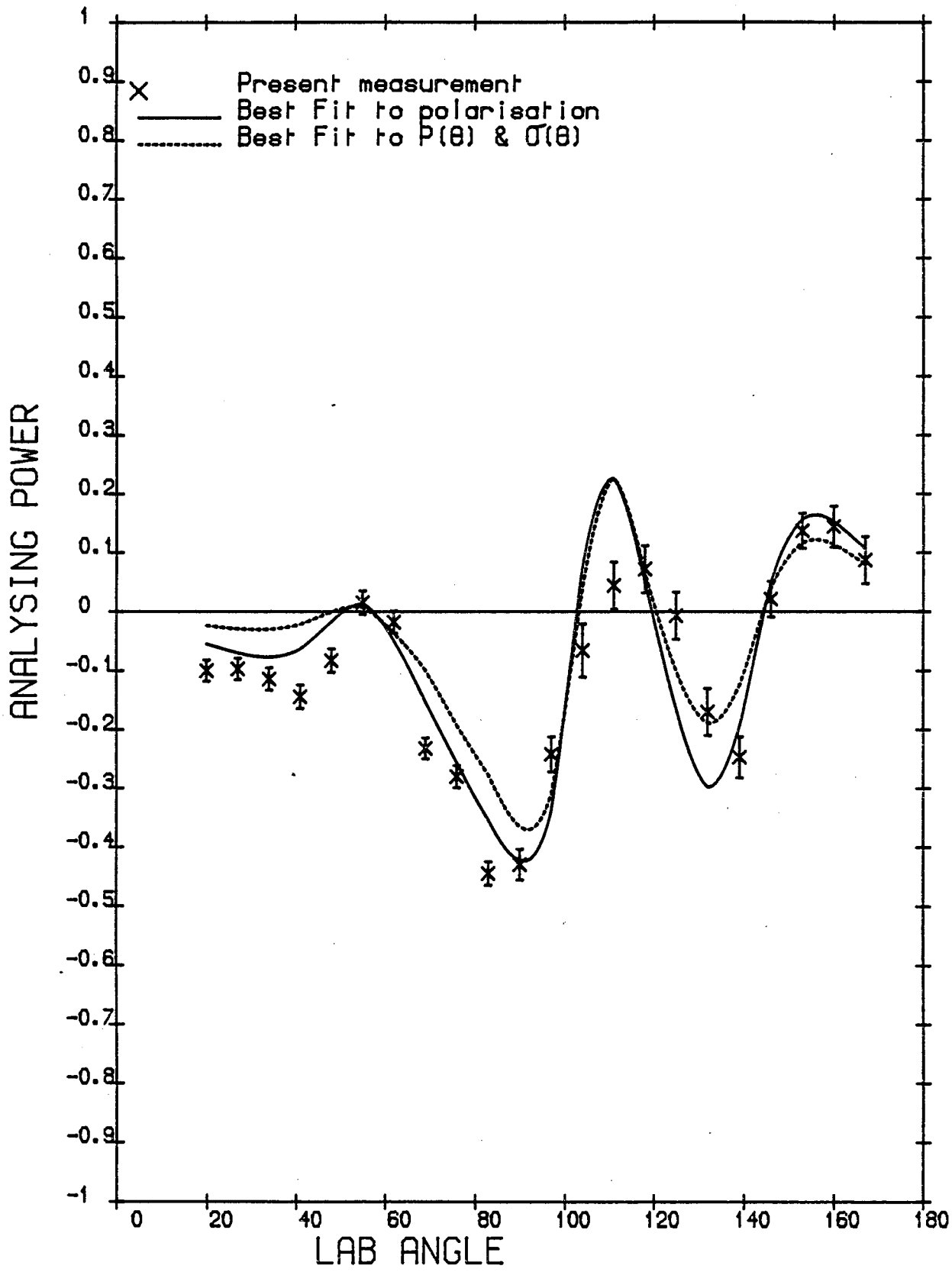
18/01/85 CADMIUM
Present measurement
Best Fit to polarisation
Best Fit to P(θ) & σ(θ)
ANALYSING POWER
LAB ANGLE
1
0.9
0.8
0.7
0.6
0.5
0.4
0.3
0.2
0.1
0
-0.1
-0.2
-0.3
-0.4
-0.5
-0.6
-0.7
-0.8
-0.9
-1
0
20
40
60
80
100
120
140
160
180

Figure 6.34.

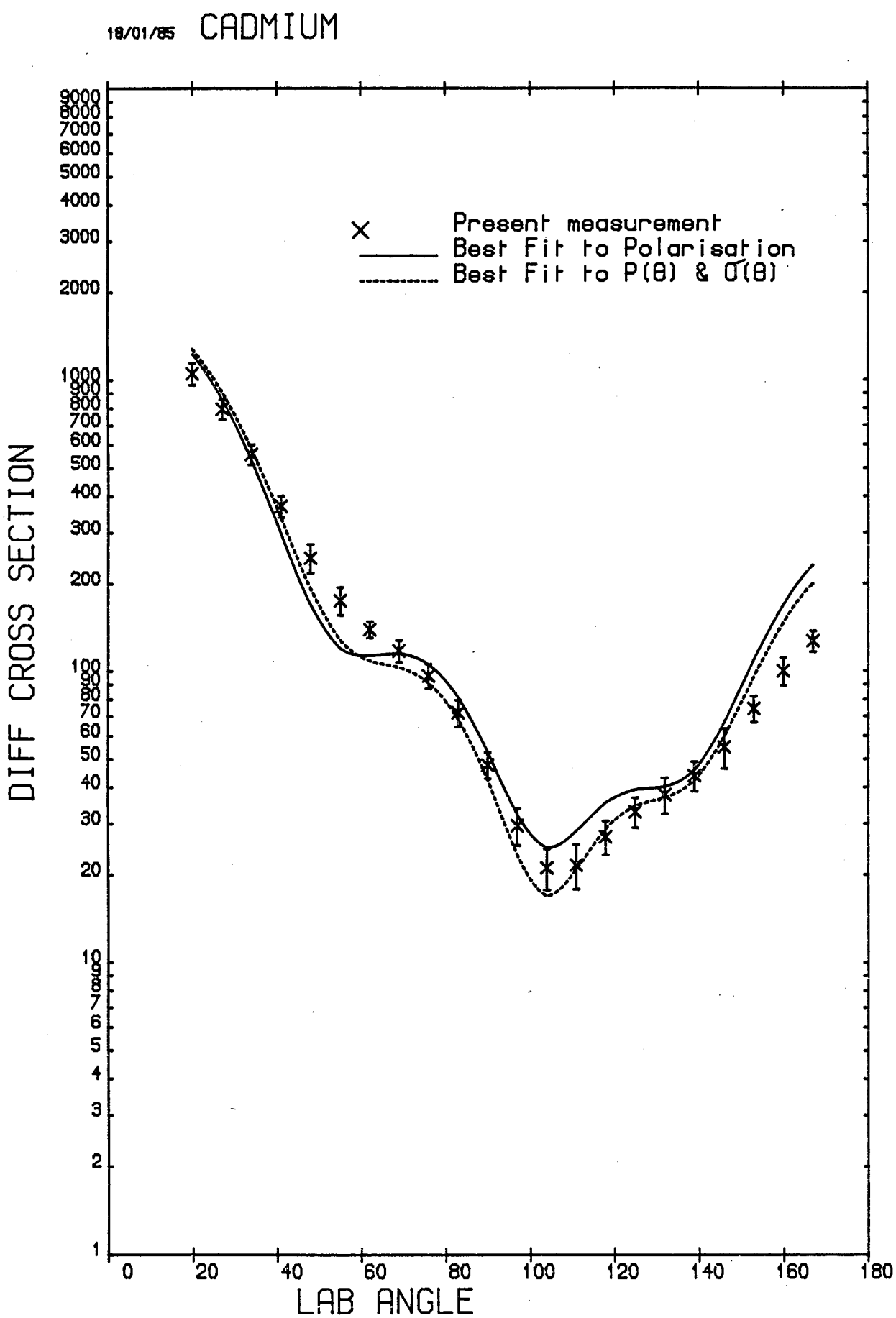
18/01/85 CADMIUM
Present measurement
Best Fit to Polarisation
Best Fit to P(θ) & σ(θ)
DIFF CROSS SECTION
LAB ANGLE
9000
8000
7000
6000
5000
4000
3000
2000
1000
900
800
700
600
500
400
300
200
100
90
80
70
60
50
40
30
20
10
9
8
7
6
5
4
3
2
1
0
20
40
60
80
100
120
140
160
180

Figure 6.35.

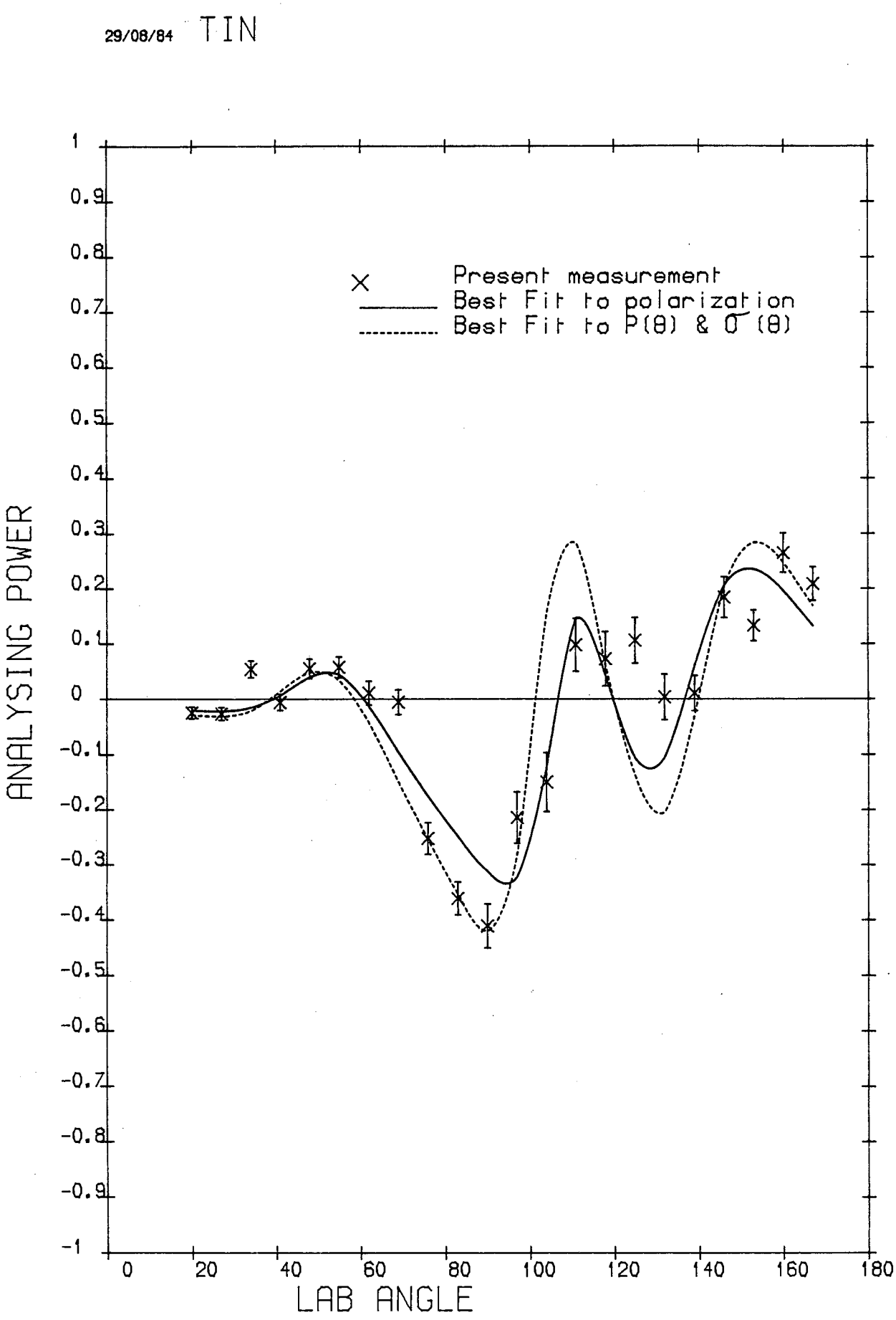
29/08/84 TIN
Present measurement
Best Fit to polarization
Best Fit to P(θ) & σ(θ)
ANALYSING POWER
LAB ANGLE
1
0.9
0.8
0.7
0.6
0.5
0.4
0.3
0.2
0.1
0
-0.1
-0.2
-0.3
-0.4
-0.5
-0.6
-0.7
-0.8
-0.9
-1
0
20
40
60
80
100
120
140
160
180

Figure 6.36.

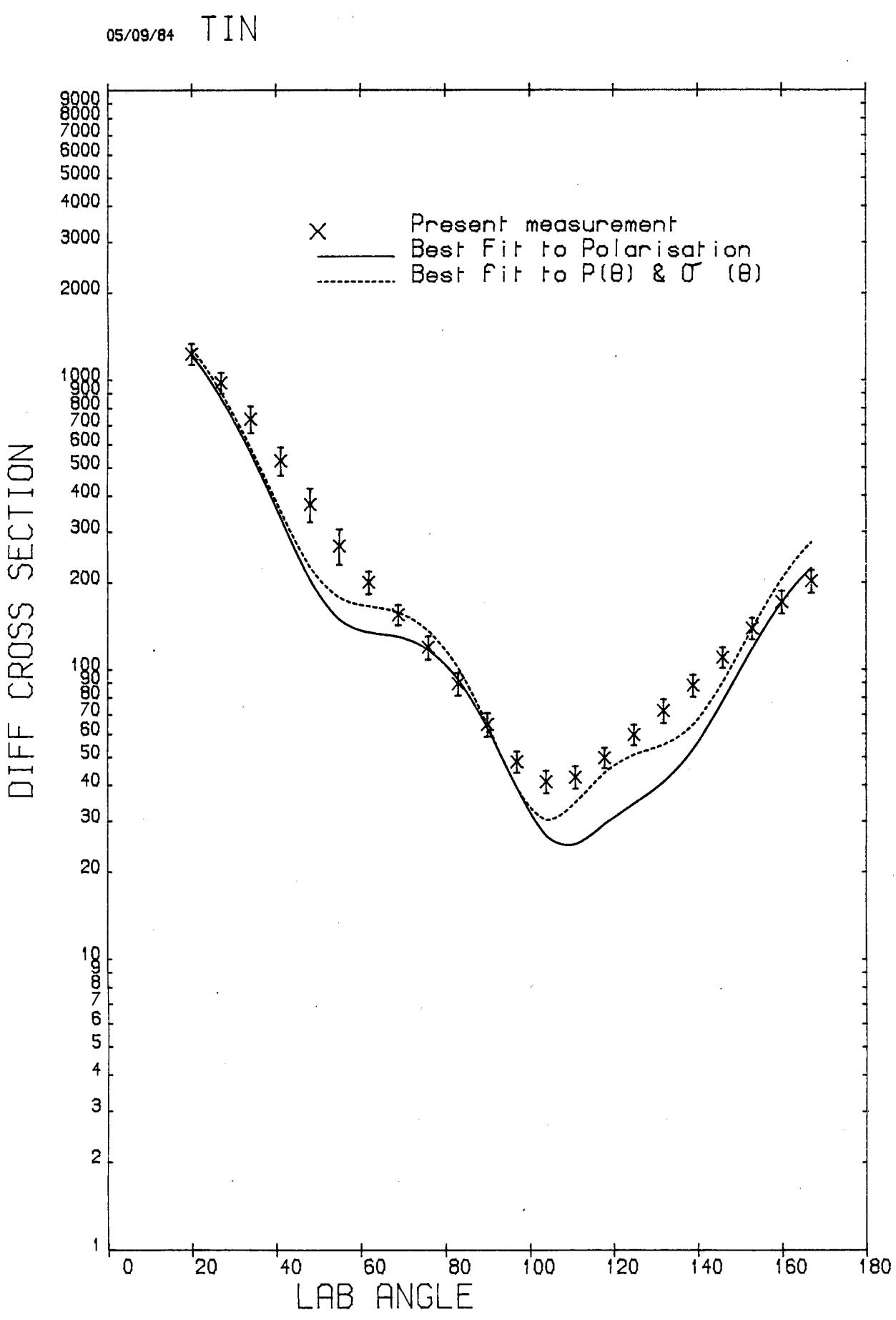
05/09/84 TIN
Present measurement
Best Fit to Polarisation
Best Fit to P(θ) & σ (θ)
DIFF CROSS SECTION
LAB ANGLE
9000
8000
7000
6000
5000
4000
3000
2000
1000
900
800
700
600
500
400
300
200
100
90
80
70
60
50
40
30
20
10
9
8
7
6
5
4
3
2
1
0
20
40
60
80
100
120
140
160
180

Figure 6.37.

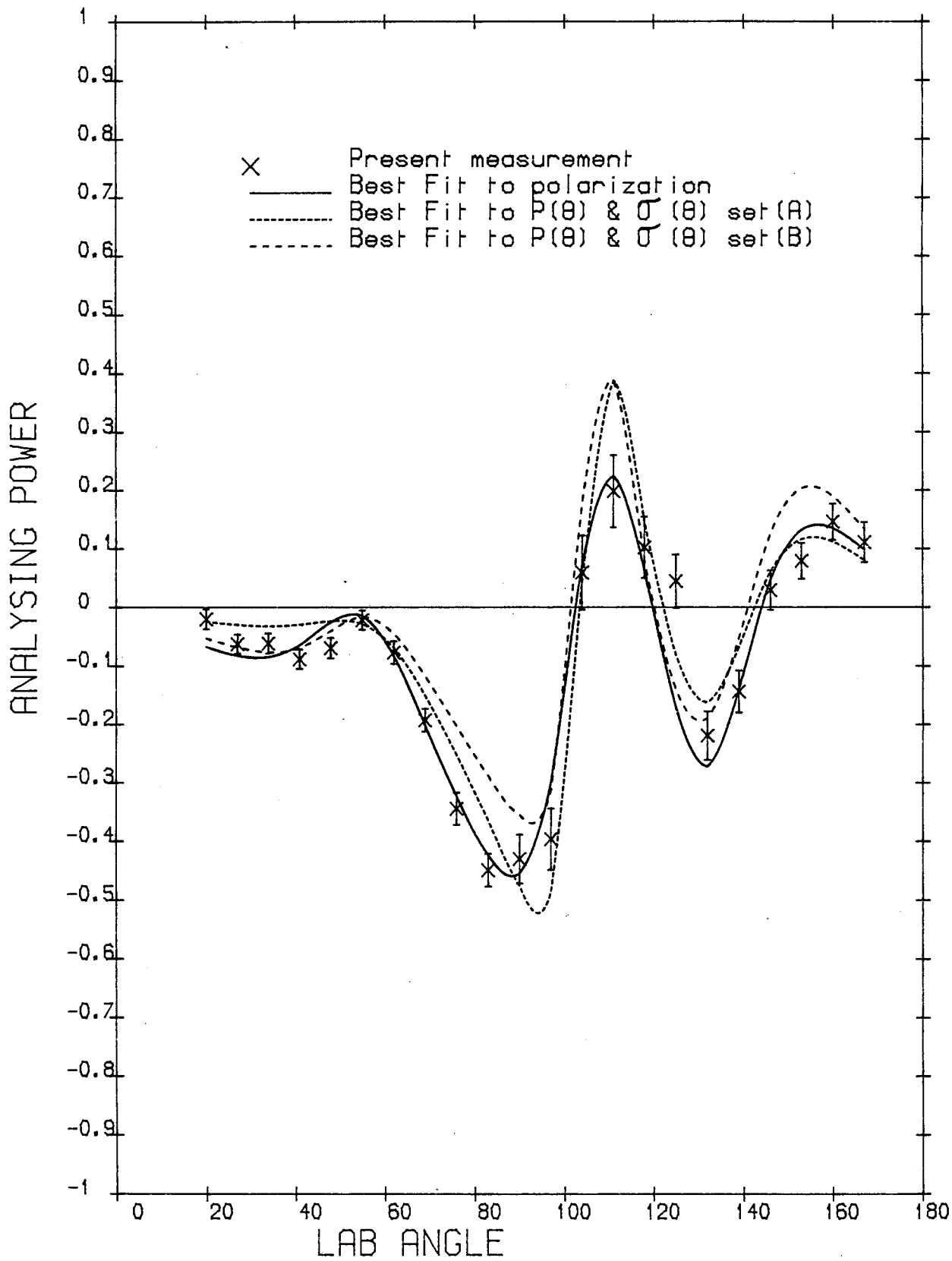
29/08/84 ANTIMONY
Present measurement
Best Fit to polarization
Best Fit to P(θ) & σ(θ) set(A)
Best Fit to P(θ) & σ(θ) set(B)
ANALYSING POWER
LAB ANGLE
1
0.9
0.8
0.7
0.6
0.5
0.4
0.3
0.2
0.1
0
-0.1
-0.2
-0.3
-0.4
-0.5
-0.6
-0.7
-0.8
-0.9
-1
0
20
40
60
80
100
120
140
160
180

Figure 6.38.

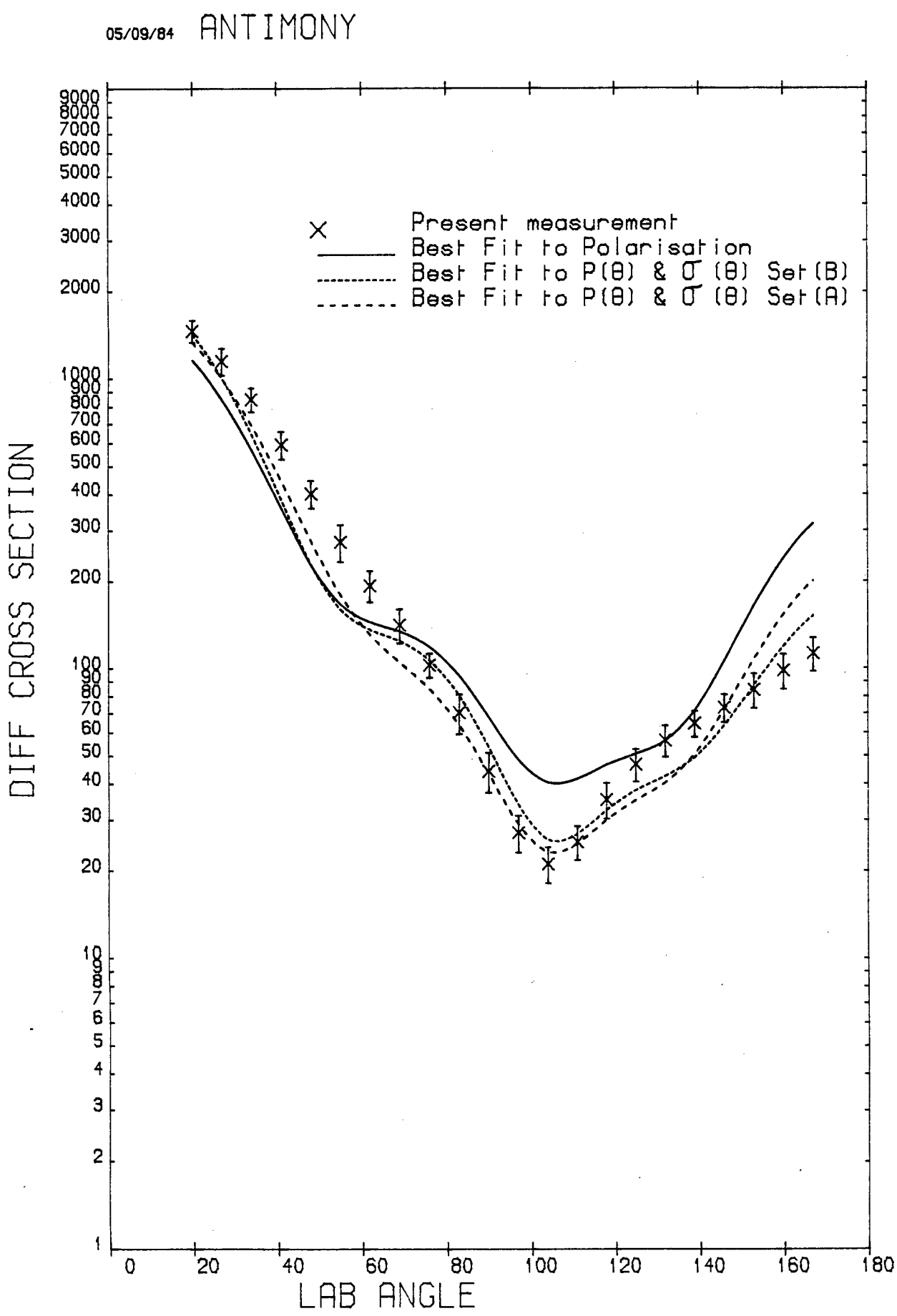
05/09/84 ANTIMONY
Present measurement
Best Fit to Polarisation
Best Fit to P(θ) & σ (θ) Set(B)
Best Fit to P(θ) & σ (θ) Set(A)
DIFF CROSS SECTION
LAB ANGLE
9000
8000
7000
6000
5000
4000
3000
2000
1000
900
800
700
600
500
400
300
200
100
90
80
70
60
50
40
30
20
10
9
8
7
6
5
4
3
2
1
0
20
40
60
80
100
120
140
160
180

Figure 6.39.

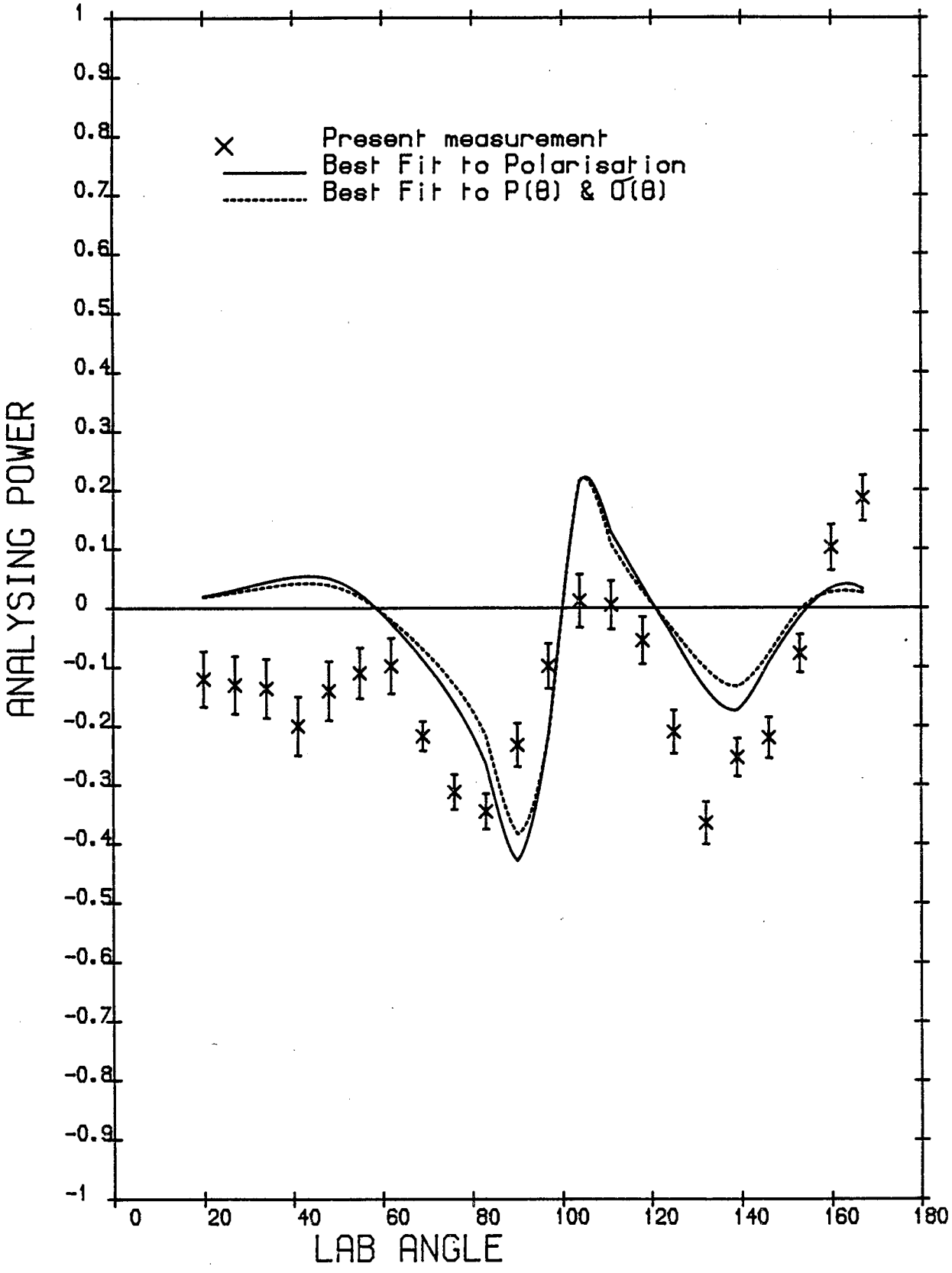
18/01/85 TELLURIUM
Present measurement
Best Fit to Polarisation
Best Fit to P(θ) & σ(θ)
ANALYSING POWER
LAB ANGLE
1
0.9
0.8
0.7
0.6
0.5
0.4
0.3
0.2
0.1
0
-0.1
-0.2
-0.3
-0.4
-0.5
-0.6
-0.7
-0.8
-0.9
-1
0
20
40
60
80
100
120
140
160
180

Figure 6.40.

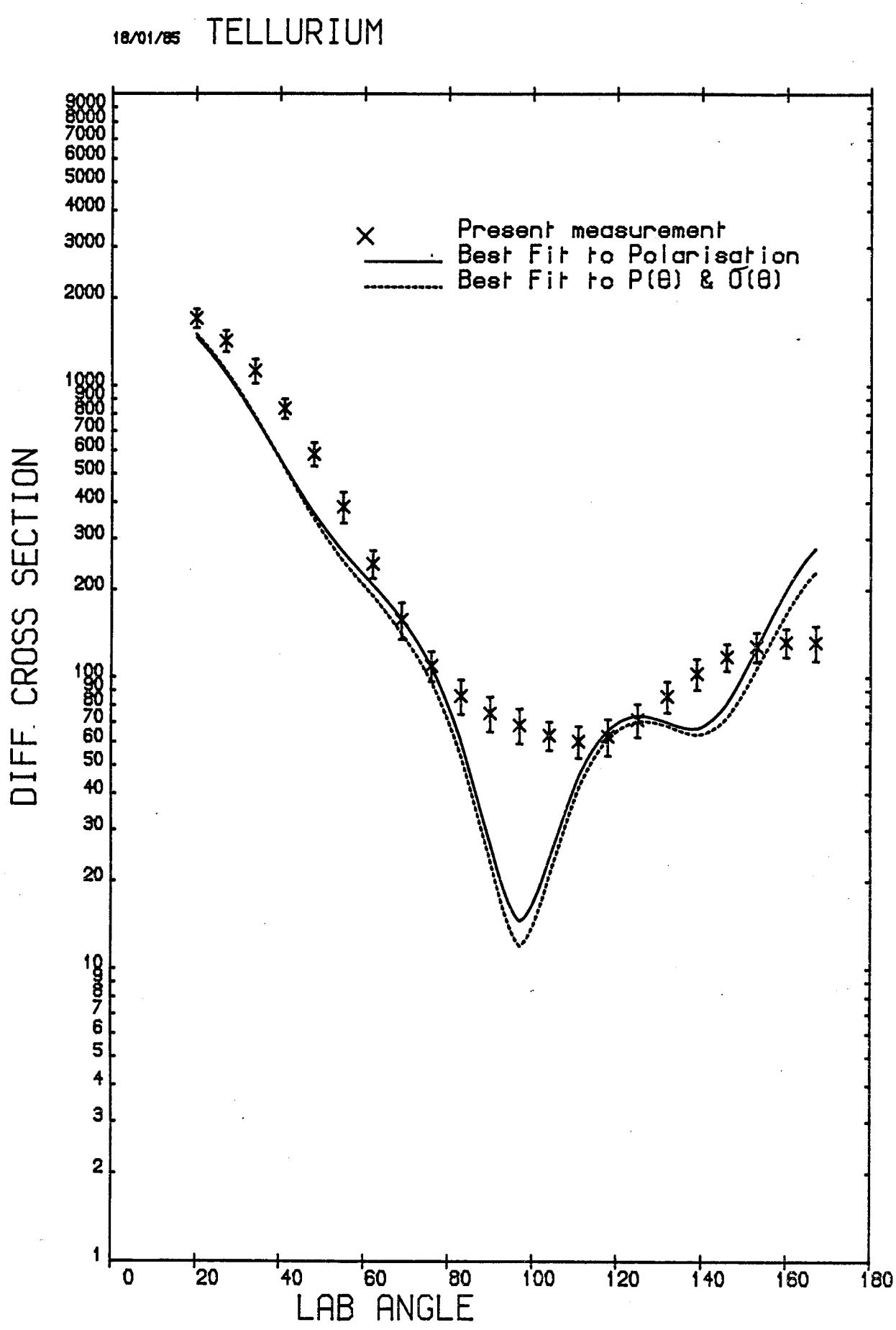
18/01/85 TELLURIUM
Present measurement
Best Fit to Polarisation
Best Fit to P(θ) & σ(θ)
DIFF. CROSS SECTION
LAB ANGLE
0
20
40
60
80
100
120
140
160
180

Figure 6.41.

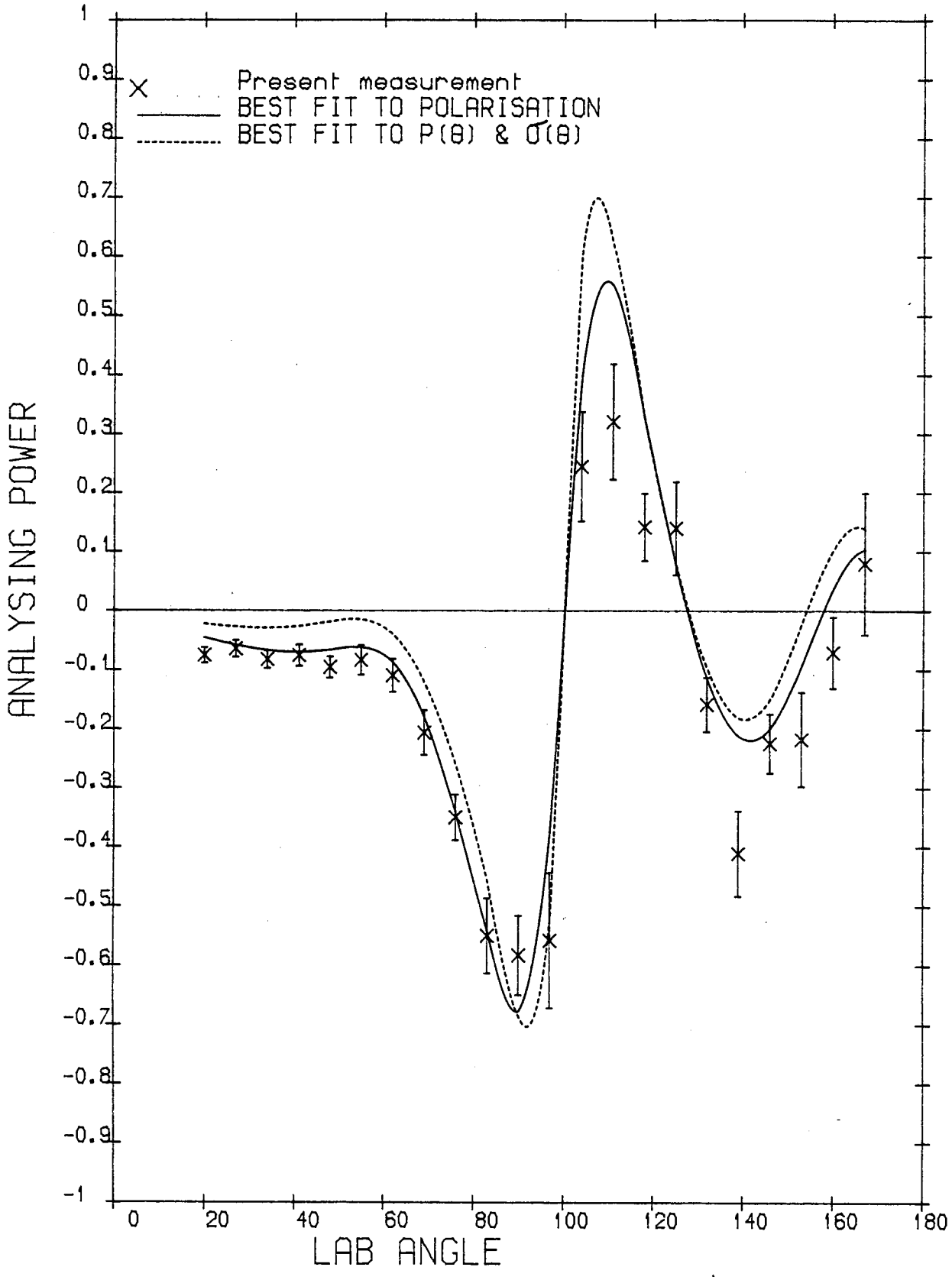
22/01/85 IODINE
Present measurement
BEST FIT TO POLARISATION
BEST FIT TO P(θ) & σ(θ)
ANALYSING POWER
LAB ANGLE
1
0.9
0.8
0.7
0.6
0.5
0.4
0.3
0.2
0.1
0
-0.1
-0.2
-0.3
-0.4
-0.5
-0.6
-0.7
-0.8
-0.9
-1
0
20
40
60
80
100
120
140
160
180

Figure 6.42.

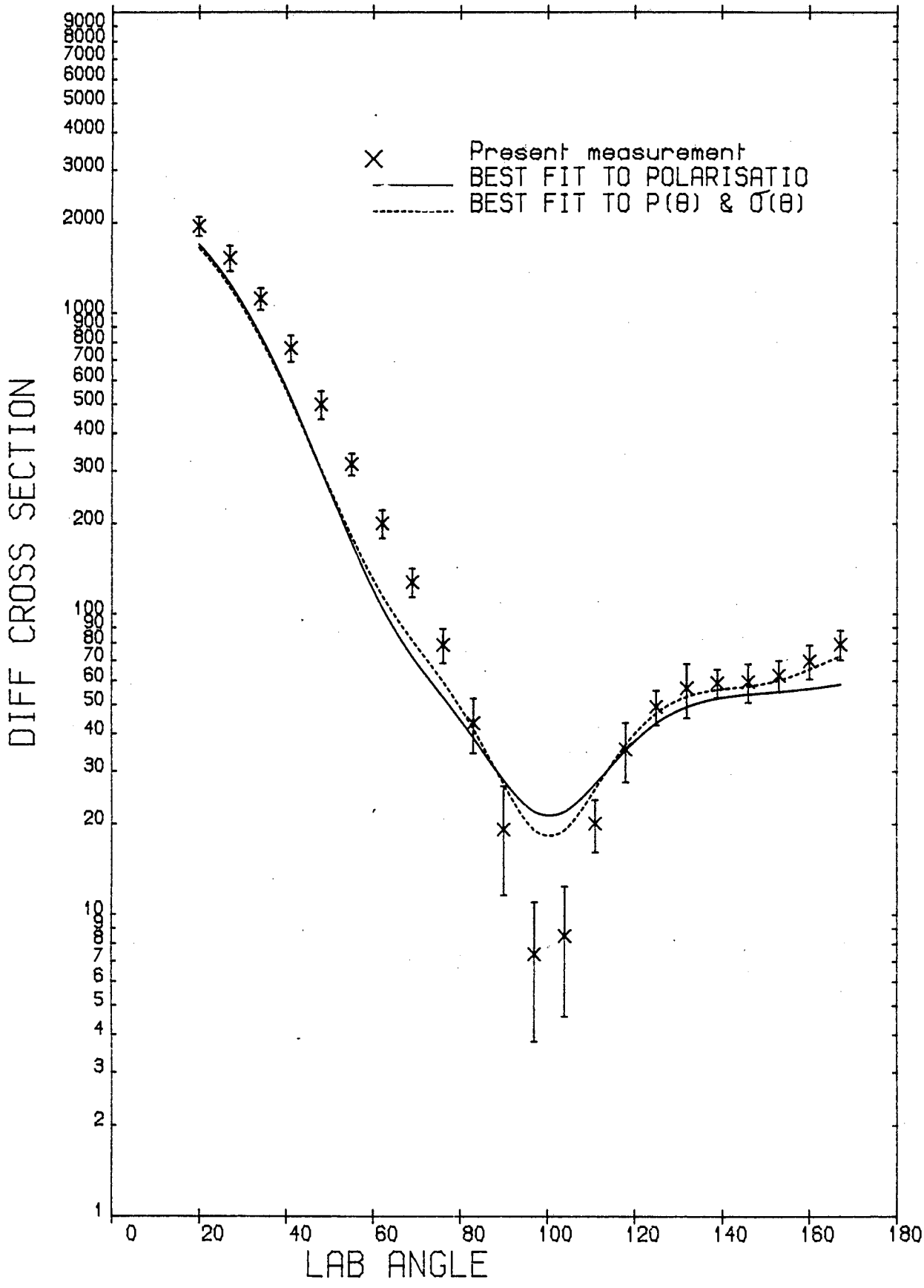
22/01/85 IODINE
Present measurement
BEST FIT TO POLARISATIO
BEST FIT TO P(θ) & σ(θ)
DIFF CROSS SECTION
LAB ANGLE
9000
8000
7000
6000
5000
4000
3000
2000
1000
900
800
700
600
500
400
300
200
100
90
80
70
60
50
40
30
20
10
8
7
6
5
4
3
2
1
0
20
40
60
80
100
120
140
160
180

Figure 6.43.

6.6 The Optical Model Analysis of the Data with a Complex Spin-Orbit Potential

As already mentioned in Section 6.2, the effect of the Imaginary Spin-Orbit term W_{so} in polarisation and cross section calculations is usually negligible. Nevertheless, recently Delaroch et al.[132] reported that for 10 MeV neutron scattering from a lead isotope ^{208}Pb this parameter has a considerable role in improving the fits to the analysing power measurements and establishes the need for $W_{so} \neq 0$ in the n + ^{208}Pb potential.

It was decided to investigate the effect of the inclusion of the Imaginary Spin-Orbit term in the present scattering data analysis at 3.0 MeV neutron energy. The Best fit parameters given in Table 6.10 for two samples, Tin and Iodine, were fixed and searches were made on the Imaginary Spin-Orbit potential. A value of 0.050 MeV for Tin and a larger value of 1.15 MeV for Iodine were obtained. Figures 6.44 and 6.45 compare experimental results with the Best fit parameters and the Best fit parameters with inclusion of the Imaginary Spin-Orbit for Tin. The same comparison is made for Iodine in Figures 6.46 and 6.47.

In the case of Tin, no difference is observed, and inclusion of $W_{so} = 1.15$ in the Best fit parameters for Iodine, resulted in a slightly better fit to the analysing power data at backward angles, while its effect at forward angle was opposite. The changes in prediction of the Iodine cross section is not considerable, and on the whole it can be concluded that for 3.0 MeV neutron scattering, the Imaginary Spin-Orbit potential does not have the importance that Delaroch et al.[132] observed for 10 MeV neutron scattering from lead.

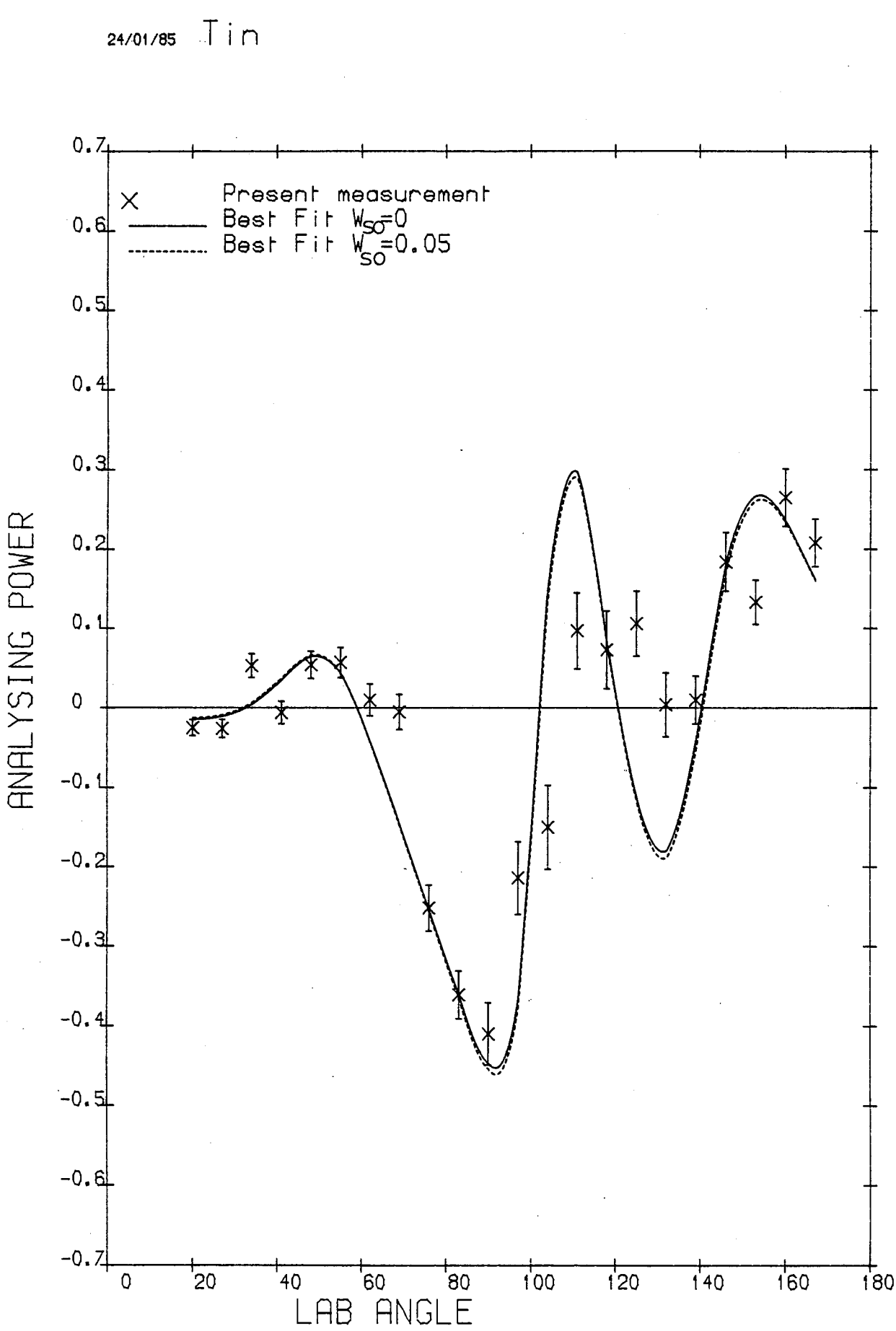
24/01/85 Tin
Present measurement
Best Fit W_{so}=0
Best Fit W_{so}=0.05
ANALYSING POWER
LAB ANGLE
0.7
0.6
0.5
0.4
0.3
0.2
0.1
0
-0.1
-0.2
-0.3
-0.4
-0.5
-0.6
-0.7
0
20
40
60
80
100
120
140
160
180

Figure 6.44.

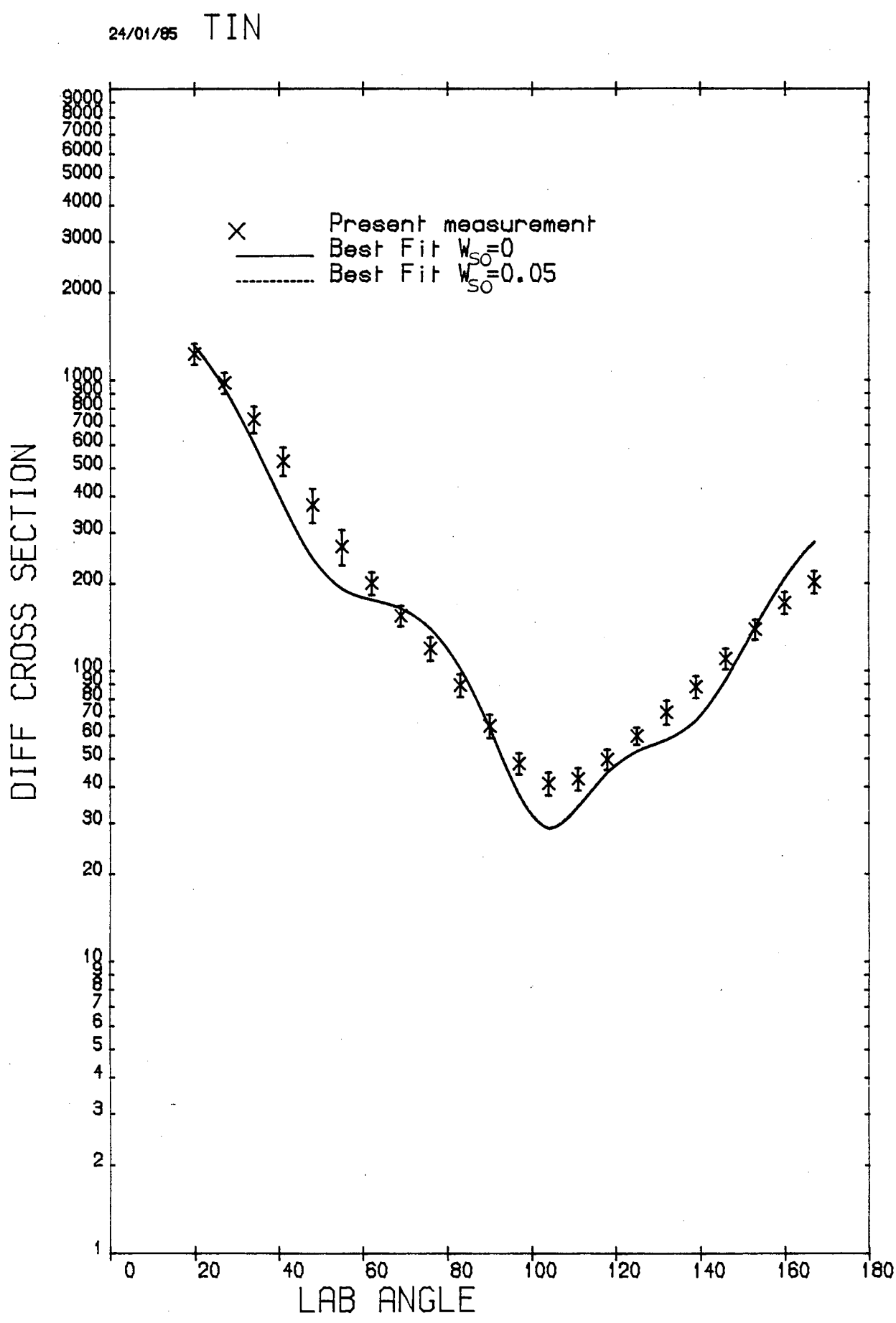
24/01/85 TIN
Present measurement
Best Fit W_{SO}=0
Best Fit W_{SO}=0.05
DIFF CROSS SECTION
LAB ANGLE
9000
8000
7000
6000
5000
4000
3000
2000
1000
800
700
600
500
400
300
200
100
80
70
60
50
40
30
20
10
8
7
6
5
4
3
2
1
0
20
40
60
80
100
120
140
160
180

Figure 6.45.

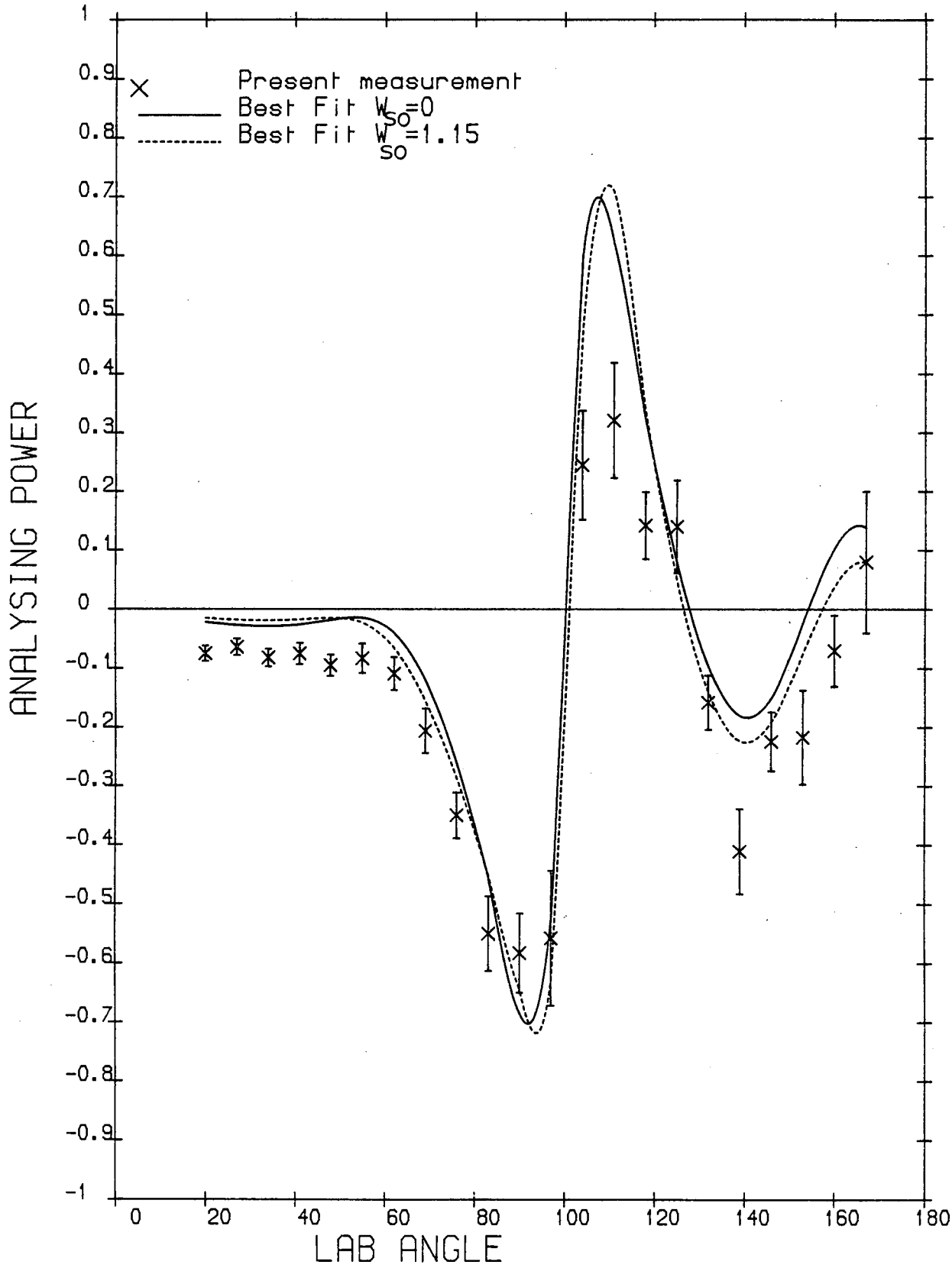
24/01/85 IODINE
Present measurement
Best Fit W_{so}=0
Best Fit W_{so}=1.15
ANALYSING POWER
LAB ANGLE
1
0.9
0.8
0.7
0.6
0.5
0.4
0.3
0.2
0.1
0
-0.1
-0.2
-0.3
-0.4
-0.5
-0.6
-0.7
-0.8
-0.9
-1
0
20
40
60
80
100
120
140
160
180

Figure 6.46.

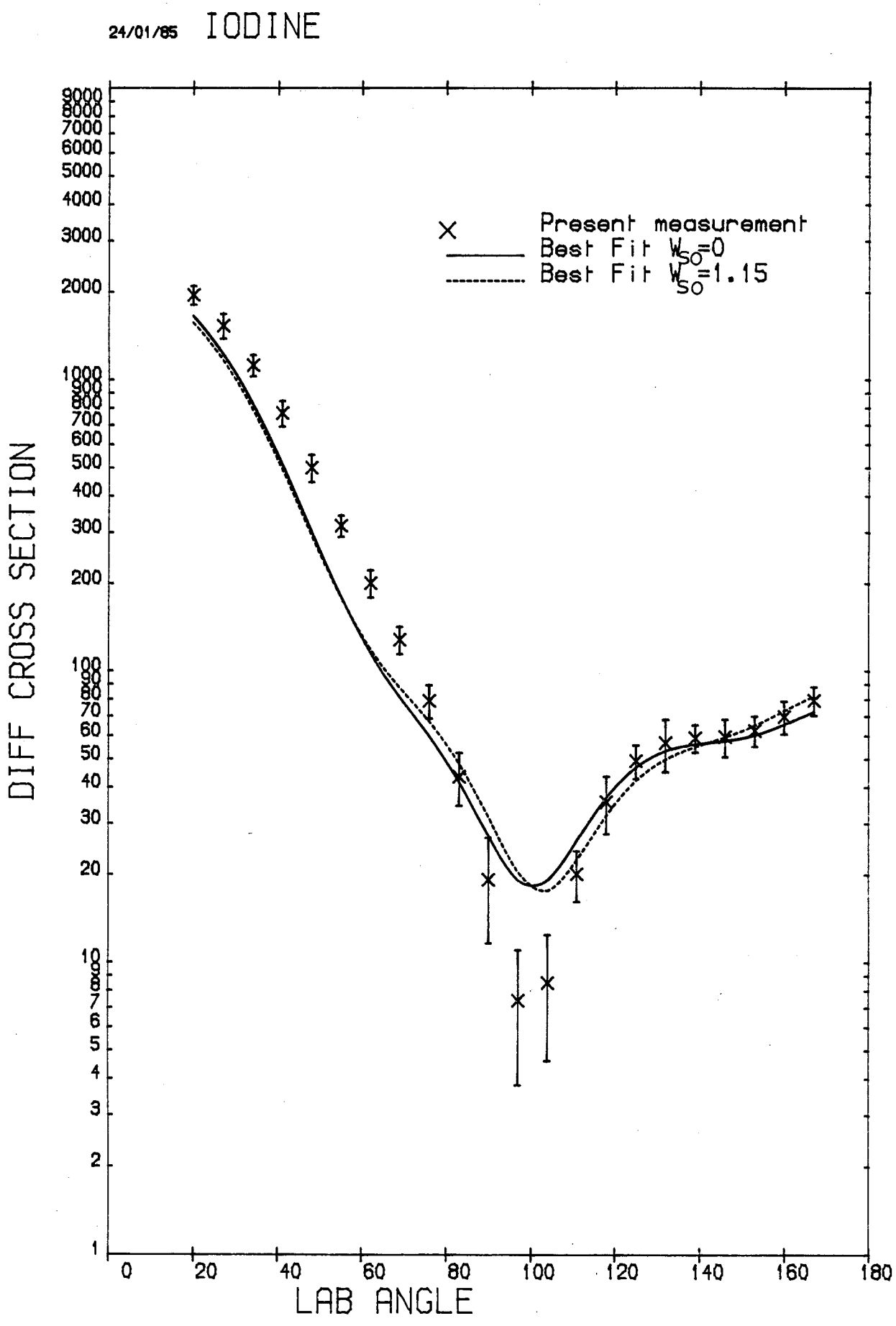
24/01/85 IODINE
DIFF CROSS SECTION
LAB ANGLE
Present measurement
Best Fit W_{SO}=0
Best Fit W_{SO}=1.15
9000
8000
7000
6000
5000
4000
3000
2000
1000
900
800
700
600
500
400
300
200
100
90
80
70
60
50
40
30
20
10
9
8
7
6
5
4
3
2
1
0
20
40
60
80
100
120
140
160
180

Figure 6.47.

6.7 Collective Nuclear Model

While nuclei near closed shells are the easiest to understand in terms of particle motion, they are very exceptional cases. Most nuclei lie between closed shells and many of these nuclei show collective nucleon effects, which lead to deformation from the spherical model. The deformation could be permanent (i.e. in the rare earth region, nuclei with $60 \lesssim Z \lesssim 72$ and $90 \lesssim Z \lesssim 110$ and in the Actinides in the region of nuclei with $150 < A < 190$ and $A > 230$ are found to have deformed ground states) or dynamic (i.e. the vibrational modes of a spherical nucleus).

In the regions $60 < A < 150$ and $190 < A < 220$ there are many even nuclei whose first two excited states with positive parity have excitation energies approximately in the ratio 2:1. Such states are presumably vibrational. The even isotopes of Cadmium (i.e. $^{114}_{48}Cd$) and even isotopes of Tellurium (i.e. $^{122}_{52}Te$) are well known vibrational nuclei. The low lying levels of both show the vibrational characteristics of deformed nuclei.

If the target nucleus is spherical, but is susceptible to vibration around that spherical shape, by substituting the radius in equation 6.2 as

$$R(\theta,\phi) = R_\alpha(1 + \sum_{\lambda\mu} \alpha_{\lambda\mu} Y_{\lambda\mu}(\theta,\phi)) \qquad (6.7.1)$$

where θ and ϕ are polar angles with respect to an arbitrary space-fixed axis and R_α is chosen to preserve volume conservation. For reality, $\alpha_{\lambda\mu} = (-)^\mu \alpha^*_{\lambda-\mu}$ volume conservation implies that

$$\frac{4\pi}{3} R_o^3 = \int_o^{2\pi} d\phi \int_o^{\pi} \sin\theta \, d\theta \int_o^{R(\theta,\phi)} r^2 dr$$

$$= \frac{4\pi}{3} R_\alpha^3 \left[1 + \frac{3\alpha_{oo}}{\sqrt{4\pi}} + \frac{3}{4\pi} \sum_{\lambda,\mu} |\alpha_{\lambda\mu}|^2 + O(\alpha^3) + \ldots \right]$$

Deformation of the type α_{oo} in the first order causes a volume change costing too much deformation energy and is therefore discarded in the treatment of low-lying modes.

Inserting equation (6.7.1) into (6.1) and expanding the latter in powers of $\Sigma\lambda_\mu \alpha_{\lambda\mu} Y_{\lambda\mu}$ and taking the series up to the second order of $\Sigma \lambda_\mu \alpha_{\lambda\mu} Y_{\lambda\mu}$, the result is a potential consisting of two components,

$$V(r, \theta, \phi) = V_{diag} + V_{couple} \qquad (6.7.2)$$

The potential V_{diag} is just the optical potential and V_{couple} gives the coupling potential between channels which have different j and I. As a result of coupling (V_{couple}), none of the quantum numbers ℓ, j, $(-)^\ell$ of the incident neutron or I_n, π_n of the target nucleus are good quantum numbers. The good quantum numbers are now

$$J = j + I_n$$

and $$\pi = \pi_n (-)^\ell \qquad (6.7.3)$$

Therefore, several partial waves whose ℓ and j satisfy (6.7.3) for a given set of J and π are coupled together through V_{couple} to form a set of coupled differential equations, which should be solved instead of the Schrödinger equation. The following deformations were considered in the calculations made in this part for Cadmium, Tin and Tellurium.

i) <<Ground state <—> One quadrupole-phonon states>> $\beta_{o2} = \beta_2$

ii) <<One-quadrupole-phonon state <—> two-quadrupole phonon states>> β_{2I}

iii) <<Ground state <—> two-quadrupole-phonon state>> β'_{o1}

β_{2I} and β'_{oI} have the following relations with $\beta_{o2} = \beta_2$ (133)

$$\beta_{2I} = q_I \beta_2$$

and

$$\beta'_{oI} = \sqrt{q_I}\, \beta_2$$

therefore $$\beta'_{oI} = \sqrt{\beta_{o2}\, \beta_{2I}}$$

iv) The deformation parameters, β''_{oI}, connect the ground state and two-phonon states. Therefore it is assumed that a non-vanishing amplitude of the one-phonon type state is admixed into that of the two phonon state. Thus, if $I = 2$ this will mean that a (small) amplitude of the one-phonon 2^+ state has been admixed into that of the second 2^+ state. Assuming that the amplitude of this admixed one-phonon like state is written as q'_I, it can be determined(133) that

$$\beta''_{oI} = q'_I \beta_I$$

The parameter β_2 was taken from <<Shigeya Tanaka -JAERT-M5984>>(46) for Cadmium and Tin equal to 0.19 and 0.113 respectively. A value of 0.18 for ^{126}Te introduced by Tamura(134) for 12.0 MeV proton scattering was used for the Tellurium sample.

The values of q_I and q'_I were obtained by a search procedure for the most abundant isotope of Tin (^{120}Sn), until the results of the theoretical coupled channels calculation using the "JUPITOR1"(135) computer code for both differential cross section and analysing power

showed a good agreement with the experimental data for the natural Tin sample. The same values of q_I and q'_I were used for the other nuclei.

Finally in this work, we followed that Tamura[133] concluded in his analysis on the Inelastic Scattering of α-particles by ^{60}Ni, as relations which should be held between deformation parameters of this kind of couple channels data analysis, they are,

$$\beta_{20} < \beta_{22} < \beta_{24}$$

$$|\beta''_{o2}| < |\beta''_{oo}| < \beta''_{o4}$$

$$\beta''_{oo} < 0, \quad \beta''_{o2} \geq 0, \quad \beta''_{o4} > 0$$

As mentioned in the beginning of this section, some nuclei are permanently deformed. In this case the radius parameter may be expressed as

$$R = R_\alpha(1 + \sum_\lambda \beta_\lambda Y_{\lambda o}(\theta, \phi) \qquad (6.7.4)$$

β_λ = deformation parameter.

Substituting equation (6.7.4) in equation (6.1) and expanding this resulting expression in terms of $\sum_\lambda \beta_\lambda Y_{\lambda o}(\theta,\phi)$, one gets exactly the same expression as (6.7.2).

None of the sample nuclei measured in this work is within the regions of permanently deformed nuclei.

6.7.1 Cadmium

Four even isotopes of Cadmium (i.e. $^{110-116}Cd$) are known as vibrational nuclei[46,134]. The coupling of first and second collective excited states of even isotopes of Cadmium (0^+, 2^+, I) were considered.

^{110}Cd $(0^+, 2^+, 0^+)$

^{112}Cd $(0^+, 2^+, 0^+)$

^{114}Cd $(0^+, 2^+, 0^+)$

^{116}Cd $(0^+, 2^+, 2^+)$

I, depending on different isotopes having different order of $(0^+, 2^+, 4^+)$ for the triad of 2 phonon states of energy of the order of two times the energy of the first excited state. The first state of the triad was taken into the calculation.

The odd isotopes of Cadmium, ^{111}Cd and ^{113}Cd were considered as odd-A vibrational (spherical) nuclei, and the coupling of following levels were taken into the coupled channels calculation

^{111}Cd	$1/2^+$	Ground state
	$5/2^+$	0.245 MeV
	$3/2^+$	0.342 MeV
	$1/2^+$	1.020 MeV
^{113}Cd	$1/2^+$	Ground state
	$3/2^+$	0.299 MeV
	$5/2^+$	0.316 MeV
	$1/2^+$	0.760 MeV

The ^{111}Cd and ^{113}Cd are odd-A nuclei with neighbouring even-even nuclei ^{110}Cd, ^{112}Cd, and ^{114}Cd or ^{114}Sn, whose properties resemble those of collective vibrational nuclei[136]. Therefore in the single particle core-excitation model the low lying levels of ^{111}Cd and ^{113}Cd are considered to be multiplets arising from the coupling of a $3s_{\frac{1}{2}}$ particle to the even-even core states which should be the same as those in the neighbouring even-even nuclei. Hence, coupling of a $3s_{\frac{1}{2}}$ particle to the first (2^+) state of the core produces $^{3}/_{2}^{+}$ and $^{5}/_{2}^{+}$ states in ^{111}Cd and ^{113}Cd, where the total energy of these two states is comparable with the first (2^+) state of either ^{110}Cd, ^{112}Cd or ^{114}Cd. Then coupling of a $3s_{\frac{1}{2}}$ particle to the second (0^+) state of either ^{110}Cd, ^{112}Cd or ^{114}Cd could produce a $(\frac{1}{2}^+)$ state in ^{111}Cd and ^{113}Cd.

Fig. 6.48 shows the low-lying levels of ^{110}Cd, ^{111}Cd, ^{112}Cd, ^{113}Cd and ^{114}Cd. The other levels between the above mentioned levels in ^{111}Cd and ^{113}Cd are the result of the $3s_{\frac{1}{2}}$ particle coupled to the higher excitation levels of the even-even neighbouring nuclei.

Figures 6.49 and 6.50 illustrate the consistency of the calculated results for all odd and even isotopes of Cadmium.

The deformation parameter β_2 was taken from ref. (46) equal to 0.19 which is given for only even isotopes. This value was also used in this calculation for odd isotopes, which produced satisfactory results, as illustrated in Figures 6.49 and 6.50. The other deformation parameters, as already mentioned in Section 6.7, were derived from $\beta_2 = 0.19$ as described in Section 6.7 and are tabulated in Table 6.11.

TABLE 6.11

Element	β_{o2}	$I_{even\ A}$	$I_{odd\ A}$	β_{2I}	β'_{oI}	β''_{oI}
Cd	0.19	0^+	$1/2^+$	0.0925	0.1326	-0.0504
		2^+	$(3/2^+, 5/2^+)$	0.0992	0.1362	0.000
		$I(0^+\ 2^+)$ or	$1/2^+$	0.1093	0.1446	0.0841

Figures 6.51 - 6.54 compare the present measurements with the prediction of the coupled channels potential for the Best Fit Optical model potential and those of Becchetti and Greenlees and Rosen et al. Table 6.12 compares the relative success of the spherical optical model and coupled channels calculations for various potentials. The coupled channels calculations slightly worsened the fit to the analysing power data, while there is not much change in the fit to the cross section data. Becchetti and Greenlees parameters showed not much change from optical model calculations, while Rosen's parameters produced a poorer fit to the analysing power data.

TABLE 6.12

Comparison of Spherical Optical Model and Coupled Channel Calculations

Parameters	Coupled Channel			Optical Model		
	X^2_{Comb}	X^2_P	X^2_σ	X^2_{Comb}	X^2_P	X^2_σ
Best Fit	13.21	20.51	5.90	9.42	13.73	5.12
Becchetti & Greenlees	35.62	56.25	15.0	34.19	56.24	12.14
Rosen et al.	46.25	79.02	13.48	34.31	54.73	13.90
Smith et al.	49.53	93.91	5.14	59.18	112.95	5.41
Zijp & Jonker	67.64	130.26	5.03	76.34	148.15	4.53

Figure.6.48

Low lying Excited States of Cadmium Isotopes

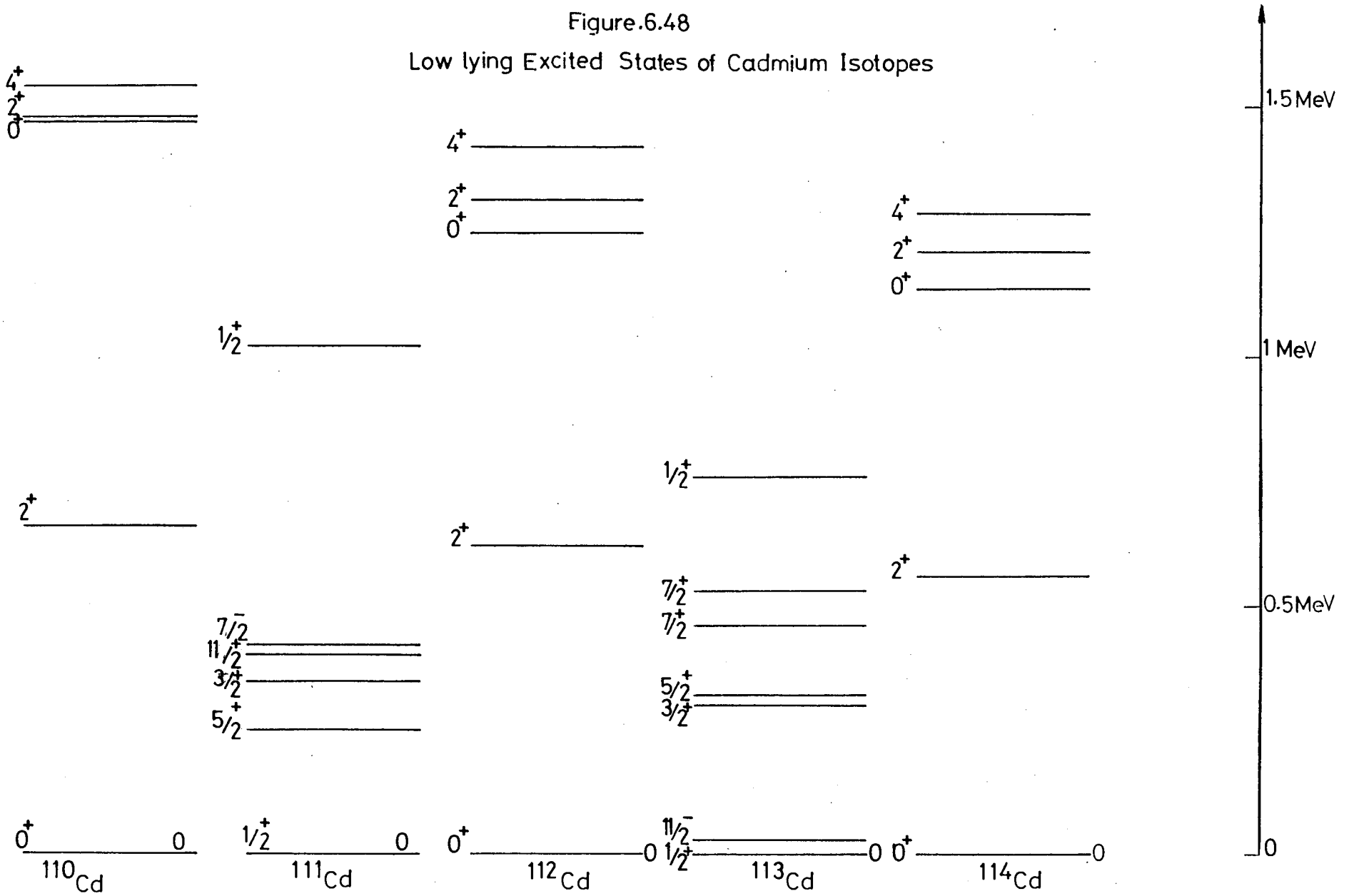

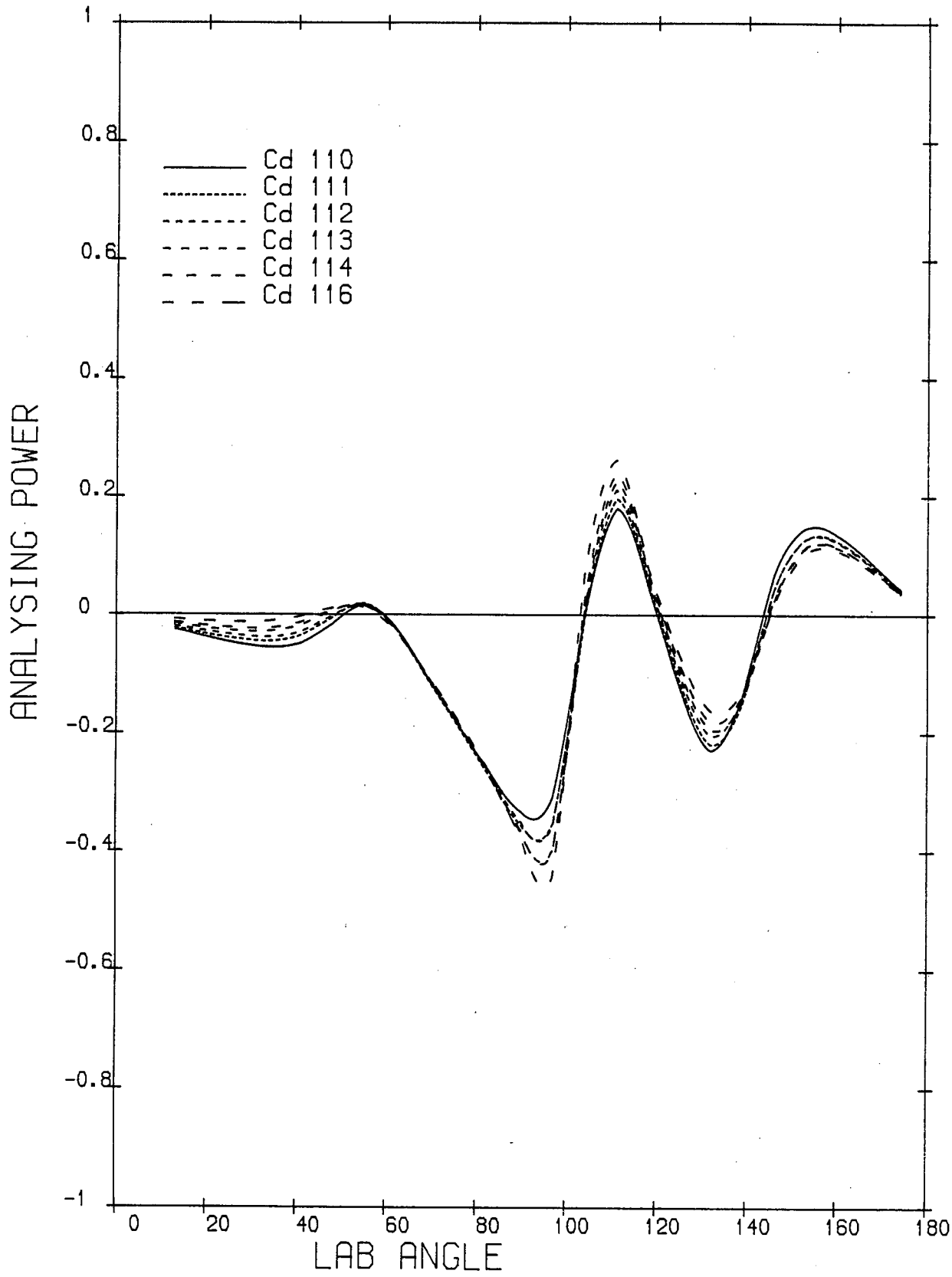
24/01/85 CADMIUM
Cd 110
Cd 111
Cd 112
Cd 113
Cd 114
Cd 116
ANALYSING POWER
LAB ANGLE
1
0.8
0.6
0.4
0.2
0
-0.2
-0.4
-0.6
-0.8
-1
0
20
40
60
80
100
120
140
160
180

Figure 6.49.

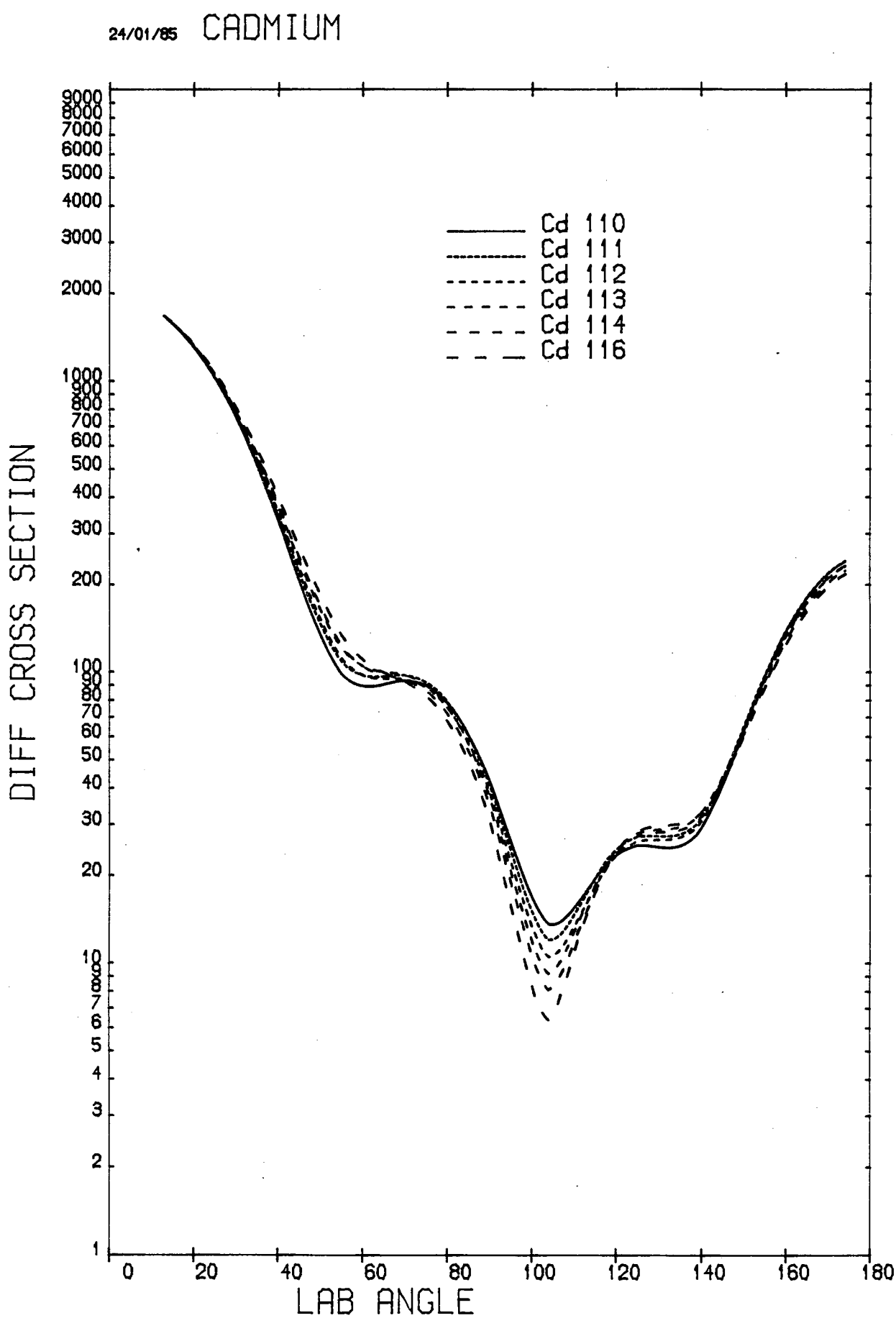
24/01/85 CADMIUM
Cd 110
Cd 111
Cd 112
Cd 113
Cd 114
Cd 116
DIFF CROSS SECTION
LAB ANGLE
9000
8000
7000
6000
5000
4000
3000
2000
1000
900
800
700
600
500
400
300
200
100
90
80
70
60
50
40
30
20
10
9
8
7
6
5
4
3
2
1
0
20
40
60
80
100
120
140
160
180

Figure 6.50.

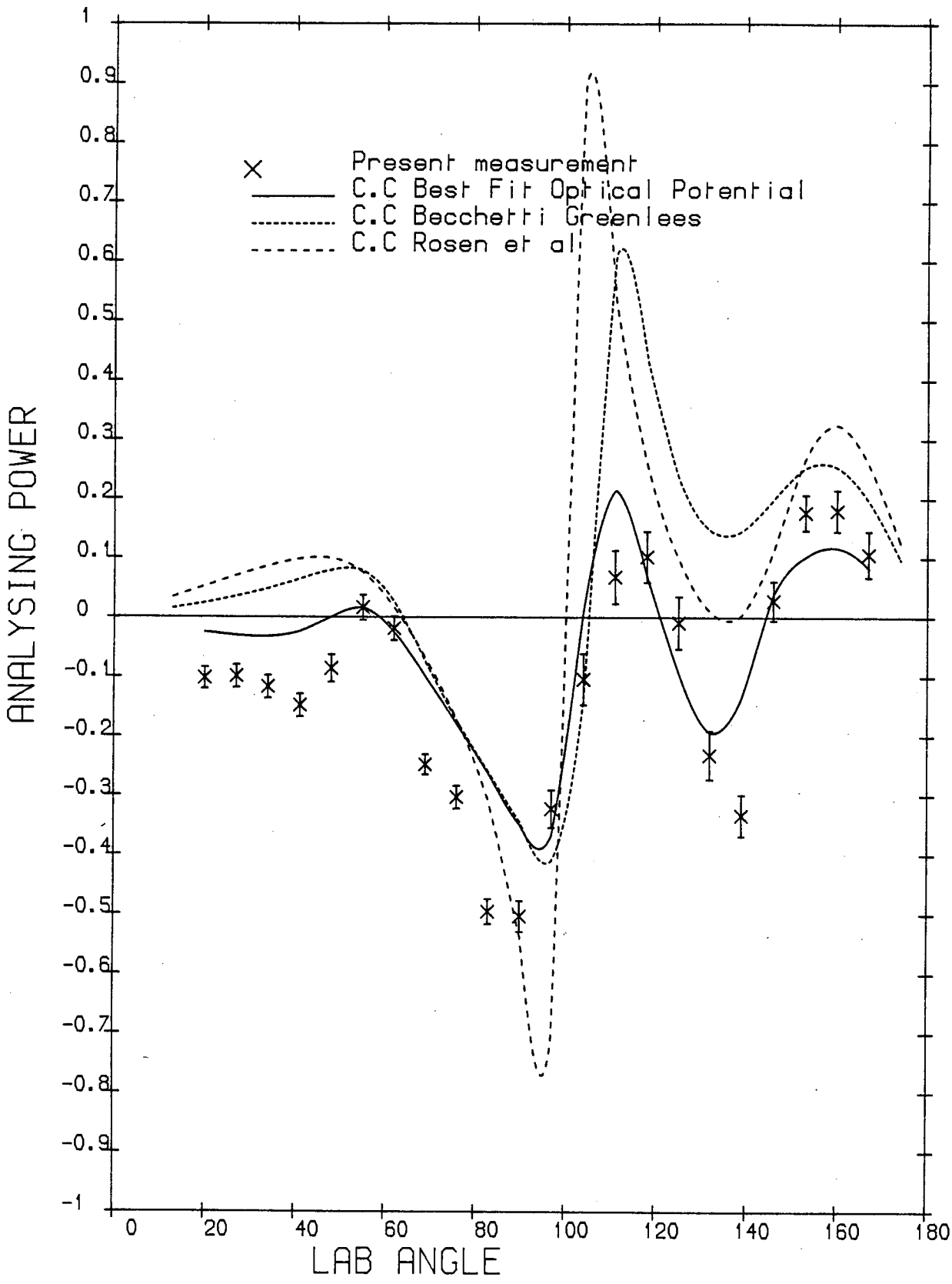
24/01/85 CADMIUM
Present measurement
C.C Best Fit Optical Potential
C.C Becchetti Greenlees
C.C Rosen et al
ANALYSING POWER
LAB ANGLE
1
0.9
0.8
0.7
0.6
0.5
0.4
0.3
0.2
0.1
0
-0.1
-0.2
-0.3
-0.4
-0.5
-0.6
-0.7
-0.8
-0.9
-1
0
20
40
60
80
100
120
140
160
180

Figure 6.51.

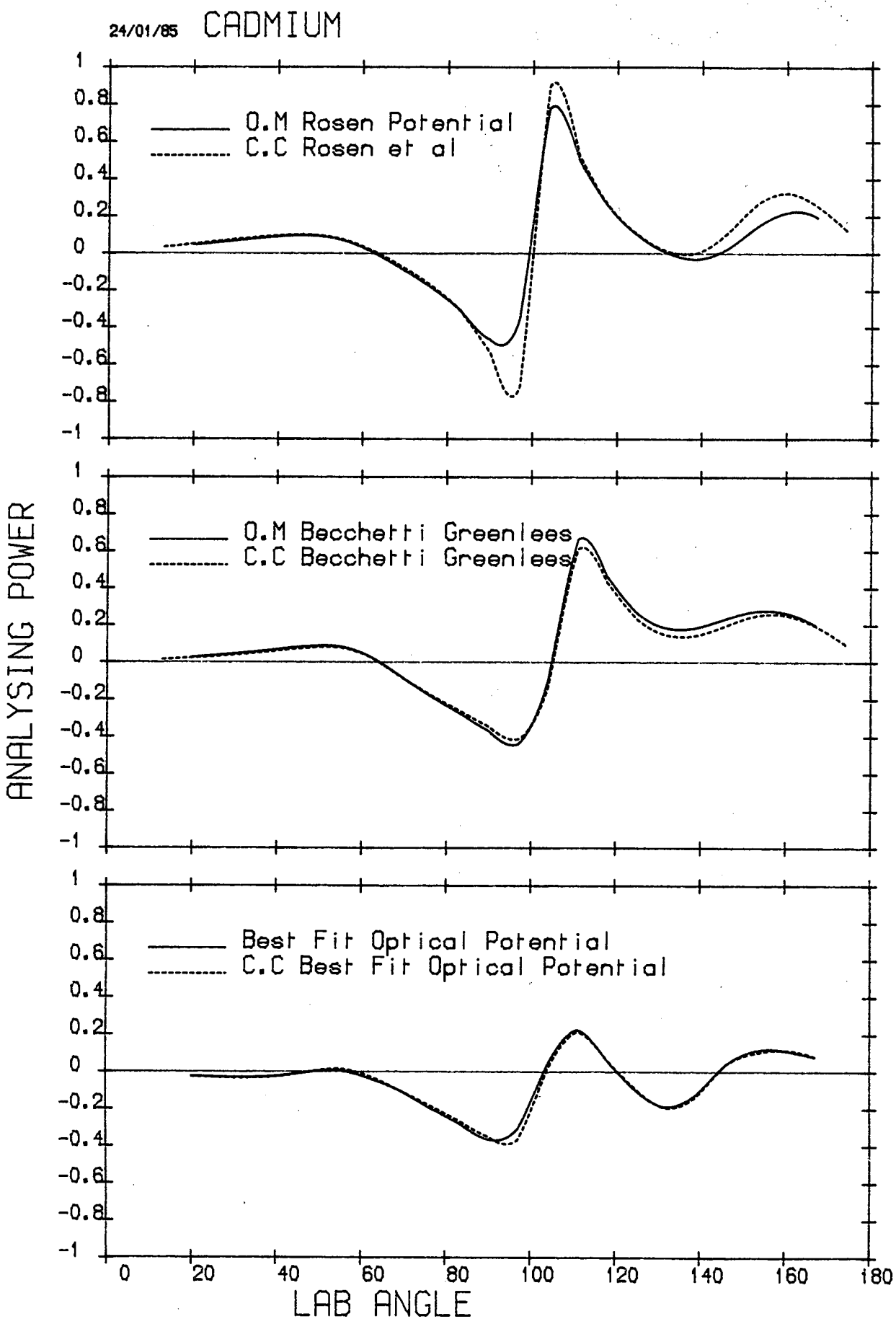
24/01/85 CADMIUM
O.M Rosen Potential
C.C Rosen et al
O.M Becchetti Greenlees
C.C Becchetti Greenlees
Best Fit Optical Potential
C.C Best Fit Optical Potential
ANALYSING POWER
LAB ANGLE
1
0.8
0.6
0.4
0.2
0
-0.2
-0.4
-0.6
-0.8
-1
0
20
40
60
80
100
120
140
160
180

Figure 6.52.

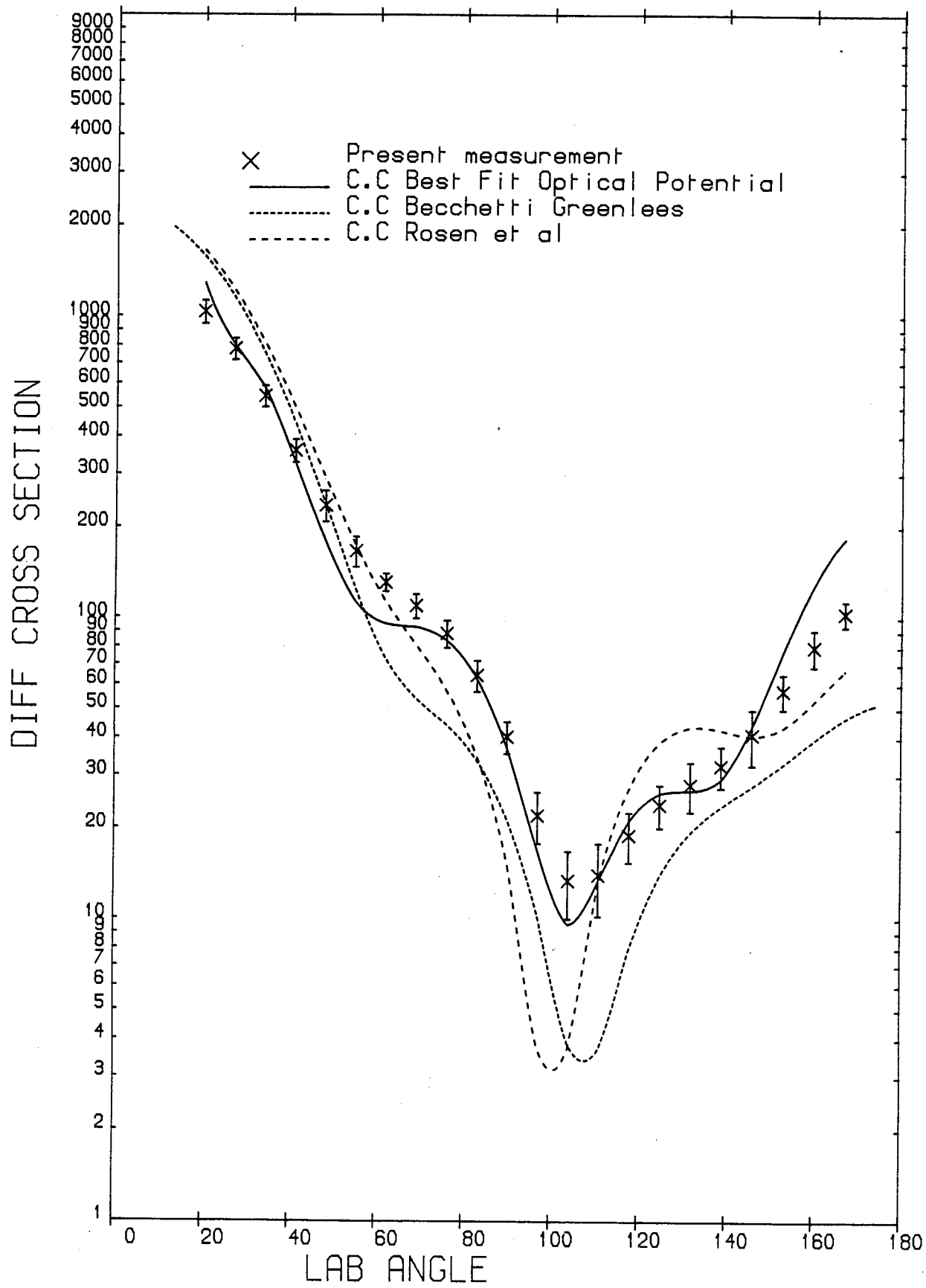
24/01/85 CADMIUM
Present measurement
C.C Best Fit Optical Potential
C.C Becchetti Greenlees
C.C Rosen et al
DIFF CROSS SECTION
LAB ANGLE
9000
8000
7000
6000
5000
4000
3000
2000
1000
900
800
700
600
500
400
300
200
100
90
80
70
60
50
40
30
20
10
9
8
7
6
5
4
3
2
1
0
20
40
60
80
100
120
140
160
180

Figure 6.53.

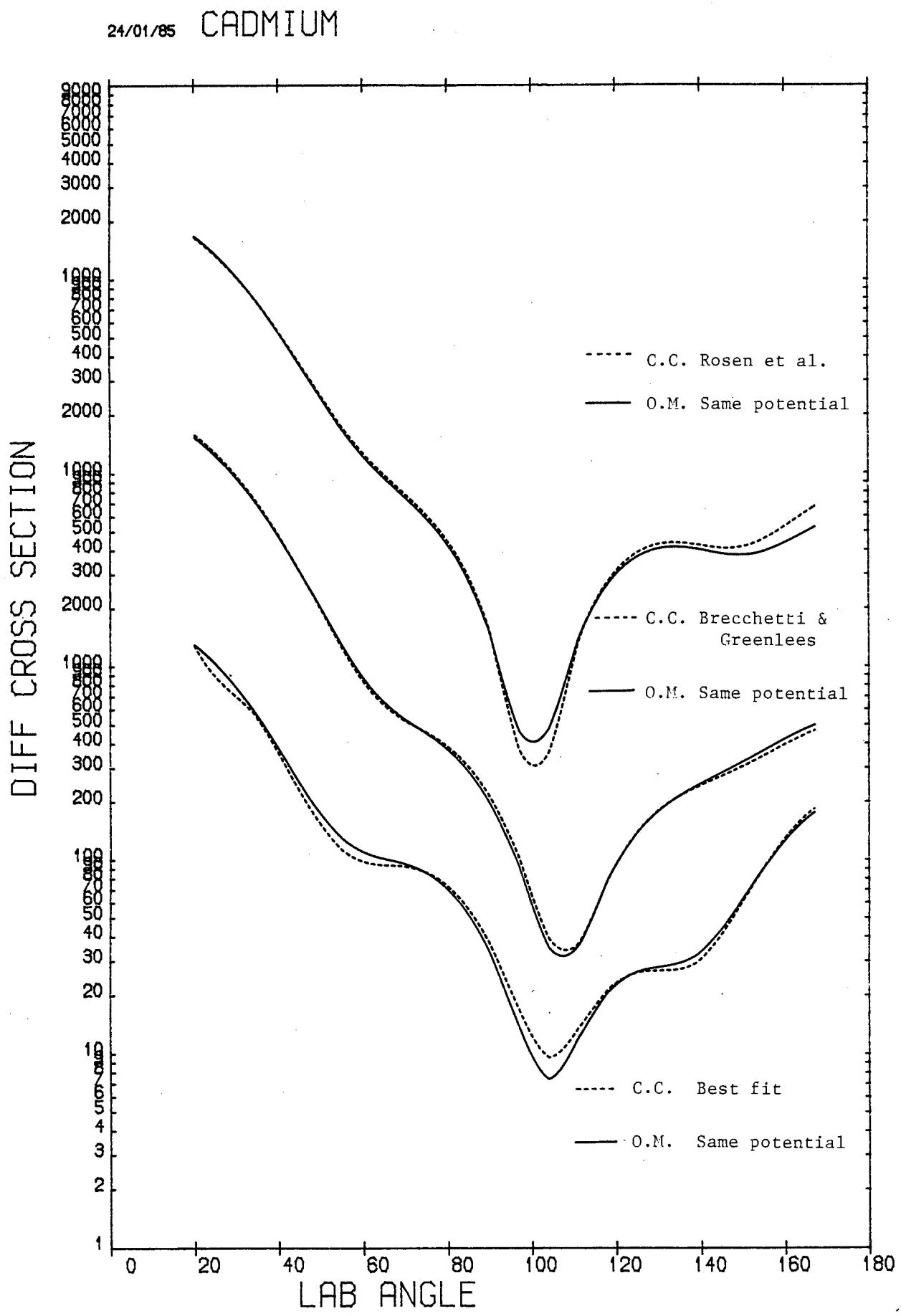
24/01/85 CADMIUM
DIFF CROSS SECTION
LAB ANGLE
C.C. Rosen et al.
O.M. Same potential
C.C. Brecchetti & Greenlees
O.M. Same potential
C.C. Best fit
O.M. Same potential

Figure 6.54.

6.7.2 Tin

The even isotopes of Tin are known as vibrational nuclei[46]. The five even isotopes of Tin comprise 82% of the natural Tin sample used in this measurement, while two odd isotopes have no more than 16% abundances together.

The coupling of first and second collective excited states of the even isotopes of Tin (0^+, 2^+, I) were considered.

The odd isotopes of Tin were considered as odd-A vibrational (spherical) nuclei, and the coupling of ($^1/2^+$, $^3/2^+$, $^5/2^+$, $^3/2^+$, $^5/2^+$) excited states were taken into coupled channels calculation. The ^{117}Sn and ^{119}Sn are odd-A nuclei with neighbouring even-even nuclei ^{116}Sn and ^{118}Sn in the case of ^{117}Sn, ^{118}Sn and ^{120}Sn in the case of ^{119}Sn, whose properties resemble those of collective vibrational nuclei[136]. Therefore, coupling of a $2S_{\frac{1}{2}}$ particle to the first (2^+) state of the even-even core produces states in ^{117}Sn and ^{119}Sn with spins and parities $^3/2^+$ and $^5/2^+$. Then, coupling of a $3S_{\frac{1}{2}}$ particle to the second (2^+) state of ^{118}Sn could give states with spin ($^3/2^+$, $^5/2^+$) in ^{117}Sn, also, coupling of a $3S_{\frac{1}{2}}$ particle to the second (2^+) of ^{118}Sn or ^{120}Sn could give states with spins and parities $^3/2^+$ and $^5/2^+$ in ^{119}Sn whose energies are comparable with the first (2^+) state of either ^{116}Sn, ^{118}Sn or ^{120}Sn.

Fig. 6.55 shows the low lying levels of ^{116}Sn, ^{117}Sn, ^{118}Sn, ^{119}Sn and ^{120}Sn for comparison. The ($^7/2^+$) state of ^{117}Sn and ($^7/2^+$) state of ^{119}Sn are the results of a $3S_{\frac{1}{2}}$ particle coupled to the (4^+) state of either neighbouring even-even nuclei, while ($^{11}/2^-$) ^{117}Sn and ($^{11}/2^-$) ^{119}Sn could be the result of higher order of multiple moment of 5 phonon transition, somehow brought down in energy.

Since the computing time for the calculation is too long, coupling of $(^{1}/_{2}^{+}, {}^{3}/_{2}^{+}, {}^{5}/_{2}^{+})$ was compared with the coupling of $(^{1}/_{2}^{+}, {}^{3}/_{2}^{+}, {}^{5}/_{2}^{+}, {}^{3}/_{2}^{+}, {}^{5}/_{2}^{+})$ using the Best fit optical model parameters for ^{119}Sn, and no difference was observed. Therefore the coupling of $(^{1}/_{2}^{+}, {}^{3}/_{2}^{+}, {}^{5}/_{2}^{+})$ only was considered, when comparing the results due to different sets of optical model parameters of several authors, Table 6.13.

The consistency of the calculated results for all odd and even isotopes of Tin can be seen in Figures 6.56 and 6.57, which confirms the interpretation of the odd isotopes states. The deformation parameter $\beta_2 = 0.113$ is taken from ref. (46), which is given only for even isotopes of Tin. The same value was also used for odd isotopes in this analysis and gave satisfactory results. Table 6.14 gives the deformation parameters.

The calculated values of differential cross section and analysing power for Tin using the Best fit, Becchetti and Greenless and Rosen's optical potential associated with the deformation parameters of the coupled channels calculations are shown in Figures 6.58 - 6.61.

The conclusions are the same as those for Cadmium for the Best fit and Becchetti and Greenlees, while Rosen's parameters produced a poorer fit to the analysing power and a better fit to the cross section data.

TABLE 6.13

Comparison of Spherical Optical Model and Coupled Channel Calculations

Parameters	Coupled Channel X^2_{Comb}	X^2_P	X^2_σ	Optical Model X^2_{Comb}	X^2_P	X^2_σ
Best Fit	5.48	6.39	4.57	4.42	4.66	4.18
Rosen et al.	13.28	16.18	10.38	16.88	11.40	22.35
Becchetti & Greenlees	15.92	10.12	21.73	17.87	8.90	26.84
Strizhak	16.14	21.26	11.01	13.11	11.31	14.91
Zijp & Jonker	16.67	20.08	13.26	16.49	12.87	20.10
Gupta et al.	19.02	31.45	6.59	16.20	23.91	8.50
Tanaka (^{120}Sn)	23.13	42.43	3.84	20.98	37.80	4.16

TABLE 6.14

The Values of the Parameter β Used in the Calculations

Element	β_{o2}	I_{evenA}	I_{oddA}	β_{2J}	β'_{oI}	β''_{oI}
Tin	0.113	0^+	$1/2^+$	0.055	0.079	-0.030
		2^+	$(3/2^+, 5/2^+)$	0.059	0.081	0.000
		$i(0,2,4)^+$	$(3/2^+, 5/2^+)$	0.065	0.086	0.050

Figure .6.55
Low lying Excited States of Tin Isotopes

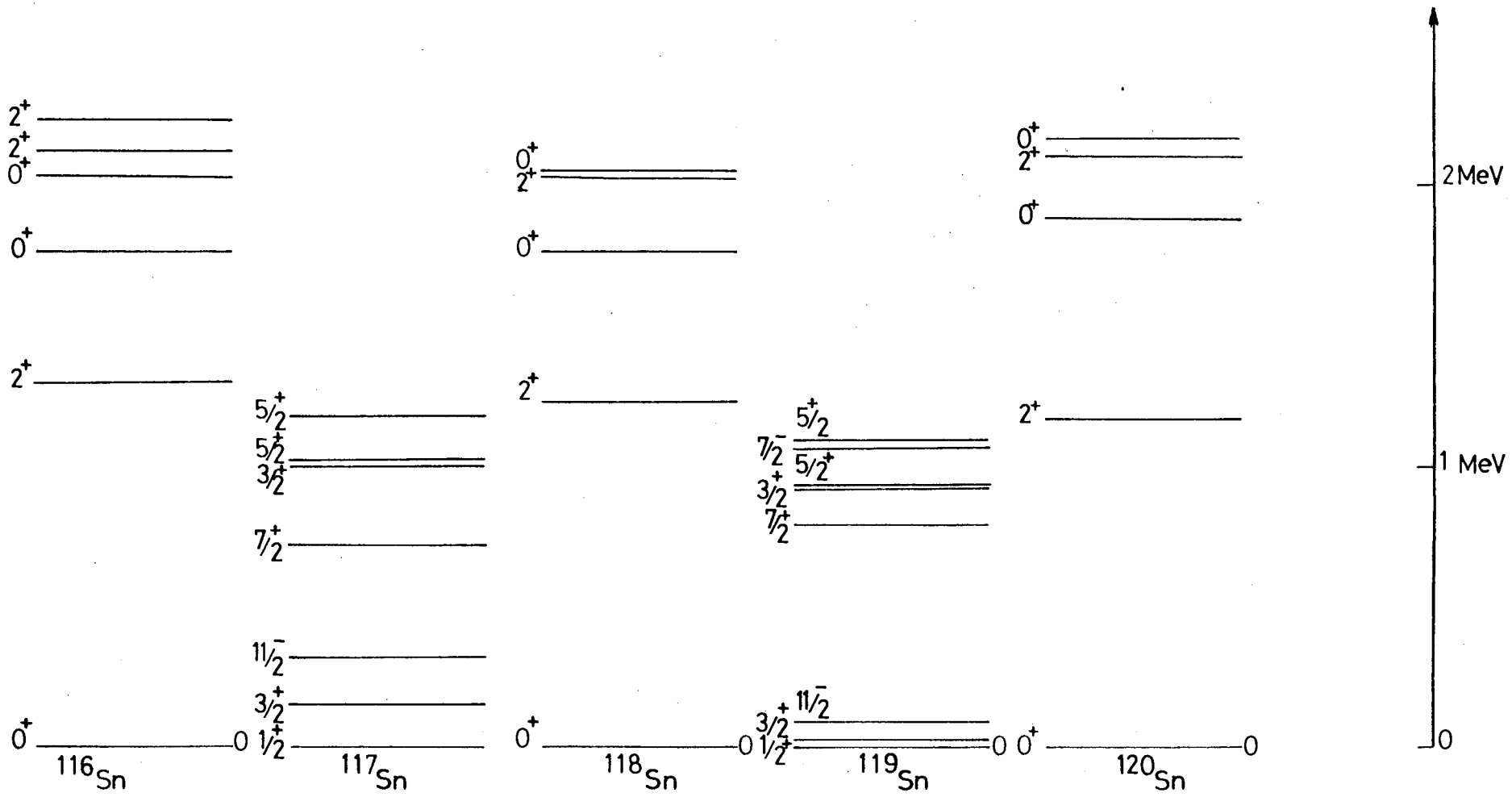

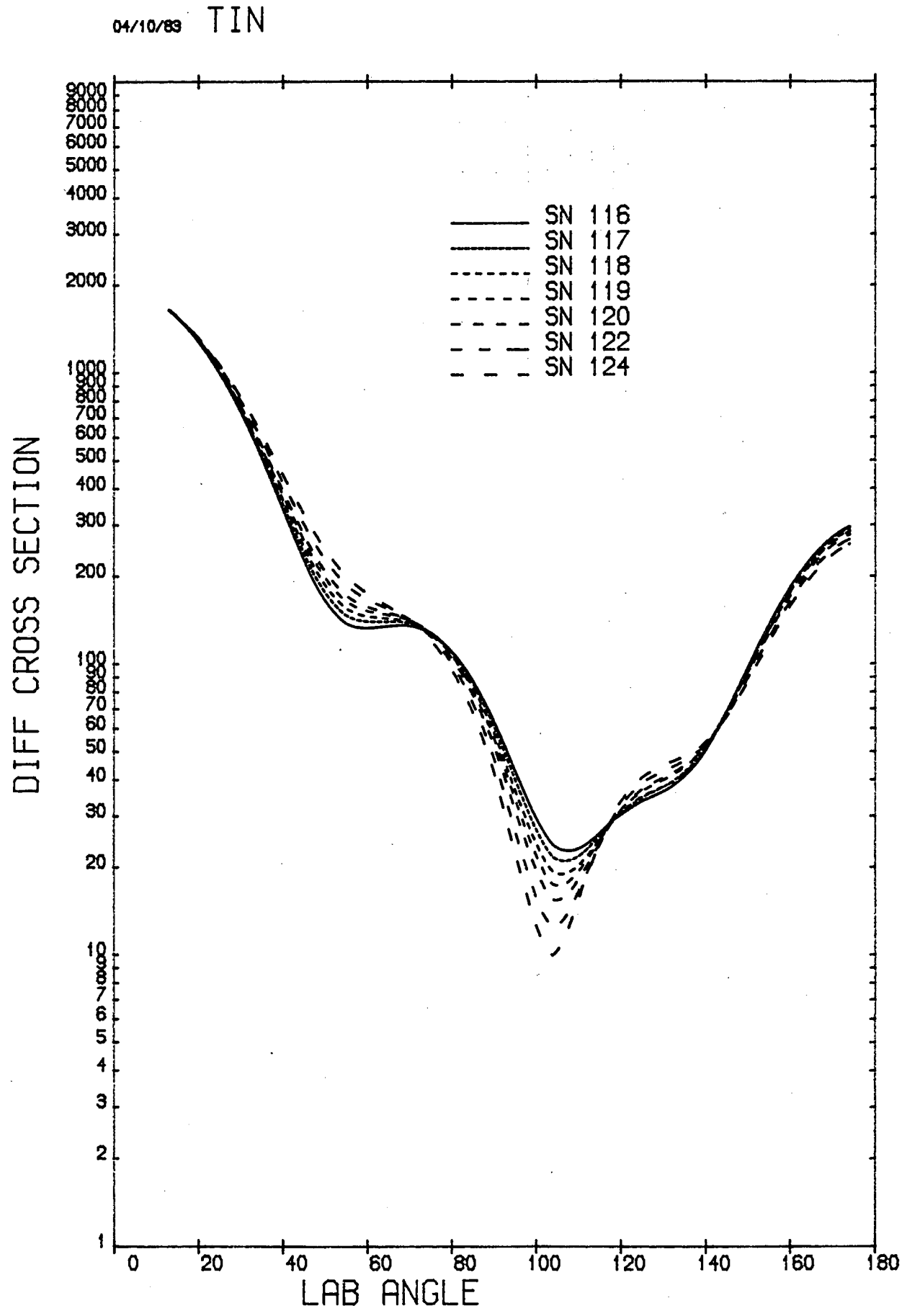
04/10/83 TIN
DIFF CROSS SECTION
LAB ANGLE
SN 116
SN 117
SN 118
SN 119
SN 120
SN 122
SN 124
9000
8000
7000
6000
5000
4000
3000
2000
1000
800
700
600
500
400
300
200
100
80
70
60
50
40
30
20
10
8
7
6
5
4
3
2
1
0
20
40
60
80
100
120
140
160
180

Figure 6.56.

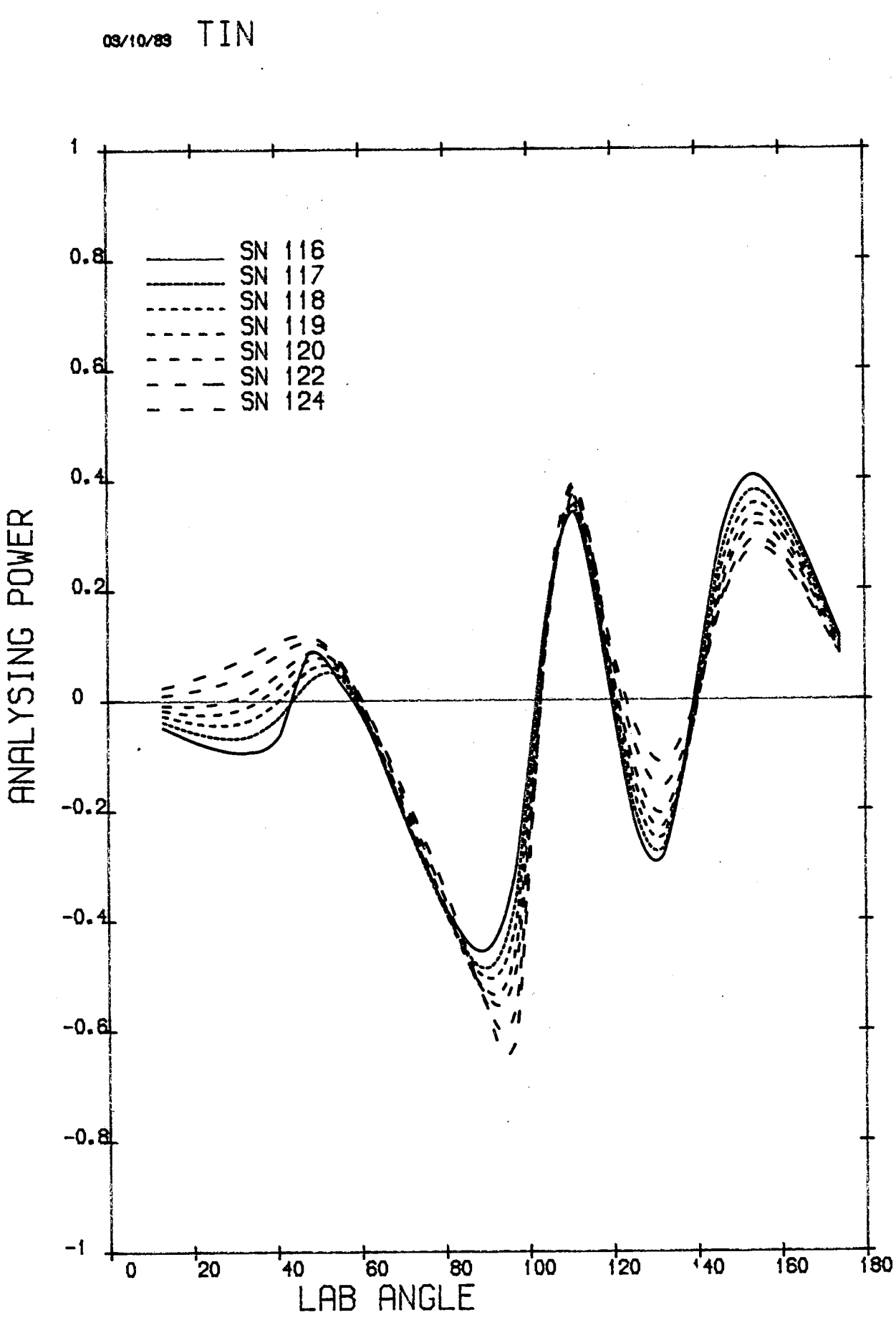
03/10/89 TIN
SN 116
SN 117
SN 118
SN 119
SN 120
SN 122
SN 124
ANALYSING POWER
LAB ANGLE
1
0.8
0.6
0.4
0.2
0
-0.2
-0.4
-0.6
-0.8
-1
0
20
40
60
80
100
120
140
160
180

Figure 6.57.

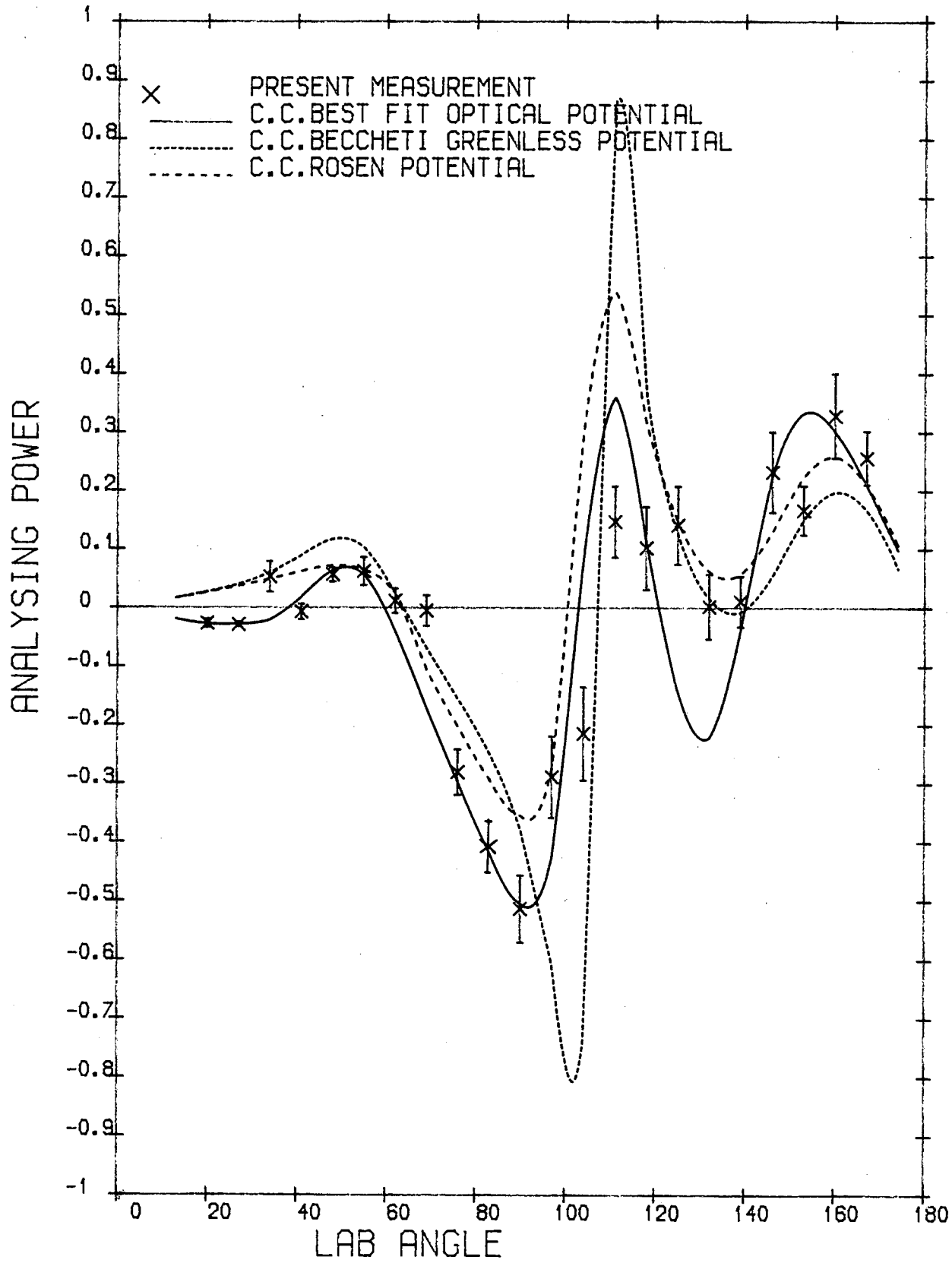
15/12/83 TIN
PRESENT MEASUREMENT
C.C.BEST FIT OPTICAL POTENTIAL
C.C.BECCHETI GREENLESS POTENTIAL
C.C.ROSEN POTENTIAL
ANALYSING POWER
LAB ANGLE
1
0.9
0.8
0.7
0.6
0.5
0.4
0.3
0.2
0.1
0
-0.1
-0.2
-0.3
-0.4
-0.5
-0.6
-0.7
-0.8
-0.9
-1
0
20
40
60
80
100
120
140
160
180

Figure 6.58.

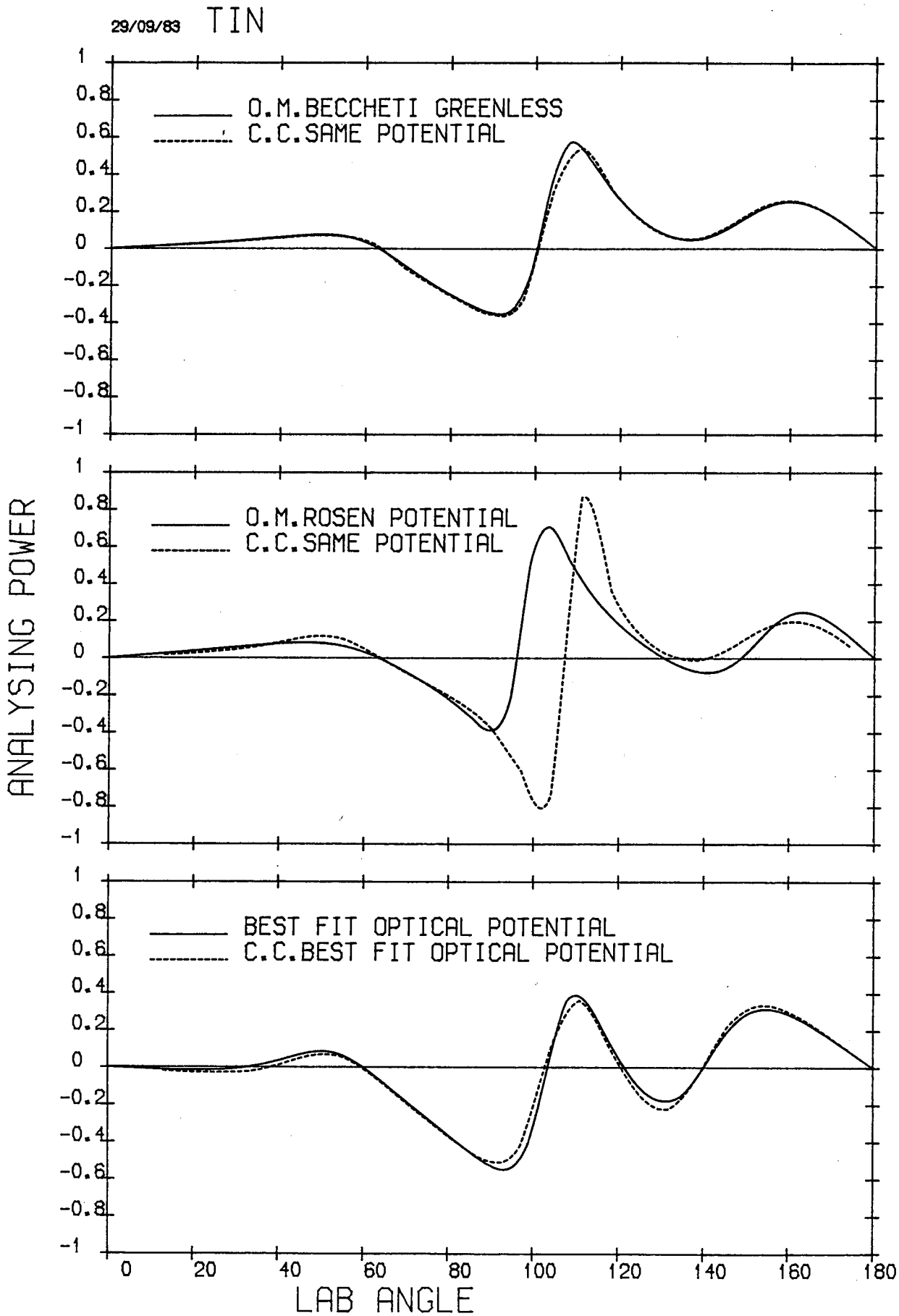
29/09/83 TIN
O.M.BECCHETI GREENLESS
C.C.SAME POTENTIAL
O.M.ROSEN POTENTIAL
C.C.SAME POTENTIAL
BEST FIT OPTICAL POTENTIAL
C.C.BEST FIT OPTICAL POTENTIAL
ANALYSING POWER
LAB ANGLE
1
0.8
0.6
0.4
0.2
0
-0.2
-0.4
-0.6
-0.8
-1
0
20
40
60
80
100
120
140
160
180

Figure 6.59.

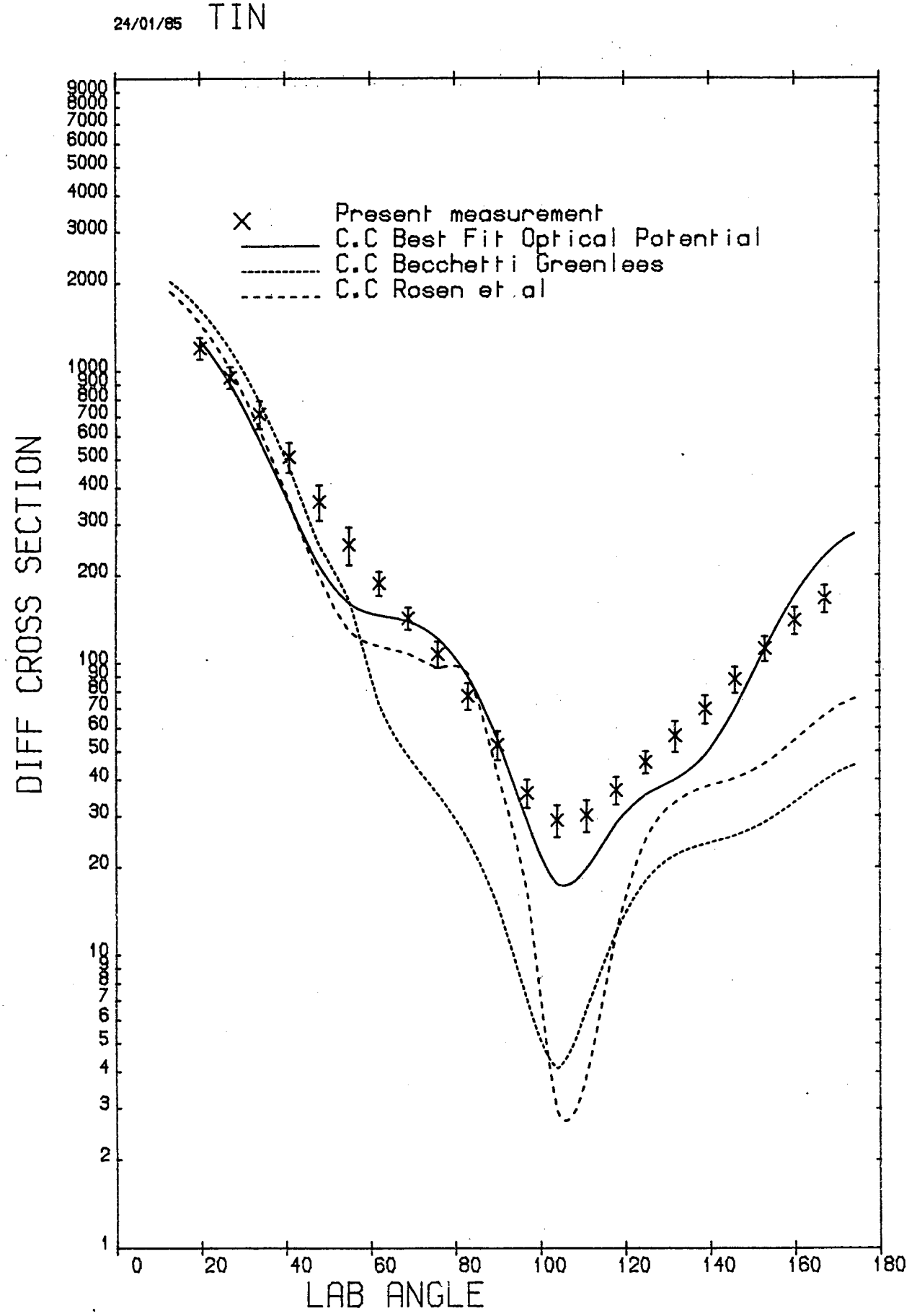
24/01/85 TIN
Present measurement
C.C Best Fit Optical Potential
C.C Becchetti Greenlees
C.C Rosen et al
DIFF CROSS SECTION
LAB ANGLE
9000
8000
7000
6000
5000
4000
3000
2000
1000
900
800
700
600
500
400
300
200
100
90
80
70
60
50
40
30
20
10
9
8
7
6
5
4
3
2
1
0
20
40
60
80
100
120
140
160
180

Figure 6.60.

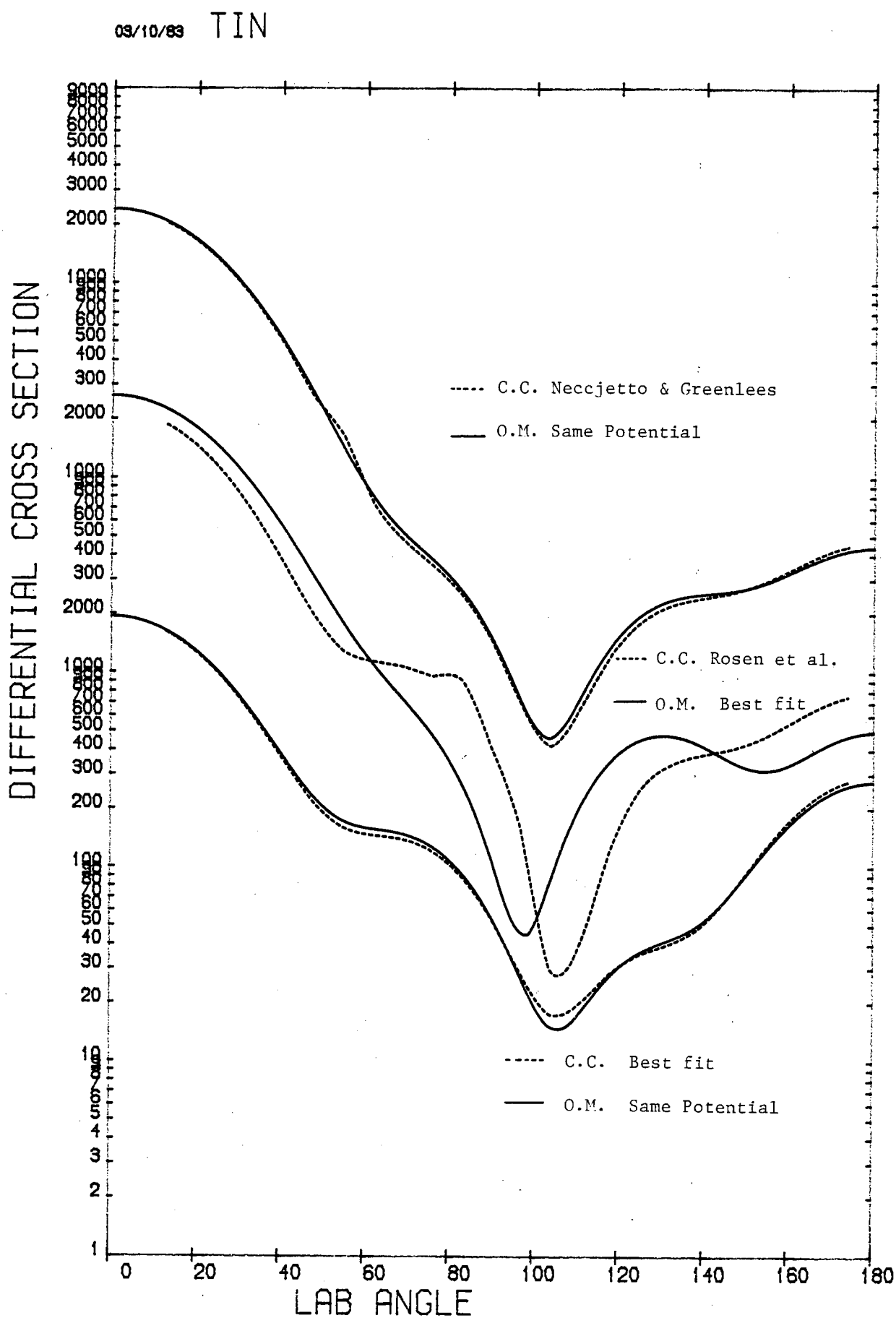
03/10/83 TIN
DIFFERENTIAL CROSS SECTION
LAB ANGLE
0
20
40
60
80
100
120
140
160
180
C.C. Neccjetto & Greenlees
O.M. Same Potential
C.C. Rosen et al.
O.M. Best fit
C.C. Best fit
O.M. Same Potential

Figure 6.61.

6.7.3 Tellurium

The even isotopes of Tellurium are good examples of vibrational nuclei[134]. The coupling of the following levels were considered

^{124}Te	$(0^+, 2^+, 4^+)$
^{126}Te	$(0^+, 2^+, 4^+)$
^{128}Te	$(0^+, 2^+, 4^+)$
^{130}Te	$(0^+, 2^+, 2^+)$

The only odd isotope of Tellurium ^{125}Te was considered as an odd-A vibrational (spherical) nucleus, and the coupling of the following levels was considered.

^{125}Te	$1/2^+$	Ground state
	$3/2^+$	0.035 MeV
	$9/2^+$	0.321 MeV

Including additional levels required unacceptably long computing time.

The neighbouring even-even nuclei to ^{125}Te are ^{124}Te and ^{126}Te. Therefore coupling of a $3s_{\frac{1}{2}}$ particle to the first (2^+) level of the even-even core produces $3/2^+$ and $5/2^+$ states. Then coupling of a $3s_{\frac{1}{2}}$ particle to the second (4^+) state of the core produces $7/2^+$ and $9/2^+$ states in ^{125}Te.

Fig. 6.62* shows the low lying levels of ^{124}Te, ^{125}Te and ^{126}Te. The $11/2^-$ and $7/2^-$ levels between the above mentioned levels are the result of the coupling to the higher excitation levels. Figures 6.62 and 6.63 show the consistency of the results for the odd and even isotopes of Tellurium. The deformation parameter $\beta_2 = 0.18$ was taken

from ref. (134). The other deformation parameters were derived from β_2 as described in Section 6.7 and are tabulated in Table 6.15.

The present measurements are compared with the prediction of the coupled channels potential for Best fit, Becchetti and Greenlees and Rosen's optical potentials in Figures 6.64 - 6.67. The relative success of the spherical optical model and the coupled channels calculations for various potentials are compared in Table 6.16.

The coupled channels calculations marginally worsened the fit to the analysing power data for the first three sets of parameters in Table 6.16, while the change to the cross section data fit is not considerable. The worst case is with Rosen's parameters.

TABLE 6.15

Element	β_{o2}	$I_{even\ A}$	$I_{odd\ A}$	β_{2I}	β'_{oI}	β''_{oI}
Te	0.18	0^+	$1/2^+$	0.0876	0.1258	-0.0478
		2^+	$3/2^+$ $5/2^+$	0.0940	0.1290	0.0000
		$I(2^+ 4^+)$ or	$7/2^+$ $9/2^+$	0.1035	0.1370	0.0796

TABLE 6.16

Comparison of Spherical Optical Model and Coupled Channel Calculations

Parameters	Coupled Channel			Optical Model		
	X^2_{Comb}	X^2_P	X^2_σ	X^2_{Comb}	X^2_P	X^2_σ
Best Fit	16.88	22.43	11.33	13.61	16.01	11.20
Becchetti & Greenlees	25.50	28.16	22.83	22.68	23.85	21.51
Rosen et al.	45.02	69.01	21.02	39.17	61.06	17.27
Zijp & Jonker	49.99	80.73	19.24	54.51	96.30	12.72
Tanaka et al.	70.56	133.0	8.12	71.98	136.01	7.94
Smith et al.	72.82	136.59	9.06	67.37	126.03	8.72

Figure.6.62*

Low lying Excited States of Tellurium Isotopes

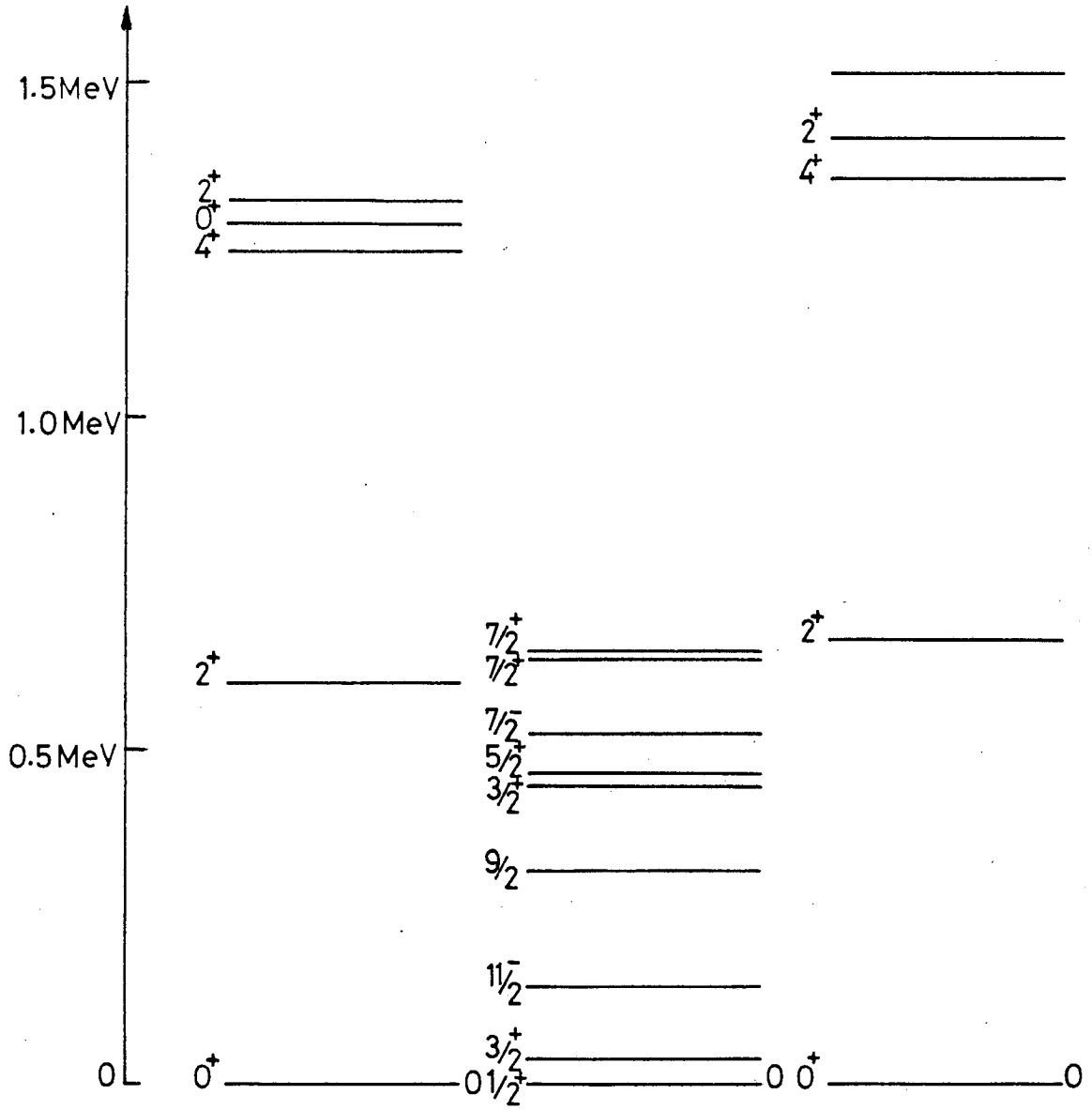

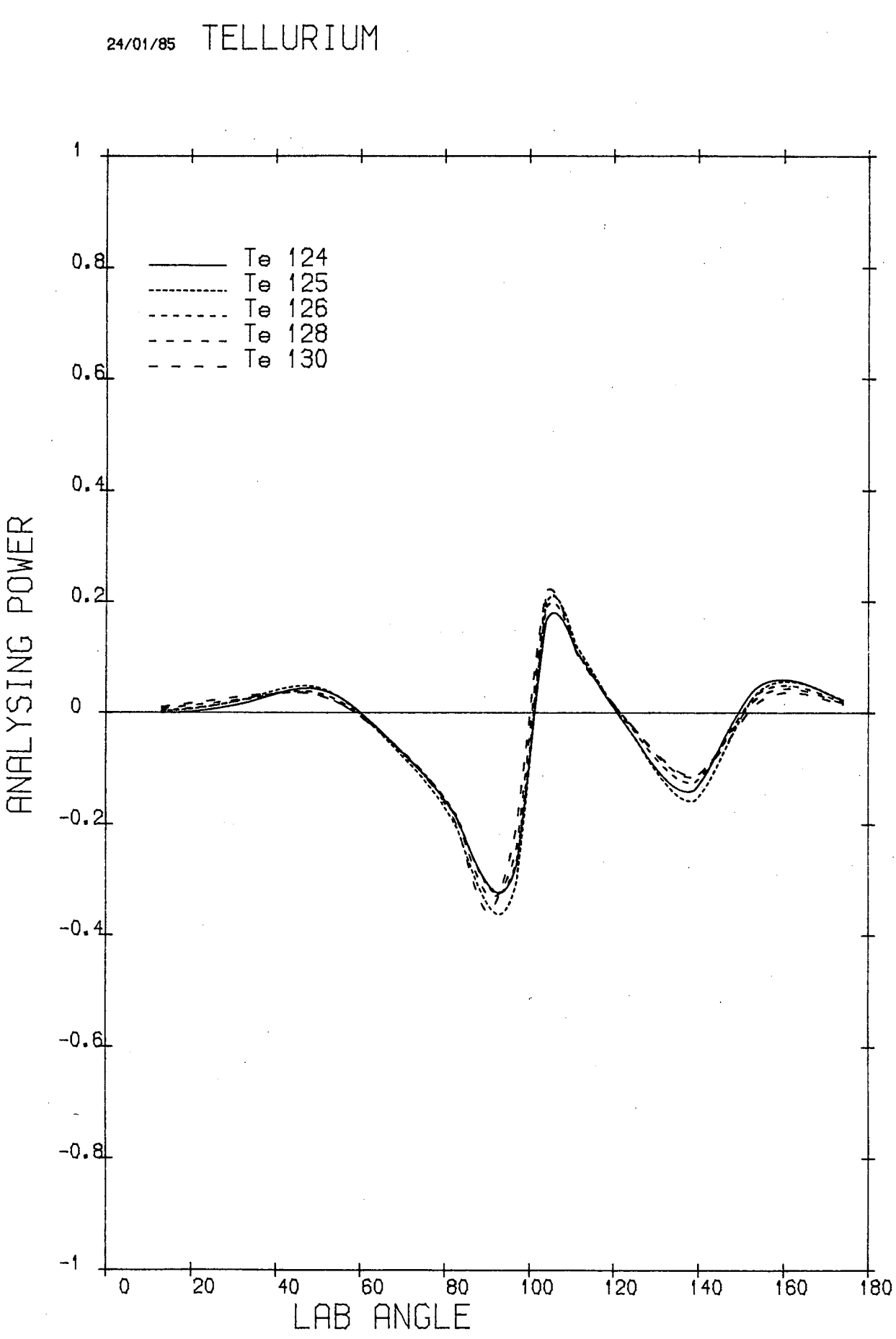
24/01/85 TELLURIUM
Te 124
Te 125
Te 126
Te 128
Te 130
ANALYSING POWER
LAB ANGLE
1
0.8
0.6
0.4
0.2
0
-0.2
-0.4
-0.6
-0.8
-1
0
20
40
60
80
100
120
140
160
180

Figure 6.62.

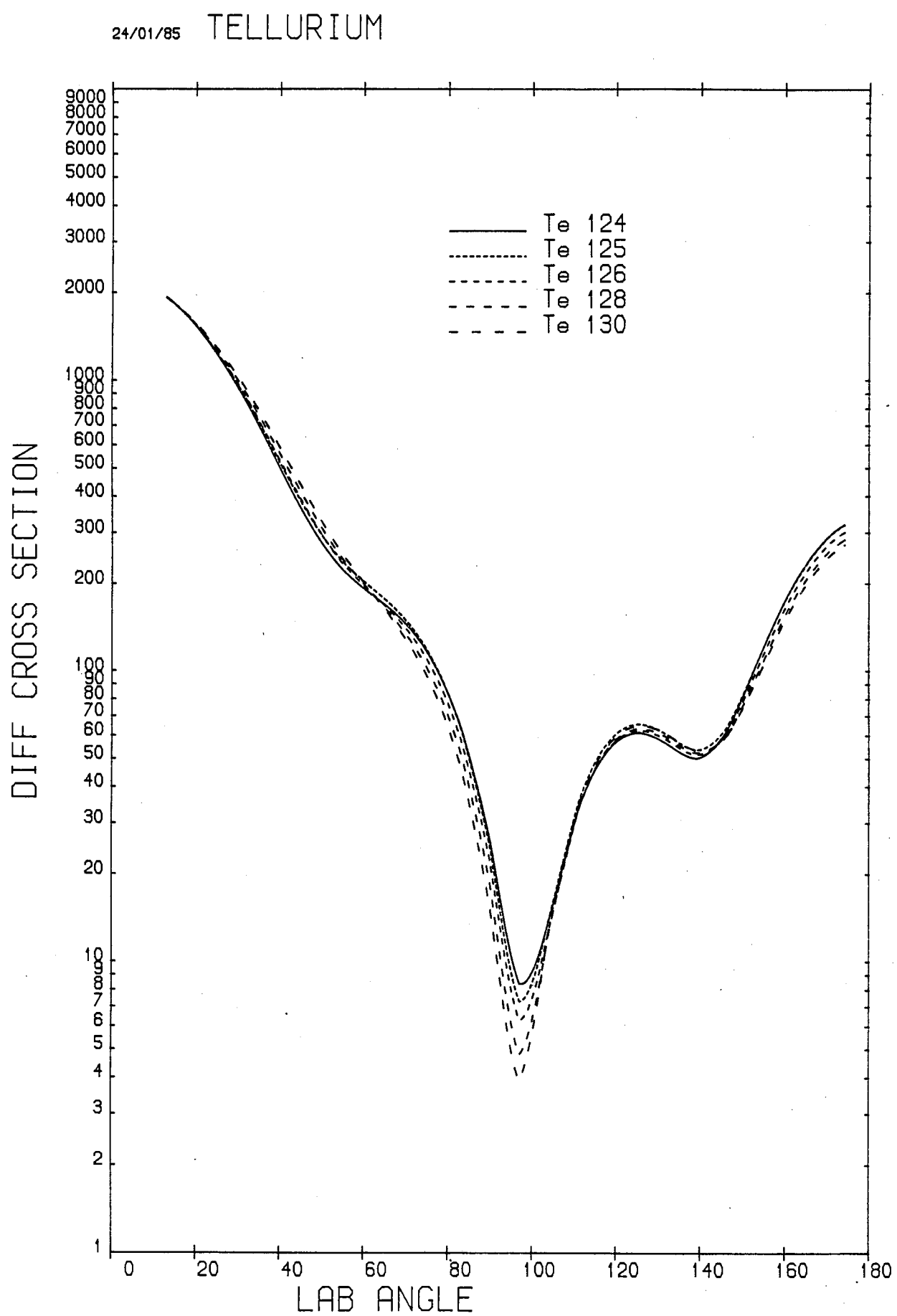
24/01/85 TELLURIUM
Te 124
Te 125
Te 126
Te 128
Te 130
DIFF CROSS SECTION
LAB ANGLE
9000
8000
7000
6000
5000
4000
3000
2000
1000
900
800
700
600
500
400
300
200
100
90
80
70
60
50
40
30
20
10
9
8
7
6
5
4
3
2
1
0
20
40
60
80
100
120
140
160
180

Figure 6.63.

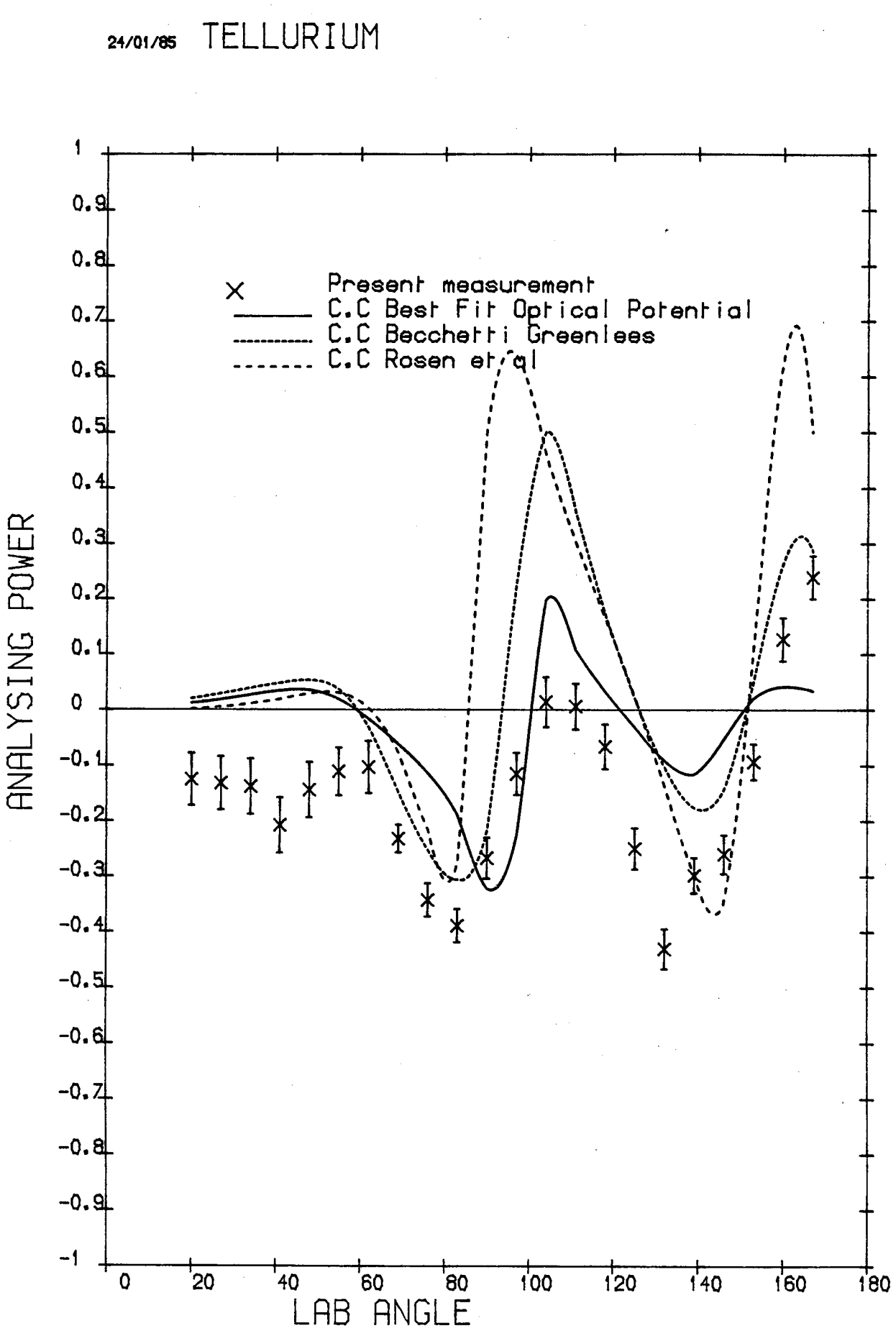
TELLURIUM
Present measurement
C.C Best Fit Optical Potential
C.C Becchetti Greenlees
C.C Rosen et al
ANALYSING POWER
LAB ANGLE
1
0.9
0.8
0.7
0.6
0.5
0.4
0.3
0.2
0.1
0
-0.1
-0.2
-0.3
-0.4
-0.5
-0.6
-0.7
-0.8
-0.9
-1
0
20
40
60
80
100
120
140
160
180

Figure 6.64.

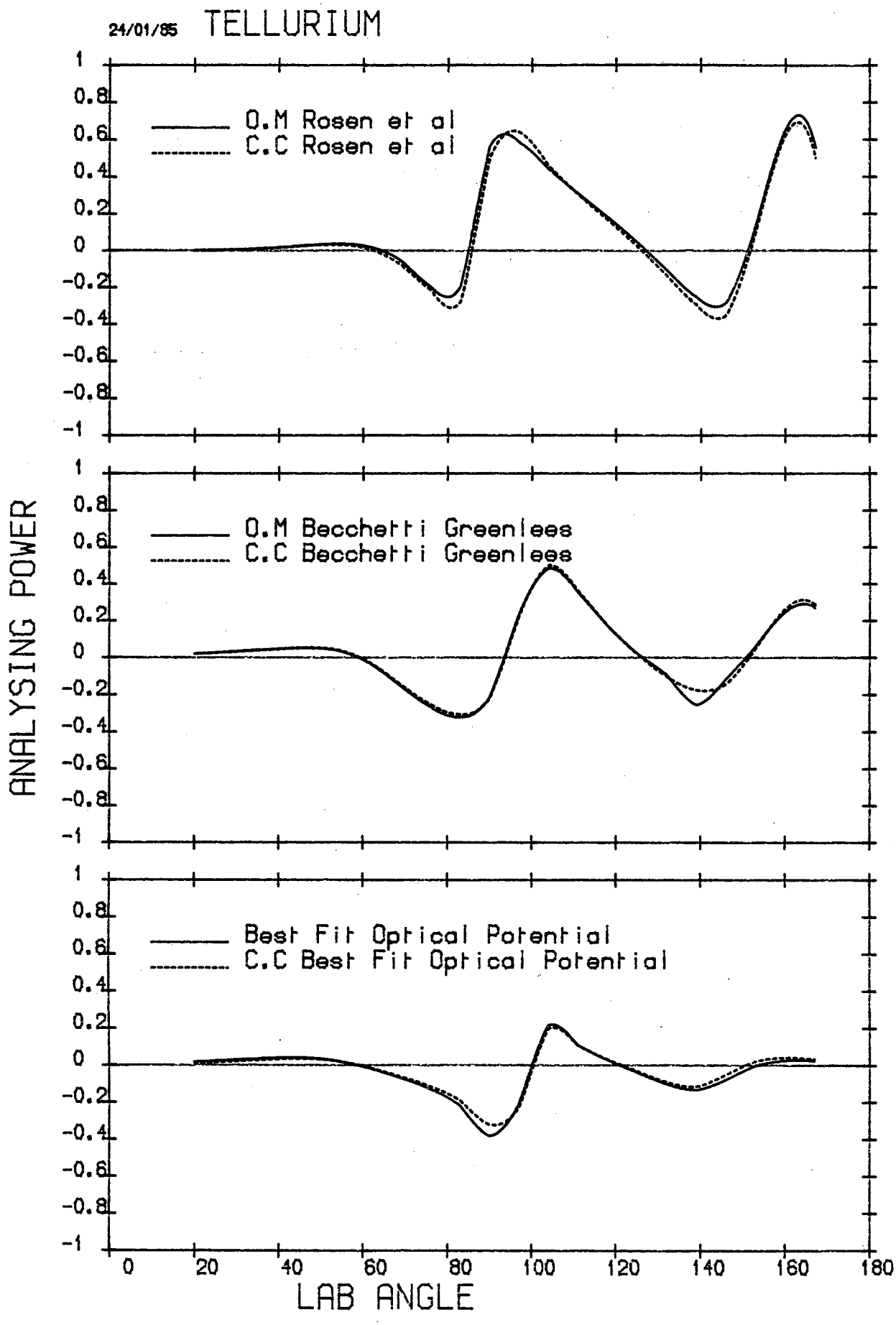
24/01/85 TELLURIUM
O.M Rosen et al
C.C Rosen et al
O.M Becchetti Greenlees
C.C Becchetti Greenlees
Best Fit Optical Potential
C.C Best Fit Optical Potential
ANALYSING POWER
LAB ANGLE
1
0.8
0.6
0.4
0.2
0
-0.2
-0.4
-0.6
-0.8
-1
0
20
40
60
80
100
120
140
160
180

Figure 6.65.

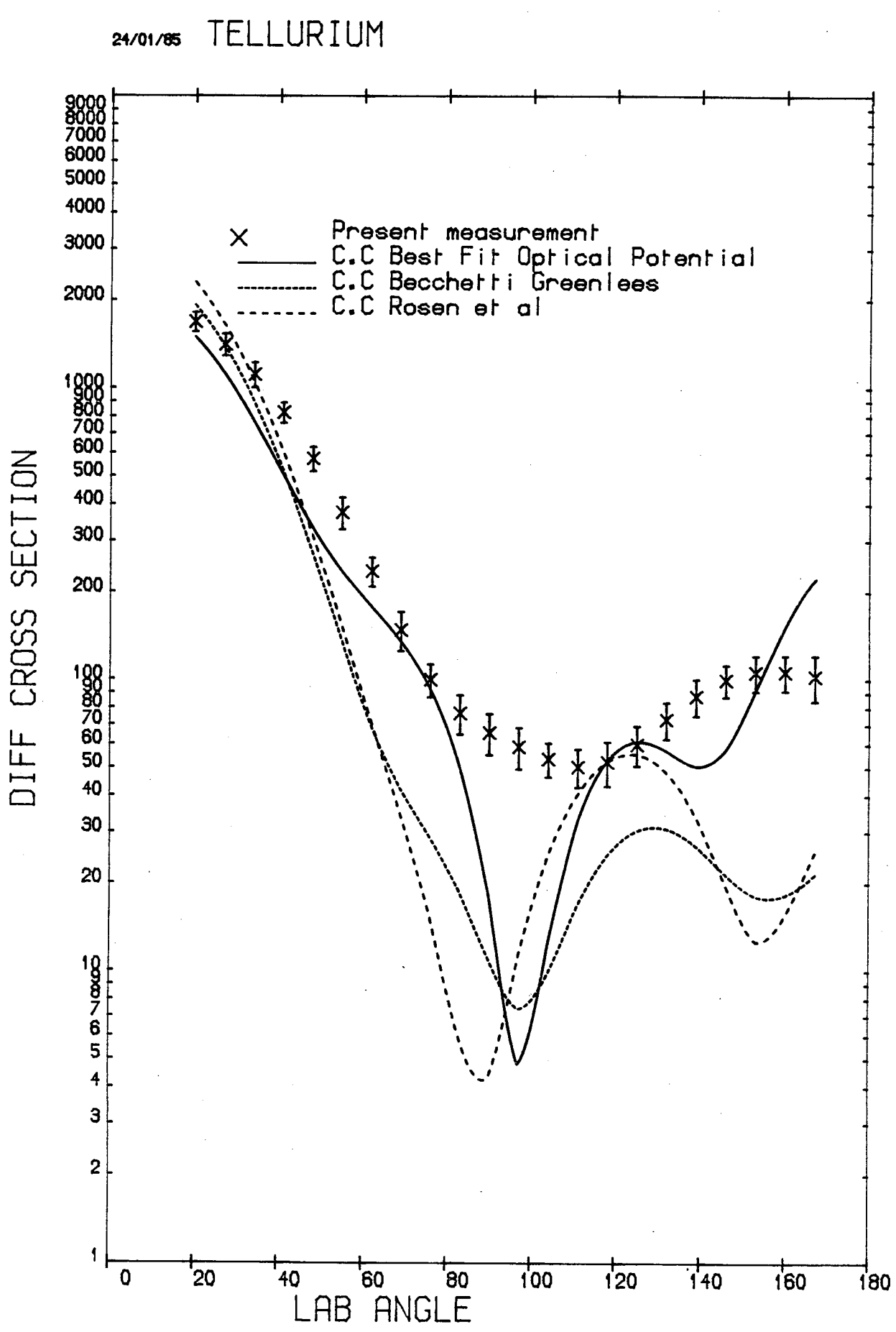
24/01/85 TELLURIUM
Present measurement
C.C Best Fit Optical Potential
C.C Becchetti Greenlees
C.C Rosen et al
DIFF CROSS SECTION
LAB ANGLE
9000
8000
7000
6000
5000
4000
3000
2000
1000
900
800
700
600
500
400
300
200
100
90
80
70
60
50
40
30
20
10
9
8
7
6
5
4
3
2
1
0
20
40
60
80
100
120
140
160
180

Figure 6.66.

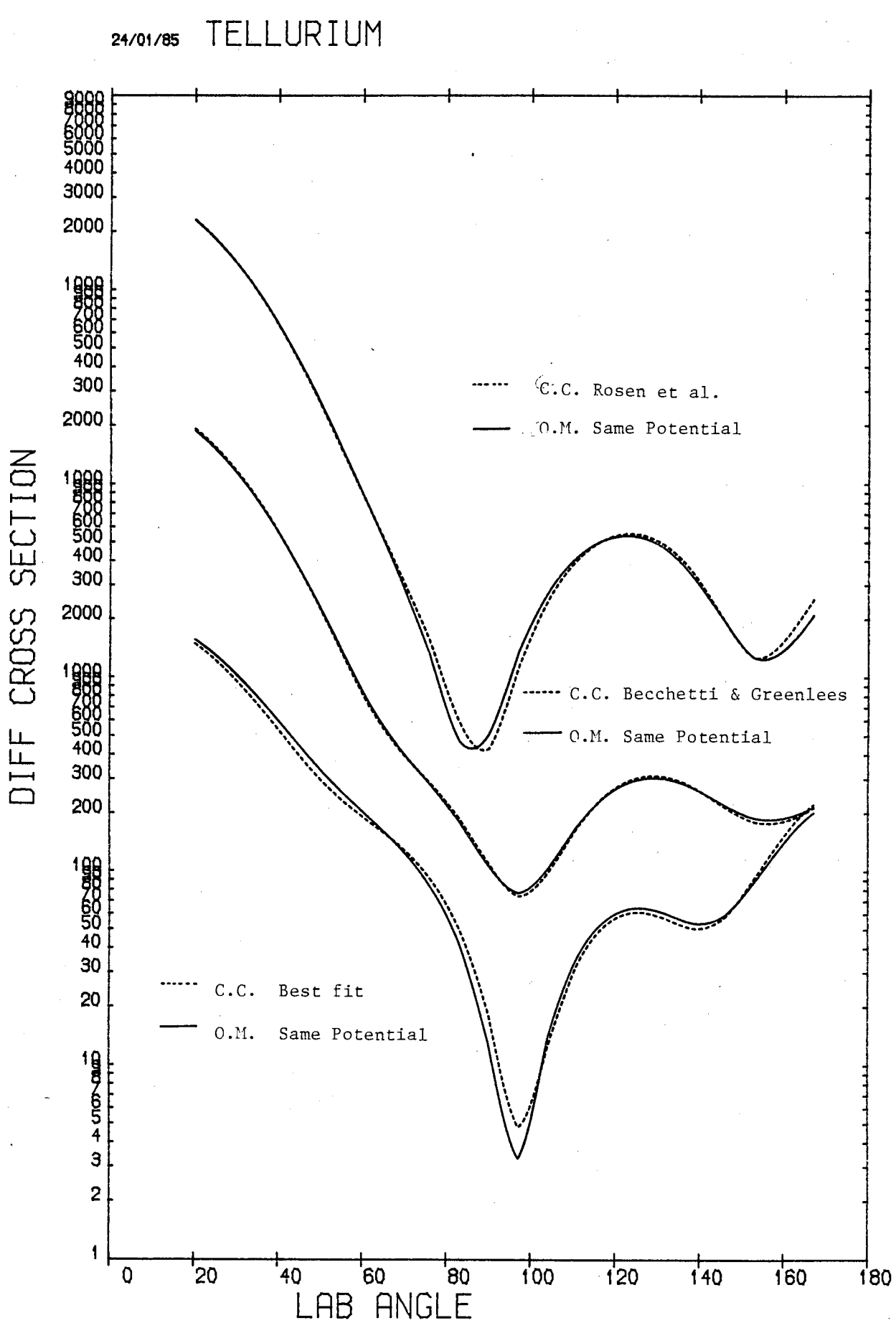
24/01/85 TELLURIUM
DIFF CROSS SECTION
LAB ANGLE
C.C. Rosen et al.
O.M. Same Potential
C.C. Becchetti & Greenlees
O.M. Same Potential
C.C. Best fit
O.M. Same Potential

Figure 6.67.

6.7.4 Conclusions

The aim of this work was to add more accurate neutron polarisation data in the region of medium weight nuclei, to that existing in the region of light nuclei[13] and heavy nuclei[16], along with the differential cross section data which was measured simultaneously with the polarisation data. Of course, the cross section data, which was of secondary importance in this work was not expected to be as accurate as those which are measured with the high resolution time-of-flight technique. It has been shown in this work that the differential cross sections observed are reliable in most cases where comparison can be made with data obtained by the time-of-flight technique, and so where no time-of-flight data exists the present data is thought to be quite reliable.

As described in Chapter 1, the most accurate polarisation data for light nuclei is by Ellgehausen et al.[13] to which a fit is provided by a set of semi global optical potentials by Rosen et al.[32] to all of the nuclei measured apart from one, Zr. In the region of heavy nuclei, measurements by Annand[16] are the most accurate, but failed to fit calculations based on any global optical potential, or on individual parameter sets, with the exception of Mercury. The investigation in this work to fill the gap between these two regions has been fulfilled by precise measurements on Cd, Sn, Sb, Te and I. None of the global optical potentials described all the measurements, but those of Becchetti and Greenlees and Rosen et al. reproduced the shape of polarisation and differential cross section distributions for all nuclei, relatively well.

Simultaneous fitting of the polarisation and differential cross

sections by an individual analysis on each nucleus, showed a good fit to all nuclei, apart from Tellurium, although the parameters given in Table 6.10 for Tellurium produced the shape of the analysing power well enough from 62° - 167° but with opposite sign at forward angles. As mentioned in Section 6.4.4, this discrepancy might be due to the lack of knowledge of the level structure of the most abundant isotopes of Tellurium.

An attempt was made to investigate the behaviour of an optical model potential based on the analysing power data only. A set of new parameters were obtained for each nucleus. These parameters improved the fitting to some extent in the case of Cd, Sb and Iodine. Although the fitting to Sn showed a smaller ^{2}X value, in fact the shape of the analysing power distribution did not improve. The inclusion of the Imaginary Spin-Orbit term in the optical potential, also did not change the prediction of the optical model distribution.

Some of the nuclei studied in this work (i.e.: Cd and Te) are well known vibrational nuclei, but the coupled channels calculations did not effect the results obtained by Spherical Optical Model calculations. Becchetti and Greenlees parameters and those of Rosen et al. are again after the Best Fit parameters, the most successful parameters in describing the distributions of the analysing power and differential cross sections for Cd, Sn and Te with the coupled channels calculations as well as with the Spherical Optical model calculations

The system used in this work was improved to a large extent from its original set up by Annand[16] by reduction of the background by changing most of the shielding as well as by the utilization of a new detector-preamplifier and neutron selector, as mentioned throughout

this work. This system still can be improved by exchanging all the old detector and neutron selector arrangements to the new arrangement, particularly if the scintillator size is reduced from 2" × 6" to 2" × 2" to obtain a better recoil proton spectrum. A good recoil proton spectrum would enable one to use the unfolding method, which is used by M.N. Erduran[137] in the Edinburgh Neutron Physics Laboratory and proved to be a satisfactory method to resolve inelastically scattered neutrons from elastic scattered ones. Following this method would reduce the ambiguities in the corrections done for inelastic contribution in the data. The disadvantage of this proposal is due to the reduction of the detection efficiency by a smaller scintillator size, which can be compensated to some extent, by a nicely focused high current deuteron beam. If the system is used for polarized neutrons of a higher energy (> 8 MeV) where the inelastically scattered neutrons are not symmetric, the unfolded recoil proton spectra can be used at the same time for the calculation of polarization of inelastic scattered neutrons. One should not ignore the fact that the shielding and the collimator of the system in this case must be changed.

REFERENCES

1) N. Bohr, Nature (London) 137 (1936) 344.

2) H.A. Bethe, Phys. Rev. 57 (1940) 1125.

3) S. Fernbach, R. Serber and T.B. Taylor, Phys. Rev. 75 (1949) 1352.

4) H. Feshbach, C.E. Porter and V.F. Weisskopf, Phys. Rev. 96 (1954) 448.

5) V.E. Weisskopf, Rev. Mod. Phys. 29 (1957) 174.

6) H. Feshbach, Annals of Physics 5 (1958) 357.

7) Proc. Intern. Symp. Polarisation Phenomena of Nucleons (Basel, 1960). Suppl. Helv. Phys. Acta 6 (1961).

8) L. Van Hove, Physica 22 (1956) 979.

9) P.E. Hodgson, Int. Phys. Conf. Ser. No. 64, Section 2. Paper presented at Conf. on Neutron and its Applications, Cambridge, 1982.

10) F.D. Becchetti, Jr. and G.W. Greenlees, Phys. Rev. 182 (1969) 1190.

11) D. Wilmore and P.E. Hodgson, Nucl. Phys. 55 (1964) 673.

12) K. Wiedemann, E. Baumgartner, D. Ellgehausen, R. Gleyvod and P. Huber, Helv. Phys. Acta 42 (1969) 259.

13) D. Ellgehausen, E. Baumgartner, R. Gleyvod, P. Huber, A. Stricker and K. Wiedemann, Helv. Phys. Acta 42 (1969) 269.

14) R.L. Walter, Polarization Phenomena in Nuclear Physics, 1980. Fifth International Symposium, Santa Fe.

15) G. Bulski, W. Grum, J.W. Hammer, H. Postner, G. Schleussner and E. Speller, Contribution Paper at International Conference on Nuclear Data for Science and Technology, Antwerp, September, 1982.

16) J.R.M. Annand, Ph.D. Thesis, University of Edinburgh, 1982.

17) J.R. Beyster, M. Walt and E.W. Salmi, Phys. Rev. 104 (1956) 1319.

18) B.M. McCormac, M.F. Steuer, C.D. Bond and F.L. Hereford, Phys. Rev. 108 (1957) 116.

19) J.D. Clement, F. Boreli, S.E. Darden, W. Haeberli and H.R. Striebel, Nucl. Phys. 6 (1958) 177.

REFERENCES (Contd.)

20) M.V. Pasechnik, I.F. Barchuk, I.A. Totsky, V.I. Strizhak, A.M. Korolov, Y.V. Hofman, G.N. Lovchikova, E.A. Koltynin and G.B. Yankov, 2nd United Nations Conference on the Peaceful Uses of Atomic Energy, Geneva, 1-13 Sept. 1958.

21) D. Brown, A.T.G. Ferguson and R.E. White, Nucl. Phys. 25 (1961) 604.

22) W.B. Gilboy and J.H. Towle, Nucl. Phys. 42 (1963) 86-94.

23) A.J. Elwyn, R.O. Lane, A. Langsdore, Jr. and J.E. Monahan, Phys. Rev. 133 (1964) B80.

24) F. Perey and B. Buck, Nucl. Phys. 32 (1962) 353.

25) R.J. Olness, K.K. Seth and H.W. Lewis, Nucl. Phys. 52 (1964) 529.

26) A.T.G. Ferguson, R.E. White and D. Wilmore, Nucl. Phys. 76 (1966) 369.

27) W.G. Vonach and A.B. Smith, Nucl. Phys. 78 (1966) 389.

28) S.G. Buccino, C.E. Hollandsworth and P.R. Bevington, Zeit. f. Physik 196 (1966) 103.

29) L. Ya Kazakova, V.E. Kolesov, V.I. Popov, V.M. Sluchevskaya and V.I. Trykova, Jaderno Fizicheskie Issledovanija, (Progress Report) USSR 3 (1966) 5.

30) F. Bjorklund and S. Fernbach, Phys. Rev. 109 (1958) 1295.

31) R.L. Becker, W.G. Guindon and G.J. Smith, Nucl. Phys. 89 (1966) 154.

32) L. Rosen, J.G. Beery and A.S. Goldhaber, Annals of Physics 34 (1965) 96.

33) A.S. Mahajan, Nucl. Phys. A95 (1967) 193.

34) G.V. Gorlov, N.S. Lebedeva and V.M. Morozov, Soviet Journal of Nuclear Physics 6 (1968) 663.
G.V. Gorlov, Proceedings of the 2nd International Symposium on Polarization Phenomena of Nucleus. Experimenta Supplementum 12 (1965) 633.

35) B. Holmqvist, Arkiv För Fysik 38 (1968) 403.

36) I.A. Korzh, I.E. Kashuba, B.D. Kozin and M.V. Pasechnik, Soviet Journal of Nuclear Physics, Vol. 7, No. 2 (1968) 190.

REFERENCES (Contd.)

37) I.A. Korzh, V.A. Mishchenko, M.P. Pasechnik, M.M. Pravdivyi, I.S. Sanshur, I.A. Tachkye, Ukr. Fiz. Zh. 12, No. 9 (1967) 1567.

38) L. Rosen, Proc. 2nd International Symposium. Polarisation Phenomena of Nucleons. Karlsruhe, Ed. p. Huber and H. Schopper, Experimenta Suppl. 12 (1965) 253.

39) M.C. Gupta and G.E. Tripard, Canadian Journal of Physics 51, Nos. 1-6 (1973) 121.

40) E. Zijp and C.C. Jonker, Nucl. Phys. A222 (1974) 93.

41) D.G. Foster and D.W. Glasgow, Phys. Rev. C3 (1971) 576.

42) R.B. Galloway and A. Waheed, Nucl. Phys. A318 (1979) 173.

43) A. Begum and R.B. Galloway, Journal of Physics G: Nucl. Phys. 7 (1981) 535.

44) A.B. Smith, P.T. Guenther and J.F. Whalen, Nucl. Phys. A415 (1984) 1.

45) C. Budtz-Jorgensen, P. Guenther and A. Smith, ANL 82 12795003 (Report, ANL-NDM-73, 8207).

46) Shigeya Tanaka, Japan Atomic Energy Research Institute, Report No. JAERI M-5984.

47) J.L. Fowler, J.A. Cookson, M. Hussain, R.B. Schwartz, M.T. Swinhoe, C. Wise and C.A. Uttley, Nucl. Instr. and Methods 175 (1980) 449.

48) P. Kuijper, C.J. Tiesinga and C.C. Jonker, Nucl. Instr. and Methods 42 (1966) 56.

49) J.B. Birks, The Theory and Practice of Scintillation Counting.

50) R.L. Craun and D.L. Smith, Nucl. Inst. and Methods, 80 (1970) 239.

51) D.L. Smith, R.G. Polk and T.G. Miller, Nucl. Instr. and Methods 64 (1968) 157.

52) K.F. Flynn, L.E. Glendenin, E.P. Steinberg and P.M. Wright, Nucl. Inst. and Methods 27 (1964) 13.

53) D.T. Ingersoll and B.W. Wehring, Nucl. Instr. and Methods 147 (1977) 551.

54) F.T. Porter, M.S. Freedmann, F. Wagner, Jr. and I.S. Sherman, Nucl. Instr. and Methods, 39 (1966) 35.

REFERENCES (Contd.)

55) C.D. Swartz and G.E. Owen, Ch. IIB, Fast Neutron Physics, Part I (J.B. Marion and Fowler).

56) C.N. Chou, Phys. Rev. 87 (1952) 904.

57) D.W. Jones and M.E. Toms, NRL Report 7324 (1971).

58) R.B. Galloway and D.G. Vass, Nucl. Instr. and Methods 83 (1970) 35.

59) J.B. Birks, An Introduction to Liquid Scintillator Counting.

60) M.N. Tompson and J.M. Taylor, Nucl. Instr. and Methods 37 (1965) 305.

61) J.R. Prescott and A.S. Rupaal, Can. J. Phys. 39 (1961) 221.

62) L.E. Beghian and S. Wilensky, Nucl. Instr. and Methods 35 (1965) 34.

63) H.H. Knox and T.G. Miller, Nucl. Instr. and Methods 101 (1972) 519.

64) G. Dietze, IEEE Trans. Nucl. Sci. NS-26 (1979)398.

65) G. Dietze and H. Klein, Nucl. Instr. and Methods 193 (1982) 549.

66) D.A. Kellogg, Phys. Rev. 90 (1953) 224.

67) M. Drosg, Nucl. Instr. and Methods 105 (1972) 573.

68) A. Bertin and A. Vitale, Nucl. Instr. and Methods 91 (1971) 649.

69) I.J. Taylor and J. Kalyna, Nucl. Instr. and Methods 88 (1970) 267.

70) R. Batchelor, W.B. Gilboy, J.B. Parker and J.H. Towle, Nucl. Instr. and Methods 13 (1961) 70.

71) A. Albergi Quaranta, A. Bertin, G. Matone, F. Palmonari, G. Torelli, P. Dalpiaz, A. Placci and E. Zavattini, Phys. Rev. 177 (1969) 2118.

72) V.V. Verbinski, W.R. Burrus, T.A. Love, W. Zobel and N.W. Hill, Nucl. Instr. and Methods 65 (1968) 8.

73) J.E. Rothberg, E.W. Anderson, E.J. Bleser, L.M. Lederman, S.L. Meyer, J.L. Rosen and I.T. Wang, Phys. Rev. 132 (1963) 2664.

74) B. Sabbah and A. Suhami, Nucl. Instr. and Methods 58 (1968) 102.

75) J. Kalyna and I.J. Taylor, Nucl. Instr. and Methods 88 (1970) 277.

76) G.S. Birth and D.P. DeWitt, Applied Optics, 10 (1971) 687.

77) R.B. Galloway and A. Waheed, Nucl. Instr. and Methods 128 (1975) 515.

REFERENCES (Contd.)

78) H. Davie and R.B. Galloway, Nucl. Instr. and Methods 92 (1971) 547.

79) A. Begum, Ph.D. Thesis, Edinburgh University, 1979.

80) N.S. Wang, Private communication.

81) M.L. Roush, M.A. Wilson and W.F. Hornyak, Nucl. Instr. and Methods 31 (1964) 112.

82) J.H. Ormrod, Nucl. Instr. and Methods 95 (1971) 49.

83) D.C. Stantry and R.D. Werner, Nucl. Instr. and Methods 188 (1981) 211.

84) W. Whalen, Handbuch der Fysik 34 (1958) 431.

85) P.J. Pasma, Nucl. Phys. 6 (1958) 141.

86) H.J. Boersma, C.C. Jonker, J.E. Nigenhuis, P.J. van Hall, Nucl. Phys. 46 (1963) 660.

87) A.F. Behof, T.H. May, W.I. McGarry, Nucl. Phys. A108 (1968) 250.

88) P. Roding and H. Scholerman, Nucl. Phys. A125 (1969) 585.

89) H. Davie and R.B. Galloway, Nucl. Instr. and Methods 108 (1973) 581.

90) A.M. Alsoraya and R.B. Galloway, Nucl. Phys. A280 (1977) 61.

91) R.B. Galloway and R. Martinez Lugo, Nuclear Instr. and Methods, 158 (1979) 153.

92) R.B. Galloway and A.S. Hall, Phys. Rev. C21 (1980) 453.

93) R.L. Walter, Polarisation Phenomena in Nuclear Reactions. Ed. H.H. Barschall and W. Haeberli, (Univ., Wisconsin Press, Madison (1971), 371.

94) J. Bloch and C.C. Jonker, Physica 18 (1952) 809.

95) S.A. Cox, Nucl. Instr. and Methods 56 (1967) 245.

96) W.E. Kinney, Nucl. Instr. and Methods 83 (1970) 15.

97) D.E. Velkley, J.D. Brandenberger, D.W. Glasgow and H.T. McEllistrem, Nucl. Instr. and Methods 129 (1975) 231.

98) G.E. Stinson, S.M. Tang and J.T. Sample, Nucl. Instr. and Methods 62 (1968) 13.

99) B. Holmqvist, B. Gustavson, T. Wiedling, Arkiv För Fysik 34 (1967) 481.

REFERENCES (Contd.)

100) O. Aspelund and B. Gustavson, Nucl. Instr. and Methods 57 (1967) 197.

101) J.R.M. Annand and R.B. Galloway, Nucl. Instr. and Methods 211 (1983) 421.

102) F.E. Bertrand, Nuclear Data Sheets 22 (1977) 135.

103) B. Harmatz, Nuclear Data Sheets 27 (1979) 453.

104) L.K. Peker, Nuclear Data Sheets 29 (1980) 587.

105) C.M. Lederer and V.S. Shirley, Table of Isotopes, 7th edition. Ed. (Wiley, New York, 1978).

106) J. Blachot and G. Marguier, Nuclear Data Sheets 35 (1982) 375.

107) J. Blachot, J.P. Husson, J. Oms and G. Marguier, Nuclear Data Sheets 32 (1981) 287.

108) G.H. Carlson, W.L. Talbert, Jr. and S. Raman, Nuclear Data Sheets 14 (1975) 247.

109) R.L. Auble, Nuclear Data Sheets 25 (1978) 315.

110) G.H. Carlson and W.L. Talbert, Jr. and S. Raman, Nuclear Data Sheets 17 (1976) 1.

111) R.L. Auble, Nuclear Data Sheets 26 (1979) 207.

112) D.C. Kocher, Nuclear Data Sheets 17 (1976) 39.

113) F.E. Bertrand, Nuclear Data Sheets B7 (1972) 419.

114) F.E. Bertrand, Nuclear Data Sheets B10 (1973) 91.

115) T. Tamura, Z. Matumoto, A. Hashizume, Y. Tendow, K. Miyano, S. Ohya, K. Kitao and M. Kanbe, Nuclear Data Sheets 26 (1979) 385.

116) T. Tamura, Z. Matumoto, K. Miyano and S. Ohya, Nuclear Data Sheets 29 (1980) 453.

117) F.E. Bertrand, Nuclear Data Sheets 10 (1973) 91.

118) T. Tamura, Z. Matumoto and M. Ohshima, Nuclear Data Sheets 32 (1981) 497.

119) T. Tamura, K. Miyano and S. Ohya, Nuclear Data Sheets 36 (1982) 227.

120) K. Kitao, M. Kanbe and Z. Matumoto, Nuclear Data Sheets 38 (1983) 191.

REFERENCES (Contd.)

121) H.R. Hiddleston and C.P. Browne, Nuclear Data Sheets 13 (1974) 133.

122) A. Hashizome, Y. Tendow, K. Kitao, M. Kanbe and T. Tamura Nuclear Data Sheets 35 (1982) 181.

123) H.H. Barshall, Phys. Rev. 86 (1952) 431.

124) ELIESE-3, Sin-iti IGARASI-JAERI-1224.

125) W. Hauser and H. Feshbach, Phys. Rev. 87 (1952) 366.

126) E. Sheldon and V.C. Rogers, Computer Physics Communication 6 (1973) 99.

127) W.R. Smith, Computer Physics Communication 1 (1969) 106.

128) Sin-iti IGARASI, Journal of Nuclear Science and Technology 12[2], pp. 67∿82, February 1975.

129) B. Holmqvist, S.G. Johannson, G. Lodin and J. Wiedling, Nucl. Phys. A146 (1970) 321-336.

130) V.I. Strizhak, E.V. Korbetskii and L.S. Sokolov, Ukrainian Physics Journal 13 (1968) 106.

131) G.W. Greenlees, F.G. Pyle and Y.C. Tang, Phys. Rev. 171 (1968) 1115.

132) J.P. Delaroche, C.E. Floyd, P.P Guss, R.C. Byrd, K. Murphy, G. Tungate and R.L. Walter, Phys. Rev. C28 (1983) 1410.

133) Taro Tamura, Supplement of Prog. Theor Phys. Nos. 37 & 38 (1966) 383.

134) Taro Tamura, Rev. Mod. Phys. 37 (1965) 679.

135) Taro Tamura, Computer Programme JUPITOR-1 for Coupled Channels Calculations, ORNL-4152 Oak Ridge National Laboratory (1967).

136) J.L.C. Ford, Jr., Cheuk-Yin Wong, Taro Tamura, R.L. Robinson and P.H. Stelson, Phys. Rev. 158 (1967) 1194.

137) M.N. Erduran, Ph.D. Thesis, University of Edinburgh, 1984.

ACKNOWLEDGEMENTS

I would like to express my sincere thanks and gratitude to Dr. R.B. Galloway, not only for suggesting this project, but also for his continual guidance, encouragement and interest. I would also like to thank Dr. D.G. Vass for his advice and encouragement.

I also wish to thank Messrs. H.J. Napier and G. Turnbull for their co-operation and helpful attitude.

To my family who have been a constant source of help and warmth.

To Mrs. Ray Chester for her help and speedy typing, my grateful thanks.

Nuclear Instruments and Methods 199 (1982) 549–555
North-Holland Publishing Company

THE DEPENDENCE ON SCINTILLATOR SIZE OF THE RESPONSE OF NE213 TO ELECTRONS AND PROTONS

Robert B. GALLOWAY and Hadi SAVALOONI
Physics Department, University of Edinburgh, Scotland

Received 17 August 1981 and in revised form 14 December 1981

The dependence of the relative light output for electron and for proton excitation of NE213 liquid scintillator has been investigated using four scintillators, two measuring 50 mm diameter by 50 mm long and two 305 mm diameter by 50 mm long. A dependence on scintillator size is found and a hypothetical explanation offered which is dependent on the presence of a conical light guide coupling the scintillator to the photomultipler. The measurements concern the proton energy range 1–14 MeV.

1. Introduction

It is a common practice when using an organic scintillation counter to detect fast neutrons to set the discrimination level using a gamma ray source and to use published data which relate the energy dependence of the light output from the scintillator due to electron excitation to that due to proton excitation. Such data for NE213 liquid scintillator are provided in refs. 1–10. There is, however, a significant spread in these data, as illustrated in ref. 1 and in fig. 7 below. Reasons suggested for variations in the relative response to electrons and to protons include differences in purity of the NE213 samples [5,11] and differences in methods used by different authors to locate the Compton edges in gamma ray spectra [1]. A dependence on scintillator size has also been suggested [9] although there is no clear support for this from consideration of all the available data [1–10]. Since each published set of data [1–10] concerns the response of one sample of NE213 it is not possible to distinguish differences truely due to variations in the properties of the NE213 samples from differences due to the measurement techniques. It was, therefore, decided to investigate sample to sample variations by making electron and proton response measurements on four NE213 scintillators described below.

1) 50 mm diameter by 50 mm long glass cell with external nitrogen bubble (NE VH1 cell, white painted externally *) mounted on 56 AVP photomultiplier.

2) 50 mm diameter by 50 mm long aluminium cylinder internally painted with titanium dioxide paint (NE 561 *) mounted on 56 AVP photomultiplier.

3) 305 mm diameter by 50 mm long internally painted aluminium cell with nitrogen expansion bubble in PTFE capillary tube (NE BA1 cell *) coupled by conical perspex light guide to XP1040 photomultiplier [12]. This scintillator had been in use for about 10 years.

4) 305 mm diameter by 50 mm long scintillator, light guide and photomultiplier combination as in (3) above but with scintillator cell freshly filled for the present measurements.

Four different production batches of NE213 are involved, of different ages, in cells of different sizes and with different constructions and so with different possibilities for contamination.

* Supplied by Nuclear Enterprises Limited, Sighthill, Edinburg, Scotland.

2. The measurements

It is well established that the light output due to the detection of electrons is a linear function of electron energy above 100 keV [5,8,13,14]. The electron response of the scintillators was, therefore, easily established from the locations of the Compton edges in the pulse height spectra due to ^{137}Cs, ^{22}Na and ^{60}Co gamma ray sources. Frequent electron response calibrations were made during the time spent on proton response measurement. The location of each Compton edge was determined by the method due to Flynn et al. [14], that is as the channel in which the number of counts equalled 72% of the mean number of counts around the maximum in the distribution. Prescott and Rupaal [15] from calculations folding together Gaussian and Klein–Nishina distributions and Beghian and Wilensky [16] from Monte Carlo calculations concluded that the Compton edge should be located at about 66% of the maximum in the distribution while Knox and Miller [17] concluded from experimental measurements that it should be at 89 ± 7%. Recently Dietze [18] has empha-

0167-5087/82/0000–0000/$02.75

Table 1
Proton response of NE213 detectors. The light output $L_p(E)$ is in arbitrarily chosen units such that one unit corresponds to the light output due to an electron of 0.48 MeV.

50 mm×50 mm scintillators				305 mm×50 mm scintillators			
Aluminium container		Glass container		Old		New	
Proton energy (MeV)	$L_p(E)$	Proton energy (MeV)	$L_p(E)$	Proton energy (MeV)	$L_p(E)$	Proton energy (MeV)	$L_p(E)$
1.96±0.08	0.91±0.11	1.92±0.08	0.94±0.11	1.33±0.01	1.01±0.10	1.06±0.01	1.05±0.10
2.17±0.09	1.04±0.14	2.10±0.09	1.12±0.12	1.64±0.01	1.27±0.10	1.33±0.01	1.16±0.12
2.63±0.11	1.14±0.14	2.17±0.09	1.24±0.12	2.00±0.01	1.57±0.12	1.71±0.01	1.54±0.15
2.74±0.11	1.54±0.15	2.53±0.10	1.27±0.12	2.11±0.01	1.67±0.14	2.01±0.01	1.83±0.15
2.98±0.12	1.66±0.16	2.74±0.11	1.45±0.13	2.39±0.01	1.78±0.14	2.34±0.01	2.02±0.15
3.24±0.13	1.91±0.16	2.98±0.12	1.58±0.13	2.75±0.01	2.22±0.15	3.09±0.02	2.72±0.18
3.40±0.14	2.08±0.18	3.19±0.13	1.70±0.15	2.87±0.01	2.52±0.15	4.29±0.03	4.16±0.25
				3.68±0.02	3.29±0.18		
2.61±0.05 [a]	1.58±0.10	– –	– –	2.61±0.05	2.06±0.13	2.61±0.05	2.24±0.13
14.05±0.03 [b]	16.97±0.25	– –	– –	13.86±0.04	17.60±0.25	13.58±0.10	17.70±0.25

[a] $^2H(d, n)^3H$ reaction.
[b] $^3H(d, n)^4He$ reaction.

sised the dependence of the location of the Compton edge on the energy and resolution of the detector and has investigated the behaviour of a 50.8 mm diameter by 50.8 mm long NE213 scintillator both by Monte Carlo calculation and by experiment. The calculations displayed for gamma-rays from ^{22}Na and the measurements for ^{137}Cs both indicate the Compton edge at about 75% of the number of counts at the maximum in the distribution. In fact our results are changed very little by changing the definition of the location of the Compton edge within the above range. The largest change would come from adopting the definition of Knox and Miller [17] which would increase the light output values in table 1 by about or less than the indicated uncertainty and would have no perceptible influence on the graphical presentation of the data in fig. 5. Thus, incidentally, it would seem that differences between past measurements of the response of NE213 as in fig. 7 are unlikely to be due to different ways of locating the Compton edge.

Proton response measurements were made using neutrons from an Am–Be source and a two scintillator time-of-flight arrangement (fig. 1) augmented by measurements on mono-energetic neutrons from the ^{2}H(d, n)^{3}He and ^{3}H(d, n)^{4}He reactions. For the measurements with the Am–Be source (fig. 1), neutrons were scattered by detector D1 through a known angle into detector D2 and the time-of-flight of each scattered neutron was determined. The 90 cm length of flight path was chosen to give an acceptable compromise between neutron energy resolution and counting-rate with the 100 mCi Am – Be neutron source used. A typical time-of-flight spectrum is shown in fig. 2. Events due to scattering of gamma rays between the detectors are clearly distinguished from events due to detection of neutrons in D2. The inherent time resolution of the system was found from measurements on the annihila-

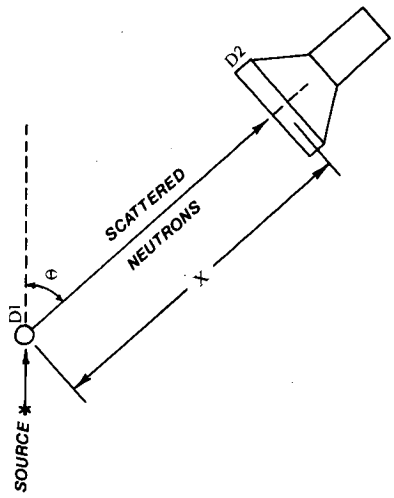

Fig. 1. The scattering and time-of-flight arrangement, $X = 90$ cm.

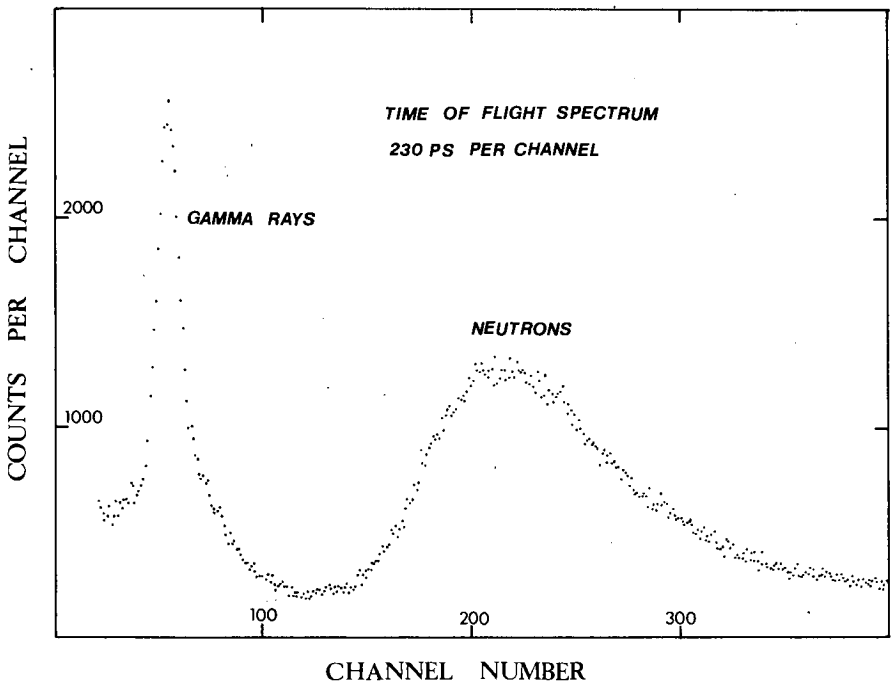

Fig. 2. A typical time-of-flight spectrum obtained with the experimental arrangement shown in fig. 1.

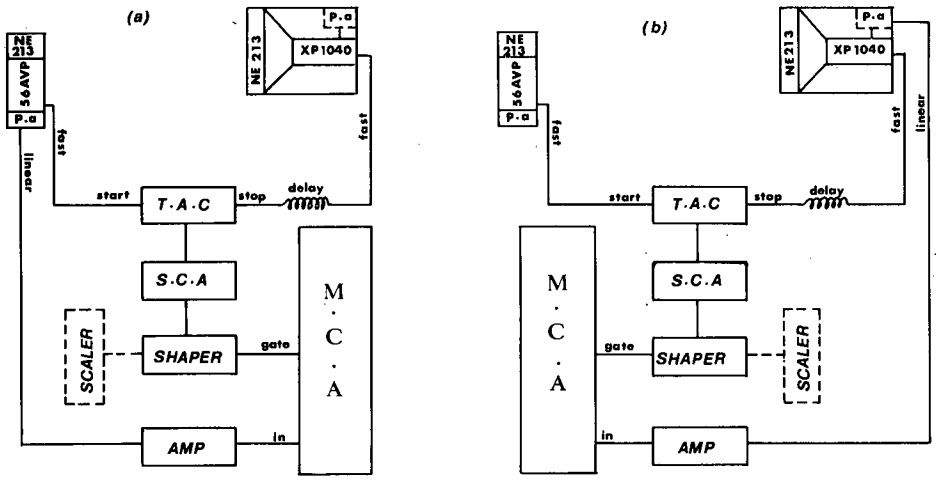

Fig. 3. (a) Block diagram of the electronic system used to observe the recoil proton pulse-height spectrum from detector D1 associated with a selected time-of-flight of scattered neutron. (b) Block diagram of the electronic system used to observe the recoil proton pulse-height spectrum from detector D2 associated with a selected time-of-flight of incident neutron.

tion photons from a ^{22}Na source placed between the detectors to be 3.5 ns. This can be compared with the uncertainty in the time of interaction of a neutron in each detector due to its 50 mm thickness which ranges from 1.5 to 3.5 ns for the energies investigated. Any attempt to place shielding near the detectors or neutron source increased the background of scattered neutrons unacceptably and so the measurements were made with the arrangement in fig. 1 without any shielding and 1.5 m away from floor and ceiling and much farther away from the walls of the room.

Considering the arrangement in fig. 1, by selecting a

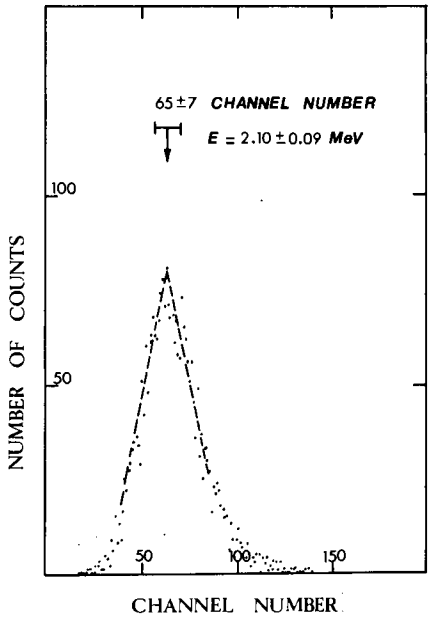

Fig. 4. A typical recoil proton spectrum from detector D1 associated with a particular scattered neutron time-of-flight. The mean proton recoil energy was 2.10±0.09 MeV.

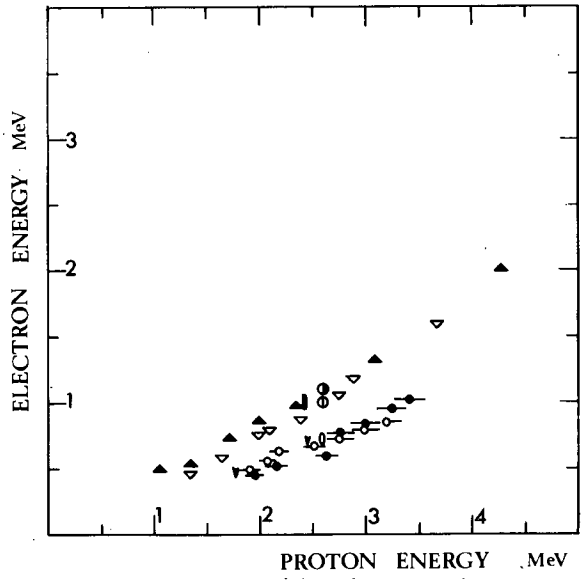

Fig. 5. Relative response of the four NE213 scintillation counters to electrons and protons. ▲ (305 mm×50 mm) new bubbled detector; ▽ (305 mm×50 mm) old detector; ○ (50 mm×50 mm) glass container; ● (50 mm×50 mm) aluminium container; ◤ (50 mm×50 mm) aluminium container as D2; ▌ (305mm×50 mm) new bubbled detector when used as scatterer D1; ◑ (305 mm×50 mm) new bubbled detector; 2.6 MeV ^{2}H(d, n)^{3}He reaction; ⊕ (305 mm×50 mm) old detector; 2.6 MeV ^{2}H(d, n)^{3}He reaction; ⓪ (50 mm×50 mm) aluminum container; 2.6 MeV ^{2}H(d, n)^{3}He reaction.

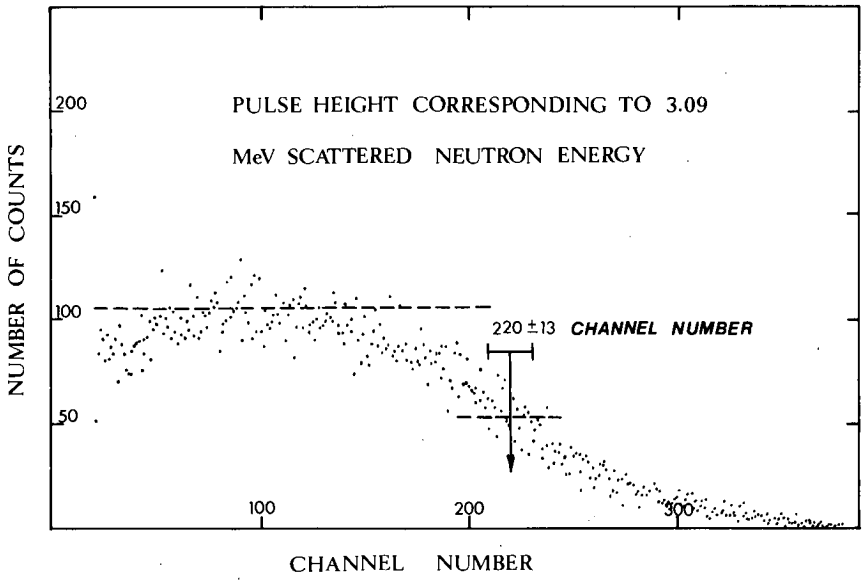

Fig. 6. A typical recoil proton spectrum from detector D2 associated with a particular neutron time-of-flight.

particular time-of-flight of scattered neutron the scattered neutron energy is defined and since the scattering angle is fixed, the energy of each associated recoil proton in detector D1 is defined. A block diagram of the electronic system used for this purpose is shown in fig. 3a. A typical pulse height spectrum from detector D1 associated with a selected scattered neutron flight time is shown in fig. 4. Thus by selecting different scattered neutron flight times the response of detector D1 to protons of different energies could be found. In interpreting the spectra such as fig. 4 account was taken of the uncertainty in the location of the peak and of the uncertainty in the associated mean proton recoil energy as deduced from the uncertainty in the mean energy of the selected scattered neutrons. Most of the response data for the two small detectors (50 mm diameter by 50 mm long) in table 1 and fig. 5 was obtained in this way. So far as detector D2 is concerned, selecting a particular time-of-flight for the scattered neutrons (as in fig. 3b) amounts simply to defining the energy of the neutrons incident on D2. Thus the pulse height spectrum from detector D2 associated with a particular flight time is the normal proton recoil spectrum for mono-energetic neutrons incident, as in fig. 6. Such spectra provided most of the response data for the two large detectors (305 mm diameter by 50 mm long) in table 1 and fig. 5. Fig. 5 clearly indicates a difference in behaviour between the large and the small detectors. The possibility was considered that this difference is in some way due to the small detectors having been used as scatterer (D1 of fig. 1) giving proton recoil spectra like fig. 4 while the large detectors were at the end of the flight path (D2 of fig. 1) giving proton recoil spectra like fig. 6. However, a measurement with a large detector as scatterer (D1) and a small detector at the end of the flight path (D2) can be seen in fig. 5 to eliminate this possibility.

As a further check on the trends in the data, detectors of both sizes were exposed to mono-energetic neutrons from the $^{2}H(d, n)^{3}He$ reaction. In this comparison the detectors and their pulse height spectra were all treated in exactly the same way and the trends of previous data confirmed as shown in fig. 5. Similar differences between the detectors were also found at higher neutron energy using neutrons from the $^{3}H(d, n)^{4}He$ reaction, table 1.

3. Discussion

The data, table 1 and fig. 5, show no significant difference in response between the two small detectors, a small difference between the two large detectors and a marked difference between the large detectors and the small detectors. The present data is compared with previous measurements in fig. 7. It can be seen that the present small detector data comes close to the data by Fowler et al. [1], Drosg [2], Bertin et al. [3], Taylor and Kalyna [4] and Batchelor et al. [10], while they tend to differ a little from the data by Alberigi Quaranta et al. [6] and Smith et al. [8]. They differ significantly from the trend of the data of Verbinski et al. [7] and markedly from the data of Rothberg et al. [9]. Thus the behaviour of both small detectors is consistent with the general trend of most previous measurements. The responses of both large detectors on the other hand differ significantly from all other measurements with the sole excep-

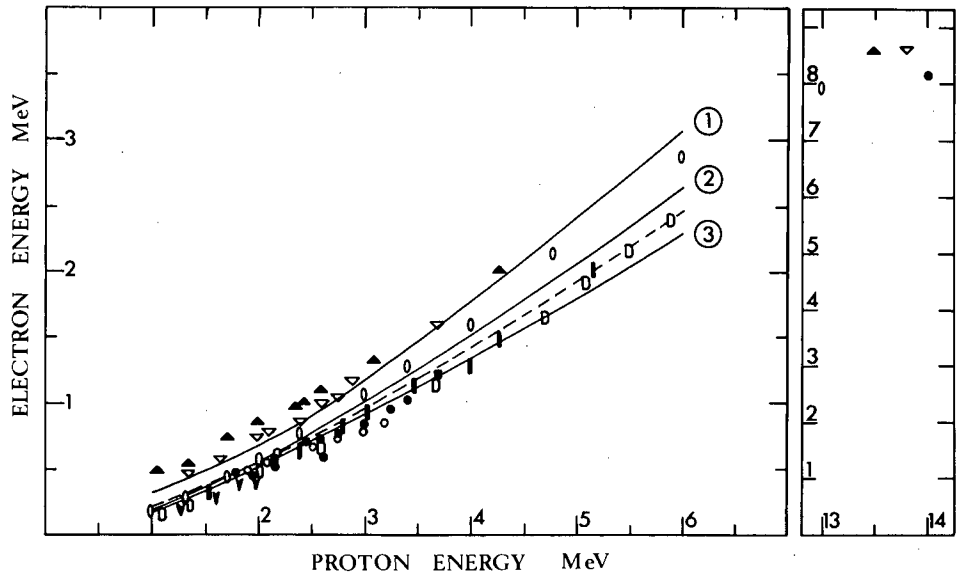

Symbol	Size	Ref.
Curve (1)	(152 mm×127 mm×101 mm)	Rothberg et al. [9]
Curve (2)	(50.8 mm×57.1 mm)	Smith et al. [8]
Curve (3)	(50.8mm×63.5 mm)	Batchelor et al. [10]
Dashed curve	(177.8 mm×101.6 mm)	Alberigi Quaranta et al. [6]
D	(120mm×57 mm)	Drosg [2]
0	(46 mm×46.5 mm)	Verbinsky et al. [7]
▬	(101.6mm×25 mm)	Taylor and Kalyna [4]
▮	(50.8 mm×38.1 mm)	Fowler et al. [1]
■	(127 mm×101.6 mm)	Bertin et al. [3]
▲	(305 mm×50 mm)	new bubbled detector
▽	(305 mm×50 mm)	old detector
●	(50 mm×50 mm)	aluminium container
○	(50 mm×50 mm)	glass container

Fig. 7. Comparison of the present and previous measurements.

tion that the curve due to Rothberg et al. [9] and the data on one of the large detectors are consistent. While it is tempting to note that the scintillator studied by Rothberg et al. [9] was the largest of the previously studied scintillators (150 mm × 125 mm × 100 mm), it is not significantly different in size from those studied by Bertin et al. [3] and by Alberigi Quaranta et al. [6]. The present large detectors (305 mm diameter by 50 mm long) are the only cases in which the scintillator is substantially larger than the photomultiplier cathode and in which a light guide is employed. These facts seem more relevant to an explanation of the behaviour than possible contamination of the NE213 in the large scintillators since one of them was newly filled for these tests while the other has been in use for 10 years. (Contamination may well account for the small difference between their responses.) Suggestions as to a possible explanation can be offered, although without any proof of correctness. An electron induced scintillation in NE213 consists principally of a "fast" component with a decay time constant of 4 ns along with a much less intense component with a decay time constant of 25 ns whereas for a proton induced scintillation the "fast" 4 ns component is accompanied by a relatively intense "slow" component of decay time constant 47 ns [19]. If the important "slow" component in the proton induced scintillation were of a different wavelength from the "fast" component which is predominant in the electron induced scintillation, then preferential absorption of the proton induced scintillation might occur in the perspex light guide. In this connection it may be noted that Kalyna and Taylor [20] discussing pulse shape discrimination with scintillators of larger diameter than the photomultiplier cathode comment on

the desirability of keeping the coupling light guide as short as possible. Alternatively, the sensitivity of a photocathode is often more wavelength dependent near the edge [21] and if the action of the light guide were to direct, by total internal reflection for example, a large proportion of the scintillations to the edge of the photocathode a different sensitivity to electron and proton induced scintillations might result compared with a small scintillator mounted without light guide when the photocathode would be more uniformly illuminated. Kalyna and Taylor [20] have commented on the greater importance of the illumination of the edge of the photocathode when a conical light guide is employed, albeit in relation to the poorer quality of zero-crossover timing pulse shape discrimination.

We conclude that for an NE213 scintillation counter with a large scintillator coupled by a conical light guide to a small photomultiplier there is a significant difference in the electron–proton relative response function from that applicable to a small sample of NE213 mounted directly on a photomultiplier.

We thank H.J. Napier and G. Turnbull for their help with the experiment.

References

[1] J.L. Fowler, J.A. Cookson, M. Hussain, R.B. Schwarz, M.T. Swinhoe, C. Wise and C.A. Uttley, Nucl. Instr. and Meth. 175 (1980) 449.
[2] M. Drosg, Nucl. Instr. and Meth. 105 (1972) 573.
[3] A. Bertin, A. Vitale and A. Placci. Nucl. Instr. and Meth. 91 (1971) 649.
[4] I.J. Taylor and J. Kalyna, Nucl. Instr. and Meth. 88 (1970) 267.
[5] R.L. Craun and D.L. Smith, Nucl. Instr. and Meth. 80 (1970) 239.
[6] A. Alberigi Quaranta, A. Bertin, G. Matone, F. Palmonari, G. Tornelli, P. Dalpiaz, A. Placci and E. Zavattini, Phys. Rev. 177 (1969) 2118.
[7] V.V. Verbinski, W.R. Burns, T.A. Love, W. Zobel, N.W. Hill and R. Textor, Nucl. Instr. and Meth. 65 (1968) 8.
[7] D.L. Smith, R.G. Polk and T.G. Miller, Nucl. Instr. and Meth. 64 (1968) 157.
[9] J.E. Rothberg, E.W. Anderson, E.J. Bleser, L.M. Lederman, S.L. Meyer, J.L. Rosen and I.T. Wang, Phys. Rev. 132 (1963) 2664.
[10] R. Batchelor, W.B. Gilboy, J.B. Parker and J.H. Towle, Nucl. Instr. and Meth. 13 (1961) 70.
[11] J.B. Birks, The theory and practice of scintillation counting (Pergamon, 1964).
[12] R.B. Galloway and D.G. Vass, Nucl. Instr. and Meth. 83 (1970) 35.
[13] D.T. Ingersoll and B.W. Wehring, Nucl. Instr. and Meth. 147 (1977) 551.
[14] K.F. Flynn, L.E. Glendenin, E.P. Steinberg and P.M. Wright, Nucl. Instr. and Meth. 27 (1964) 13.
[15] J.R. Prescott and A.S. Rupaal, Can. J. Phys. 39 (1961) 221.
[16] L.E. Beghian and S. Wilensky, Nucl. Instr. and Meth. 35 (1965) 34.
[17] H.H. Knox and T.G. Miller, Nucl. Instr. and Meth. 101 (1972) 519.
[18] G. Dietze, IEEE Trans. Nucl. Sci. NS-26 (1979) 398.
[19] B. Sabbah and A. Suhami, Nucl. Instr. and Meth. 58 (1968) 102.
[20] J. Kalyna and I.J. Taylor, Nucl. Instr. and Meth. 88 (1970) 277.
[21] G.S. Birth and D.P. DeWitt, Appl. Opt. 10 (1971) 687.